Time Domain Metrology for MeerKAT Systems

by

Nardus Matthysen

Thesis presented in partial fulfilment of the requirements for the degree of Master of Science in the faculty of Electrical and Electronic Engineering at Stellenbosch University

The Department of Electrical and Electronic Engineering,
University of Stellenbosch,
Private Bag X1, Matieland 7602, South Africa.

Supervisor: Prof H.C. Reader
Dr P.G. Wiid

December 2014

Declaration

By submitting this thesis electronically, I declare that the entirety of the work contained therein is my own, original work, that I am the sole author thereof (save to the extent explicitly otherwise stated), that reproduction and publication thereof by Stellenbosch University will not infringe any third party rights and that I have not previously in its entirety or in part submitted it for obtaining any qualification.

December 2014
Nardus Matthysen

Acknowledgements

- The University of Stellenbosch for the use of their facilities.
- Professor Howard Reader, for his guidance and supervision and allowing me to benefit from his experience and knowledge in metrology.
- Dr Gideon Wiid, for his guidance and supervision and help with the final phases of the project and thesis.
- My fiancée, Marli. Your support during my masters was invaluable.
- My family. Thank you for listening and motivating me.
- Mr J. Coetzee. Thank you for your time and final touches to the thesis.
- Mr Wessel Croukamp and Mr Lincoln Saunders, for their assistance with the mechanical construction of the IRA and pulse generators.
- Miss Anneke Bester, for her assistance with the calibration and measurements of the IRA system on the roof and in the laboratories.
- The CHPC and SKA for the financial backing and opportunity to be part of a larger project.
- EMRIN-G: Antheun Botha, Joelly Andriambeloson, Hardie Pienaar, Stephan Combrink, Temwani Phiri and Stanley Kuja. Thank you for your contribution and assistance with my masters. You made mundane office days very entertaining.
- *Soli Deo gloria*

Abstract

Time Domain Metrology for MeerKAT Systems

N. Matthysen

The Department of Electrical and Electronic Engineering,
University of Stellenbosch,
Private Bag X1, Matieland 7602, South Africa.

Thesis: Master of Science in Electronic Engineering

December 2014

This work in this study covers a powerful technique to derive propagation and scattering information in an expedient fashion. Expedient because time-domain (TD) data gathers a broad spectrum in a single transmitted pulse. TD has been criticised because of a lack of dynamic range, which has now been overcome by the direct sampling system, RATTY and RTA. This study focuses on the investigation of a TD metrology system, to assist with the characterisation of MeerKAT systems. The elementary components of the system include a fast-rising impulse generator that was coupled with an impulse radiating antenna (IRA). The system was calibrated and tested before practical measurements and preliminary testing in the Karoo were done.

For TD metrology a larger bandwidth accelerates measurements without the loss of accuracy. The pulse generator's (PG's) fundamental components are an avalanche transistor and a step recovery diode (SRD), to sharpen the leading edge of the pulse. Improving the rise-time of a pulse increases its bandwidth in the spectrum. The external circuitry around these components is pivotal and it determines the shape, amplitude and rise-time of the pulse. In the course of the investigation, the general circuitry around the PG was improved to obtain the best possible pulse for measurements inside a reverberation chamber (RC) and for measurements in the Karoo. In light of this, a second and third PG source were obtained. For measurements in the Karoo, a larger amplitude pulse was required to increase the spectral content and this is essential for propagation measurements over distance and the shielding effectiveness (SE) of structures. Stacking avalanche transistors allow larger amplitude pulses and it improves the dynamic range of the spectrum. A PG incorporating stacked avalanche transistors, was designed, built and measured to assist with RC and small-scale field measurements in the Karoo. The third PG was bought for the practical measurements in the Karoo. The PG produces kilovolt pulses with pico-second rise-times that extend the spectral range of the current PGs at our disposal.

With these PGs, an antenna is required for the radiation of impulse-like transients. The IRA is a high-gain large-bandwidth antenna. The IRA consists of a parabolic reflector, conical-plate transmission lines that are terminated through resistors onto the dish, and a feeding balun. The IRA design was thoroughly discussed and a first model for metrology was designed, measured and optimised. The IRA was also simulated with computation software code, *FEKO*.

Before deployment of the TD system, calibration and characterisation measurements are required. The measuring devices used within this study were sampling oscilloscopes and direct sampling systems. The limitations of each device were explored and are discussed. The final measurements that

were conducted contribute to work related to the SKA. This incorporated antenna pattern calibration, propagation over distance and the SE of a berm built from Karoo soil. The system investigated the propagation attenuation over the Karoo soil and vegetation, with great promise. A broad spectrum was measured over a few kilometres and compared to free-space loss. The SE of the berm covered the same spectral bandwidth. In this measurement, scattering effects and knife-edge diffraction were observed.

Uittreksel

Tydgebiedmetings vir die MeerKAT Stelsels

N. Matthysen

Die Departement van Elektries en Elektroniese Ingenieurswese,
Universiteit van Stellenbosch,
Privaatsak X1, Matieland 7602, Suid Afrika.

Tesis: Magister in die Natuurwetenskappe in Elektroniese Ingenieurswese

Desember 2014

Die werk in hierdie studie dek 'n kragtige tegniek wat gebruik kan word om die voortplanting en die verstrooiingsinligting van elektromagnetiese golwe op 'n voordelige manier af te lei. Dit is voordelig, want tydgebieddata versamel 'n wye spektrum in 'n enkele oordraagbare puls. Tydgebied is in die verlede baie gekritiseer omdat dit 'n dinamiese reikwydte kortkom en dit is nou oorwin deur die direkte steekproefnemingstelsel, RATTY en RTA. Hierdie studie fokus op die ondersoek van 'n tydgebiedmetingssisteem en dit help met die karakterisering van MeerKAT sisteme. Die elementêre komponente van die sisteem bestaan uit 'n vinnig-stygende impulsgenerator wat gekoppel is aan 'n impulsuitstralende-antenna (IRA). Die sisteem is gekalibreer en getoets voordat praktiese metings en toetse in die Karoo uitgevoer kon word.

Vir tydgebiedmetings versnel 'n groter bandwydte die metings sonder om die akkuraatheid daarvan te beïnvloed. Die pulsgenerator se fundamentele komponente is 'n stortvloedtransistor en 'n stap-herstel diode (SRD) wat die voorpunt van die puls verskerp. Die eksterne stroombaan rondom hierdie komponente is noodsaaklik en dit bepaal die vorm, amplitude en die stygtyd van die puls. Deur die loop van hierdie ondersoek is die algemene stroombaan rondom die puls verbeter, om die beste moontlike puls vir metings binne in die weerkaatsingskamer en vir metings in die Karoo, te verkry. Na aanleiding van dit is 'n tweede en derde pulsgenerator bron verkry. Vir die metings in die Karoo is 'n puls met 'n groter amplitude vereis om die spektrale inhoud te vermeerder. Dit is noodsaaklik vir elektromagnetiese golf voortplantingsmetings oor afstand asook die beskermings effektiwiteit (SE) van die strukture. Stapel-stortvloed transistors skep pulse met groter amplitudes en dit verbeter die dinamiese reikwydte van die spektrum. 'n Pulsgenerator wat gestapelde stortvloedtransistors insluit is ontwerp, gebou en gemeet om te help met metings in die weerkaatsingskamer en kleinskaal veldmetings in die Karoo. Die derde pulsgenerator is gekoop vir praktiese metings in die Karoo. Die pulsgenerator vervaardig kilovolt pulse met pikosekond stygtye, wat die reikwydte van die spektrum van ons huidige puls uitbrei.

Hierdie pulsgenerators vereis 'n antenna vir die uistraling van impulsagtige seine. Die IRA is 'n hoë-wins, groot-bandwydte antenna. Die IRA bestaan uit 'n paraboliese weerkaatser, konieseplaat transmissielyne wat deur weerstande op die skottel getermineer word, asook 'n voedings "balun". Die IRA ontwerp is deeglik bespreek en 'n model is ontwerp, gemeet en verbeter. Die IRA is ook gesimuleer met behulp van 'n rekenaarsagtewareprogram, *FEKO*.

Voordat die tydgebiedsisteem benut kan word, moet dit gekalibreer word en karakteriserings-metings moet ook daarmee uitgevoer word. Die meetinstrumente wat in hierdie studie gebruik is, is steekproefneming-ossilloskope en direkte steekproefneming-sisteme. Die tekortkominge van elke instrument is ondersoek en bespreek. Die finale meting wat uitgevoer is, dra by tot die werk wat geassosieer word met die SKA. Dit behels antennapatroonkalibrasie, voortplanting van elektromagnetiese golwe oor afstand en die SE van ’n "berm"wat gebou is uit Karoo-grond. Hierdie sisteem is gebruik om die voortplantings-verswakking oor die Karoo-grond en plantegroei te ondersoek en dit lyk baie belowend. ’n Wye spektrum is oor ’n paar kilometer gemeet en dit is met wrywinglose ruimte vergelyk. Die SE van die "berm"het dieselfde spektrale bandwydte gedek. In hierdie meting is verstrooiingseffekte en mespunt-diffraksie waargeneem.

Contents

Declaration i

Acknowledgements ii

Abstract iii

Uittreksel v

List of Figures ix

List of Tables xiii

Nomenclature xiv

1 Introduction 1

2 Literature study 3
2.1 Pulse generators . . . 3
2.2 Impulse radiating antenna . . . 7
2.3 Time-domain metrology . . . 10
2.4 Conclusion . . . 12

3 Pulse generators 13
3.1 Single avalanche transistor impulse generator (30V Pulse) . . . 14
3.2 Stacked avalanche transistor impulse generator (50V Pulse) . . . 28
3.3 Characteristics of the CPS1 PG (A commercial PG bought from Kentech industries) . . . 32
3.4 Conclusion and recommendations . . . 34

4 Impulse radiating antenna 36
4.1 Design components of the IRA . . . 36
4.2 Simulation . . . 45
4.3 Characterisation and optimisation of final IRA design . . . 51
4.4 Final model with measured results . . . 63
4.5 Conclusion . . . 65

5 Time-domain metrology 67
5.1 Direct measurements with transmitting sources and sampling devices . . . 68
5.2 Experimental measurements with IRA and PG sources into free-space . . . 74
5.3 Final calibration of the IRA and CPS1 PG with RTA for practical Karoo metrology . . . 80
5.4 Conclusion . . . 85

6 Practical metrology of the TD system at the Karoo core-site 88
6.1 Antenna pattern measurement . . . 88

6.2 Propagation measurements over distance . . . 91
6.3 Shielding effectiveness measurements of the berm . . . 96
6.4 Conclusion and recommendations . . . 101

7 Conclusion and recommendations 103
7.1 Conclusion . . . 103
7.2 Recommendations . . . 104

Bibliography 106

A Final components and values for the PG and IRA 110
A.1 30 V PG Design components and PCB . . . 110
A.2 50 V PG Design components and PCB . . . 111
A.3 Splitter first and second design . . . 112

B Matlab code for calculations, figures and measuring equipment 113
B.1 Pulse generators . . . 113
B.2 IRA . . . 115
B.3 Metrology . . . 115

C Data sheet of SRD 130

D Air breakdown calculations 131
D.1 Peak power handling of a coaxial cable . . . 131

E Pulse generator external measurements 133
E.1 Biasing SRD at different voltage levels . . . 133
E.2 Amplitude changes over a long record length . . . 134

F Components and cable responses 135
F.1 Cable losses . . . 135
F.2 30 dB 100W and 110 dB 4 GHz attenuators spectrum . . . 136
F.3 Anechoic chamber measurements . . . 137
F.4 GLPDA gain, reflection coefficient and antenna factor . . . 138

List of Figures

2.1 Electron and hole diffusion of a NPN transistor biased in the forward-active mode, after [6]. 4
2.2 Collector current versus collector-emitter voltage [9]. 5
2.3 A simple PG model with a SRD circuit. 6
2.4 Basic mercury-wetted switch PG circuit. 7
2.5 Basic IRA design. 8
2.6 Aperture antenna with a specified tangent electric field. 9
2.7 Real-time sampling with the reconstructed signal, after [25]. 11
2.8 Sequential sampling of a sampling oscilloscope with the reconstructed signal, after [25]. . 11

3.1 Typical impulse generator circuitry, after [25]. 14
3.2 30V PG circuit schematic. 14
3.3 Time and frequency responses of PG after simulated 10 dB increase in spectrum. 16
3.4 Time and frequency responses of PG after simulated linear increase in spectrum. 17
3.5 Changing the capacitance per unit length of the microstrip line 18
3.6 Results from the PG with three different impedances at the collector line. 19
3.7 Collector line PG test circuit schematic. 19
3.8 Shorted line output pulse and circuit configuration, after [3]. 20
3.9 Comparison of the pulses measured from the PGs with the different shorted lines and SRDs. 21
3.10 Spectral content of the pulses measured from the PGs with the different shorted lines and SRDs. 22
3.11 Pulses with the different capacitors at the output of the PG. 24
3.12 Spectrum of the filtered pulses by the different capacitors placed at the output of the PG. . 24
3.13 Picture of the test board and the test PGs. 25
3.14 Photograph of the 30 V PG. 26
3.15 Final pulse measured on HP 54750A with the 30 V PG. 26
3.16 Spectral density of final pulse measured on HP54750A with the 30 V PG compared to previous PG models. 27
3.17 Stacked PG circuit schematic. 28
3.18 Pulse of the stacked PG measured on Yokogawa sampling scope in the interleaved mode. . 29
3.19 Spectral content of the stacked PG measured on Yokogawa sampling scope in the interleaved mode. 30
3.20 Picture of the stacked PG. 30
3.21 Final pulse of the stacked PG measured on HP54750 sampling scope. 31
3.22 Final spectral content of the stacked PG measured on HP 54750 sampling scope compared to the 30 V PG. 32
3.23 Pulse produced by CPS1 impulse generator. 33
3.24 Spectrum of the CPS1 impulse generator. 33

4.1 The basic parts of the impulse radiating antenna. 37
4.2 The IRA with the conical plate design equations. a)Side view. b)Front view. [39] 38
4.3 A single fed 150 Ω IRA, after [44]. 40

4.4 A three-port resistive power divider. . . . 41
4.5 The T-junction model simulated in CST. . . . 41
4.6 Comparison of the resistive splitter simulated on CST and Microwave Office. . . . 42
4.7 A picture of the T-junction Splitter. . . . 42
4.8 Dimensions of constructed and simulated IRA. A side view as well as a 3D view of the corner of the IRA. . . . 44
4.9 The front and backside of the IRA with splitter mounted on the back. . . . 45
4.10 Feeding point of the IRA. . . . 45
4.11 Model of IRA in FEKO. . . . 45
4.12 The Gain (S_{21}) of the antenna over frequency. . . . 46
4.13 The vertical polar pattern of the IRA at various frequencies. . . . 46
4.14 The horizontal polar pattern of the IRA at various frequencies. . . . 46
4.15 The half power beamwidth of the IRA vertically polarised. . . . 48
4.16 Magnitude and Phase of IRA Impedance over Frequency. . . . 48
4.17 Smith Chart of IRA Impedance. . . . 49
4.18 Reflection Coefficient of IRA. . . . 49
4.19 The Far-field of the IRA in 3D format. . . . 50
4.20 The currents on the IRA in 3D format. . . . 50
4.21 Picture one of the measuring setup with IRA and VNA into anechoic chamber. . . . 51
4.22 Picture two of the measuring setup with phase stable cables 51
4.23 Measurement setup for optimisation and characterisation of antenna system. . . . 52
4.24 An electrical circuit representation of antenna. . . . 52
4.25 Time low-pass response of the antenna system. . . . 54
4.26 Splitter measuring setup with vector network analyser. . . . 55
4.27 TD analysis of splitter - time gated. . . . 55
4.28 S-parameters of splitter with both measuring configurations. The ripples indicates a problem with multiple reflections because of the mismatch, which time gating removes 56
4.29 S-parameters of splitter with both measuring configurations and the CST results. . . . 57
4.30 Low-pass responses of known discontinuities with step and impulse response [46]. . . . 58
4.31 Comparison of FD of antenna and gated without the splitter response. . . . 58
4.32 Mitred bend design of the splitter. . . . 59
4.33 Y-Junction design of the splitter 59
4.34 Splitter Results compared from CST 60
4.35 Splitter currents compared on 3D models. . . . 60
4.36 Improved splitter measured on the VNA with two mismatched output ports. . . . 61
4.37 Improved splitter measured with the IRA and time gated on the VNA 62
4.38 Improved IRA feed in the TD. . . . 62
4.39 Improved IRA feed in the FD. . . . 63
4.40 Picture of old and new splitters compared. . . . 64
4.41 Picture of old and new focal points compared. . . . 64
4.42 Final picture of the IRA. Picture is taken in the Karoo during an atenna pattern measurement. 64
4.43 Final Results of IRA with the improved splitter (time gated) and compared to simulated reflection coefficient in FEKO. . . . 65

5.1 Measurement configuration of the 30 V PG for direct pulse measurements. . . . 69
5.2 Transient response of pulses from the 30 V PG measured on measuring equipment. . . . 70
5.3 Frequency response of pulses from the 30 V PG measured on measuring equipment. . . . 70
5.4 Multiple pulses captured by RATTY to indicate the varying amplitudes. . . . 71
5.5 Measurement configuration of the CPS1 PG for direct pulse measurement. . . . 72
5.6 TD pulses of the CPS1 measured with different measuring equipment. . . . 73
5.7 Spectrum of measured pulses with different measuring equipment. . . . 73
5.8 Dry-run configuration of IRA with TEM Horn and 30V pulse generator. . . . 75

5.9 Picture of the dry-run configuration of IRA with TEM Horn and 30V pulse generator. . . . 75
5.10 Time-domain pulses measured with TEM Horn on the ground and lifted 500 mm from the ground. . . . 76
5.11 Spectrum of pulses measured with TEM Horn and HP54750A with a calculated expected spectrum. . . . 77
5.12 Dry-run configuration of IRA with LPDA and CPS1 impulse generator. . . . 78
5.13 Transient measurement of IRA with LPDA and CPS1 impulse generator. Green pulse is from RATTY band 1 and red pulse is from RATTY band 2 to show the dispersion 78
5.14 Spectrum of IRA with LPDA and CPS1 impulse generator. . . . 79
5.15 RTA gain calibration over the respective bands. . . . 81
5.16 Configuration of a direct pulse measurement with RTA and the CPS1 pulser. . . . 82
5.17 Direct measurement with RTA and the CPS1 pulser only for band 1. . . . 83
5.18 Log-domain and time-domain of selected pulses 83
5.19 Spectrum from maximum and average pulses with two different time-gated lengths applied. 84
5.20 Delta between maximum and average spectrum. . . . 85
5.21 Spectrum of CPS1 Pulse on all four bands in RTA. . . . 86

6.1 Picture of antenna pattern measurement. . . . 89
6.2 Antenna pattern measurement configuration - side view. . . . 89
6.3 Antenna pattern measurement configuration - top view. . . . 89
6.4 Spectrum of antenna pattern measurement. . . . 90
6.5 Photographs of the propagation measurements at 10 m, 100 m and 400 m - taken by P.G. Wiid 91
6.6 Propagation measurement over 10 m, 100 m and 400 m with a FSPL calculated spectrum. 92
6.7 Difference between expected FSPL spectrum and measured propagation spectrum at 100 m and 400 m. . . . 93
6.8 Propagation measurement at 400 m across the gravel road and over the Karoo foliage. . . 93
6.9 Pictures of propagation measurements over the Karoo foliage - taken by P.G. Wiid 93
6.10 Google Earth map of long distance propagation. . . . 94
6.11 Propagation results at Meysdam, M60 and M59. . . . 95
6.12 Picture of PCB-LPDA during a for propagation measurements during sunset - taken by P.G. Wiid. . . . 96
6.13 Karoo array processor building, berm and Losberg in perspective with KAT7. . . . 97
6.14 Berm measurement configuration. . . . 97
6.15 Measurement of berm attenuation with the IRA at all TP's and RTA at the different distances behind the berm. . . . 98
6.16 Berm attenuation compared to three different transmitting heights at certain meters away from the berm. . . . 100
6.17 Panoramic pictures of the berm measurements and KAPB environment. . . . 102

A.1 30 V PCB scaled 1:1. . . . 111
A.2 50 V PCB scaled 1:1. . . . 112
A.3 PCB of both the splitters scaled 1:1. . . . 112

C.1 Data sheet of the SRD with biasing currents. . . . 130

E.1 SRD biased with four different biasing voltages. . . . 133
E.2 All four pulses sampled in one record length with different amplitudes. . . . 134
E.3 All four pulses separately sampled and displayed on one graph. . . . 134

F.1 Cable Losses of a Sucoflex 104 3.1 m and 8 m cable. . . . 135
F.2 Reflection and transmission coefficient of the 30 dB 100 W 1 GHz attenuator. . . . 136

F.3 Reflection and transmission coefficient of the 110 dB 4 GHz variable attenuator on a 10 dB setting. . . . 137
F.4 Gain measurements in anechoic chamber. . . . 137
F.5 GLPDA Gain at the lower frequencies. . . . 138
F.6 GLPDA Gain. . . . 138
F.7 GLPDA reflection coefficient at the lower frequencies. . . . 138
F.8 GLPDA reflection coefficient. . . . 138
F.9 GLPDA Antenna Factor at the lower frequencies. . . . 138
F.10 GLPDA Antenna Factor. . . . 138

List of Tables

4.1 Dimensions, characteristics and components of the IRA 43

6.1 Locations and distances of the long propagation measurement. 94

A.1 Table including all the component values for the 30 *V* PG. 110
A.2 Table including all the component values for the 50 *V* PG. 111
A.3 Components and characteristics of splitter. 112

F.1 Cable attenuation table from Huber and Suhner 136

Nomenclature

Abbreviations

BJT	Bipolar junction transistor
BW	Bandwidth
CAD	Computer aided design
CHPC	Centre for high-performance computing
CST	Computer simulation technology
DC	Direct Current
D.U.T	Device under test
E-field	Electric field
EM	Electromagnetic
EMC	Electromagnetic compatibility
FD	Frequency-domain
FSPL	Free-space path loss
FWHM	Full-width half maximum height
IRA	Impulse radiation antenna
KAT	Karoo array telescope
LPDA	log-periodic dipole array
PCB	Printed circuit board
PGs	Pulse Generators
RATTY	Real-time transient analyser
RC	Reverberation Chamber
RF	Radio frequency
RFI	Radio frequency interference
RMS	Root mean square
RTA	Real-time analyser
SE	Shielding Effectiveness
SKA	Square Kilometre Array
SRD	Step recovery diode
TD	Time-domain
TDR	Time-domain reflectometry
TEM	Transverse electromagnetic
TM-line	Transmission line
VNA	Vector network analyser

Constants

c	Speed of light (3×10^8)
η_0	Free-space wave impedance (377 Ω)

Variables

α	Current gain of transistor
α_0	Current gain of transistor at low biasing voltages
I_C	Collector current
I_E	Emitter current
M	Multiplication factor inside a BJT
τ	minority carrier lifetime
Q	Charge
i	Current
J_S	Electric current density
M_S	Magnetic current density
s	Laplace transform
μ_o	Permeability
ϵ_o	Permittivity
λ	Electromagnetic wavelength

Vectors

$\vec{\boldsymbol{l_o}}$	Direction vector

Chapter 1

Introduction

The Square Kilometre Array (SKA) forms part of an international project determined to build the world's largest radio telescope and to deliver a transformational increase in science when it is operational. This project intends to probe the origins of the universe and these telescopes are aimed to equip astronomers to monitor the sky in unprecedented detail. The SKA will be 50 times more sensitive and will have one million times faster surveying speeds than any radio astronomy instrument that currently exists. The SKA is based in South-Africa and Australia. SKA South-Africa is located 90 km from the small town Carnarvorn, in the Karoo. The SKA has constructed and designed the Karoo Array Telescope (KAT) which is currently built. Seven telescopes (KAT7) are operational. Another 64 will be deployed across the Karoo to form part of an array of telescopes called *MeerKAT*.

MeerKAT receives electromagnetic (EM) waves from cosmic radio sources that reflect from a main and sub-reflector into a feed horn. The EM waves of interest are far from the full universe and require low radio frequency (RF) noise levels. This is one of the main reasons the SKA has chosen the Karoo environment to host this project. Due to the highly sensitive receivers in MeerKAT, radio frequency interference (RFI) in the vicinity can cause receivers to saturate. The SKA requires an extremely quiet EM environment and this study is aimed at contributing to make a quiet environment possible.

The focus for this study is time-domain (TD) metrology for MeerKAT systems. Previous investigation of EM quiet zones were implemented in the frequency-domain (FD). FD analysis required a signal generator, a radiating antenna, a receiving antenna and a measuring instrument. Single frequency points were transmitted and received in order to characterise the Karoo environment. Propagation measurements were done for certain distances, over the Karoo soil and foliage, and only distinct frequency points could be compared. For a broader spectrum, more time for measurements is required and this is not always available. FD metrology remains powerful and contributes significantly to the EM and metrology field, but has limitations that can be improved by the TD equivalent. The first work in TD electromagnetics began in the 1960's with Bennett and Ross [1], where attempts were made to classify the analytical solution of the transient behaviour of a TEM-mode microwave network. The impulse response of the network was classified as a train of impulses. By using a periodic transient impulse, a linear time-invariant network could be completely specified by its impulse response. With the improvement of sampling oscilloscopes and the baseband-pulse generator with a sub-nanosecond rise-time, greater observation of the transient response of distributed networks and materials can be made [1]. With a well-defined impulse response, the injection of a pulse into a microwave network can determine the transfer function of the device under test (D.U.T.), by analysing reflections and transmission from the D.U.T.

TD analysis provides speed-up without the loss of accuracy [2]. A single pulse with a sub-nanosecond rise-time can produce instantaneous energy from DC up to microwave frequencies. The previous limit from FD analysis can be overcome by injecting a high-amplitude large-bandwidth pulse over

Karoo soil in order to calibrate the environment. TD analysis can also be implemented to test the shielding effectiveness (SE) of cables, connectors, enclosures and for this study, a berm built by Karoo soil. The focus for this study was to develop, design and deploy a TD transmitting system to assist with metrology around the Karoo environment. The system consists of an impulse generating device and an impulse radiating antenna (IRA) that is used to radiate these transients.

Chapter 2 contains a short literature study on pulse generators, impulse radiating antennas and sampling oscilloscopes. A brief description on the measuring equipment used during this study is included.

Chapter 3 focuses on the design and optimisation of the impulse generator. Two pulse generators (PGs) are designed and measured. The different techniques applied in order to optimise the PG circuit are discussed. The techniques explored consisted of the following: increasing the potential at the collector of the transistor by increasing the width of the microstrip line at this point; implementing and improving the shorted line technique used in [3]; filtering the output of the pulse. Stacking avalanche transistors are also examined in this chapter and the results from stacked transistors are discussed. The chapter concludes with final measurements of an industrial PG bought from Kentech industries.

Chapter 4 thoroughly discusses the design, simulation and final results of an impulse radiating antenna (IRA). The IRA is simulated in FEKO and optimised with measurements.

Chapter 5 documents the calibration and TD metrology of fast-rising impulses on four sampling devices. The four devices that are discussed are: A 50 GHz HP 54750 sampling oscilloscope, the 500 MHz DLM2052 Yokogawa sampling oscilloscope and two direct sampling systems - a real-time transient analyser (RATTY) and real-time analyser (RTA). More information about the direct sampling systems can be read in [4]. The chapter will explain how pulses are measured, analysed and processed for practical measurements in the Karoo.

Chapter 6 contains all the practical measurements of the TD system in the Karoo. The antenna pattern of the IRA is measured as well as propagation measurements over distance and the SE of a berm ("nuweberg"). During the propagation measurements the limits of the system are tested through long distance measurements, preliminary testing and characterising the propagation attenuation of the Karoo foliage. The SE of the berm is tested by placing the transmitting antenna at three different heights and receiving the pulse three distances behind the berm.

Chapter 7 provides an overview of the project with conclusions and recommendations.

Chapter 2

Literature study

2.1 Pulse generators

Today, electronics are mostly classified as circuits that implement transistor applications or multiple transistors. Bell Telephone Laboratories first investigated semiconductor technologies in 1947 and since then, the field of electronics has significantly evolved [5]. The transistor operates as an amplifier or switch, in most integrated circuit designs.

Another technique that is commonly used with a transistor, is the implementation of a fast-rising switch for impulse generation. Operation of transistors in a non-ideal state allows for such designs. Transistors are usually forward biased and forced into breakdown to create fast-rising impulses for comb generators, timers and various other applications. For this study a transistor is forced into avalanche breakdown, which greatly increases current through the transistor to create sub-nano second impulses. The pulse is shaped by a step-recovery diode (SRD) to sharpen the leading edge of the pulse. The pulse generator will be used for shielding measurements inside a reverberation chamber, pulse propagation around Karoo vegetation and TD metrology.

2.1.1 Avalanche transistors

The Bipolar Junction Transistor (BJT) is part of the semiconductor family. The BJT has three separately doped regions, consisting of either two positively doped regions and one negative region (PNP), or two negatively doped regions with one positive region (NPN). The three regions are called the base (centre region), emitter and collector region (two side regions). As this is a three terminal device with two pn-junctions, the transistor can be biased in four different modes. During transistor biasing, both of the electrons and holes will diffuse between the pn-junctions, with the biasing potential determining the mode of operation [6]. For a normal NPN transistor, biased in the forward-active mode, electrons will be injected from the emitter into the base region, creating an excess of minority carriers in the base region. The collector-base junction is reversed bias, therefore most of the injected electrons will tend to diffuse across the base region and be swept into the collector region by the electric field (E-Field). Although some of the injected electrons will combine with the majority carriers (holes) in the base, most will diffuse into the collector region creating the collector current (I_C). A simple diagram of the electron and hole flow of an NPN BJT is shown in figure 2.1.

The number of electrons that are injected from the emitter and diffused through the base region into the collector region, is classified as current multiplication (α), or the current gain of the transistor [7].

$$\alpha = \frac{dI_C}{dI_E} \tag{2.1.1}$$

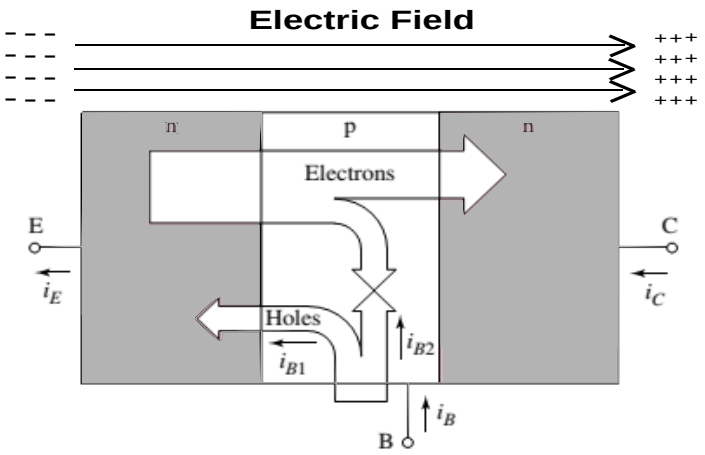

Figure 2.1: Electron and hole diffusion of a NPN transistor biased in the forward-active mode, after [6].

where

I_C = the collector current.
I_E = the emitter current.

Transistors are mostly used in their linear state as amplifiers and switches. In this condition the E-field at the collector-base or collector-emitter region is below breakdown conditions and α is less than or equal to unity. In this thesis the transistor will be controlled under a nonlinear condition for the creation of fast impulse-like transient signals, a phenomenon known as *Avalanche Breakdown*.

Avalanche breakdown in transistors occur when the E-field in the reverse breakdown region (collector-base) is larger than ideal E-field strengths. Minority carriers diffuse from the emitter region into the collector region, because of a high E-field. These carriers form external electron-hole pairs from colliding atoms in the outer shell of the semiconductor. Additional electron-hole pairs are then produced by freed minority carriers from collision, which result in an avalanche effect [8]. The additional electrons and holes that were created increase the current gain of the transistor, resulting in a higher collector current or an α greater than unity. Thus the stronger the E-field in the region, the more electrons will be produced, which directly increase the current gain of the transistor. A simple graph of the collector current versus collector-emitter voltage (V_{CE}) is depicted in figure 2.2 below.

There is a clear distinction between the linear and avalanche state of the transistor. During avalanche breakdown the collector current (I_C) strives towards infinity. Because of the avalanching effect, an empirical expression has been formulated:

$$M = \frac{1}{1-(\frac{V}{V_B})^n} \tag{2.1.2}$$

M is the multiplication factor, V is the potential at the collector, V_B is the junction body breakdown voltage and n is a parameter which changes with semiconductor material. M is also related to the current gain of the transistor as below:

$$\alpha(V) = \alpha_0 M(V) \tag{2.1.3}$$

where α_0 is the current gain of transistor at low biasing voltages [8].

Considering these equations, the current gain of the transistor will increase when M is increased or the potential at the collector is increased. This enhances the understanding of the avalanche phe-

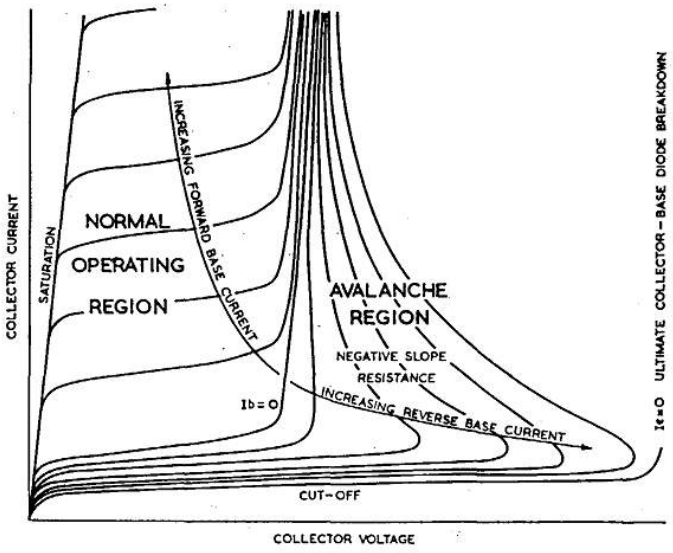

Figure 2.2: Collector current versus collector-emitter voltage [9].

nomenon and allows designers to create fast-rising transient pulses for TD metrology more confidently.

From the early 1960s, avalanche breakdown in transistors has been used to effectively produce fast-rising pulses for various applications [10]. For this thesis avalanche transistors, with SRDs and external circuitry, will be integrated for the creation of fast-rising transient pulses.

2.1.2 Step recovery diode

Another component used for the creation of fast transient pulses, is the SRD. Similar to a normal diode with one pn-junction, the SRD is a semiconductor with a PIN-junction. There is a lightly doped intrinsic layer between the two heavily doped p and n regions of a normal diode. The diode is mostly used in RF switches as well as pulse shaping and waveform generation [11]. It can also be used for frequency comb generation and harmonic frequency multiplication.

The SRD is used as a charge controlled switch, but with its dynamic characteristics, it is different than normal pn-junction diodes. The SRD switches from a very low, to a high impedance upon the removal of charge stored in the internal capacitance of the diode. These characteristics of storing charge and rapidly changing impedance levels, allow the SRD to be used for the above-mentioned applications. The switching type SRD is thoroughly TD tested during manufacturing and good knowledge of the switching characteristics is required in order to use the diodes correctly.

Through the following equations the switching characteristics of the SRD can be explained. As mentioned previously, the SRD switches from a low to a high impedance upon the removal of charge. When the diode is forward biased, charge is stored in the diode and as soon as a reverse current is applied, the diode discharges and switches between its two states. From Hewlett Packard's, *Pulse and Waveform Generation with Step Recovery Diodes*, the charge stored under forward bias conditions can be obtained from the charge continuity equation [11]

$$i(t) = \frac{dQ}{dt} + \frac{Q}{\tau} for (Q > 0) \tag{2.1.4}$$

where

i = total instantaneous diode current
Q = charge stored at diode pn-junction
τ = minority carrier lifetime of diode

For a constant charging current applied to the SRD

$$Q_F = I_F \tau (1 - e^{-t_F/\tau}) \tag{2.1.5}$$

Q_F = total stored charge from forward current
I_F = forward charging current
t_F = length of time forward current is applied

when a reverse current is applied to remove the stored charge, the time required to do so will be

$$\frac{t_s}{\tau} = \ln\left(1 + \frac{I_F(1 - e^{-t_F/\tau})}{I_R}\right) \tag{2.1.6}$$

t_s = the total time required to remove the charge stored by I_F
I_R = reverse current

With these equations the SRD is better understood and therefore a thorough design of a circuit with a SRD can be implemented. The switching from low to high impedances normally takes less than one nanosecond, which makes it an acceptable component for the creation of fast-rising transient pulses. A simple diagram of a pulse generator (PG) with a SRD is depicted below.

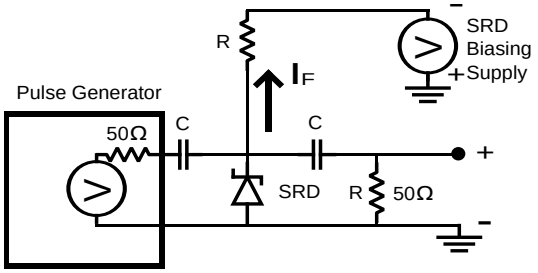

Figure 2.3: A simple PG model with a SRD circuit.

The SRD is constantly biased by the negative supply voltage to ensures that the diode is in a low impedance state. This effectively shorts the output of the PG to ground and nothing will the be measured across the load . When the PG produces a positive output pulse, it reverse biases the SRD, allowing the reverse current to discharge the diode and switch to a high impedance. The switching takes a couple of picoseconds which sharpens the rising edge of the pulse. The diode is seen as an open circuit upon the complete removal of charge, with a sharpened pulse delivered into the 50 Ω load. The rise-time of this pulse is extremely close, if not the same, to the switching time of the SRD. In chapter three, the SRD will be used to improve the rise-time produced by an avalanche transistor for the creation of a fast-rising impulse generator.

2.1.3 External analog devices

Other than the above-mentioned components, are there a couple of other techniques and devices available for creating impulse generators. The development of pulse generators has become more common amongst designers because of the significant evolution in technology and the large variety

of academic papers readily available for researchers. From the semiconductor family there are two popular devices that can be used for creating pulses; the silicon transistor and tunnel diode.

Silicon transistors, used as switches, allow for the generation of fixed rise-time pulses. They can achieve 2 V pulses with 1.5 ns rise or fall-times into a 50 Ω load. The repetition rate of these transistors range around 165 MHz and are used at the output stage of the pulse generator to avoid saturation effects [12].

Tunnel Diodes are extremely fast rise-time devices. They can produce pulses with 20 ps rise-times, but are limited to low amplitudes of 250 mV and slow repetition rates. They have a unique 'S' type current-voltage (I-V) curve that is different to common diode I-V curves. These diodes have been around since the 1960's and have operated under microwave frequencies as amplifiers, switches and oscillators [12, 13].

A common technique used to sharpen the leading edge of pulses, is the use of nonlinear transmission lines (NLTL). Similar to the characteristics of a transmission line, the NLTL consists of series inductors and shunt varactor diodes. NLTLs are used to improve the rise-time of pulses to less than 5 ps, with a repetition rate of 500 kHz. The only setback about this device, is that it is bandwidth limited and acts as a low-pas filter, because of its transmission line characteristics [12].

The last component that is evident in some pulse generator circuits, is the mercury-wetted switch. It is connected in series as a switch for high speed applications. The figure depicted below will be used to explain the basic operation of the switch.

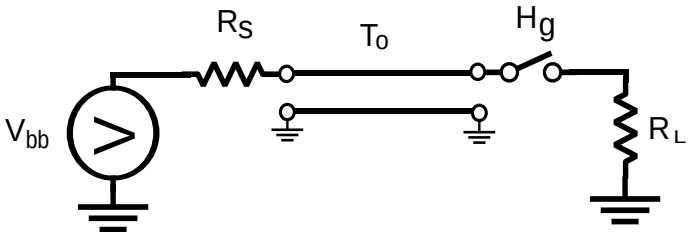

Figure 2.4: Basic mercury-wetted switch PG circuit.

Andrews, Bell and Baldwin [14] implemented the following PG design with a mercury-wetted switch. The transmission line (T_0) is charged through the source resistance (R_S) by the potential source (V_{bb}). When the transmission line reaches a potential equal to the switching characteristic of the mercury switch (H_g), which is usually equal to V_{bb}, the switch will close and discharge T_0 into the load resistor. This can create pulses with an effective rise-time faster than 100ps. If the characteristic impedance of the transmission line is equal to the the load impedance, a rectangular output pulse will be produced.

2.2 Impulse radiating antenna

The creation of fast-rising impulse generators, introduced a strong need to effectively radiate these impulses using an antenna. Carl E. Baum first investigated this problem in the late 1960's [15]. His studies led to a design now known as an *Impulse Radiating Antenna* (IRA). The antenna uses a lens or parabolic reflector in order to convert an outgoing inhomogeneous TEM-wave, propagating on a conically symmetric feed line structure, into a plane wave [16]. The IRA's basic features are two

transverse-electromagnetic (TEM) conical plate transmission lines, that are terminated through resistors onto a reflector dish (see figure below).

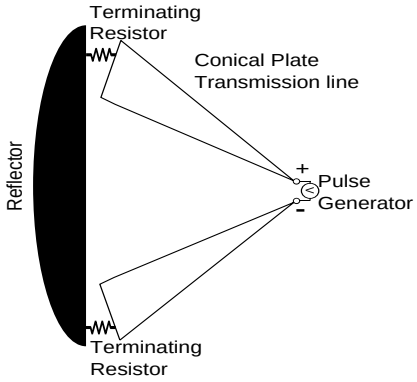

Figure 2.5: Basic IRA design.

The impulse is fed at the focal point of the dish and propagates down the conical plate transmission lines towards the dish. The E-field formed between the plates, act as a travelling wave that propagates towards the dish and it gets reflected back in the direction the dish is facing. This limits the antenna to radiate pulses into a specific direction, but allows a much higher gain over a wider band. The applications for this antenna are radar, high frequency and power electromagnetics [17, 18]. For this thesis and study the antenna will be used for wideband TD metrology experiments.

The basic theory of the IRA can be explained by looking at an antenna that is modelled as an aperture. Solving the radiation characteristics of aperture antennas using mathematics, can be challenging. For a dipole or similar antenna, the radiation characteristics can be calculated from the known current distribution on the antenna. For an aperture system, there are anomalies that limit the precise calculation of the current distribution on the antenna. In order to solve this problem, an alternative method or technique, known as the field equivalence principle, is used.

The principle is based on replacing actual sources (antenna, transmitter, etc.) by equivalent sources, which produce the same fields in a bounded region. It was introduced by S. A. Schelkunoff [19] in 1936 which states that "*each point on a primary wavefront can be considered to be a new source of a secondary spherical wave and that a secondary wavefront can be constructed as the envelope of these secondary waves.*" The principle is also based on the uniqueness theorem, which states that "*a field in a lossy region is uniquely specified by the sources within the region plus the tangential components of the electric field over the boundary, or the tangential components of the magnetic field over the boundary, or the former over part of the boundary and the latter over the rest of the boundary.*"

These two theorems can be used to assist designers with aperture related problems. From the field equivalence theorem, the fields outside an imaginary closed surface can be obtained by placing suitable electric (J_s) and magnetic-current (M_s) densities over the closed area. This satisfies boundary conditions. The current densities are chosen to ensure that the fields inside the closed area are zero and on the outside they are equal to the radiation produced by the actual sources. From the uniqueness theorem, if the tangential electric or magnetic fields inside a closed area are known, the fields in a source-free region can be determined. In other words, if the fields inside the closed area are zero, the chosen current densities will be equal to the tangential components of the electric and magnetic fields. These techniques allow you to obtain the radiated fields outside a closed area, by selecting the sources enclosed within it. This formulation is said to be exact, but requires integration

over the closed surface and the degree of accuracy depends on the knowledge of the tangential components [19].

The IRA design is approached as an aperture antenna problem. The tangential electric field on the aperture (S), focused at infinity in a direction ($\vec{l}_0$), is specified as a plane wave. Thus taking a step-function as outgoing source, the aperture illumination leads to an impulse function, with a width narrowing as the observer ($\vec{l}_r$) approaches $\vec{l}_0$ [20].

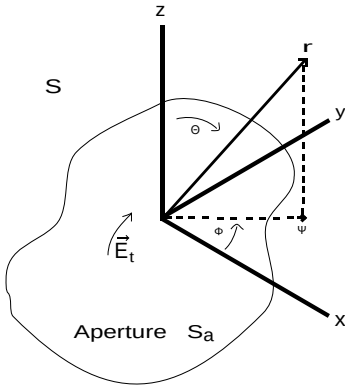

Figure 2.6: Aperture antenna with a specified tangent electric field.

As shown in figure 2.6, let the source coordinates be x' and y' with the aperture on the z = 0 reference plane. The tangential electric field can then be specified as:

$$\vec{E}_t(x',y';t) = l_z \cdot \vec{E}(x',y',0;t) = \big(E_x(x',y',0;t), E_y(x',y',0;t), 0\big) \tag{2.2.1}$$

with the following definitions applied:

$\vec{r}' = (x',y',0)$ = source coordinates	$\vec{r} = (x,y,0)$ = observer coordinates
$l = \vec{l}_x\vec{l}_x + \vec{l}_y\vec{l}_y + \vec{l}_z\vec{l}_z$	$1_z = l - \vec{l}_z\vec{l}_z = \vec{l}_x\vec{l}_x + \vec{l}_y\vec{l}_y$
$R = \lvert\vec{r} - \vec{r}'\rvert = [(x-x')^2 + (y-y')^2 + z^2]$	$\vec{l}_R = \frac{\vec{r}-\vec{r}'}{R} = \frac{\vec{x}-\vec{x}'}{R}\vec{l}_x + \frac{\vec{y}-\vec{y}'}{R}\vec{l}_y + \frac{z}{R}\vec{l}_z$
s = Laplace-transform variable	$c = \frac{1}{\sqrt{\mu_0\epsilon_0}}$
$\gamma = \frac{s}{c}$ = free-space propagation constant	~ = Laplace-transform

From [20] the tangential electric field, after extensive mathematical calculations and with the aperture focused at infinity in a direction $\vec{l}_0$, is:

$$\vec{E}_t(\vec{r}',s) = e^{-\gamma\vec{l}_0\cdot\vec{r}} E_0 \tilde{f}(s)\vec{g}(\vec{r}') \qquad \text{as } r \to \infty \tag{2.2.2}$$

where $\tilde{f}(s)$ is a waveform on the aperture in the frequency domain and $\vec{g}(\vec{r})$ is the aperture spatial distribution. Equation 2.2.2 is a plane-wave distribution with a uniform time dependence of $f(t)$ in the TD. It is then further showed that the radiated field is:

$$\tilde{\vec{E}}_f(\vec{r},s) = e^{-\gamma r}\frac{E_0 A}{2\pi c r}\tilde{\vec{F}}(\vec{l}_r,s) \tag{2.2.3}$$

where A = Aperture Area and:

$$\tilde{\vec{F}}(\vec{l}_r, s) = s\tilde{f}(s)\tilde{\vec{F}}_a(\vec{l}_r, s) = \text{far-field waveform function} \tag{2.2.4}$$

$$\tilde{\vec{F}}_a(\vec{l}_r, s) = \frac{1}{A}[(\vec{l}_z \cdot \vec{l}_r)l - \vec{l}_z\vec{l}_r] \cdot \int_S e^{\gamma[\vec{l}_r - \vec{l}_0]\cdot\vec{r}'}\vec{g}(\vec{r}')dS' = \text{aperture function} \tag{2.2.5}$$

These equations can be simplified if a uniform plane wave is specified in the aperture and the observation point (l_r) is on boresight (l_0). Thus the aperture spatial distribution and function becomes:

$$g(r') = \begin{cases} l_y & \text{on } S \\ 0 & \text{off } S \end{cases} \tag{2.2.6}$$

$$\tilde{\vec{F}}_a(\vec{l}_r, s) = l_y \tag{2.2.7}$$

$$\tilde{\vec{E}}_f(\vec{r}, s) = e^{-\gamma r}\frac{E_0 A}{2\pi c r}s\tilde{f}(s)l_y \tag{2.2.8}$$

Equation 2.2.8 is the simplified radiated far-field of an aperture antenna as showed by Baum [20, 21]. One can note that if the waveform on the aperture ($\tilde{f}(s)$), or the source, is a unit-step function in the TD, the radiated field on boresight will be:

$$\tilde{\vec{E}}_f(\vec{r}, t) = \frac{E_0 A}{2\pi r c}\delta(t - \frac{r}{c})l_y \tag{2.2.9}$$

From equation 2.2.9 the radiated far-field will be some dirac-delta (impulse) function on boresight, if a uniform step function is applied over the aperture. Baum and Farr [21, 22, 23] have done extensive mathematical and physical research on the IRA by publishing notes of a few models.

These equations are the basic fundamentals behind the operation of the IRA. Further design equations will be discussed in chapter 4, where a design and simulation of an IRA will be shown. The antenna will be used with an impulse generator to effectively radiate pulses in the Karoo for propagation and shielding effectiveness measurements. This will be required for the SKA project in South Africa.

2.3 Time-domain metrology

Metrology is the science of measurement which originates from the Greek word "metron", which means measure and "logos", which means speech, oration, study, calculation or reason. From Ancient Greek times, the word "Metrologia" meant the theory of ratios. As mentioned in chapter 1, TD analysis provides speed-up without the loss of accuracy [2]. One single pulse, with a sub-nanosecond rise-time, can produce instantaneous energy from DC up to microwave frequencies. Characterisation and measurements of these fast-rising transients are determined by large bandwidth sampling oscilloscopes. The sampling oscilloscope acts as an analog sample-and-hold device with an extremely narrow sample time, to allow analysis of transient responses with microwave frequency components [24]. This is different from the newer digital scopes or an analogue oscilloscope. In a real-time scope, the transient signal is directly sampled for data processing or on-screen display. The signal is sampled 1:1 and is limited by the Nyquist criterion [25]. An illustration of real-time sampling is shown in figure 2.7.

For fast-rising transients with high frequency content, a larger bandwidth oscilloscope is required. The electronics inside a real-time scope is not able to sample a fast-rising impulse 1:1 and requires a different method of sampling. Sampling oscilloscopes introduce and use a different improved technique, known as sequential sampling. The oscilloscope is synced with a synchronising pulse that informs the oscilloscope a signal is inbound. Once the oscilloscope is triggered, a sample is taken. After the n^{th} sample, the signal is reconstructed and displayed on a new time-scale. An example of sequential sampling is displayed in figure 2.8. This technique is not bound to the Nyquist criterion and allows accurate reconstruction of fast-rising impulse-like transients.

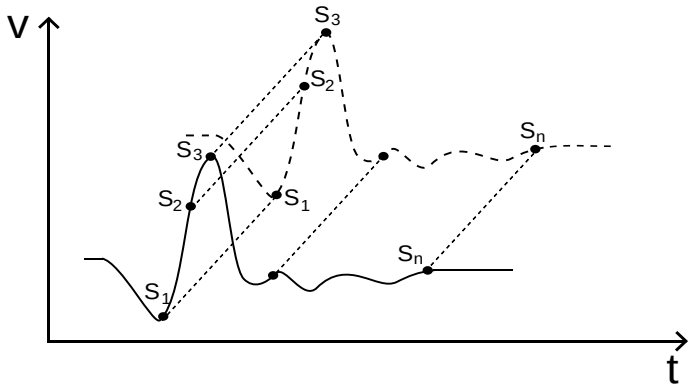

Figure 2.7: Real-time sampling with the reconstructed signal, after [25].

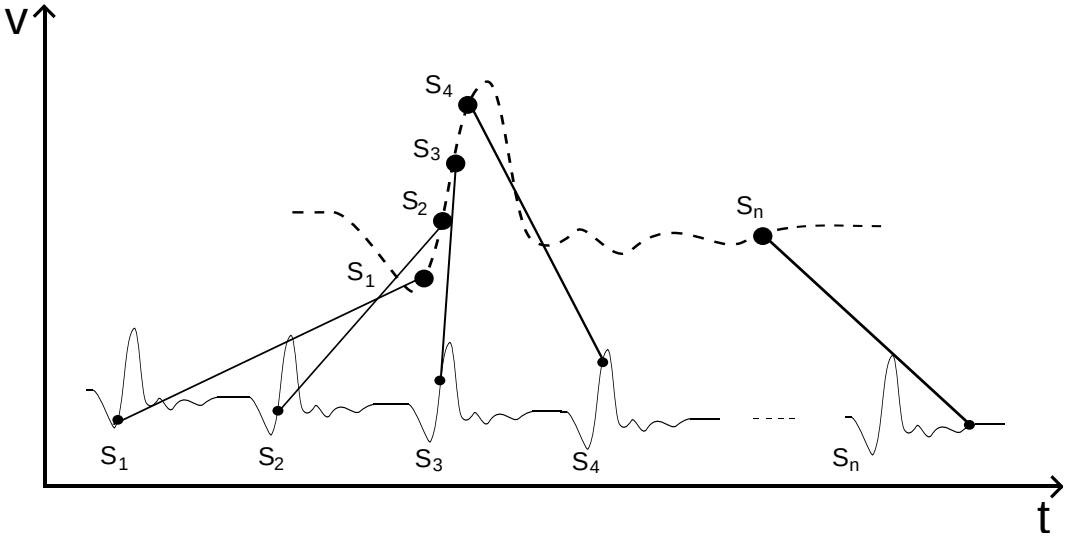

Figure 2.8: Sequential sampling of a sampling oscilloscope with the reconstructed signal, after [25].

2.3.1 Sampling devices used in this study

Sampling is the process of converting a transient input signal into discrete electrical values for processing. In this study, four devices are used to measure fast-rising impulses.

The HP Agilent 54750A 50 GHz sampling oscilloscope is a powerful scope with a large bandwidth. The device is capable of measuring pulses accurately with a time interval accuracy of less than 8 ps ±0.1% to both sides. The time interval resolution is either 62.5 fs or(screen diameter)/(record length), whichever is larger. The time interval resolution limits the device to accurately characterise and measure a small (100 ps) signal, which has a long triggering period. The maximum trigger signal or input signal that can be received by the scope is ±2 V_{DC} + AC peak (+ 16 dBm). The HP 54750 scope will be used to accurately calibrate and measure the impulse generators that are built during this study.

The **Yokogawa DLM2052** scope is a less accurate sampling scope than the HP 54750A, but does not require an external triggering source for measurements. The bandwidth of the scope is 500 MHz, but can be operated in an interleaved mode with an improved bandwidth of 1.25 GHz. The scope can alter between two input impedances for protection against unknown transients that have to be characterised. The 1 $M\Omega$ input impedance can receive a maximum input signal of 130 V_{DC} and the 50 Ω - 10 V. The device is mostly used for testing during experimental phase, before accurate mea-

surements are made.

The last two devices used, the **ReAl-Time Transient Analyser (RATTY)** and **Real-Time Analyser (RTA)**, are direct sampling devices that were designed to assist with RFI measurements in the Karoo [4]. The devices are portable and are used during measurements in the Karoo. RATTY has two operating bands. Band one operates roughly up to 800 MHz and band two from 800 MHz - 1.4 GHz. RTA has four operating bands that cover a large band from DC - 1.7 GHz and 1.8 GHz - 2.7 GHz.

2.4 Conclusion

The purpose for this project is to design and implement a TD transmitting system that will be able to electromagnetically characterise the Karoo environment. The foundational components for this TD system is a pulse generator and impulse radiating antenna. With a characterised impulse-like signal, the transfer function of microwave systems can be determined. For this study it will be implemented for propagation and shielding measurements in the Karoo. The IRA is a directive antenna that allows effective radiation of impulse-like signals, which will be measured with the sampling devices mentioned earlier in the chapter. This chapter has briefly introduced each fundamental component and has discussed the theory and literature behind them. The following chapters will cover an in-depth design and optimisation of the impulse generator and IRA. The last chapters will cover TD metrology in laboratories and the Karoo environment.

Chapter 3

Pulse generators

Pulse generators (PG's) date back to the 1960s [12]. Multiple PG designs have been investigated with many purely electronic generators making use of transistor avalanche breakdown characteristics. A defining characteristic for impulse generators is their fast rise-times (t_r). The rising-edge of a pulse is directly proportional to the instantaneous bandwidth (BW) of the pulse. This is calculated by:

$$BW = \frac{0.35}{t_r} \tag{3.0.1}$$

With a fast rising-edge a high instantaneous bandwidth can be achieved and have been implemented for TD metrology studies [2, 13].

The focus of this chapter is the design of two impulse generators to test the SE of enclosures, chambers and also the transfer impedance of cables. The designs originate from a similar design used in [13]. An avalanche transistor, forced into its breakdown region, with a step-recovery diode (SRD) is used to generate the pulse. An industrial PG CPS1 is also bought from Kentech industries which produces kilo-volt pulses. This PG will be used for propagation and shielding measurements in the Karoo. From past experience with a 15 V - 30 V PG, the amplitude from these pulses were too low for measurements, which is why the Kentech Pulser is bought.

A basic circuit design of an impulse generator is depicted in figure 3.1. The capacitor C_{out} is charged through R_C and R_L in order to bias the transistor and force it into breakdown. As soon as the transistor is triggered, the avalanche transistor conducts and is forced into a non-linear state by the potential created by the dynamic load R_L and C_{out}. This effect causes the potential at the collector to collapse, until a stable operation point is reached. The duration of this process is proportional to the switching time of the chosen transistor, which can be a nanosecond or less. After C_{out} is discharged the transistor cannot maintain the avalanche effect and is switched off. This allows C_{out} to recharge until the next trigger is applied [25].

Two PG's are designed in this study. The first consists of single avalanche transistor design with a SRD to sharpen the leading edge of the pulse. The external circuitry is optimised in order to produce the best pulse with a 2N2369A avalanche transistor. The design, optimisation and results of this PG are incorporated in section 3.1. The second design is similar to the first, but two transistors are stacked to improve the peak amplitude of the pulse. Increasing the amplitude of the pulse will increase the dynamic range of the spectrum. All the PG models are measured with the HP 54750A 50 GHz sampling oscilloscope. The scope is triggered by the same pulse that triggers the PG to synchronise the two components and inform the scope when to sample.

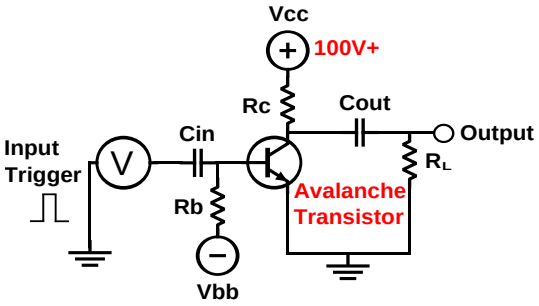

Figure 3.1: Typical impulse generator circuitry, after [25].

3.1 Single avalanche transistor impulse generator (30V Pulse)

The PG external circuitry plays a pivotal role in the design of the impulse generator. Changing the circuitry around the basic design of an impulse generator will have a significant effect on the outcome of the pulse. These components can be used to shape the pulse into a desired pulse for the required purpose. A circuit of the PG designed in this study is depicted in the figure below.

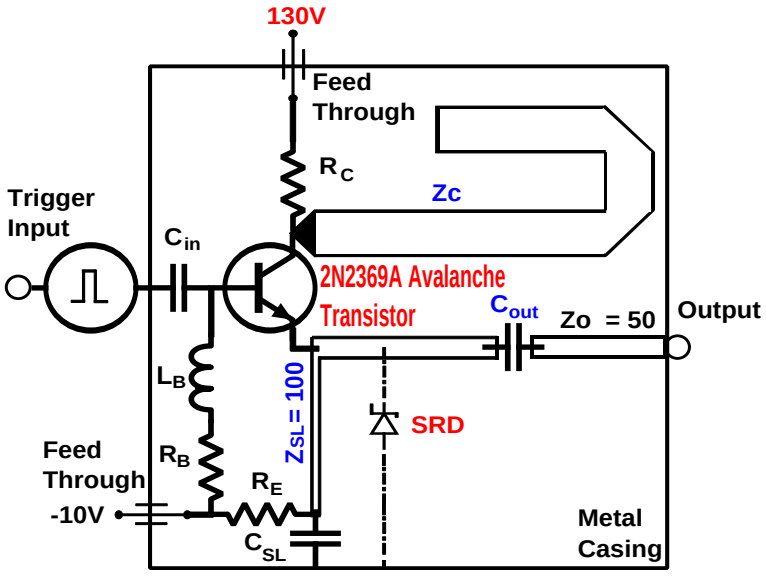

Figure 3.2: 30V PG circuit schematic.

This design is modified from the typical PG circuit in figure 3.1. The capacitor at the collector is replaced by a mircrostrip line. This gives the designer the opportunity to control the width of the pulse by changing the length of the line. The connection at the emitter is changed, because a SRD is placed at the output of the transistor and is biased through a biasing network. The output is moved to the emitter to produce a positive output pulse instead of the negative pulse usually measured at the collector. The collector line Z_C is charged to a potential that is between $65V$ and $70V$ when the transistor is on. During its off-state it charges to V_{CC} (130 V). This value changes with the size of the microstrip line and the resistor (R_C) at the collector. From chapter 2, the voltage at this point controls the current gain of the transistor. Setting it to an absolute maximum possible value is desired in order to achieve the best possible pulse amplitude without causing the transistor to fail. The biasing network at the base of the transistor, forward biases both the transistor and the SRD. When the transistor is triggered the SRD gets reverse biased and all the charged stored in the SRD is removed. The time for this transition and removal of charge determines the rise-time of the pulse. The inductor

L_B ensures the pulse at the output does not couple back into the base of the transistor, which can cause unwanted effects in the output. A reflected pulse is coupled into the system if the inductor and shorted line method is not implemented in the circuit. The size of the inductor is 100 μH. The size of the resistor at the collector is 120 $k\Omega$ and R_B is 75Ω. The shorted line Z_{SL} is 100Ω. R_E is also 100Ω so that it is matched to the impedance of the line. The capacitor at the shorted line acts as a short circuit for an electromagnetic wave travelling down this mircostrip line. The reason for the short circuit implementation will be explained in section 3.1.1.2. C_{IN} and C_{OUT} in the circuit are DC blocks and where C_{OUT} will be configured to give a high-pass filter response to the pulse for RC measurements.

A pulse is applied at the base of the transistor to trigger the transistor. Once the transistor is triggered the stored charge at the collector collapses and the pulse formed at the collector travels down the collector line and reflects back to switch off the transistor. The pulse captured at the emitter is sharpened by the SRD and the width of the pulse is equal to double the electrical length of the collector line. The main pulse measured at the emitter is also shortened by the technique applied with the shorted line and SRD. This was implemented in [13]. In the next section the PG circuit in figure 3.2 will be optimised by changing the size of the microstrip line at the collector, improving the shorted line method and filtering the output of the pulse.

3.1.1 Design and optimisation

Multiple PG's have been designed and tested during a final year undergraduate project, which are now improved and redesigned to obtain an optimal pulse. From [26, 27] a broadband impulse generator was designed. The pulse was shaped and optimised by changing the capacitor, cable length and resistor values at the collector as well as the resistor values at the emitter of the transistor. The final pulse produced from past work had an amplitude of 15 V with a respective rise-times of 200 ps and a full-width half maximum height (FWHM) of 330 ps. There is a strong desire to improve this PG design by further investigating the circuitry around the pulse.

Current impulse generators used in the laboratory have a faster spectrum roll-off at higher frequencies. The aim is to increase the dynamic range of the spectrum by increasing the amplitude and improving the rise-time of the PG through optimisation of external circuitry. From Parseval's theorem the energy that is associated with a TD function ($f(t)$) is directly related to the Fourier transform of that function. Assuming $f(t)$ is the energy of a voltage or current source over or through a resistor, it can be determined by [28]:

$$W = \int_{-\infty}^{\infty} f^2(t)\,dt \tag{3.1.1}$$

This leads to Parseval's theorem which is the same function integrated over a frequency range in the FD.

$$\int_{-\infty}^{\infty} f^2(t)\,dt = \frac{1}{2\pi}\int_{-\infty}^{\infty} |F(\omega)^2|\,d\omega \tag{3.1.2}$$

Thus if $f(t)$ has a certain amplitude the FD amplitude of the same signal will be equal to the amplitude of the TD function times the width of the signal. The goal is to increase the spectral content in the FD, by either increasing the amplitude of the pulse or improving the amplitude and narrowing the width of the pulse. In order to improve the current PG's, the spectrum from these impulse generators was mathematically altered to a desired spectrum. This spectrum was inverse Fourier transformed to obtain the characteristics of the pulse that was required. The figures below (fig. 3.3 and 3.4) indicate the current PG amplitudes and spectrum, with the desired pulses and spectrum.

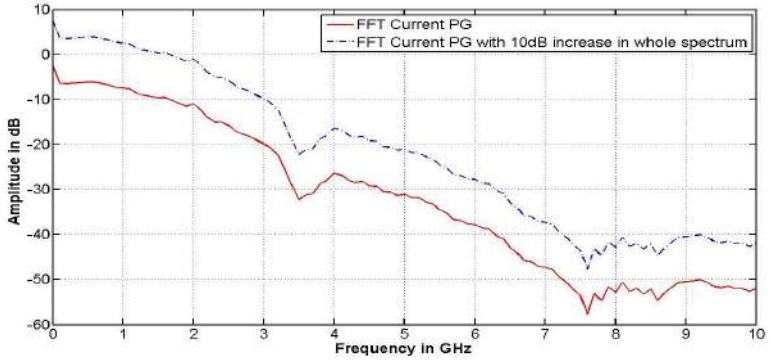

(a) FFT with simulated 10 dB increase in spectral amplitude.

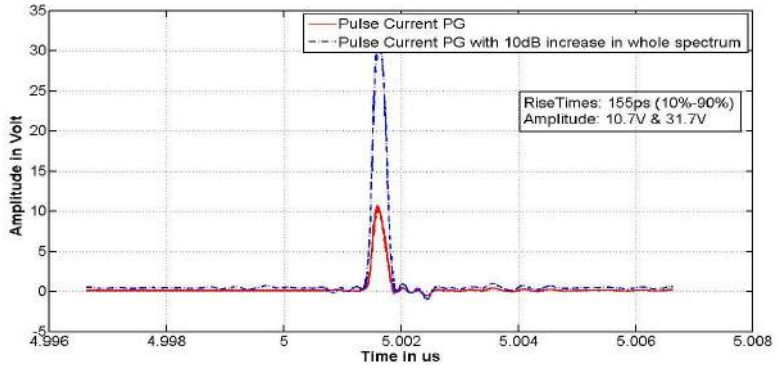

(b) Current PG with a 10 dB improved pulse.

Figure 3.3: Time and frequency responses of PG after simulated 10 dB increase in spectrum.

The current PG model is an impulse generator model built during a final year project in [26] and the JAA model is built for RC measurements in [2]. The rise-times of the original models are 155 ps and 200 ps respectively for the current and JAA PG. The current model is mathematically improved by increasing the amplitude in the spectrum by 10 dB, while the JAA model was multiplied by a linearly increasing function to only improve the higher frequencies of the spectrum. The amplitude increase, from the current PG gave a pulse with an increased amplitude with the same FWHM and rise-time. The increased spectrum at the higher frequencies for the JAA PG showed not only an amplitude increase, but more importantly, a faster rise-time was achieved. The effect that is applied to the current PG is a good example of Parseval's theorem and indicates that a constant increase of spectral content over the whole band increases the amplitude of the TD pulse, without changing the other characteristics. In order to improve the spectrum at the higher frequencies of the pulse, the rise-time of the pulse has to be improved. For each of the pulses obtained with the JAA model, the rise of spectral content at the higher frequencies increased the amplitude as well as the rise-time of the pulse.

Multiple designs and tests were done to improve the response of the current PG circuit. The aim was to increase the amplitude and rise-time of the pulse. To obtain an optimal pulse the collector and shorted lines were thoroughly investigated in order to increase the amplitude of the pulse. Components and the biasing network to the SRD were also changed and tested, to obtain the best possible rise-times. Changes made to the current PG circuit are explained in the following sections.

3.1.1.1 Changing the width of the collector delay line

From past experience the size of the capacitor at the collector not only shaped the pulse, but also raises the potential at the collector of the pulse which directly increases the amplitude of the pulse produced during the avalanching effect. Because a normal ceramic or lead capacitor changes at ra-

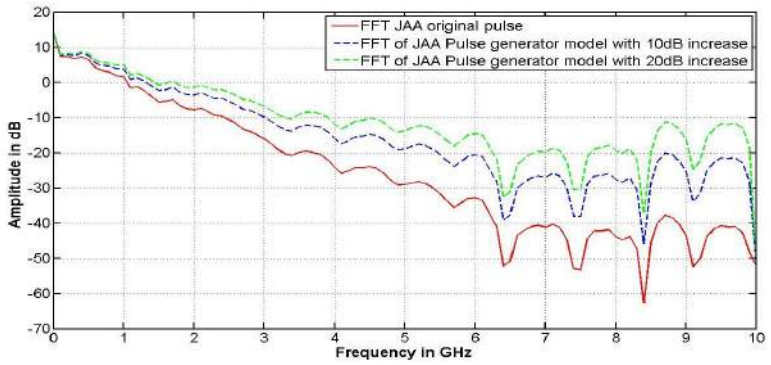

(a) FFT of JAA PG with simulated linear increase in spectral amplitude.

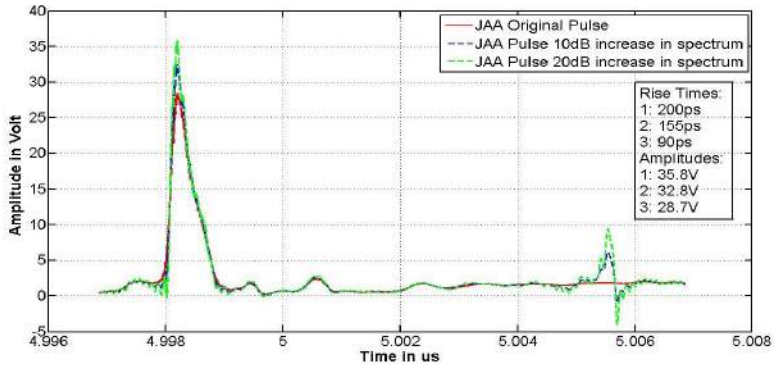

(b) JAA PG with two improved pulses, obtained by multiplying it with a linear function.

Figure 3.4: Time and frequency responses of PG after simulated linear increase in spectrum.

dio frequency (RF), a microstrip line was used. Changing the width of the microstrip line increases its capacitance and decreases the impedance of the line. For all the PG designs a Rogers Duriod 4003C substrate was used. The characteristics of the substrate are shown in the table below.

Property	**Value**
Dielectric constant (ϵ_r)	3.38 + 0.05
Dissipation factor (tan δ)	0.0021 - 0.0027
Height (h)	1.524 mm
Copper layer (t)	17 μm

The width of a microstrip line with a specified centre frequency and impedance can be calculated, if these values are known. Txline from AWR was used for calculating the width of the line, but it can be calculated by the following equations.

$$\epsilon_{r,(eff)} = \frac{\epsilon_r + 1}{2} + \frac{\epsilon_r - 1}{2}\left[\frac{1}{\sqrt{1 + \frac{12h}{W}}}\right]^{\frac{-1}{2}} \tag{3.1.3}$$

$$Z_C = \frac{\frac{120\pi}{\epsilon_{r,(eff)}}}{\frac{W}{h} + 1.393 + 0.667 ln\left[\frac{W}{h} + 1.444\right]} \tag{3.1.4}$$

where Z_C is the characteristic impedance of the line, $\epsilon_{r,(eff)}$ is the effective permittivity, W is the width and h is the height of the substrate being used [29].

Three different collector-line-width PG circuits were designed and constructed to compare different TD results. The widths of the lines were chosen accordingly. Increasing the capacitance per millimetre will increase the total stored charge on the microstrip line. A function of capacitance per unit length over the impedance and width of the line is illustrated in figures 3.5a and 3.5b. The code for plotting these results can be found in appendix B.

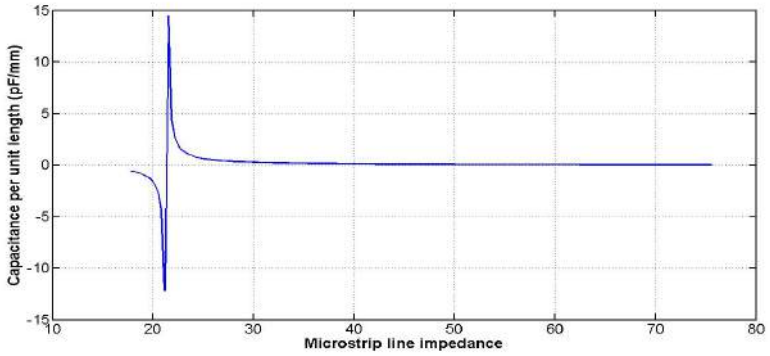

(a) Capacitance per unit length versus impedance.

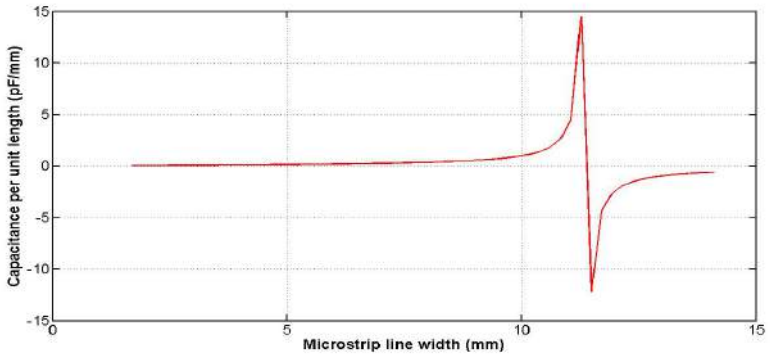

(b) Capacitance per unit length versus mircrostrip width.

Figure 3.5: Changing the capacitance per unit length of the microstrip line

A resonant point is shown at 21.50 Ω or 11.27 mm in width. At this point the capacitive response of the microstrip line becomes inductive and would therefore be the lowest possible value that can be chosen as the width of the collector line. Because this is a precise value and a very thin line, the margin for error was small and the first impedance for the collector line was chosen to be 22 Ω which yields a width of 11 mm and more than 10 pF/mm. The other two impedances that were chosen was 26 Ω and 33 Ω. The width of these lines is 8.9 mm and 6.43 mm with 2.5 pF/mm and 0.6 pF/mm. The 33 Ω line were chosen as the smallest line with the least amount of storage capacity and the 26 Ω line roughly in the centre between the middle of the 22 Ω and 33 Ω line. From theory the 22 Ω line will give the highest amplitude pulse and the smaller two widths were chosen to prove this.

The results from these measured PG's are depicted in figure 3.6. A basic PG circuit was implemented only to test the differences between the widths of the mirotstrip lines at the collector. The test circuit is shown in figure 3.7.

From the results the respective measured amplitudes are 23.4 V for the PG with a 22 Ω collector line, 22.2 V for the PG with a 26 Ω line and 15.6 V for the PG with a 33 Ω. There is not a big difference between the 22 Ω and 26 Ω PG amplitudes, but the 33 Ω PG's amplitude is significantly lower. The

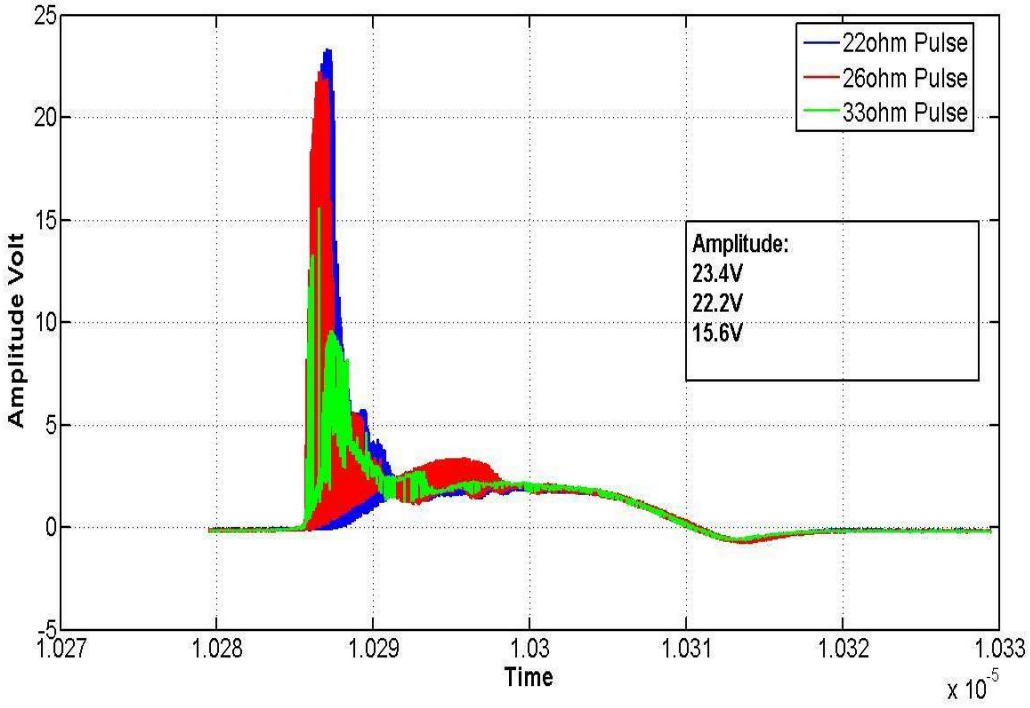

Figure 3.6: Results from the PG with three different impedances at the collector line.

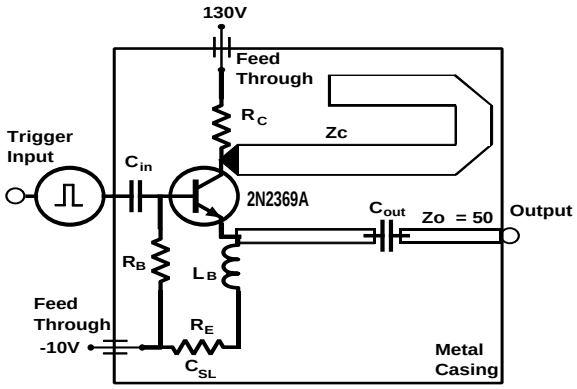

Figure 3.7: Collector line PG test circuit schematic.

stored charge on a 33 Ω microstrip line is significantly smaller than the capacitance per unit length for the PG with a wider collector lines. With more stored charge at the collector of the transistor, the stronger the potential at the collector of the transistor. This increases the current gain of the transistor and directly increases the amplitude of the pulse produced by the avalanching effect in the transistor. The harmonic content at the back of the pulse originates from the coupling between the output and triggering part of the circuit. The inductor impedance, at the emitter of the transistor, ensures that the high frequency content of the output pulse is not coupled back to the base of the transistor, but has a smaller impedance for the lower frequencies. The content at the back of the pulse is the triggering pulse that is coupled into the output pulse. A 5 V pulse with a 20 ns width is used to trigger the transistor and the width of the content at the back of these pulses measured is 20 ns. The potential of the triggering pulse has dropped because of the resistors R_E and R_B, but the shape and characteristics of the harmonic content at the back of the pulse is the same as the pulse used to trigger the PG. In order to remove this a short circuit can be connected between the output and input of the transistor and change the size of the inductor. This will be explained in the next section.

3.1.1.2 Implementing a shorted line technique with the SRD

One method to change the width of the pulse is by changing the length of the collector line at the collector of the transistor [10]. From [3] the width of the pulse is changed by implementing a shorted line method at the emitter of the transistor. An illustration of a shorted line method is shown in figure 3.8.

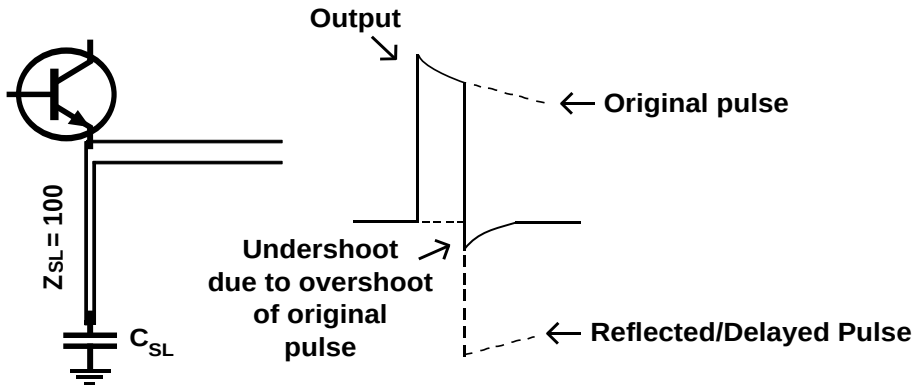

Figure 3.8: Shorted line output pulse and circuit configuration, after [3].

When the transistor gets triggered, the pulse that is produced at the emitter of the transistor propagates down the shorted line, sees a short circuit, due the capacitor shorted to ground, and gets reflected back negatively. The original pulse continues at the output and as soon as the negative reflected or delayed pulse arrives at the transistor, it is subtracted from the main pulse, as long as they are exponential. The length of the pulse can be determined by the delay of the reflected pulse, which is the line effective velocity. An example of the pulse is shown in figure 3.8. The size of the capacitor used at this point is calculated to ensure that the high frequency waves propagating down this microstrip line sees a short circuit to ground. The value of the capacitors is 100 nF to ensure a short circuit at kilohertz frequencies and higher.

Choosing the correct length of the shorted line is pivotal and explained. Because a SRD is placed at the output of the transistor to sharpen the leading edge of the pulse, the length of the line has to be longer than the switching time of the SRD. The SRD is biased through a feed-through capacitor and resistor (figure 3.2). As soon as the transistor gets triggered the pulse reverse biases the SRD, which removes stored charge accumulated in the SRD and it switches from a low impedance to a high impedance. This transition time of the SRD determines the rise-time of the pulse. If the switching time of the SRD is known, the length of the shorted line can be determined. If the line is too short, the peak amplitude of the pulse will never be achieved. The reflected pulse will arrive at the output before the SRD has changed states, denying the pulse to rise to its original pulse amplitude. Because the rise-times are pico-seconds long, lengths implemented should be precise.

Three SRD's and PG's were tested with three shorted line lengths. The length of the lines were calculated by the following equations, where v is the propagation speed of the pulse over the microstrip line, t is the desired time for the pulse to travel that distance and c is the speed of light.

$$v = \frac{c}{\sqrt{\epsilon_{r,(eff)}}} \tag{3.1.5}$$

$$l_{SL} = v * t \tag{3.1.6}$$

A table of the SRD transition times and shorted line lengths are shown. The length of the lines is a fraction longer than the transition time of the SRD's to ensure the peak of the pulse is not clipped by the delayed pulse.

SRD	Transition time	Shorted line length (l_{SL})	Shorted line length in time (t)
MMD820-T86	$80-100ps$	16.36 mm	100 ps
MMD810-T86	$200-250ps$	24.50 mm	150 ps
MMD805-T86	$250-300ps$	32.67 mm	200 ps

The PG's are measured and the results are displayed in figures 3.9 and 3.10. The red pulse in the figure is the PG with the shortest line at the emitter and the fastest SRD. The rise-time of the pulse is faster than the length of the line, but slower than the transition time of the SRD. The length of the line is long enough to ensure the pulse is not clipped, but the SRD is not biased at its optimal state to deliver the best rise-time achievable. The rise-time of the pulse is 185 ps with an amplitude of 20.6 V. The blue pulse is built with the intermediate SRD with a switching time of $200-250$ ps and a shorted line length of 24.5 mm. The pulse is biased at its optimal state with the best rise-time obtainable with this SRD (250 ps) and an improved amplitude of 21.8 V. The last pulse, has the longest shorted line and slowest SRD. The pulse measured has a rise-time of 400 ps and an amplitude 20.9 V.

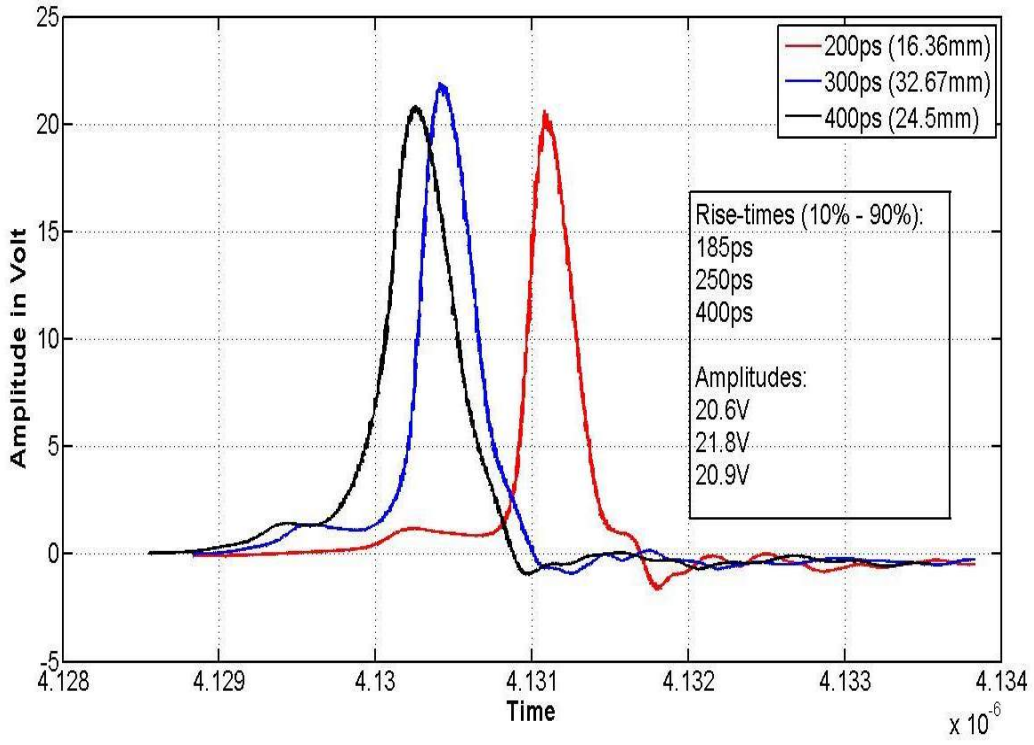

Figure 3.9: Comparison of the pulses measured from the PGs with the different shorted lines and SRDs.

The SRDs are sensitive diodes and any ripples in the biasing current can influence the response during switching [11]. Selecting the biasing voltage is important in order to obtain the best switching times with the SRD. Changing the biasing voltage will change when the SRD snaps-off during reverse bias and will in effect change the rise-time and amplitude of the pulse. The harmonic content at the front-end of these measured pulses are the amount of stored charge accumulated in the SRD. This

changes if the biasing voltage is changed. The back-end of the pulse is as explained in figure 3.8. Because the negative reflected pulse arrives a few pico-seconds after the main pulse, the difference between them causes the small undershoot due to the overshoot of the original pulse. In appendix E the biasing amplitude of the SRD are changed and the effects on the amplitude of the pulse and the amount of stored charge in the SRD, are shown.

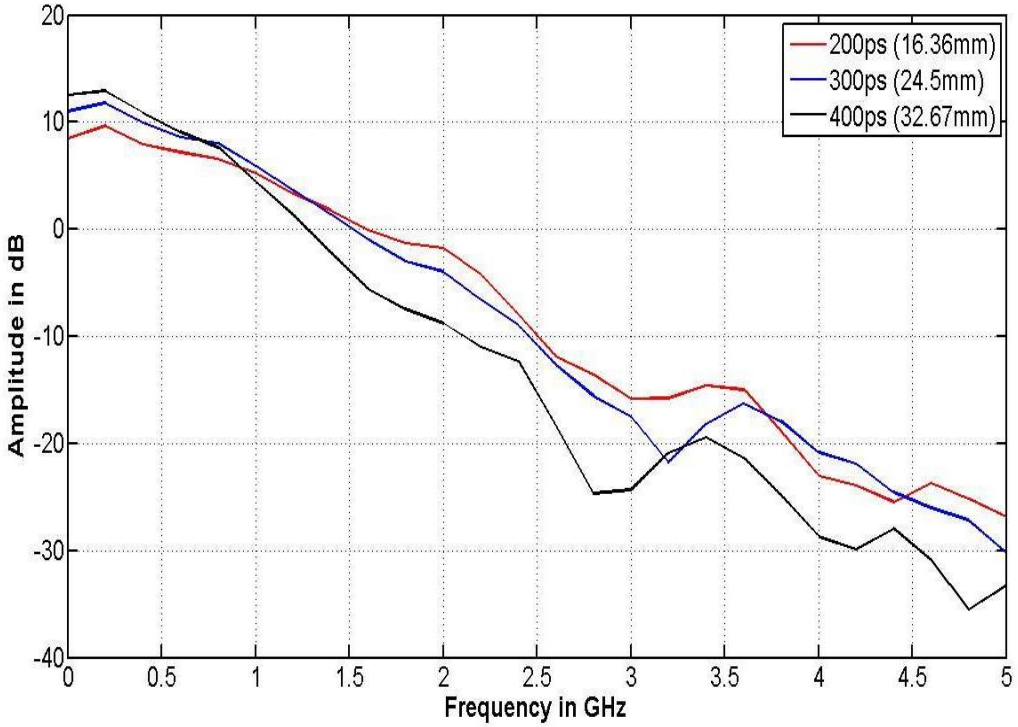

Figure 3.10: Spectral content of the pulses measured from the PGs with the different shorted lines and SRDs.

If the spectrum is observed the effect of different rise-times are seen at the higher frequencies. The rise-time of the pulse determines the bandwidth of the pulse. With a faster rise-time pulse the spectral content are equally spread over a larger band. With a slower rise-time pulse the voltage amplitude in the spectrum drops faster as frequency increases. From the figure the slower rise-time pulse (black spectrum) is 4 dB more than the fastest rise-time pulse (red spectrum) at the lower frequencies. After 900 MHz the amplitude of the black spectrum drops below the blue and red pulses. It has a smaller bandwidth due to the slow rise-time. For the faster rise-time pulses, the spectrum of the pulse at 2 GHz has only dropped by 10 dB, where the spectrum of the slower pulse has dropped by more than 20 dB. There is a 10 dB difference in the spectrum, but only 200−150 ps in time. A small improvement in rise-times can be a large difference in spectral energy. The red and blue pulses differ in amplitude and 70 ps of rise-time. If their spectral contents are compared, the high frequency content of the faster rise-time pulse is slightly better. There is a 1 dB difference between the red and blue pulses at the lower frequencies, and after 1.5 GHz another 1 dB difference, but the faster rise-time pulses have the broader bandwidth. Although the amplitude of the fastest rise-time pulse is a bit lower than the other pulses, its faster rise-time has an improved the bandwidth that is desired. These results indicate that the amplitude of the pulse as well as the rise-time has to be improved in order to obtain the largest bandwidth pulse and spectral content. This agrees with the hypotheses made in section 3.1.1, where spectral content were inverse Fourier transformed to obtain the characteristics of the pulse.

3.1.1.3 Applying a filtered response at the output of the impulse generator

The last optimisation that was made to the PG circuit was applying different capacitors at the output of the PG to filter the lower frequencies of the pulse. The RC is band limited at lower frequencies and accurately works from 200 MHz. The measuring device (RATTY) used for RC measurements also gets saturated with the lower frequency content of the pulse. To overcome this issue a high-pass filter at the output of the PG was implemented. The easiest filter that can be applied is a capacitor in series with the mircostrip line at the output. The capacitor was previously used to remove DC content in the pulse and is now required to filter the output more specifically at the lower frequencies.

For a high-pass filter the impedance of the capacitor has to be small at the high frequencies and extremely large at the lower frequencies. This would require a small capacitor at the output to enable a low frequency cut-off point. The cut-off frequency was calculated by equation 3.1.7.

$$f_C = \frac{1}{2\pi RC} \tag{3.1.7}$$

R in equation 3.1.7 is taken as 50 Ω, the impedance of the microstrip line. The table below indicates the capacitors that were tested at the output of the PG.

Cut-off frequency (f_C)	**Capacitance**
680 MHz	4.7 pF
180 MHz	18 pF
100 MHz	33 pF
320 kHz	10 nF

The capacitors were placed at the output of the PG and the measured results are illustrated in figures 3.11 and 3.12. With the different capacitors placed at the output, different pulse shapes were obtained. Applying a filtered characteristic will change the shape of the pulse. The smallest capacitor (4.7 pF) at the output reduced the amplitude of the pulse as well as increased the harmonic content at the back-end of the pulse. Most of the spectral energy in a pulse is located at the lower frequencies and removing them with this capacitor reduces the amplitude and significantly change the shape of the pulse. The other three pulses have smaller differences in amplitude, but different cut-in frequencies. Most of the low frequency content from these pulses are not removed.

The frequency response from each pulse is different in the first 1 GHz of the spectrum which is expected. The 10 nF pulse does not have a specific cut-in frequency and was previously used to remove DC on the output line. The 33 pF and 18 pF responses have a respective -3 dB cut-in frequency of 100 MHz and 150 MHz. The amplitude difference between these pulses are 0.75 V. The 4.7 pF pulse has a cut-in frequency of 450 MHz, and the largest amplitude. The RC has a cut-in frequency around 200 MHz. From calculations the 18 pF capacitor that should be used at the output of the PG, but if the 33 pF and 18 pF spectral content are compared, the best capacitor to filter the PG is the 33 pF capacitor. It has an improved amplitude and has a 0.5 dB - 1 dB increased spectrum after 1 GHz. Although the -3 dB cut-in frequency is lower than the 200 MHz cut-in-frequency of the chamber, the peak spectral energy of this pulse is at 200 MHz as observed in the spectrum.

3.1.1.4 Conclusion

From these previous investigations and improvements, the final pulse generator can be designed and built. In this section the microstrip line width was changed to increase the amount of capacitance per millimetre. If the stored charge at the collector of the transistor is improved it increase the current gain of the transistor, which increases the amplitude of the pulse. The shorted line method was

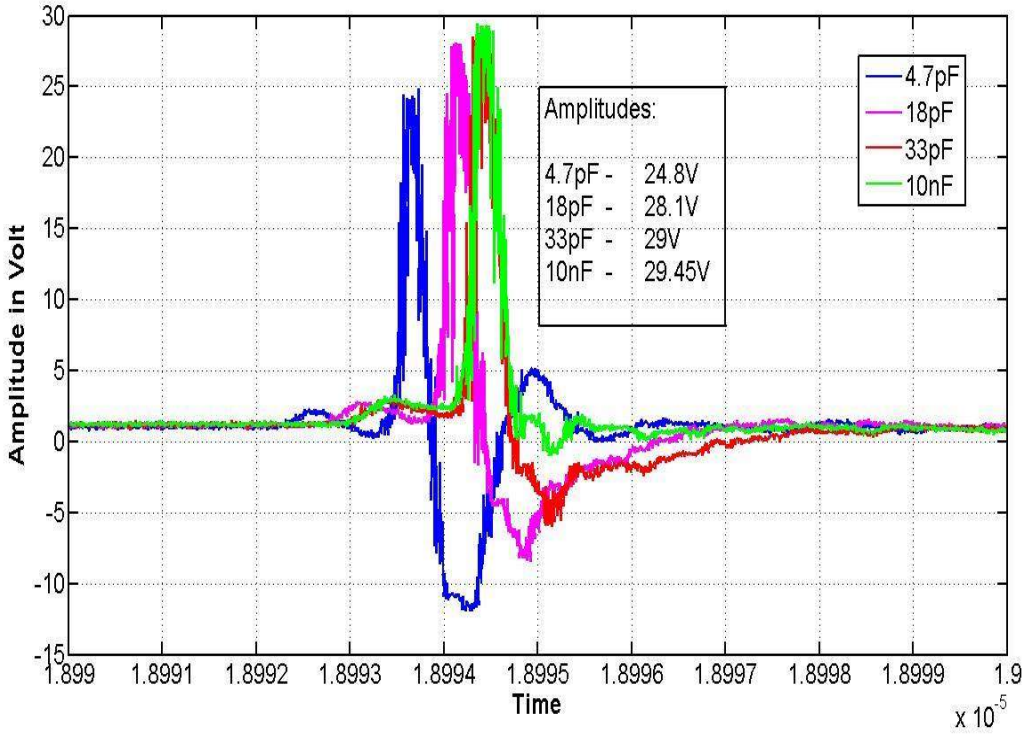

Figure 3.11: Pulses with the different capacitors at the output of the PG.

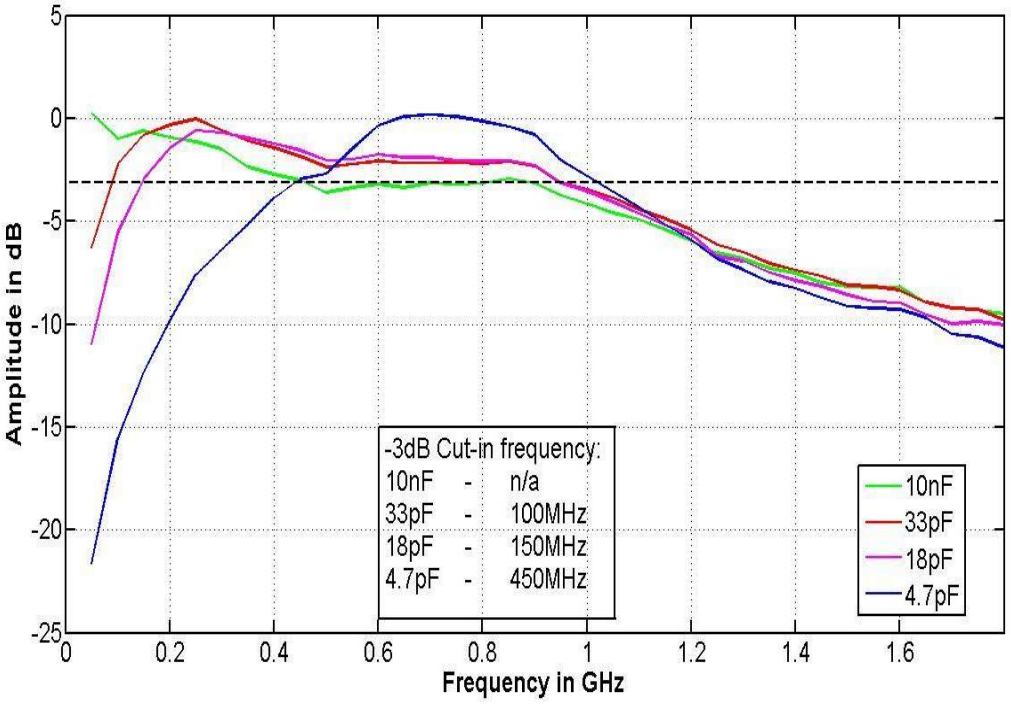

Figure 3.12: Spectrum of the filtered pulses by the different capacitors placed at the output of the PG.

implemented to remove the coupling of the triggering pulse into the output pulse and optimise the width and rise-time of the pulse. This directly influences the spectral content to increase the amplitude in the FD according to Parseval's theorem. Precise shorted line lengths had to be implemented in order to obtain a peak amplitude pulse. The biasing network for the SRD is also pivotal and any alter in current will not give optimal pulse amplitudes and rise-times. The amount of stored charge in the SRD will determine the rise-time and amplitude of the pulse. The last improvement was filtering the output pulse to work with the RC and RATTY. The different capacitors at the output of the PG changed the shape of the pulse and had an influence on the amplitude of the pulse. The transistor and SRD are sensitive semiconductors and any unstable biasing currents and potentials with capacitor values will not give an optimal output pulse. Pictures of the test circuit and set-ups are depicted in figure 3.13.

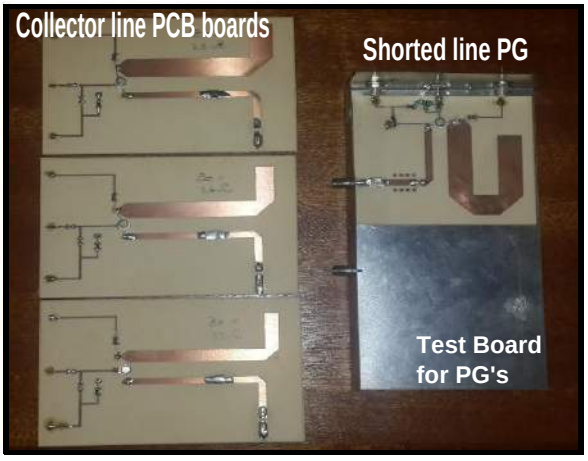

Figure 3.13: Picture of the test board and the test PGs.

3.1.2 Final design of the 30 V PG with the measured results

The final PG can now be designed and tested. The external circuitry around the transistor and SRD form a pivotal role when PGs are designed. The width, amplitude, shape and rise-time of the pulse are determined by these components. Design experience and optimisation methods as discussed in previous sections led to the final design of the PG. The PG was designed and built on a Rogers Duriod 4003C substrate with passive components. A metal casing was placed around the substrate and feed through capacitors were used to bias the transistor and SRD. These are good design principles to prevent coupling from internal circuitry with power supplies, signal generators and sampling oscilloscopes. The layout of the printed circuit board and components used for this PG design can be found in appendix A.1. The final PG circuit is the same as in figure 3.2 and a picture of the PG is shown in figure 3.14.

The two major differences are R_E and the capacitors placed at the shorted line. R_E was changed from 100 Ω to 1.1 $k\Omega$ to lower the SRD biasing current. If too much forward current is supplied to the SRD, more stored charge will be accumulated in the diode. For a faster transition time between the two states of the SRD, the lowest possible forward current is supplied to ensure the minimum amount of charge is obtained that is required for the SRD. From the data sheets, in appendix C, a 10 mA forward current is ideal and the 1.1 $k\Omega$ resistor provides this current. The reason for choosing the different capacitors at the shorted line was to remove a reflected pulse that occurs a few nano-seconds after the main pulse. This reflected pulse has also been recorded in [26]. The PG was triggered by a

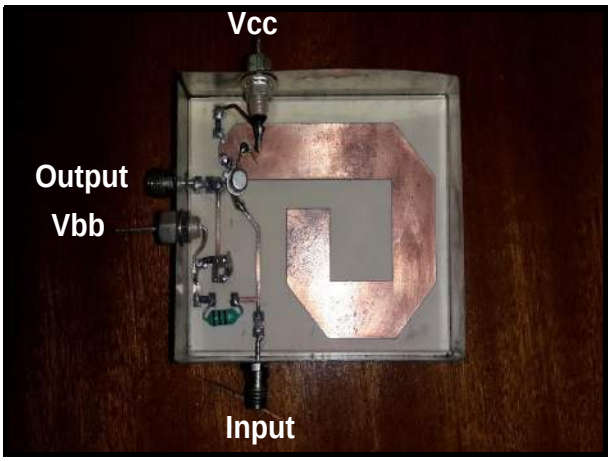

Figure 3.14: Photograph of the 30 V PG.

5 V pulse with a 20 ns width. The fastest tested repetition rate of the trigger was 2 us and the repetition rate for RC measurements were between 10 us and 20 us. The results of the final 30 V pulse generator are shown in figures 3.15 and 3.16. Phase stable cables were used during measurements and the pulse was sampled by the 50 GHz sampling oscilloscope.

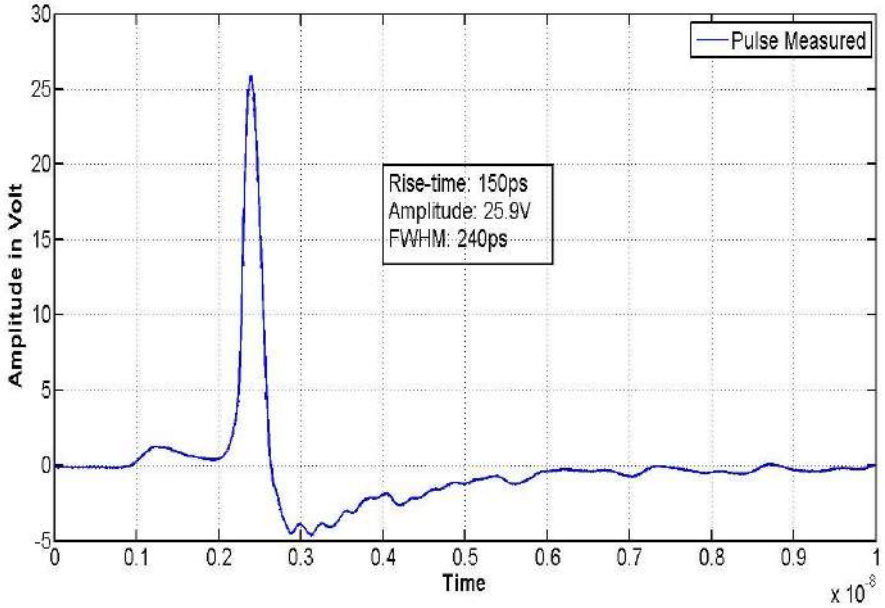

Figure 3.15: Final pulse measured on HP 54750A with the 30 V PG.

The peak amplitude obtained by the pulse generator with cable losses is 25.9 V. It is 2 V lower than the expected voltage obtained during the filtered measurements. This is caused by the change of capacitors at the shorted line. The three capacitors at the shorted line are used to remove a reflected pulse after the main pulse, which slightly reduces the amplitude of the pulse measured. During measurements if the biasing voltage of the SRD is changed, the amplitude of reflected pulse also changes. Using the same capacitors for the shorted line as in [3], removed the reflected pulse and dropped the amplitude of the pulse. The sample oscilloscope is also set to average the pulse to remove small amounts of jitter. This tends to drop the peak of the pulse by a small amount as well. The rise-time

of the pulse is 150 ps. This can vary slightly due to the stability of the DC power supply, biasing the SRD. Slight changes in the biasing voltage affect the measured amplitude and rise-time. The optimal biasing point for this pulse generator is at -7.5 V, as measured with a digital multimeter. The FWHM of the pulse is 240 ps. The pulse, when compared to previous measurements, has an improved rise-time of 30 ps - 35 ps from test results and a slight amplitude difference (-2 V). The filtered response of the 33 pF capacitor is seen at the back end of the pulse and the small lump in front of the pulse is the stored charge in the SRD. The spectrum of the PG is depicted in figure 3.16.

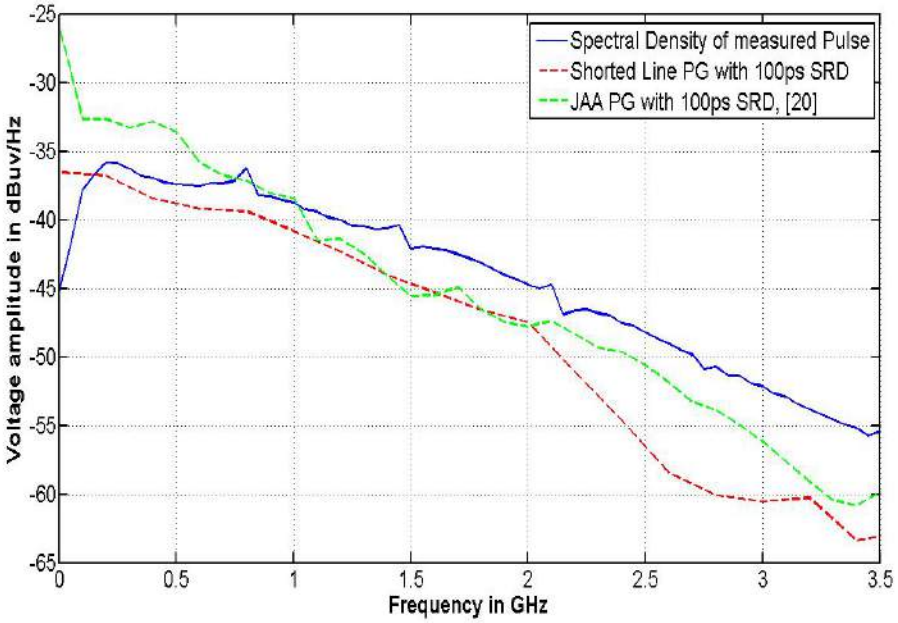

Figure 3.16: Spectral density of final pulse measured on HP54750A with the 30 V PG compared to previous PG models.

The cut-in frequency of the filter applied to the output is at 200 MHz. The bandwidth of a pulse is determined by the first 3 dB drop in the FD. In our case it is determined by the maximum frequency range that can be measured for our systems or equation 3.0.1. RC measurements with RATTY allow spectral content that can be measured up to 1.4 GHz. Therefore by improving the spectral density by decreasing the rise-time of the pulse, in our case, is an improved bandwidth. The final PG has an improved bandwidth when compared to the other two bands. There is a 1 dB - 3 dB improvement from 200 MHz up to 2 GHz, when the spectrum is compared to the test PG with the shorted line and SRD (dotted red line). After 2 GHz the spectral content of the test PG drops by more than 10 dB over 500 MHz. If the spectrum of the final PG is compared to the JAA PG, there is 2 dB - 3 dB difference in the first part of the spectrum, but after 750 MHz the bandwidth of the final PG is significantly better. The bandwidth was improved, by optimising the shorted line at the emitter of the transistor and sufficiently biasing the SRD. This gave an improved rise-time to increase the spectral density of the pulse at the higher frequencies. The overall improvement at these frequencies is around 3 dB over $1-3.5$ GHz.

Small changes were made to circuit elements to obtain an optimized pulse for the RC measurements. Because rise-times of pico-seconds were required, small changes in components affect the characteristics of the pulse produced. The avalanche transistor and SRD technique is a reliable and stable design method for impulse generators and produce significant amplitudes for shielding mea-

surements in the RC. The final design is currently being used for tests inside the Stellenbosch University RC.

3.2 Stacked avalanche transistor impulse generator (50V Pulse)

In addition to the 30 V PG design, a second PG was designed. The goal for this model was to improve the amplitude without changing the rise-time and width of the pulse. Although the 30 V PG has an improved spectrum from previous models, increasing the spectral content of the pulse will benefit measurements in a noisy environment. Stacking avalanche transistors is implemented in [30,31,32]. Stacked avalanche transistor give an increase in amplitude due to an increase in current. The serial connection force the transistors to discharge simultaneously and obtain a higher amplitude [32]. The peak voltage limit of one single transistor can be doubled if the losses between the leads of the transistors are kept as small as possible.

The external circuitry was left unchanged and only two transistors were stacked in series to improve the amplitude of the pulse. A figure of the circuit is shown in 3.17. The SRD used for the stacked PG is the MMD810-T86. It has a transition time of $200-250$ ps with a breakdown voltage of 50 V. Because the amplitude of the pulse is increased with stacking, the faster SRD used in the 30 V PG had to be replaced. The previous SRD had a breakdown voltage of 40 V and may fail if the peak amplitude of the pulse is double the amplitude of the 30 V PG. This also forced a longer shorted line, to ensure the peak amplitude of the pulse is not subtracted by the reflected pulse from the short circuit. The length of the line was increased to 24.5 mm, which would take a pulse 300 ps to travel to the end of the line and back.

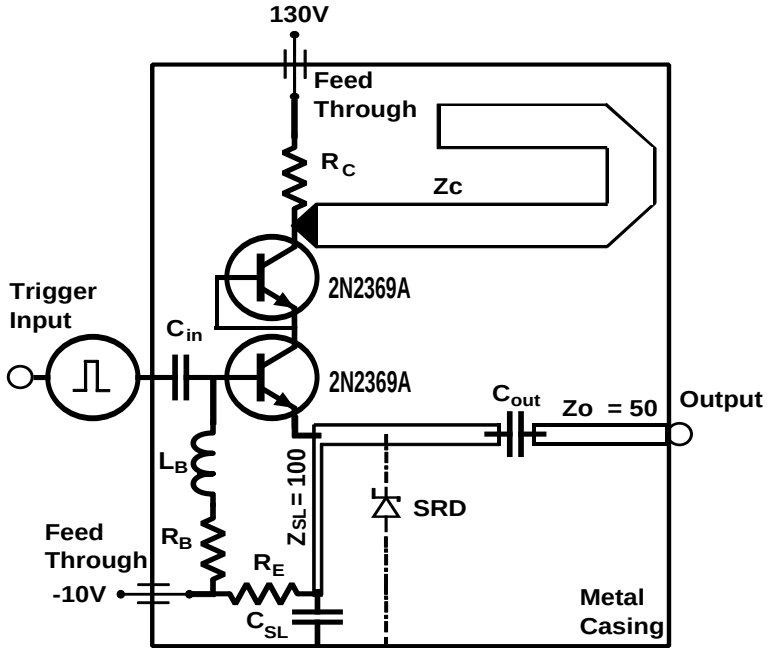

Figure 3.17: Stacked PG circuit schematic.

Because a higher amplitude pulse was expected the PG was measured on a more robust lower bandwidth oscilloscope that can handle higher voltages. The Yokogawa is band limited to 500 MHz, but it is effective and easy to use for testing purposes. Because of its band limitation the higher frequencies of the pulse will be filtered, which will reduce the amplitude of the sampled pulse. A test PG circuit was built and measured on the Yokogawa sampling oscilloscope. The different results are

depicted in figures 3.18 and 3.19 below.

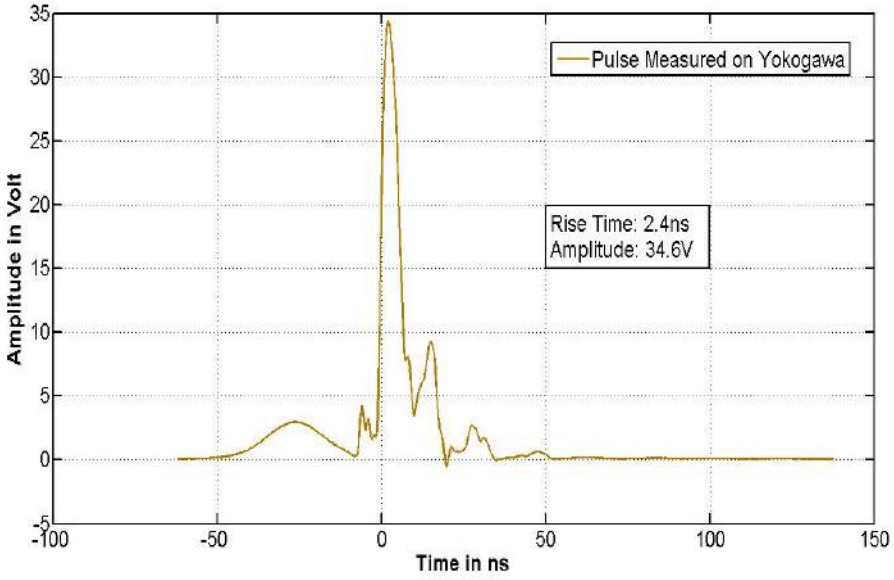

Figure 3.18: Pulse of the stacked PG measured on Yokogawa sampling scope in the interleaved mode.

The pulse amplitude cannot be calculated and required caution in measurements to protect sampling oscilloscopes. The PG was first tested on the Yokogawa. Setting the input impedance of the Yokogawa to 1 $M\Omega$ reduces the current of an incoming pulse and allow higher amplitude pulses to be measured. This also protects the input ports and electronics inside of the Yokogawa. After the amplitude of the pulse is measured on the high input impedance and attenuators are used to reduce the peak amplitude of the pulse, the input impedance of the scope is changed to 50 Ω and sampled for processing. Changing the impedance back to 50 Ω will give the correct amplitude and shape of the pulse produced by the stacked PG.

The pulse produced by the stacked PG is 34.6 V, with a rise-time of 2.4 ns. The stored charge in the SRD can again be seen in the front end of the pulse with unusual content at the back end. The band limitation of the Yokogawa reduces the amplitude of the pulse and this measurement was done to test the stacked PG circuit. The limit of the Yokogawa can also be seen in the spectrum of the pulse. The energy of the pulse is sampled up to 1.25 GHz, which is allowed if the sampling oscilloscope is used in an interleaved mode. The enables an extra 750 MHz of spectral content to be sampled.

3.2.1 Final design with measured results.

The final design for the 50 V PG was similar to the 30 V Pulse generator. The PG was built on a Rogers Duriod 4003C substrate with a metal casing and feed-through capacitors. The only difference from this design is the resistor value used at the collector of the first transistor. A 10 $k\Omega$ resistor was placed at the collector to control the current supplied to both of the transistors and ensure both the transistors were forced into the avalanche region. With a larger resistor, the potential at the collector was too low to force it into breakdown. The table of all component values and the printed circuit board (PCB) design can be found in appendix A.2. The circuit is shown in figure 3.17 and a picture of the PG is displayed in figure 3.20.

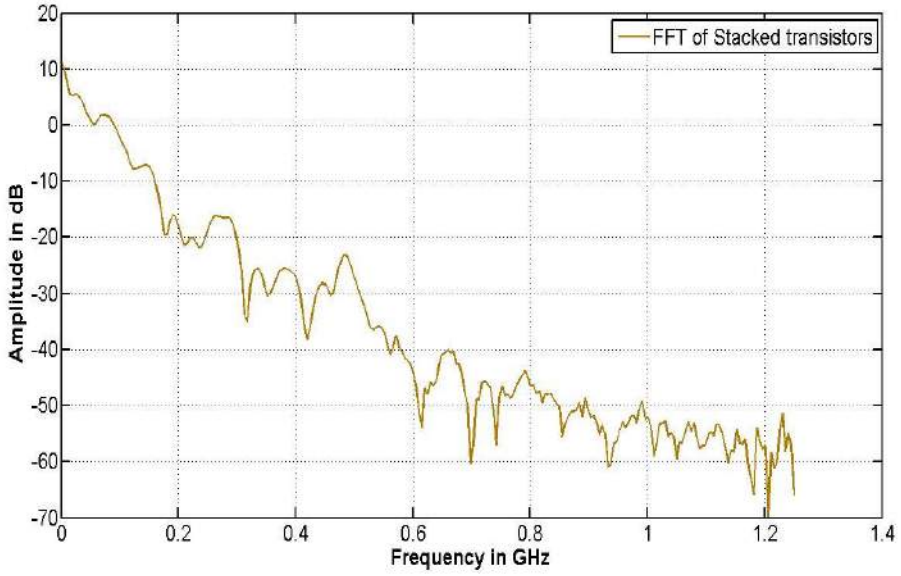

Figure 3.19: Spectral content of the stacked PG measured on Yokogawa sampling scope in the interleaved mode.

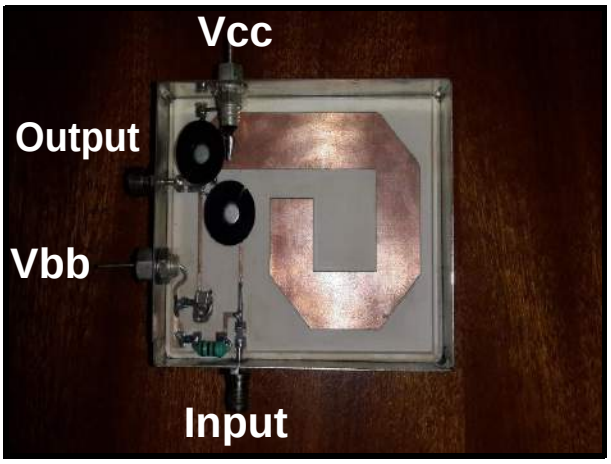

Figure 3.20: Picture of the stacked PG.

The pulse was triggered by a 5 V 20 ns width pulse, with a slower repetition rate than the 30 V pulse generator. A faster repetition rate increased the RMS power, which distorted the output pulse. With a slower trigger a more stable pulse was produced, because it gives more time for both transistors to reach a stable operating point before the next trigger arrives. A faster repetition rate forces both transistors to breakdown more frequently which may cause transistors to fail. The limit with our stacked PG was that it cannot be triggered for longer than a couple of minutes, before the pulse distorts. This problem occurs from internal overheating inside of the transistors or SRD. During measurements cold air was blown onto the circuit which stabilised the pulse to confirm that the problem was overheating. Decreasing the repetition rate improved the stability, but after a couple of minutes the same phenomenon occurred and caused a distorted pulse. Heat sinks were attached to each transistor which did not resolve the problem. The SRD might also be at its limit because of the final peak voltage obtained by this PG. The breakdown voltage of the SRD is 50 V and this was close to measured results. The measured results, for this PG when a stable pulse is produced, are displayed in figures 3.21 and 3.22.

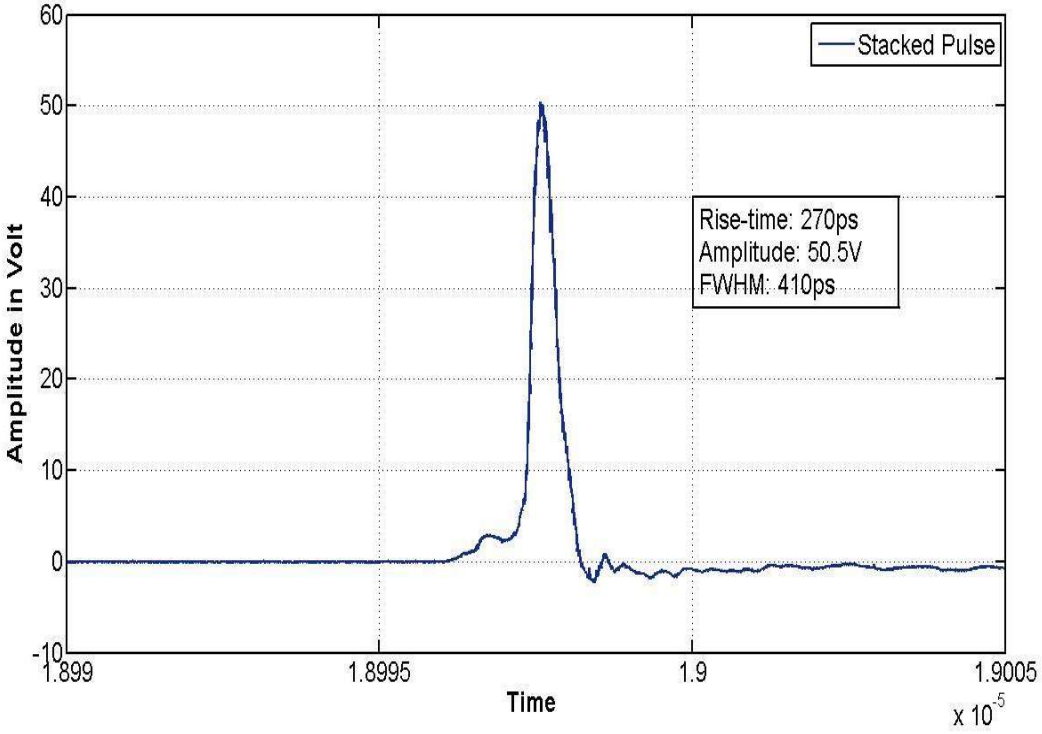

Figure 3.21: Final pulse of the stacked PG measured on HP54750 sampling scope.

The rise-time of the pulse is 270 ps, 20 ps slower than the switching time of the SRD, which means the SRD is optimally biased. As shown in previous results when the SRD biasing voltage is changed the amplitude and rise-time of the pulse changes. The amount of internal stored charge inside of the SRD determines when these characteristics of the pulse. The amplitude of the pulse is almost double the amplitude of the single avalanche transistor at 50.5 V. This is a good indication that with stacked transistor the dynamic range of the pulse can be increased. The width of the pulse is 410 ps. There is no filtered characteristic at the output of this pulse.

The spectrum of the stacked PG is compared to the single (30 V) PG. The improved amplitude increases the energy in the spectrum by 9 dB at 200 MHz, and reduces with frequency until they are equal at 1.4 GHz. The stacked PG has more dynamic range for the first 1.4 GHz of the spectrum and drops quicker than the faster rise-time PG. If RC measurements require an extra 10 dB of dynamic range for the first GHz of the measurement a stacked PG design can be used for the measurements. If a larger bandwidth PG is required with the best possible rise-times, the 30 V single avalanche transistor would be a better design. The 30 V PG is more stable and reliable.

Although the amplitude of the PG is improved by the stacked transistors, the optimal design for our purpose is a single transistor with the fastest possible SRD. This improves the spectral density at the higher frequencies. Stacking transistors can become beneficiary when large amplitude (100's of volts) pulse are required with sub-nanosecond rise-times. A non-linear transmission line design might be implemented at the output of stacked transistors to obtain pico-second rise-times, with larger breakdown values than SRD's. With available components and breakdown values of components, the best design for measurements inside the RC is the PG with a single avalanche transistor with a 80 $ps - 100$ ps rise-time. The improved rise-time increased the bandwidth of the pulse which enabled a larger scope of frequencies that are instantaneously swept with one injected pulse. The D.U.T can be characterised over a broader spectrum with a fast rising transient pulse. This section

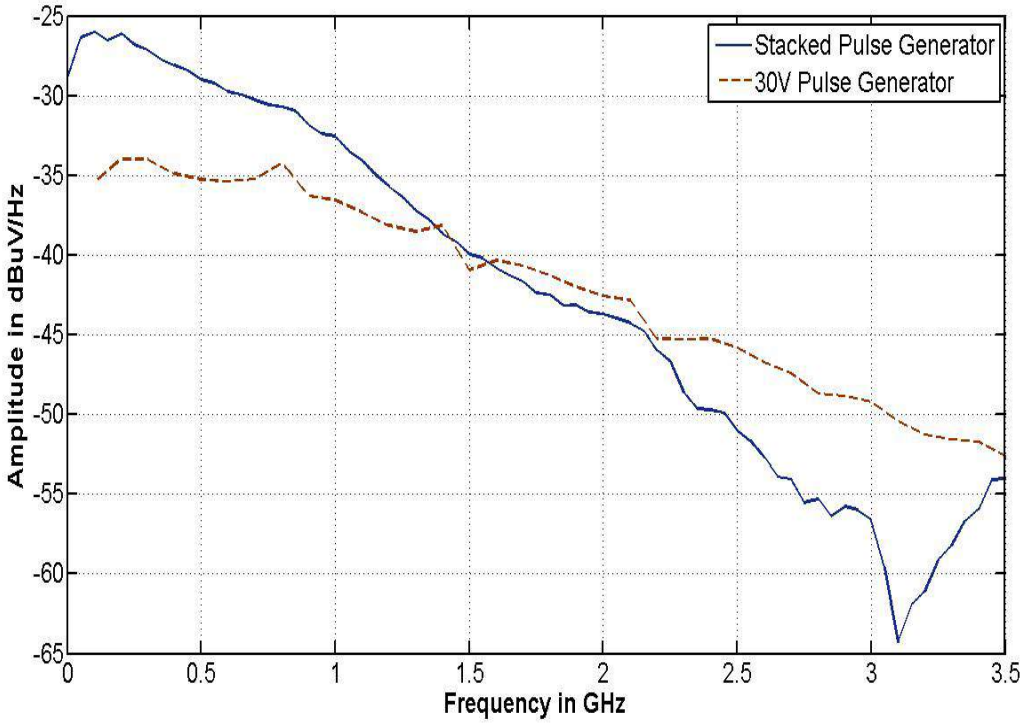

Figure 3.22: Final spectral content of the stacked PG measured on HP 54750 sampling scope compared to the 30 V PG.

has shown the design of a stacked transistor PG. The current limitation for this design is overheating and further investigation of external circuitry is required to improve the current design. The SRD can be replaced by a slower SRD, like the MMD805-T86, that has a breakdown voltage of 60 V. We found that temperature-related effects had an influence with time particularly when the pulse was on the verge of the SRD transition voltage. This was notice if the PG ran for a long period of time. Slower trigger rates were also tested which slightly improved the stability and operating time of the PG, but also distorted after a few minutes. With a slower repetition rate the transistors are allowed to reach a stable point before the next trigger pulse arrives and the total average power in the system is reduced, which decreases the overall heat dissipated in the system. Semiconductors are sensitive in general and circuit and ambient temperature play a significant role when they are operated.

3.3 Characteristics of the CPS1 PG (A commercial PG bought from Kentech industries)

Two PG models have been designed in this chapter to assist with RC measurements. In this study a TD system is designed to characterise the Karoo environment. For this a stronger pulse (kilovolts) with more dynamic range and a large bandwidth is required. The CPS1 PG is bought from Kentech industries to assist with TD metrology in the Karoo. From past measurements the 30 V PG disappeared into the surrounding RF noise that were generated in the vicinity. For propagation measurements and shielding measurements over longer distances than 10 m, a higher amplitude pulse with a fast rise-time is required. The CPS1 is one of many PG design models available at Kentech. This particular design consists of stacked avalanche transistors to produce a $\pm$ 2.5 kV pulse, which is sharpened to a rise-time of 150 ps. The CPS1 pulse and spectrum are depicted in figures 3.23 and 3.24.

The amplitude of the pulse is 2.42 kV with a rise-time of 150 ps. The pulse has a fast rising edge,

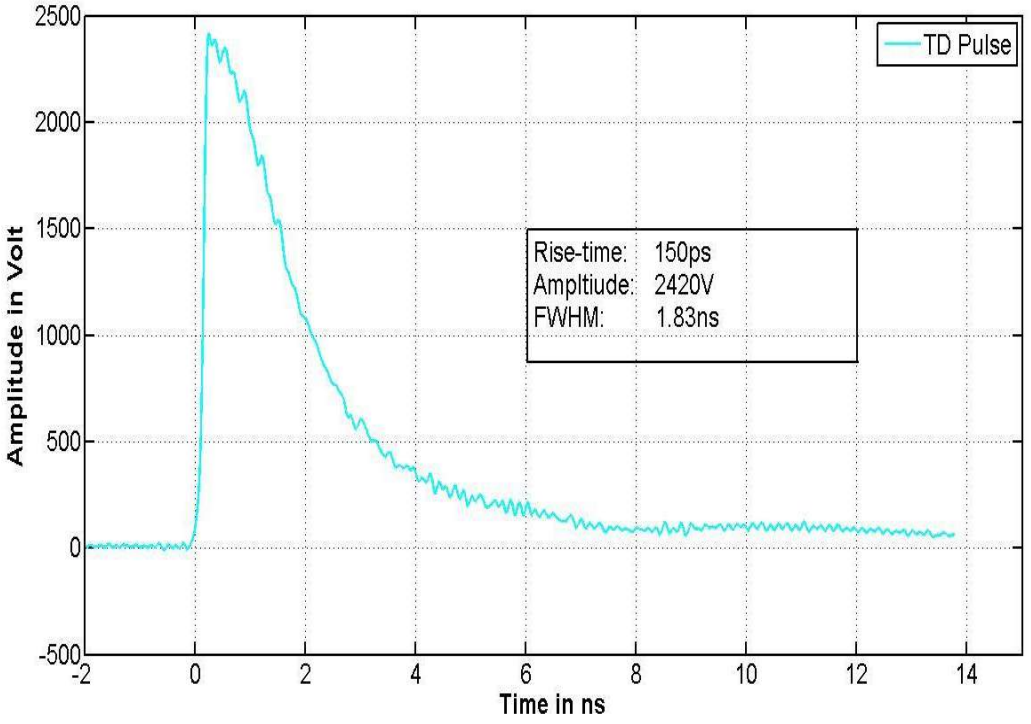

Figure 3.23: Pulse produced by CPS1 impulse generator.

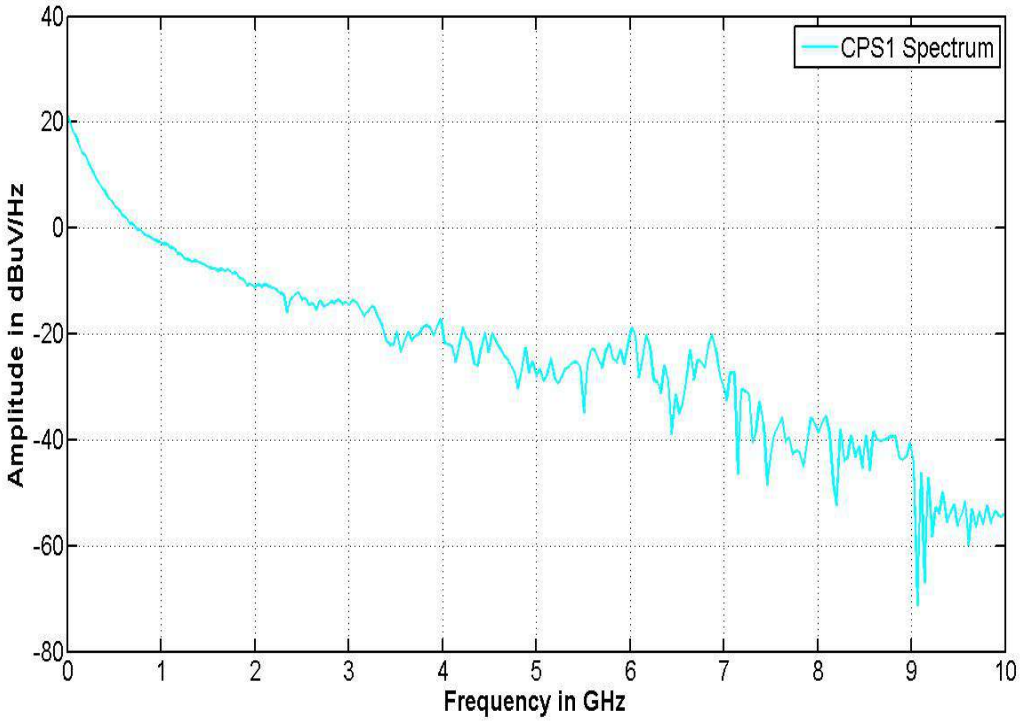

Figure 3.24: Spectrum of the CPS1 impulse generator.

but a slow exponential like falling edge of 5 $ns - 7$ ns. The FWHM of the pulse is 1.8266 ns. The slow falling edge is not of importance, because the CPS1 will be used with an IRA antenna that differenti-

ates the signal in the far-field, to form an impulse. The IRA will design will be explained in the next chapter. The peak amplitude in this spectrum is 50 dB more than the two pulse generator results shown earlier in this chapter. The amplitude drops by 20 dB in the first 1 GHz of the spectrum from where its falling rate decrease to -20 dB per 3 GHz up to 6 GHz. The bandwidth of the pulse is between 6 and 7 GHz before it starts to drop into the noise floor. The CPS1 will be used with RTA that can efficiently sample a TD signal in four bands up to 2.7 GHz. More of this device will be explained in chapter 5. A picture of the CPS1 is depicted below.

3.4 Conclusion and recommendations

Throughout this chapter the design of two PGs were discussed. An avalanche transistor with a SRD were the elementary parts behind these PG designs. The pulse was created by the avalanching phenomenon and the SRD sharpened the leading edge of the pulse. The external circuitry around these components was essential and it determined the final pulse that was produced. The collector line method was optimised by increasing the total stored charge at the collector of the transistor, in order to increase the amplitude of the pulse through an increase in transistor current gain. The shorted line technique from [3] was implemented to shorten the width of the pulse and to ensure that there was no coupling between the output pulse and the trigger of the PG. It was also used to obtain the best amplitude of the pulse, by ensuring that the length of the line was longer than the transition time of the SRD. The fastest available SRD was placed at this point and biasing it with the correct current levels, helped to achieve the best rise-time for the pulse. The last optimisation that was implemented in the PG design, was an output filtered characteristic. A high-pass filter removed DC and the lower frequency content from the pulse that caused saturation in RATTY. The operating band for the RC was also considered and the capacitor applied for the filter ensured a -3 dB cut-in frequency at 100 MHz and peak amplitude in the spectrum at 200 MHz. The final pulse characteristics that were obtained with a single transistor, had an amplitude of 25.9 V and a rise-time of 150 ps. The spectrum of the pulse was compared to previous PG design models and the bandwidth was significantly improved. The spectral content at 2.5 GHz dropped by 10 dB where previous results dropped by roughly 15 dB and 20 dB. The 30 V PG is currently used in the RC to assist with a PhD thesis for TD metrology work in a shielded enclosure.

Stacking transistors were also implemented in this study to obtain a larger amplitude pulse. The general circuit design around the transistor was kept the same and only two transistors were stacked in series to improve the the total current during breakdown. This doubled the pulse amplitude obtained with one transistor. Increasing the amplitude would allow more dynamic range in the spectrum which could help with measurements in a noisy environment. The design does work, but has limitations which need to be considered and improved to increase the stability of the pulse. Almost double the amplitude can be achieved by stacking transistors and is definitely an effective method to obtain high amplitude pulses. The peak amplitude of the pulse obtained by stacking transistors was 50.5 V with a rise-time of 270 ps. A slower SRD was used in this model because the breakdown voltage of the faster SRD was 40 V and it would have failed if it was used. Recommendations for the stacked pulse generator design, would be to change external circuitry components in order to stabilise the pulse through current control. The resistor at the collector can be changed to control the current. The repetition rate of the pulse can also be slowed. During measurements, the pulse became more stable when a slower trigger was applied to the system. This reduced the total average power in the system to prevent component overheating and to allow the transistor to reach a stable point before the next trigger, but it did not solve the problem. After a couple of minutes, the pulse becomes distorted. Heat sinks were attached to both transistors and this still had little to no effect. The use of the SRD affects the stability of the pulse and replacing the SRD, to a slower or different model diode can also be explored. Because the peak amplitude of the pulse was at the limit of the breakdown voltage of the SRD, a more robust SRD with a higher breakdown voltage, can be implemented to stabilise the

pulse.

We also bought a high-voltage 2.5 kV PG, the CPS1, from Kentech industries. This PG will be used for metrology in the Karoo and it will be discussed in a subsequent chapter. Because of its high voltage and fast rise-time, the dynamic range of the PG is almost 50 dB more than our current PGs. This would make propagation measurements over long distances and SE test more effective because of the increased spectral density of the pulse. The CPS1 will be used with a radiating antenna and this will be discussed in the next chapter. Practical measurements and tests with the PG and antenna system will be explained in chapters 5 and 6.

Chapter 4

Impulse radiating antenna

The purpose of this project is to design a TD measuring system for electromagnetic compatibility (EMC) and RFI related measurements, in the Karoo environment, for the SKA project currently under development in South-Africa. An external pulse generator source has been developed and discussed in chapter 3 and requires an efficient transmitting source to radiate these transients. The impulse radiating antenna (IRA) is exactly what it says it is, an antenna that effectively radiates transient impulses. As mentioned in chapter 2 section 2.2, the concept behind the IRA originated from Carl E. Baum. D. Giri and E.G. Farr continued his work and were the first to built these IRAs and use it for their line of work, which include high power electromagnetics and radar. One of Dave Giri's IRA designs is a parabolic lens IRA for the radiation of high-powered sources [17]. The antenna is used for high-power EMC measurements and consists of a parabolic lens at the focal point of the dish. Farr has constructed multiple IRAs for different purposes. The IRA's mostly consist of a balun to feed a 200 Ω IRA [18, 33, 34, 35] and is mostly related to radar applications. The balun matches a 50 Ω pulse generator source to the 200 Ω antenna.

For our work the antenna will be used to radiate a high-voltage fast-rising impulse for SE tests and propagation measurements in the Karoo. In this chapter a thorough design of the Stellenbosch IRA and optimisation techniques applied, will be shown. The design is built and simulated in FEKO. The design was limited to the available components and follows a similar pattern to Farr's designs. The first section will cover the design of the IRA with final geometrical dimensions for the Stellenbosch IRA. Secondly the IRA is simulated in FEKO. The gain, reflection coefficient and impedance of the IRA is discussed. Polar patterns and far-fields are also shown. The last two sections will cover antenna measurements and optimisation leading to a final design for the IRA.

4.1 Design components of the IRA

The building blocks of the IRA are a feeding point, four conical plate transmission (TM) lines that are terminated through resistors onto a reflector dish and a balun. The balun forms part of the feeding point and will be discussed in a later section. A picture of the IRA building blocks is shown in figure 4.1 following four sections to describe each block with its design equations.

4.1.1 Parabolic reflector and impedance of IRA

Parabolic reflectors are commonly used around the world in radar and satellite communication. They can yield high gains and are robust, but can be extremely large in size and are very directive. The fundamental part of the IRA is a parabolic reflector. The size of the reflector will determine the total gain that can be achieved as well as the input impedance of the antenna. The size of the reflector is the designer's preference and will mostly depend on the project environment, budget, outcome and mostly what reflector is available. For our project the main factors taken into consideration were

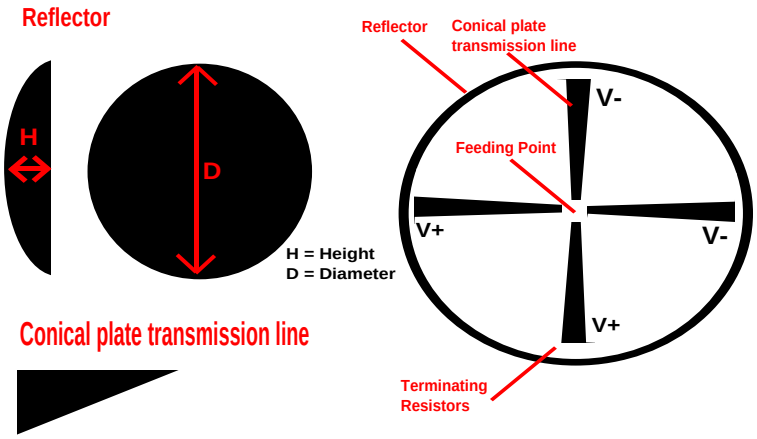

Figure 4.1: The basic parts of the impulse radiating antenna.

transportation over a long distances through rough terrain and a restriction that only two reflectors were available in our department for use. The dish that was accessible had a diameter (D) of 1250 mm and height (h) of 290 mm. Using the following equations the focal point (f) of the dish could be calculated:

$$z_0 = f - \frac{D^2}{16f} \tag{4.1.1}$$

$$z_0 = f - h \tag{4.1.2}$$

where z_0 is the distance from the focal point to the edge of the rim along the axis of the reflector. After substituting equation 4.1.2 into 4.1.1 the focal point is:

$$f = \frac{D^2}{16h} \tag{4.1.3}$$

The focal point is calculated to determine the F/D ratio of the parabolic reflector. Most of the IRA designs from Farr and Baum had F/D ratios of 0.4. The F/D ratio is chosen because it simplifies the size, but from Baum [36] and Farr [21] pages 4-6, the F/D ratio can determine the area of the pre-pulse (A_p) and area of the impulse (A_i). A theoretical pre-pulse and impulse is calculated from a number of assumptions: an ideal matching circuit and small aperture blockage. If the area of the pre-pulse equalises the area of the impulse, the trailing end of the pulse will be small. Thus the F/D ratio is also chosen to decrease harmonic content that can form at the back of the radiated pulse.

The focal point of the available reflector is 336.7 mm and has an F/D ratio of 0.27. Because a 0.4 F/D ratio was common amongst most of the designs, the diameter of our reflector was reduced to 850 mm to yield an F/D ratio of 0.4. This also reduced the size of our reflector, which made it more convenient for travelling over long distances.

4.1.2 Conical plate transmission lines

The input impedance of the antenna and size of the reflector are pivotal when designing the conical plate TM-lines. The impedance affects the size of the TM-lines, which directly influences aperture blockage. From [21, 22] and microwave theory the smaller the impedance the larger is the object. This will increase aperture blockage, but will make it easier to match the antenna to standard 50 Ω

systems. The smaller the impedance the better the aperture blockage, but it is harder to match to a standard system. The ideal impedance chosen for the TM-lines is 400 Ω. This gives the best gain with the least aperture blockage when compared to 200 Ω and 100 Ω plates. The IRA can be designed with two or four conical plate TM-lines as shown in figure 4.1. The IRA is normally designed with four TEM feeding structures. This allows larger impedance plates that can be designed to reduce aperture blockage. For this project a four-arm IRA is designed where two of the arms are coupled together in parallel. Parallel configuration reduces the combined impedance of the plates by half and enable easier matching to a PG system. This section will cover all design equations and mathematical resources used to simplify the design of these TM-lines.

For this project the impedance of the plates were chosen accordingly. The input impedance had to be matched to a 50 Ω impulse generator system. The generator produced a 2.5 kV pulse which could cause damage to equipment if the right components are not used. The break down values of all the cables, connectors and components were selected to ensure safety and fitting for our system. Calculated breakdown values for components in the IRA system can be obtained in Appendix D. Because of limited cables and connectors available, the input impedance of the IRA was selected to be 150 Ω.

The feeding plates are calculated using stereographic projection, conformal mapping and elliptical integrals of the first kind [36, 37, 38]. A figure (4.2) of the IRA with design variables is depicted below with the input impedance of the antenna chosen as 150 Ω. With the diameter, focal point and input impedance known, the conical plates, spaced an angle (ϕ_0) from the y-axis, can be calculated by the following equations.

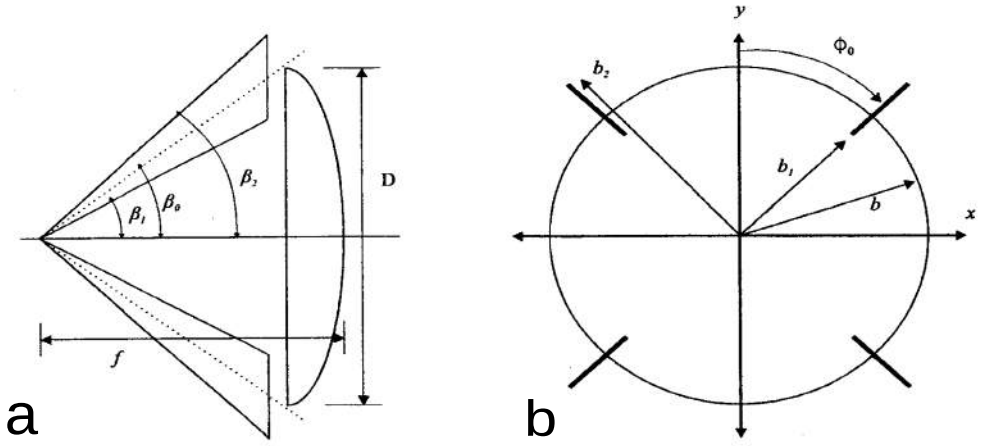

Figure 4.2: The IRA with the conical plate design equations. a)Side view. b)Front view. [39]

The impedance of the TEM feed is defined as

$$Z_c = \eta_0 \frac{K(m)}{K'(m)} \tag{4.1.4}$$

where Z_c is the characteristic impedance of the plates, η_0 is the free-space wave impedance and $K(m)$ is an elliptical function of the first kind. For a four-arm design, the characteristic impedance is double the input impedance of the antenna. Combining the two plates in parallel will match it to the 150 Ω desired impedance. Equation 4.1.4 can be re-written as

$$f_g = \frac{K(m)}{K'(m)} \tag{4.1.5}$$

with

$$f_g = \frac{Z_c}{\eta_0} \tag{4.1.6}$$

Because both the input and free-space wave impedances are known, the elliptical function can be solved by using conversion table 17.3 in [40]. Interpolating from table 17.3 the parameter m can be obtained. Once m is known, the TEM feeding plate parameters as shown in figure 4.2 can be calculated with these last set of equations.

$$k = m^{\frac{1}{2}} \tag{4.1.7}$$

$$\beta_0 = \arctan\left(\frac{1}{\frac{2f}{D} - \frac{D}{8f}}\right) \tag{4.1.8}$$

$$\beta_1 = 2\arctan\left(\sqrt{k}\tan\left(\frac{\beta_0}{2}\right)\right) \tag{4.1.9}$$

$$\beta_2 = 2\arctan\left(\frac{\tan\left(\frac{\beta_1}{2}\right)}{k}\right) \tag{4.1.10}$$

β_0, β_1 and β_2 are the conical plate feeding structure parameters, which are related to the equivalent longitudinally symmetric structure parameters (b, $b1$, $b2$, D, f) as shown in figure 4.2.

$$b = \frac{D}{2} \tag{4.1.11}$$

$$b1 = \frac{\tan\left(\frac{\beta_1}{2}\right)}{\tan\left(\frac{\beta_0}{2}\right)} b \tag{4.1.12}$$

$$b2 = \frac{\tan\left(\frac{\beta_2}{2}\right)}{\tan\left(\frac{\beta_0}{2}\right)} b \tag{4.1.13}$$

$$b = \sqrt{b1\,b2} \tag{4.1.14}$$

With normal trigonometry, the side lengths of each conical plate transmission line can be calculated. After each plate size is calculated, the configuration of the four plates has to be determined. The general IRA topology is a 45°angle from the y-axis (see figure 4.2), but slight enhancements to the IRA has been reported by placing it at 30°and 15°from the y-axis [41,42,43]. For this project a 30°angle will be used to improve the gain and cross-polarisation of the antenna.

4.1.3 Resistive termination to parabolic reflector

The reflector dimensions and input impedance have been discussed in section 4.1.1 and an arbitrary design of the IRA TEM feeding plates has been shown in section 4.1.2. These two components of the IRA are electrically connected by terminating the conical plate transmission line with resistors onto the parabolic reflector.

The resistor sizes are chosen to match the combined impedance (150 Ω) of the feeding plates. Farr and Bowen [41, 43] has recorded slight improvements in the TD reflectometry (TDR) when the resistors are placed in different positions. They have done multiple optimisation experiments using different resistors and configurations as well as cable and choke positioning when feeding the IRA. The concluding result from their work is that the mechanical positioning of the IRAs did not have a large effect on the TDR. Most of the resistor connections are spread across the plates to ensure equal current flow from the plates to the dish.

Our IRA consisted of 8 quarter-watt surface-mount resistors equally spaced on both sides of the plate to account for the currents on the plates. The 8 resistors are chosen to reduce overloading of peak power from a 2.5kV pulse generator source and to ensure all the currents on the plate are equally transformed from the TEM feeding structure to the reflector.

4.1.4 Balun and splitter

The last important component of the IRA antenna is the balun. The balun consist of two major components, a balanced feed with a one-to-two splitter. Although most IRAs use a $50-200\Omega$ balun, a $50-150\Omega$ balun is required for our system. A number of design baluns and feeding options have been suggested by Baum in [44]. Different designs incorporate different baluns and each depend on the individuals preference and availability of components. As mentioned earlier, the most common IRA designs are the parabolic lens IRA, where the source or switch is mostly placed at the focal point with an external charge line, or an IRA with a balun, where the signal is fed through a coaxial cable on a feed arm.

Because an external pulse-generating source will be used, the IRA will be fed with an coaxial cable through a $50-150\ \Omega$ balun. This idea originated from Baum [44] and will be incorporated into this IRA as shown in the figure below.

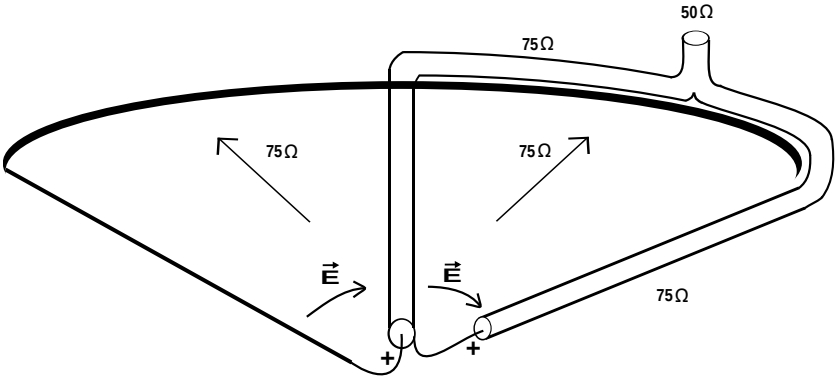

Figure 4.3: A single fed 150 Ω IRA, after [44].

The first part of this balun is a 50 Ω to 75 Ω splitter. After the splitter two 75 Ω cables are led to the focal point of the dish. One through the centre of the reflector and the other along the side of a conical plate transmission line. Two of the conical plates will be positively excited with the other two negatively excited. Thus two 300 Ω feeding plates in parallel form a 150 Ω E-field between the two polarities. The cable feeding the antenna through the centre of the reflector divides the 150 Ω E-field into half, forming the 75 Ω match to the cables. This balun technique has been implemented into most of Farr's designs and is the common method of excitation for this antenna.

Choosing the right splitter design for this antenna is also important. A resistive splitter was chosen because a large bandwidth is obtainable without extensive design limitations. A quarter-wave transformer was also an option, but it is band limited and frequency dependent. The resistive divider is classified as a T-junction power divider [45]. It contains lossy components to match all of its ports, but cannot be isolated at its output ports. A simple design figure with equations is depicted below.

In order to match $Z_{in} = 50\ \Omega$ to $Z_{out} = 75\ \Omega$ the following design equations are used to get R_{in} and R_{out}, where $R_{in} = R_{out}$.

$$Z = \frac{R_{out} + Z_{out}}{2} \tag{4.1.15}$$

and

$$Z_{in} = R_{in} + Z \tag{4.1.16}$$

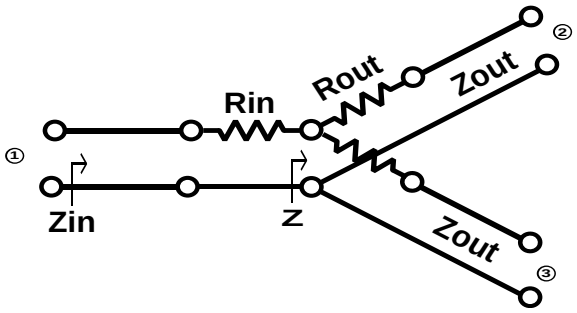

Figure 4.4: A three-port resistive power divider.

Substituting 4.1.15 into 4.1.16 the resistor values for the three-way power divider can be calculated as:

$$R = \frac{2Z_{in} - Z_{out}}{3} \tag{4.1.17}$$

The resistive divider was designed and simulated in AWR Microwave Office and CST to see what kind of reflection and transmission coefficients are expected for this splitter. The CST model is accurately designed according to connector and material sizes that will be used during construction. Resistive sheets with the correct properties are used to replicate the surface mount resistors. A figure of the model and results are shown in figures 4.5 and 4.6.

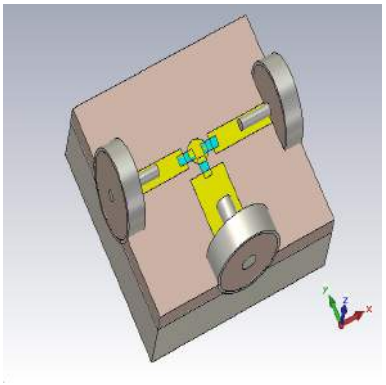

Figure 4.5: The T-junction model simulated in CST.

The AWR results assume ideal components and does not account for any losses in the design. Thus a very good reflection coefficient (S_{11}) is obtained. A more accurate S_{11} is the one from CST. Achieving better than $-20\ dB$ reflection coefficient for almost half of the simulated frequency range is extremely good. The reason for choosing a 6 GHz frequency range is because of the energy available from our generated pulse. The CPS1 pulse generator, designed by Kentech, produce a 2.5 kV pulse with a bandwidth up to 6 GHz. Because of the instantaneous energy in one pulse all the IRA components are desired to work up to 6 GHz. After 3 GHz the reflection coefficient of the CST simulated splitter worsen, but stays acceptable and under $-10\ dB$. With a higher reflection coefficient, most of the injected power will be reflected back into the transmitting system without transmitting it into the antenna. For the transmission coefficient (S_{21}) the AWR simulation also results in a flat line being achieved. The ideal case without component losses and frequency limitations are simulated in AWR. The CST results agree with the AWR results for most of the spectrum. Both the results have losses equal to $-4.7\ dB$ over the band, but after 4 GHz the CST results degrade. CST incorporated component and material losses at the simulated frequencies, unlike the AWR results.

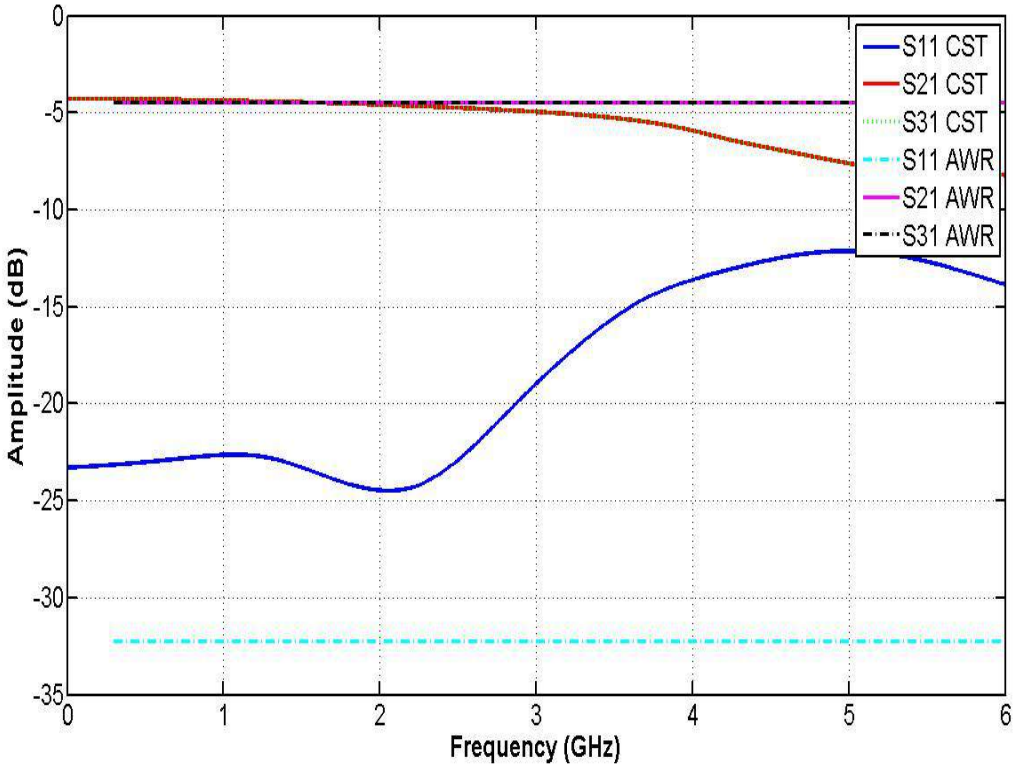

Figure 4.6: Comparison of the resistive splitter simulated on CST and Microwave Office.

The CST results would be the most likely response for the splitter when it is constructed and measured. It is a more accurate simulator than AWR, which includes component losses and frequency limitations to component sizes. Lossless power dividers such as a quarter-wave transformer would usually give a $-3\ dB$ S_{21} instead of $-4.7\ dB$, but because lossy components (resistors) are used in the resistive splitter, the transmission coefficient is expected to be a few dBs lower.

The over all results from the designed and simulated splitter are acceptable. The splitter is constructed and built on a thick substrate to ensure electrical breakdown inside the substrate does not occur from a high voltage peak pulse. The components used for the splitter with substrate characteristics are given in appendix A.3. The splitter was constructed and shown in the figure 4.7.

Figure 4.7: A picture of the T-junction Splitter.

4.1.5 Final design and geometrical sizes of the IRA

From all the external sources and designs available the IRA has shown promise in its field of work. With the above-mentioned techniques and design equations the fundamental components of the IRA can now easily be designed. This section will cover the final design values as well as the simulated and built IRA that will be used for the measuring campaign at the SKA core site in the Karoo.

Reflector	
Diameter (D)	850 mm
Focal point (f)	342.65 mm
Height (H)	100 mm
Conical Plate Transmission Lines	
Diameter selected for feeding plates	680 mm
β_0	52.77°
β_1	39.42°
β_2	68.98°
b	340 mm
b_1	245.50 mm
b_2	470.80 mm
Side$_a$	416 mm
Side$_b$	360 mm
Side$_c$	207 mm
ϕ_0	30°
Electrical Properties	
Input Impedance	150 Ω
Termination resistors	8x 1.2 $k\Omega$ (Parallel)
Cables and Connectors	
Feeding Cable	2x 817 mm LMR400-75
Cable Connectors	2x LMR400-75 75 Ω Plugs
Splitter Connectors	2x 75 Ω Panel Mounts
	1x 50 Ω Panel Mount
Other Parts	
Copper Pipe	ϕ15 mm
Perplex block	50 mm x 20 mm
Cable Ties	8

Table 4.1: Dimensions, characteristics and components of the IRA

Table 4.1 incorporates all the dimensions of the IRA with figure 4.8 indicating all the parameters. These dimensions were calculated with the previous design equations and using CAD software as a displaying tool. An important note that can be made is that the dish diameter and diameter length used for the design of the TEM feeding structures are not equivalent. The reason for choosing the diameter of the feeding plates smaller than the original dish diameter, was to ensure a smaller radiated backfield. When the diameter of the conical plate design is 850 mm, the plates will extend across the edge of the dish which could potentially cause a larger back-lobe for the antenna. Enclosing the plates within the dish would enable a reduction in the back-lobe. Fields created between the plates and around the plates will be caught in the dish instead of creeping behind as it would have when the plates are extended across the edge of the reflector.

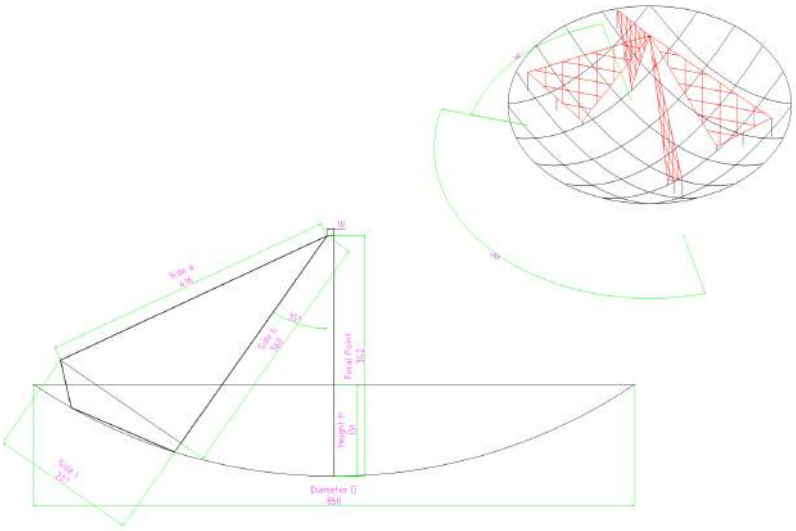

Figure 4.8: Dimensions of constructed and simulated IRA. A side view as well as a 3D view of the corner of the IRA.

The conical plates are constructed using a substrate that is plated with copper on both sides. This allowed a sufficient method for soldering the resistors onto the conical lines as well as connecting it to the reflector and feeding points. A $\phi 15\ mm$ copper pipe is placed from the apex of the dish to the centre of the reflector. This is used to house the centre-fed cable from behind the dish to the feeding point. In order to separate the conical plates and the copper pipe electrically a 2.5 mm perplex block is placed between them. The conical plates are bolted onto the dish and screwed onto the perplex and pipe to ensure some stability. The two cables from the splitter are led to the apex of the dish, one through the copper pipe in the middle of the dish and the other on one of the conical TM-lines (negatively polarised transmission line). The splitter is placed at the back of the reflector. At the feeding point the centre pin of the cable through the copper pipe is connected to the top two conical TM-lines. The other cable is the negatively polarised feeding point. Its centre pin is connected to the outside conductor of the cable in the copper pipe. It is very important to note that both cables had to be the same length to ensure the pulses arrive at the apex at the same time. The IRA is mounted on a tri-pod for quick adaptability when moved during measurements.

The cables and connectors used for the IRA are chosen because they are able to manage the peak power of the CPS1 pulse generator. The LMR400-75 cable can withstand 2 kV DC power, which will be enough if a fast repetitive signal is applied to it. N-type connectors are chosen for their robustness and ability to sustain the 2.5 kV pulse from the CPS1 generator. SMA connectors can provide high frequencies, but might cause breakdown between conductors because of its smaller size. Brief air breakdown calculations are shown in appendix D. A picture of the apex, the final constructed IRA and connections are depicted in figures 4.9 and 4.10.

Figure 4.9: The front and backside of the IRA with splitter mounted on the back.

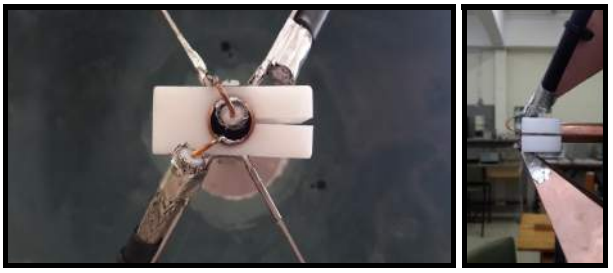

Figure 4.10: Feeding point of the IRA.

4.2 Simulation

With new advances in technology the confidence when using CAD software for design problems has grown. With accurate designs and the correct boundary conditions, problems can be solved using CAD software to ensure a working model before construction.

The IRA was designed and simulated in FEKO which is an EM simulator that can be used solve complex antenna structures. This section will cover the simulated results of the IRA antenna with brief interpretations. The IRA is simulated with a voltage source that is connected to the four conical TM-lines which are terminated onto the reflector. The source is a normal voltage source that polarises two plates positively with the other two grounded. Including the balun and feed will make the simulation computationally expensive and was not implemented in the simulation. The IRA FEKO model is depicted in the figure below.

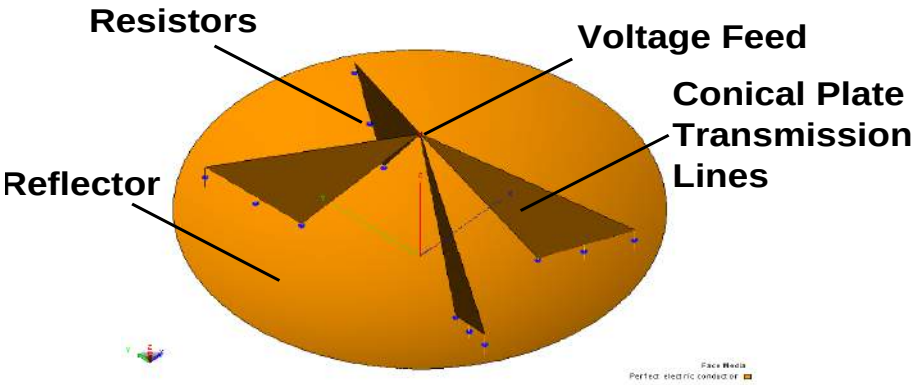

Figure 4.11: Model of IRA in FEKO.

The gain, reflection coefficient and impedance will be discussed in the first part of this section and a brief illustration of the far-field and currents will be sown in the last part of this section.

4.2.1 Gain, reflection coefficient and impedance

The three most important parameters of the IRA or any antenna would be its gain (S_{21}), reflection coefficient (S_{11}) and input impedance (Z_{in}). From them it can be determined if the antenna is working, how well it will work and if it can be matched to a transmitting source. The gain and polar patterns are illustrated in figures 4.12 to 4.14.

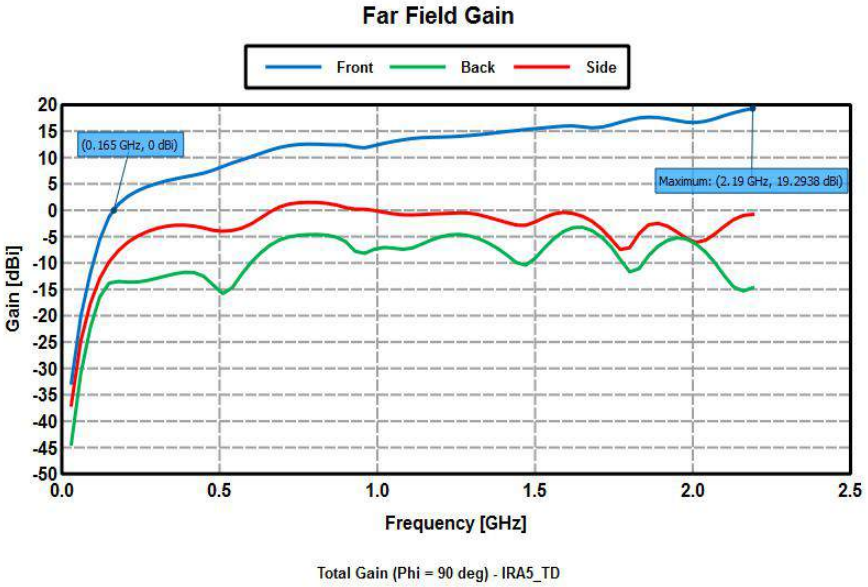

Figure 4.12: The Gain (S_{21}) of the antenna over frequency.

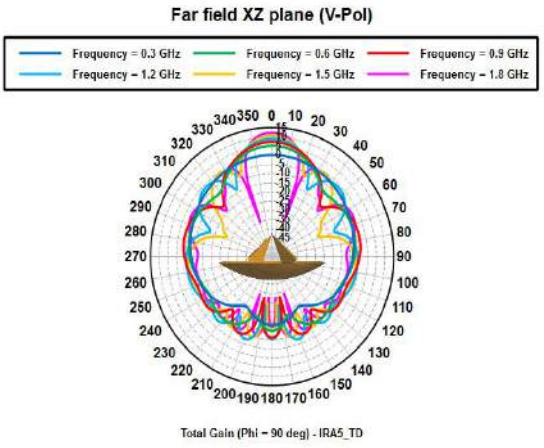

Figure 4.13: The vertical polar pattern of the IRA at various frequencies.

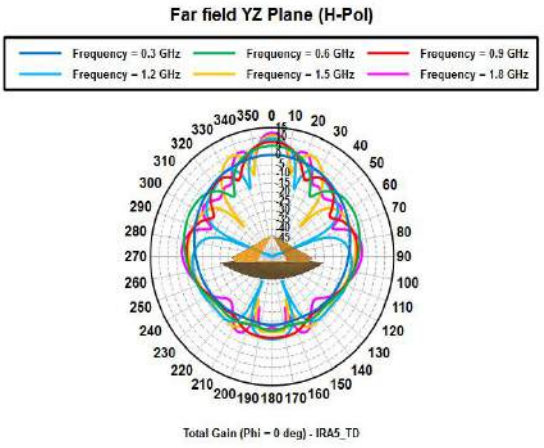

Figure 4.14: The horizontal polar pattern of the IRA at various frequencies.

The IRA has a positive gain from 165 MHz as indicated in the figure below. From theory and referenced designs the IRA is a large bandwidth antenna that can operate up to 20 GHz. Because the IRA is geometrically large it is computationally expensive when simulated at higher frequencies. The structure becomes electrically too large for simulation. Simulation of the IRA was submitted to the Centre for High-performance Computing (CHPC), which has greatly helped speed-up of simulation

for characterising the IRA.

The front gain or boresight gain of the IRA increases with increasing frequency. This would benefit the pulses that are radiated from the antenna. The spectrum of the impulse generators that will be used with the IRA are displayed in chapter 3. The peak energy of the pulse is located in the lower frequencies of the spectrum and drops as the frequency increases. If the spectrum of the pulse is amplified by the gain of the antenna the higher frequencies will be benefit more from the gain of the IRA because the increasing gain with frequency seen in figure 4.12. The gain is mostly above 10 dBi, which is a high gain for an antenna. The gain increases to above 15 dBi beyond 1.5 GHz to almost 20 dBi at 2.2 GHz. The high gain of the antenna is achieved because of a reflector design. A reflector focuses the fields enclosed with in it to a specific direction more efficiently with an increase in frequency.

Defining the front and back-lobes of the antenna is also important. Because a high-voltage broadband pulse will be radiated from the antenna a large back-lobe or side-lobe can damage expensive equipment in the vicinity. The back-lobe of the antenna is below -5 dBi at the high frequencies and -12 dBi at the lower frequencies, as shown in the figures. The peak energy of the pulse that will be transmitted, from chapter 3, is in the lower frequencies. The back-lobe shielding of the IRA at these lower frequencies are higher (-15 dBi up to 500 MHz) which will reduce the energy of the pulse at the lower frequencies. Because the energy of the transmitted pulse drops with increase in frequency, the degrading back-lobe shielding of the IRA can be neglected. The side-lobe of the antenna is mostly around 0 dBi and should be taken into consideration when the IRA is deployed during measurements. Placing equipment to the side of the IRA, when a high-power pulse is injected can cause damage. If the surrounding area contains scatters (metal buildings), reflections from these scatters should be taken into account.

If figures 4.13 and 4.14 are studied the directivity of the antenna can be observed with the increase of frequency. Studying the polar patterns of an antenna give valuable information of the fields around the antenna. At lower frequencies the antenna has a broad main beam and at higher frequencies the antenna has a strong directive main beam. A cardioid pattern is formed at the lower frequencies and an extreme directive pattern at the higher frequencies. The increase in frequency shapes the far-field pattern and different forms are displayed as the fields enclose around the antenna. With the IRA vertically polarised a more defined main lobe is achieved with nulls at 20°and -340°. From the polar pattern the nulls of the antenna, at the different angles, can be indicated as well as the size of the main and back-lobes. The horizontal polar pattern has similar far-field patterns and gains at respective frequencies, but has a more deformed and broad main beam. The clear nulls at 20°either side of boresight is removed. The cardioid pattern at the lower frequencies are also changed with clear nulls at 70°and 290°. Because a defined main lobe is desired, the antenna is vertically polarised. A picture of the half power beamwidth of the IRA is shown in figure 4.15. This confirms the cardioid pattern at the lower frequencies and a beamwidth of 20°at the highest frequency of 1.8 GHz. The beamwidth changes by almost 70°as the frequency increases from 300 MHz to 1.8 GHz.

The impedance of the antenna is another important factor that has to be considered. The IRA is designed to have an input impedance of 150 Ω.

From figures 4.16 and 4.17 it is evident that the input impedance varies with frequency. This phenomenon is mostly seen in antenna applications. From the Cartesian and Smith chart the impedance matches the desired input impedance more as frequency increase. There is a large variation in impedance at the lower frequencies, which causes reflections because it is unmatched. The better the antenna is matched to the designed input impedance, the lower the reflections will be on the antenna. The significant changes in impedance leads to the current level of the reflection coefficient response shown in figure 4.18.

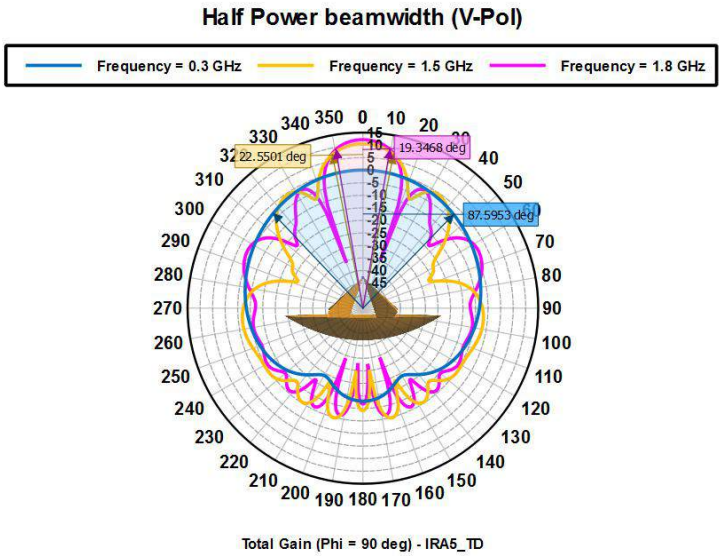

Figure 4.15: The half power beamwidth of the IRA vertically polarised.

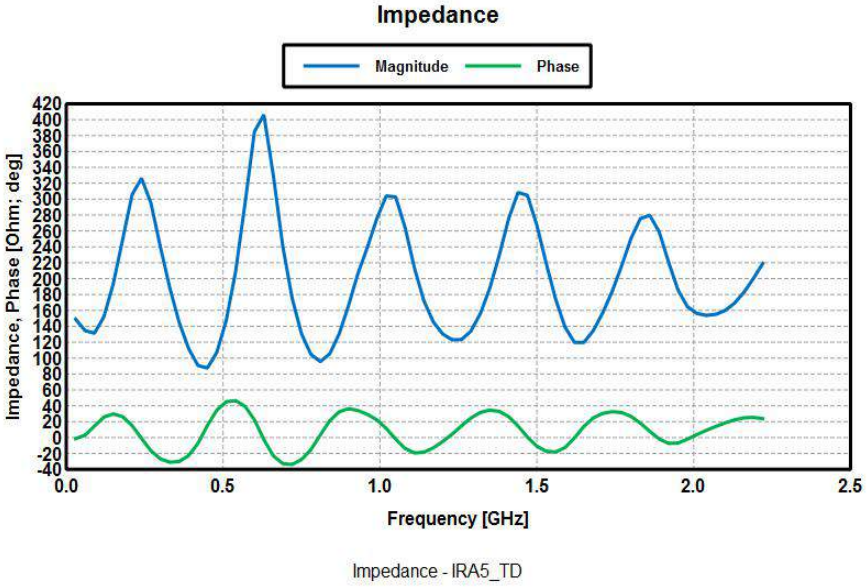

Figure 4.16: Magnitude and Phase of IRA Impedance over Frequency.

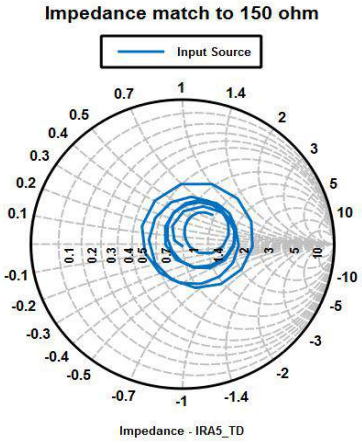

Figure 4.17: Smith Chart of IRA Impedance.

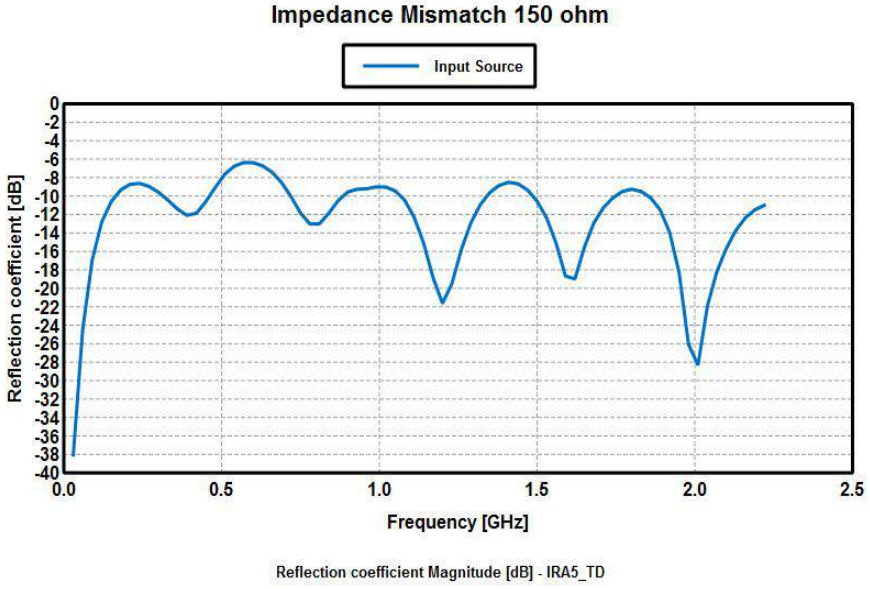

Figure 4.18: Reflection Coefficient of IRA.

The antenna reflection coefficient is above $-10dB$ at the lower frequencies, which agrees with the impedance mismatch at these frequencies. The reflections occur because of the mismatch in impedance. This cause the IRA to ineffectively radiate transients or signals at the lower frequencies, because most of the energy is reflected back and forth on the antenna and feeding structure. At the higher frequencies S_{11} drops below $-10\ dB$, which is an indication that the signal at theses frequencies will radiate more effectively. The IRA model simulated in FEKO is not the exact replica of the built model. The feeding balun as discussed is not incorporated as well as all the cables and connectors. Including theses factors would make the simulation more computationally expensive. From these simulations the IRA operates more efficiently at the higher frequencies, where the antenna becomes more matched.

4.2.2 Far-field and currents

The final section on simulation illustrates the fields enclosed around and currents on the dish. The 3D models from both these results are shown at 1.8 GHz, where the gain is high and the directivity of

the antenna can be illustrated. These figures gives a good indication of how the fields wrap around the reflector. The main lobe is projecting from the focal point of the dish and the nulls in the far-field are located near the termination of the conical plate TM-lines onto the reflector. This is expected because the tangential E-fields at a perfect electric conductor is zero. The gain of the antenna is also at an maximum at the focal point of the antenna and lower at the sides and back of the antenna. Figure 4.20 gives a good indication of the currents on the dish. When the currents on the model are examined, most of the currents are on the edges of the plates and at the termination points. The peak currents are located at the focal point and are distributed over the plates until it is terminated onto the dish.

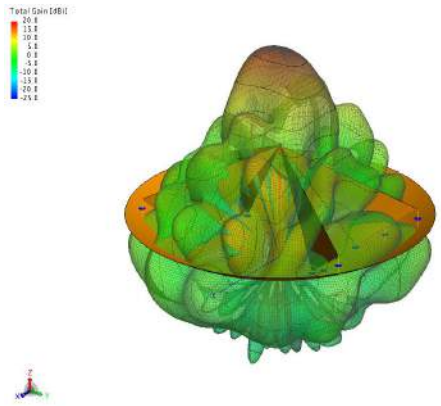

Figure 4.19: The Far-field of the IRA in 3D format.

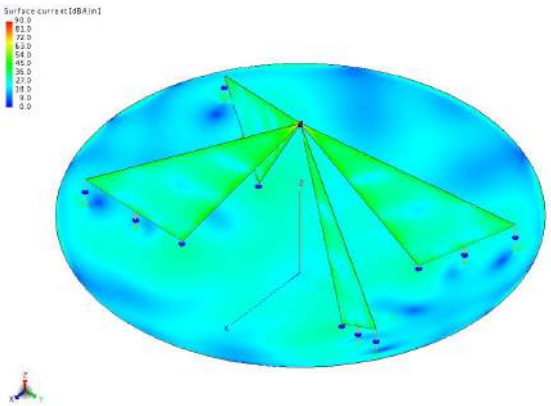

Figure 4.20: The currents on the IRA in 3D format.

4.2.3 Conclusion

The simulation results depicted above have given enough insight on the response of the IRA and studying them can assist during measurements. Although simulators help in the design of components, they should never be taken as an absolute. Simulation does not include all the losses in a system and temperature of components during measurements will change and could have an effect on the results. For accurate and precise simulations that agree with measurements, an accurate design with all the losses and components in the system has to be included. In some cases the design cannot be simulated with the correct connectors and ports. This will cause a difference between the measured results, that incorporate the physical connector, and simulated results. The simulation can give a respective response of a system or component and when it agrees with measurements it is rewarding. FEKO and other simulation software implemented in this project was used to assist in the design and characterisation of the IRA system. The simulated model is compared with measured results, which can then used to improve the simulated models and replicate the built and measured models.

The IRA has been simulated on FEKO and this section has briefly discussed the gain, impedance, reflection coefficient, polar pattern and 3D models of the antenna. The IRA gain, impedance and reflection coefficient improves with increasing frequency. The simulated gain is above 10 dB from 500 MHz and onwards in the spectrum. The maximum gain of the antenna is 19.3 dB at 2.2 GHz. The polar pattern has indicated the directivity of the antenna at the higher frequencies with a cardioid pattern that is formed at the lower frequencies. As gain increases the directivity of the antenna also increases. The radiated energy is not distributed over a large area, as in the lower frequencies, but focused in a certain direction to yield this high gain. The front-to-back ratio of the antenna is between -18 dB and -25 dB across the simulated band. The simulated impedance is not well matched at

the lower frequencies, but as frequency increases the antenna becomes more matched to the input impedance of the antenna. The reflection coefficient is directly coupled to the match of the antenna. Because the antenna is not well matched at the lower frequencies the antenna reflection coefficient at these frequencies are not optimal and below $-10\ dB$. In the next section the IRA is measured and optimised. The measured results are also compared with simulated results.

4.3 Characterisation and optimisation of final IRA design

The first set of measurements on the designed IRA was made to characterise the antenna. The measurements were done with a HP 8510 vector network analyser (VNA) and Rohde and Schwarz FHS4 spectrum analyser. The antenna is faced into an anechoic chamber with phase-stable high frequency cables connected to the network analyser (see figures 4.21 and 4.22). The VNA is calibrated to known standards with a 50 Ω measuring system. Only port 1 of the VNA is calibrated because a time low-pass analysis and reflection coefficient measurement are done. Figure 4.23 depicts the measuring setup with all the components in the system as well as an electrical diagram (figure 4.24) of the antenna system.

Figure 4.21: Picture one of the measuring setup with IRA and VNA into anechoic chamber.

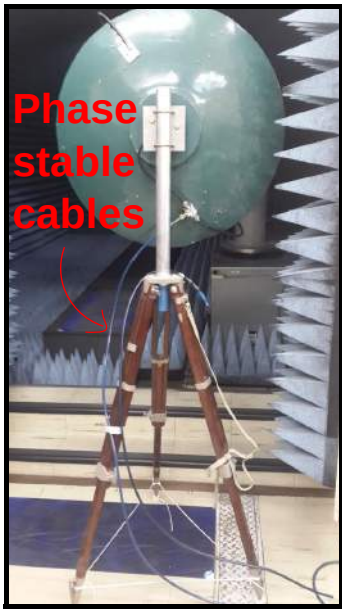

Figure 4.22: Picture two of the measuring setup with phase stable cables

The first part of the antenna is a 50 Ω to 75 Ω resistive splitter. From the splitter two 817mm 75 Ω LMR400-75 cables were used to feed the dish at the focal point. A dummy cable is placed on the opposite side of the dish to act as a balun (see figure 4.23). The dish was cut to the appropriate size as discussed in section 4.1.1. The conical plate TM-lines were constructed with copper plated PCB boards with eight 1.2 $k\Omega$ resistors soldered in parallel to terminate onto the reflector. The PCBs are bolted to the dish for a rugged support. A $\phi 15\ mm$ copper pipe is mounted in the centre of the dish. The pipe houses one of the cables connected to the splitter and gives extra support for the feeding point. The centre conductor of the cable coming through the pipe is connected on the top two conical TM-lines. The second cable, from the splitter, follows on the outside of the dish. The outer conductor is connected to the bottom two conical TM lines and the centre conductor is soldered to the copper pipe. This forms part of the balun as discussed in section 4.3.

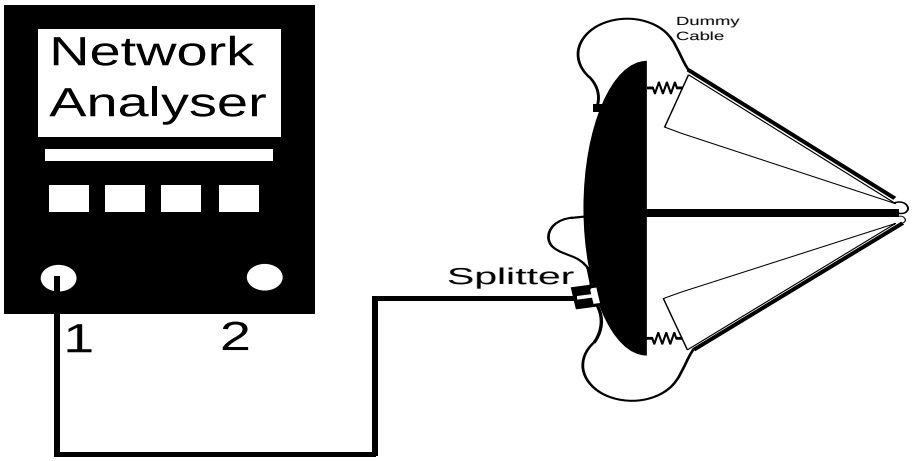

Figure 4.23: Measurement setup for optimisation and characterisation of antenna system.

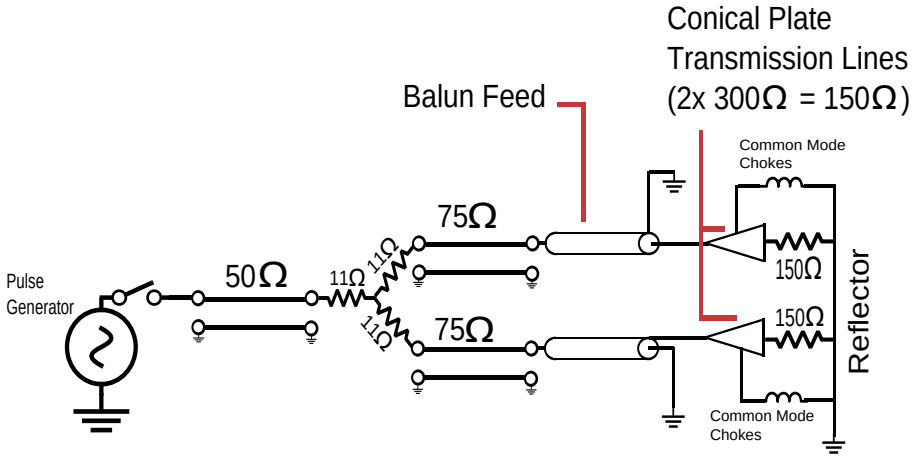

Figure 4.24: An electrical circuit representation of antenna.

The network analyser injected a 10 dBm signal into the antenna. By looking at the time low-pass response from 0 to 15 ns the following can be seen. A time analysis or TDR shows the time it would take for a pulse to travel from the splitter to the reflector part of the IRA with reflections. Analysing each reflection can share pivotal information on the design of the component under test. The following conclusion is drawn from the analysis (see figure 4.25).

Starting with a mathematical formulation, the time (t_1) from the splitter to the focal point is:

$$t_1 = t_s + t_c \tag{4.3.1}$$

where

t_s = time in splitter.
t_c = time in cables.

The cables have a propagation velocity (v_{pc}) of 0.85 (see Appendix C) and are 817 mm long. Therefore the time for a pulse to travel from the end of the splitter to focal point of the antenna is:

$$\begin{aligned} t_c &= \frac{1}{v_{pc} \times c} \\ &= 3.922\ ns.m^{-1} \end{aligned} \tag{4.3.2}$$

where c is the speed of light ($3 \times 10^8 m.s^{-1}$).

Taking the cable lengths into account shows that a pulse would take 3.204 ns to travel from the end of the splitter to the focal point of the antenna. If the splitter is considered, a pulse would travel at 3.3 $ns.m^{-1}$ ($\frac{1}{c}$) in free space and implementing equation 3.1.5, will give the speed in time for a pulse on a microstrip line. The microstrip lines on the splitter are approximately 11.69 mm for the 50 Ω (l_{50}) line and 12.16 mm for the 75 Ω (l_{75}). This would yield a time in the splitter (t_s) of:

$$\begin{aligned} t_s &= \left(\frac{l_{50}\sqrt{\epsilon_{r,(Eff)}}}{c}\right) + \left(\frac{l_{75}\sqrt{\epsilon_{r,(Eff)}}}{c}\right) + t_x \\ &= (11.69\ mm \times 5.565\ ns.m^{-1}) + (12.16 \times 5.424\ ns.m^{-1}) + t_x \\ &= 130\ ps + tx \end{aligned} \tag{4.3.3}$$

where t_x represent small discrepancies from the connectors and resistors.

Assuming an extremely small t_x it can neglected. The total time for a pulse to travel from the splitter to the focal point of the dish would equal:

$$\begin{aligned} t_1 &= t_s + t_c \\ &= 130\ ps + 3.204\ ns \\ &= 3.335\ ns \end{aligned}$$

The time from the focal point to the dish (t_2):

$$\begin{aligned} &= 3.3\ ns.m^{-1} \times 400\ mm \\ &= 1.32\ ns \end{aligned}$$

The total time (t_3) from the beginning of the splitter to the dish is:

$$\begin{aligned} t_3 &= t_1 + t_2 \\ &= 3.335\ ns + 1.32\ ns \\ &= 4.655\ ns \end{aligned} \tag{4.3.4}$$

This is an estimate of the time it would take a pulse to travel through the antenna system, with small discrepancies from connectors and resistors that are not included in calculations. Analysing the time low-pass response (see figure 4.25) of the antenna will confirm that these calculated times agree with measured times from a pulse propagating through the system. The time reflections, as indicated in figure 4.25, originate from a pulse that is injected from the VNA into the antenna system. If there is a mismatch between different components or a discontinuity in the system, a reflection from the injected pulse will be returned. There are three reflections clearly marked on this response, one being from the splitter and the other from the focal point and dish of the antenna. These reflections originate from specific discontinuities in the antenna system and is located by the time of the pulse injected from the VNA to the dish point and back. The time calculations above does not take into account the reflected time back to the VNA and has to be multiplied by two, to agree with the measured times.

The reflections from the antenna feed point are located 6.92 ns after the signal is injected into the system. The calculated time to the feed point and back is $(3.335\ ns + t_x) \times 2$. This equals $6.67\ ns + 2t_x$,

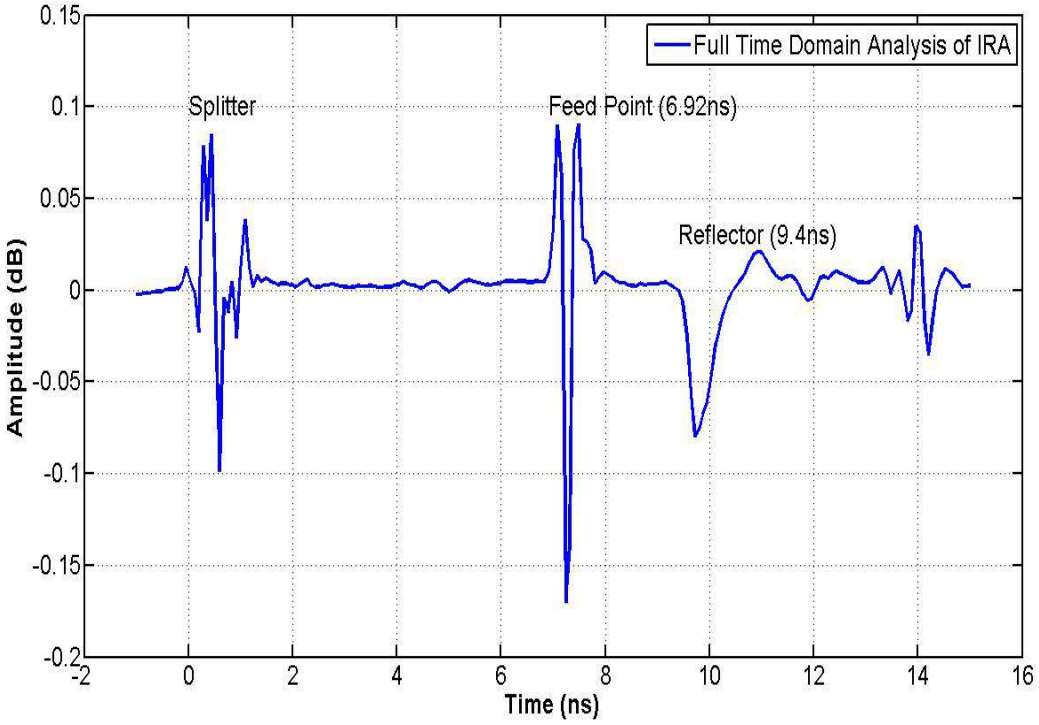

Figure 4.25: Time low-pass response of the antenna system.

which agrees with the measured time for the pulse to travel from the VNA to the focal point and back. The same conclusion can be made with the measured and calculated time of the reflector. The measured time is 9.4 ns to the reflector and back, with the calculated time equal to 9.31 ns. By investigating the time low-pass response different elements in the antenna system can be identified, time gated and analysed separately. In the following sections the splitter, feed and IRA will be analysed.

4.3.1 Splitter analysis

The three-port divider is an important part of the antenna and balun. The resistive splitter is chosen because of its easy design, large bandwidth and low design limitations. The splitter designed in section 4.1.4 was an exploratory first design. The splitter was measured by two techniques, a full three port measurement on the HP 85047A and a reflection coefficient measurement using the time low-pass response and time-gating function of the HP 8510 VNA. Gating provides a simple means of adding or removing selective responses in time. This allows investigation of a single component or discontinuities in time, which can be Fourier transformed and analysed in the FD.

With the full three port measurement the reference impedances were different. The splitter is designed to match two 75 Ω outputs to a single 50 Ω input. The VNA had to be calibrated accordingly; one port to a reference impedance of 50 Ω and two ports to 75 Ω. Because a 75 Ω calibration kit was not available and the splitter had 75 Ω connectors, the measurement had to be improvised in order to match it to the available 50 Ω system and calibration kit. The system was calibrated using two 75 Ω cables with 75 Ω connectors on the one side and 50 Ω connectors on the other. This formed a mismatch at the two output ports which can later be renormalized to the desired impedances, because of known cables lengths and impedances. An illustration of the full three port measurement system, as explained above, is depicted in figure 4.26.

The setup is measured and compared to the second technique where the splitter is time gated and analysed. A figure of the TD analysis is shown in figure 4.27. Fourier transforming this response will

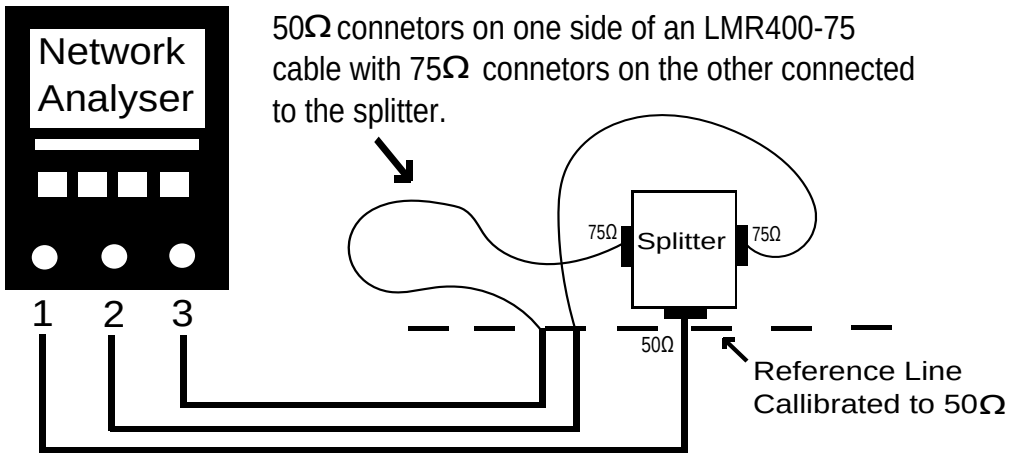

Figure 4.26: Splitter measuring setup with vector network analyser.

give the reflection coefficient (S_{11}) of the splitter. The advantage of this technique is that the system is matched to one port. The disadvantage is that only the reflection coefficient can be measured and not the transmission coefficient.

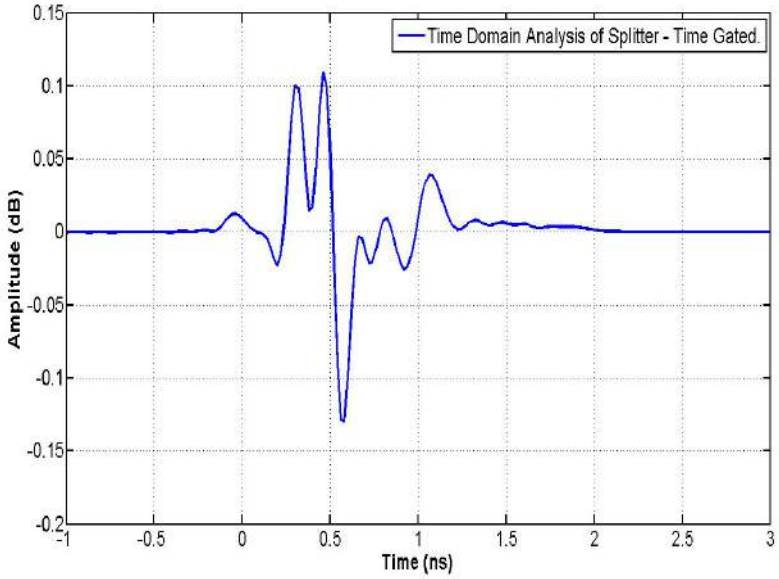

Figure 4.27: TD analysis of splitter - time gated.

Gating a signal can work exceptionally well if the gate is applied at the right place. By placing the gate at the wrong point in time could remove data that forms part of the reflection from a discontinuity or component that is analysed. A short explanation of time gating is that the gated value at any point is determined by convolution. A much more in depth explanation is shown in [46]. To ensure an accurate response the gate is applied at the nulls after the discontinuity or reflection. Setting the VNA to show the log-magnitude will ensure an accurate position for the gating window.

The results from both measurement setups are depicted in figure 4.28. The time-gated measurement (blue in figure) would be the most accurate reflection coefficient measurement for the splitter. The reason for this will be explained. As shown in figure 4.25 a TD analysis can be taken of the whole antenna system. Time gating allow analysis of single components or discontinuities in the system. TD and FD are related by the Fourier transform and with a known TD response of the splitter, the

FD can be calculated. When the splitter is time gated the pulse injected into the system from the VNA sees an infinite TM-line at the point where it is time gated, which implies a matched network. Once the injected pulse arrives at the end of the splitter and the point of the time gate, it will see an infinitely long TM-line which will allow no reflections beyond that point, thus an equivalent perfect match.

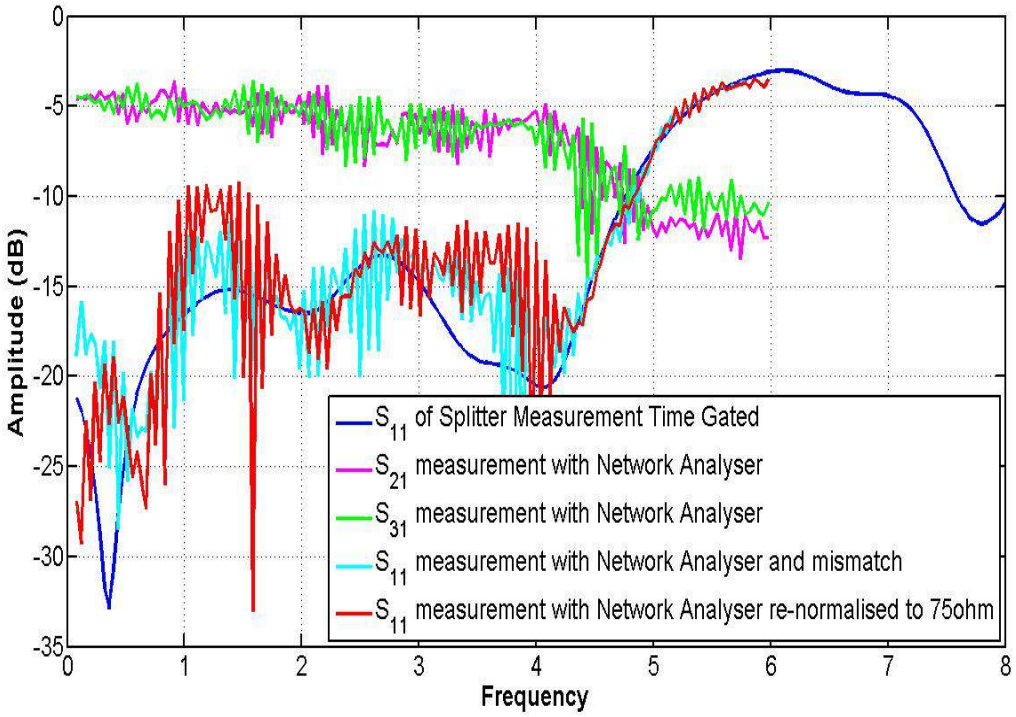

Figure 4.28: S-parameters of splitter with both measuring configurations. The ripples indicates a problem with multiple reflections because of the mismatch, which time gating removes

The splitter works well from DC up to 4 GHz where most of the energy injected at port one will get reflected back to the source. This can be seen by analysing the reflection coefficient (S_{11}) of all measurements. S_{21} and S_{31} are around the -4 dB to -5 dB level and drop after 4 GHz. S_{21} and S_{31} indicates the injected power that is lost when measured at the output of ports 2 and 3 of the splitter, this indicating the gain or losses of the splitter. There is resonance (ripples in the results) on the full three port measuring technique. This originates from the extra cables that are used at port two and three in order to match it to the 50 Ω system of the network analyser. This can be confirmed by taking the length of the cable and comparing it to the period of the ripples. The ripples occur every 72 MHz and one wavelength can be defined as:

$$\lambda = \frac{c}{f} \tag{4.3.5}$$

Thus a 72 MHz signal would have a wavelength of 4.1667 m, which is the length of the cables used at the end of ports 2 and 3. In the full three port measurement there is a mismatch at the two output ports. The outputs of the splitter are 75 Ω and they are measured on a 50 Ω system. From figure 4.28 there are two S_{11} measurements displayed from the three-port measurement. The one is the direct measurement with the 50 Ω system (light blue/cyan line) and the other is a re-normalised reflection coefficient to match a 75 Ω system (red line). This was done by defining 75 Ω output ports in AWR instead of 50 Ω, which automatically re-normalises the reflection coefficients. This will not affect the transmission coefficients and is not shown for S_{21} and S_{31}. There is a small difference between these

two measurements, but the normalisation technique used in ARW to re-normalise the impedances has degraded the response around 1 GHz and 4 GHz. The important thing to note is the shape of the three-port measurements compared to the time-gated reflection coefficient measurement. They mostly follow the same trend, but the measurement without normalisation has a closer resembles to the time-gated low-pass analysis, which is a more accurate reflection coefficient measurements. The normalisation technique used in AWR is not fully understood and is neglected from future measurement results. Both measurements show that the splitter has a sufficient reflection coefficient below -10 dB and that at 4.5 GHz the response degrades.

Figure 4.29 compare the simulated results from the CST model with the measured results. The transmission coefficient agree well with the simulated results, with a 0.5 dB difference. There is a large discrepancy between the simulated and measured reflection coefficient. The measured results show that S_{11} has a larger bandwidth than the simulated results. The measured S_{11} increases after 4 GHz, with the simulated results rising after 2.5 GHz.

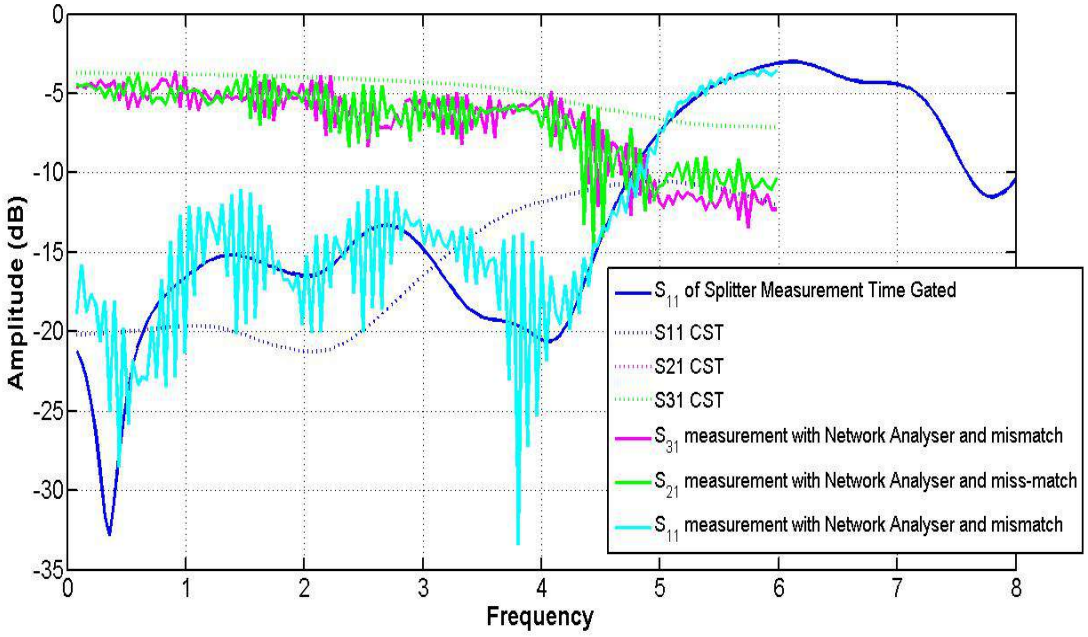

Figure 4.29: S-parameters of splitter with both measuring configurations and the CST results.

4.3.2 Antenna analysis

The whole antenna TD response was shown in the beginning of this section. When we investigate the feed of the antenna with additional information from [46] chapter 4, each reflection can be categorised. A reflection occurs at a discontinuity in the system and using the time low-pass response each reflection can be associated with a specific impedance type, such as a resistive, capacitive, inductive, open and short discontinuity. The reflections change depending on the type of transient input waveform used on the network analyser. Figure 4.30 depicted below indicate the different reflection types.

By studying the impulse response of the antenna (figure 4.25) an inductive discontinuity at the feed of the antenna is observed. If a photo of the focal point in figure 4.10 is studied, the long centre conductor of the feeding cable, from the copper pipe, confirms this inductive response. A single piece of wire is implemented as an inductor at microwave frequencies. Time gating the feed and the

Element	Step response	Impulse response
Open	Unity reflection	Unity reflection
Short	Unity reflection, –180 °	Unity reflection, –180 °
Resistor $R > Z_0$	Positive level shift	Positive peak
Resistor $R < Z_0$	Negative level shift	Negative peak
Inductor	Positive peak	Positive then negative peaks
Capacitor	Negative peak	Negative then positive peaks

Figure 4.30: Low-pass responses of known discontinuities with step and impulse response [46].

reflector of the IRA and Fourier transforming the TD, will give the reflection coefficient of the antenna. Although the splitter can be removed by the gating, its effect is not completely excluded from the frequency response, but significantly reduced. This will be shown in figure 4.31.

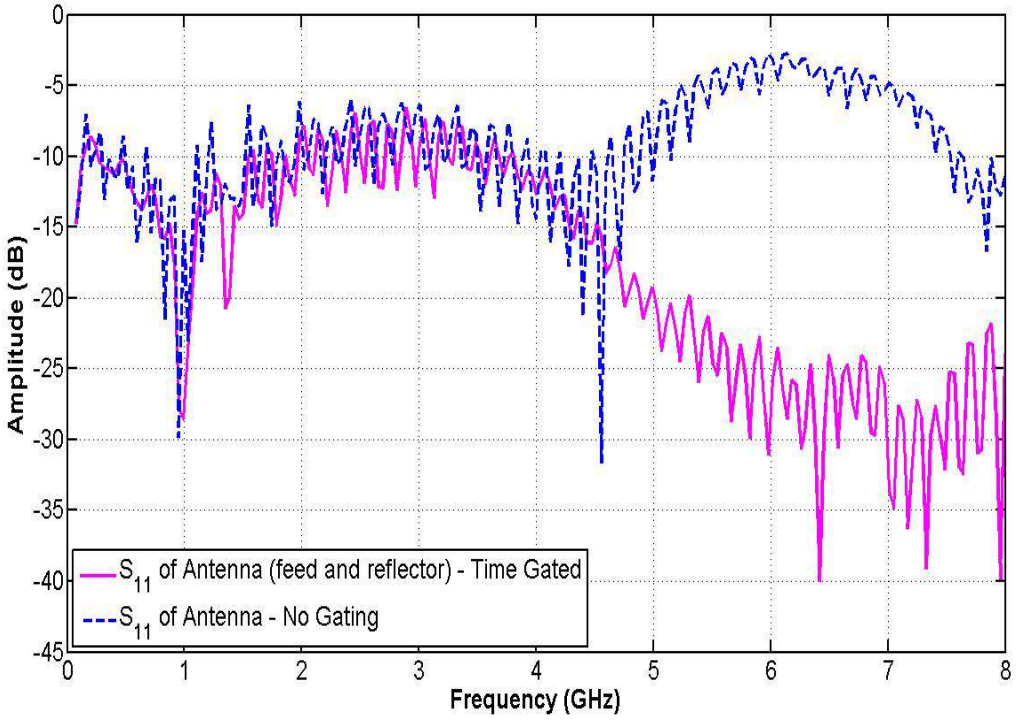

Figure 4.31: Comparison of FD of antenna and gated without the splitter response.

The solid line indicates the reflection coefficient of the antenna with the splitter gated out, and the dotted line the splitter included. There is little to no change for the first half of the spectrum, but a complete separation occurs after 4 GHz. If you look at the spectrum of the splitter after 4 GHz, there is some agreement, from both measuring techniques used for the splitter and the dotted line in this figure. They follow the same trends as well as a rise in the reflection coefficient to a similar level.

It is also important to note that the first half of the spectrum from the splitter is much lower than the reflection coefficient in figure 4.31. If the splitter is gated out, the spectrum drops after 4 GHz to below $-25\ dB$ and the first part of the spectrum remains the same. When compared to the splitter's reflection coefficient, the S_{11} of the splitter is much lower below 4 GHz. From these remarks it can be concluded that figure 4.31 indicates the reflection coefficient of the IRA with and without the splitter. The solid line can thus be taken as the reflection coefficient of the antenna without the splitter.

For an ideal antenna response the reflection coefficient is below $-10\ dB$ in its operating bandwidth. This is to ensure that most of the energy injected into the antenna is radiated and not returned to the transmitting source. The IRA is above this limit between 2 and 4 GHz and the rest of the IRAs spectrum is below this point, especially after 4 GHz. Because of the inductive response at the focal point of the antenna most of the energy injected into the antenna is reflected back. A $-10\ dB$ or better results is desired for the IRA and by optimising this point the reflection coefficient response of the IRA can be improved.

4.3.3 Improvements

After a time analysis and investigating each component separately two components can be modified to greatly improve the reflection coefficient of the IRA. The T-junction design of the splitter has shown that a lot of the energy injected into the splitter gets reflected back at the higher frequencies of the design and the inductive response at the feed of the antenna. These improvements are discussed in this section.

For the splitter two new designs are compared with the original design using CST, to improve the overall results of the splitter. The original design was a T-junction model. EM waves in TM-lines are similar to waves animated with water in a pipe or container. Any object in the path of the wave would cause a reflected wave back into the opposite direction. Both waves are influenced and reduced in size. The one propagating forward is reduced by the amount that gets reflected. If a T-junction figure is visualised with water waves, the injected wave will collide with the T-junction reflecting a lot of waves back with the others spread to the left and right exits. A similar result occurs with EM waves. In order to improve the original design the path of influence should be optimised to ensure a more effective wave flow. Thus a mitred-bend and Y-junction design is implemented in CST. These models are shown in figures 4.32 and 4.33. The Y-design is tested with one and two resistors at the 50 Ω microstrip line.

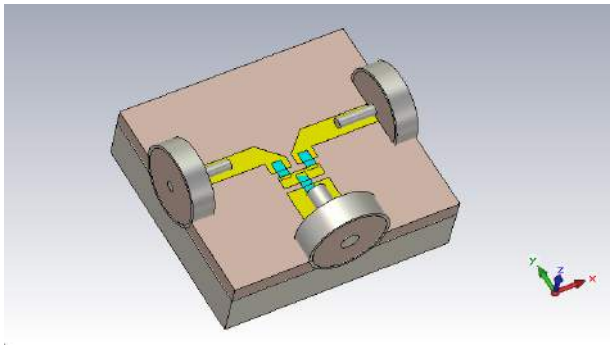

Figure 4.32: Mitred bend design of the splitter.

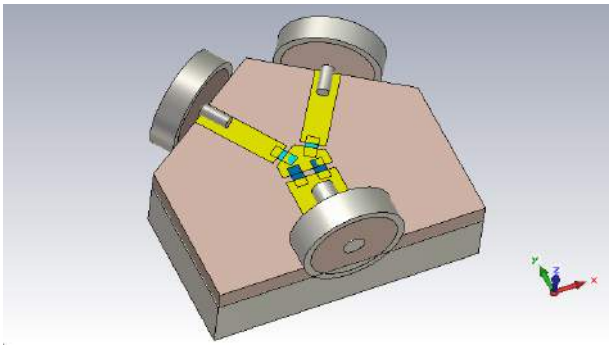

Figure 4.33: Y-Junction design of the splitter

Figure 4.34 details all the simulated models from CST. The red dotted-line is the original T-junction design reflection coefficient. If compared to the other models, the mitred bend has the worst reflection coefficient, but both Y-junctions have improved reflection coefficients from the original design.

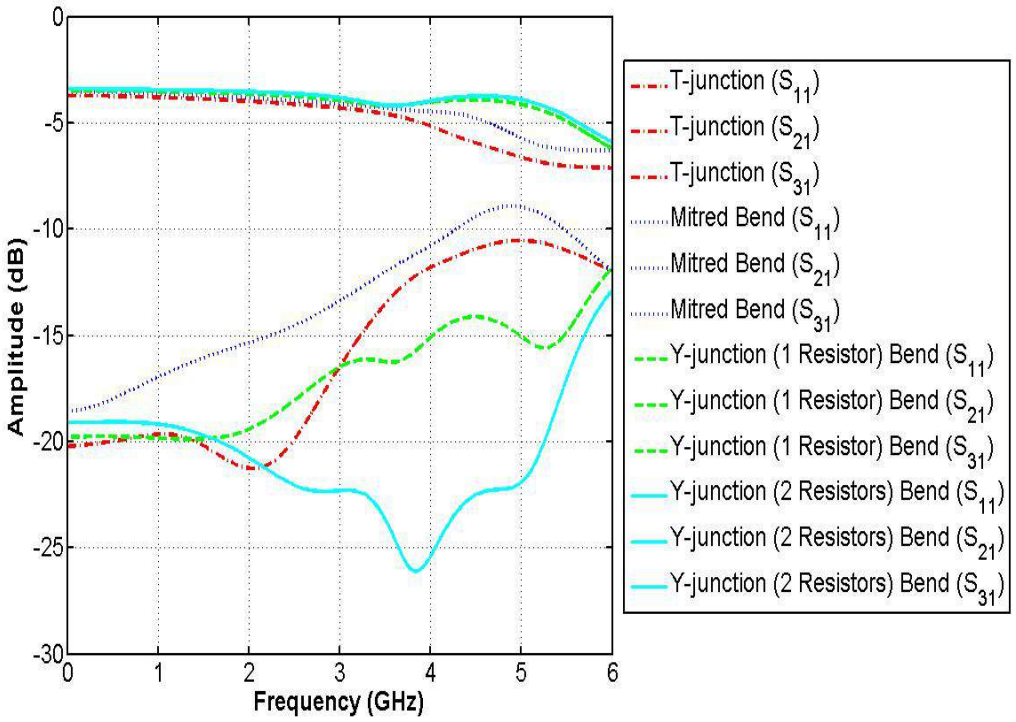

Figure 4.34: Splitter Results compared from CST

There is a 4 dB improvement from the T-junction design to a Y-junction design with one resistor, but a significant 10 dB improvement is obtained when two resistors are placed in parallel at the input side. With two resistors the currents are not forced through one resistor, but are equally spaced over the microstrip line to ensure a more equal flow of currents from the 50 Ω microstrip line to the microstrip pad in the middle. A 3D figure of the currents is illustrated in figure 4.35.

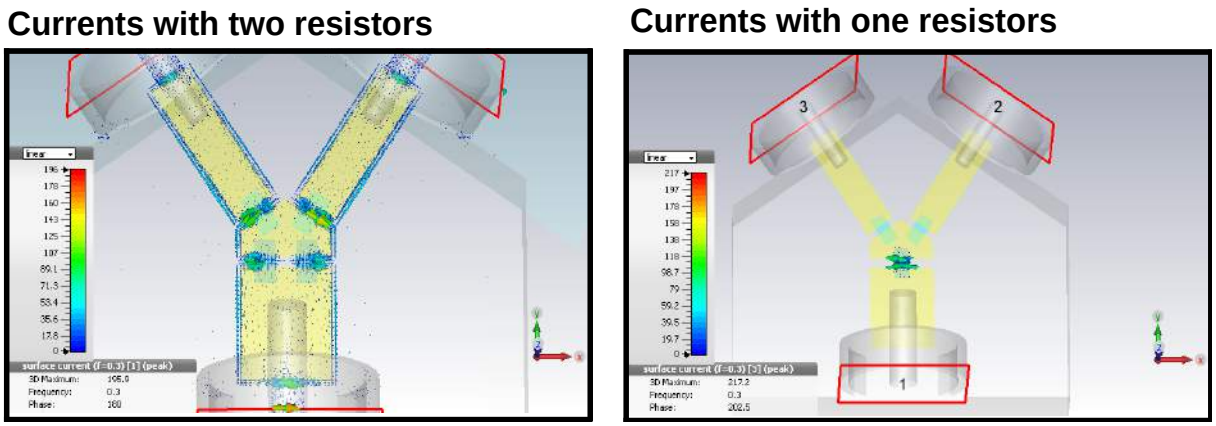

Figure 4.35: Splitter currents compared on 3D models.

From the 3D models the currents on the splitter with two resistor are equally spread across the microstrip line and flow through both resistors. For the one resistor design the currents have to move to the centre of the microstrip line and through the resistor. This causes more reflections and is a reason why the reflection coefficient is worse with one resistor, than two equally spaced over the microstrip line. The Y-design splitter with two resistors was built and measured with the HP 85047A VNA

and a time-gated measurement with the HP 8510 VNA. Both results are shown in figures 4.36 and 4.37.

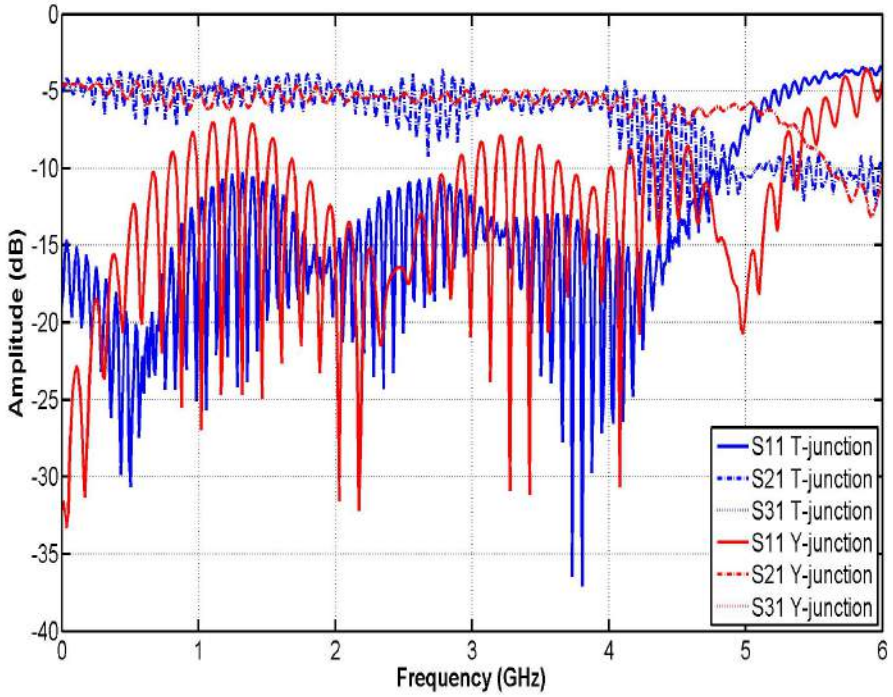

Figure 4.36: Improved splitter measured on the VNA with two mismatched output ports.

There is a slight rise in the reflection coefficient with the Y-design results, but the improved splitter design is below $-11\ dB$ to $-15\ dB$ over the operating band of the splitter. The reflection coefficient has not changed significantly, but the bandwidth of the signal has improved from 4.7 GHz to 5.5 GHz. Over the band it does not seem like a large improvement, but by changing the shape of the splitter a 700 MHz increase in bandwidth was obtained, which is extremely good especially at the higher frequencies. The higher the frequency the smaller are the wavelengths. This makes designs at those higher frequencies more sensitive to small changes, because more reflections will occur and will be difficult to design. The current bandwidth of the new splitter from DC to 5.5 GHz is acceptable for our system as our impulse generator provides instantaneous energy across this band.

The second improvement made to the antenna is the focal point of the IRA. The cable fed through the copper pipe had a large inductive response which originated from the centre conductor that is connected to the two positive TEM feed plates. Two techniques are considered to improve the response. Placing a capacitive impedance in series with the inductive wire from [47] or, if possible, shortening the centre conductor. Shortening the centre conductor would reduce the inductive response and will be the quickest way to resolving this problem. The feed point was shortened and improvements are shown in figures 4.38 and 4.39.

A small length of wire can be equal to nH's of inductance that can make a significant difference to antenna or amplifier systems at high frequencies. By reducing the centre conductor the antenna, the reflection coefficient greatly improved. The time low-pass analysis in figure 4.38 indicate the removal of the inductive response at the feed of the reflector. The current response is a capacitive response which originate from the fields between the positive feeding plates and the copper pipe specifically at the feed point. When the time low-pass is Fourier transformed the spectrum confirms the significant change that has been implemented in the antenna feed. The reflection coefficient of the antenna is

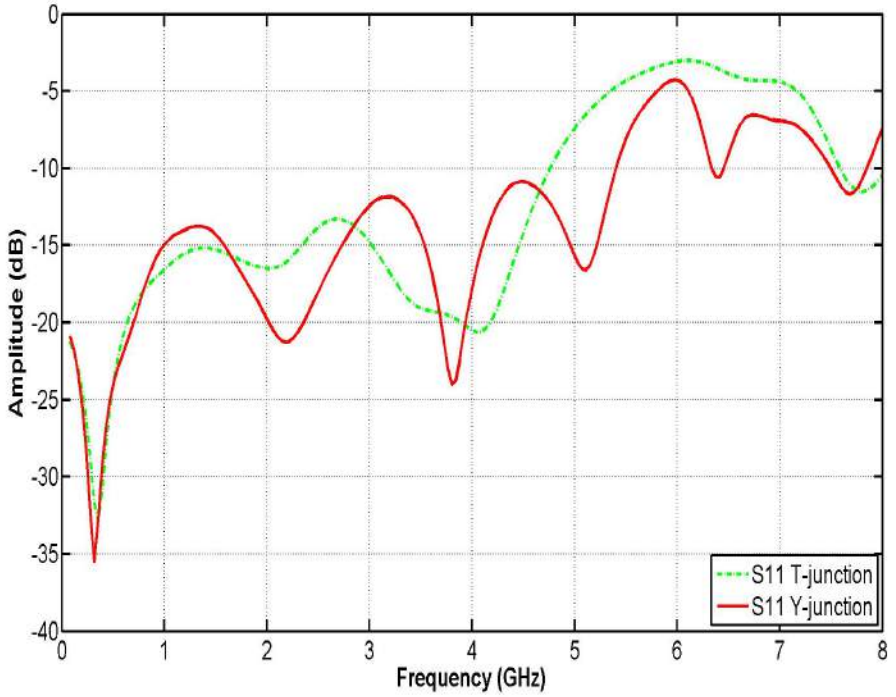

Figure 4.37: Improved splitter measured with the IRA and time gated on the VNA

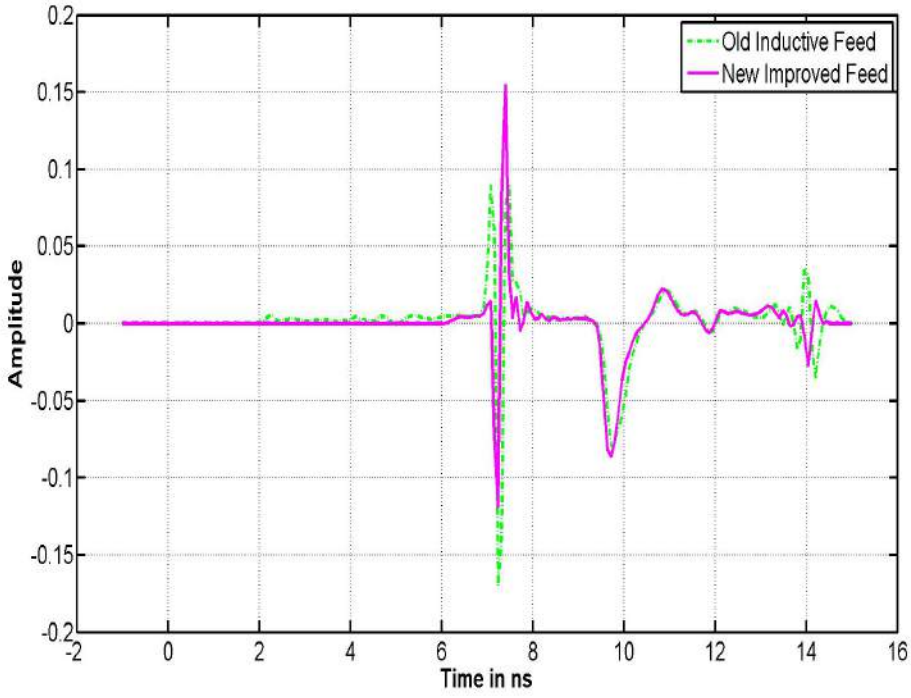

Figure 4.38: Improved IRA feed in the TD.

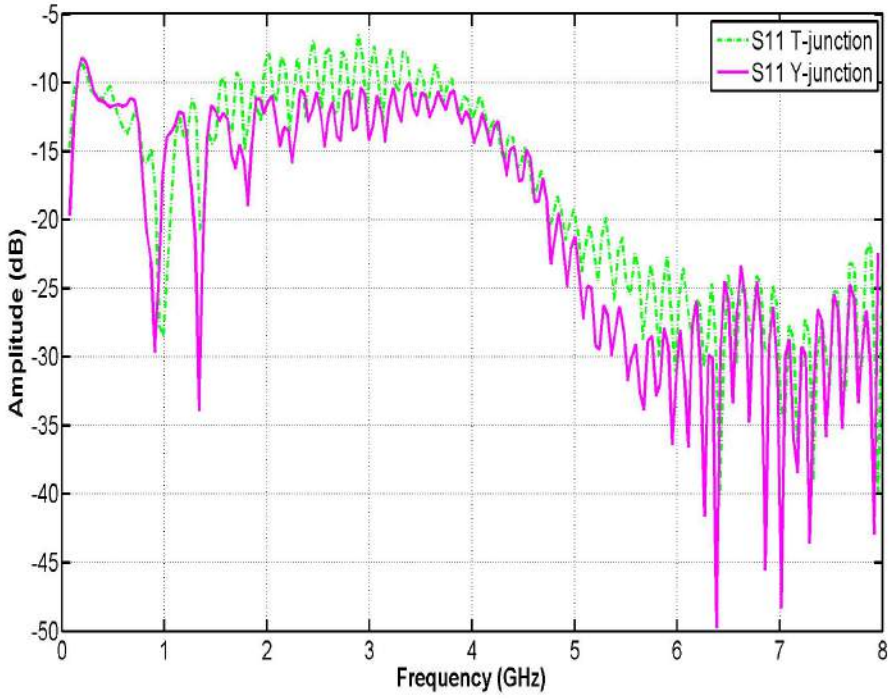

Figure 4.39: Improved IRA feed in the FD.

completely below $-10\ dB$ for the entire operating band of the antenna, except for one point in the lower frequencies, which can be neglected.

A picture of the new and improved splitter and focal point are compared to the old one and shown in figures 4.40 and 4.41. These small improvements made on two components have significantly improved the overall response of the antenna. The reflection coefficient from both these components were improved to increase the bandwidth of the IRA system and ensure effective radiation of energy over the operating band. This chapter will conclude the final build IRA with improvements shown at the feed and splitter. The results of the final model will also be compared against the simulated results to indicate the difference between simulation and actual design. All measurements were thoroughly done with correct calibration of measuring equipment where possible and all cable and connectors were cleaned for more accurate measurements and protecting connectors for long term use.

4.4 Final model with measured results

The final IRA has been improved by designing a new splitter for the balun and improving the feed point of the IRA to reduce the inductive response that originated from the centre conductor of the feeding cable. A picture of the IRA is depicted in figure 4.42. With the improved changes from each component the antenna is measured and compared to simulated results. The HP 8510 VNA is used to measure the final reflection coefficient of the IRA with the improved splitter attached to the reflector dish. Gain measurements will be explained in the next chapter. Previous results were made with each part individually and the full integration of the antenna and splitter measured on the VNA is illustrated in this section.

As mentioned earlier the simulation could only be run up to 2.2 GHz because it is mathematically expensive at the higher frequencies. The balun included in the antenna system matches the antenna at the lower frequencies and is illustrated when compared with the simulated results that does not

Figure 4.40: Picture of old and new splitters compared.

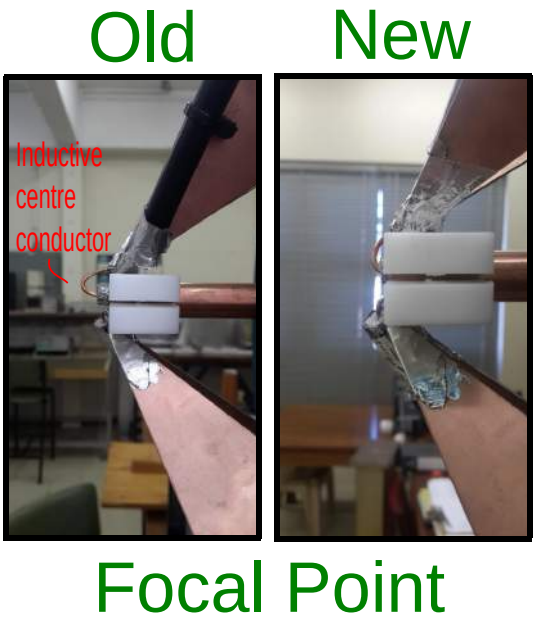

Figure 4.41: Picture of old and new focal points compared.

Figure 4.42: Final picture of the IRA. Picture is taken in the Karoo during an atenna pattern measurement.

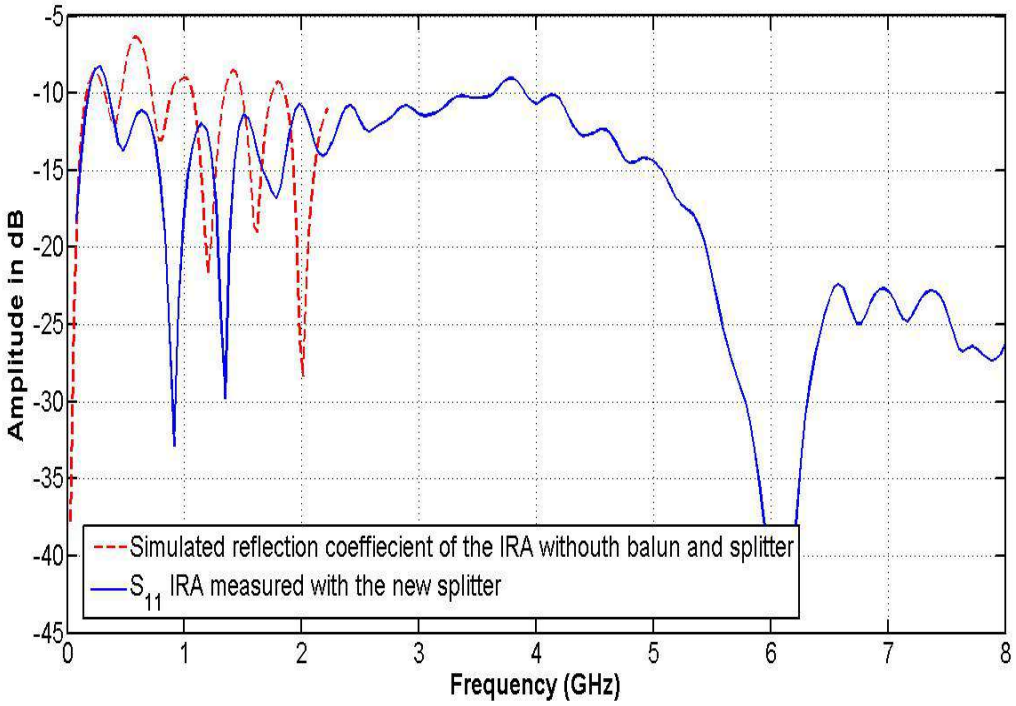

Figure 4.43: Final Results of IRA with the improved splitter (time gated) and compared to simulated reflection coefficient in FEKO.

include a balun. There is a 2 dB improvement in the measured result over the first 2 GHz of the spectrum. The overall reflection coefficient of the IRA with the splitter time-gated, is below -10 dB which will ensure most of the energy injected into the antenna system will not be returned back into the transmitter. The measured bandwidth of the antenna is 200 MHz up to 8 GHz, but bandwidths up to 15 GHz has been recorded in [48].

4.5 Conclusion

In this chapter a 150 Ω input impedance IRA was designed, simulated, measured and optimised. All of the design equations of the elementary building blocks for the IRA, were thoroughly discussed and design equations were shown. Once a desired input impedance was chosen, the reflector, conical feed-arms and balun were designed. The IRA that was designed within this study, consisted of a parabolic reflector, four TEM-conical feeding-arms positioned 30°from the vertical y-axis, eight termination resistors and a balun to match it to a 50 Ω PG source. The reason for choosing a 30°angle was to reduce cross-polarisation and to increase the gain of the antenna. The balun feeds the IRA through a resistive power divider and two coaxial cables, one positively polarised and the other negatively polarised.

For the balun, an effective 1 to 2 power divider was required. In this chapter three splitters were designed and simulated. The first model implemented a T-junction design, which had a return-loss under -12 dB from DC up to 4.75 GHz. This model was improved by a Y-junction design that increased the bandwidth by a further 750 MHz. A small optimisation on this design further improved the return-loss of the splitter, which led to the final design. The final design implemented a Y-junction with two resistors, as shown in figure 4.35. This was done to ensure that the currents travelling on the line equally flowed through both of the resistors and that it did not force through one, as was observed with the first design. This had a significant improvement in the simulated design and it was

implemented in the final design.

The IRA was also simulated using FEKO software code. The gain of the antenna was above 10 dB for most of the spectrum, with a peak gain of almost 19 dB at 2.2 GHz. The impedance and return-loss at the lower frequencies of the simulation, were not well matched to the desired input impedance. The simulated model did not include the balun of the antenna and this is most likely the reason for this small mismatch. The polar pattern of the antenna was displayed. This gave great insight of the fields around the IRA at different frequencies. A cardioid pattern was formed at the lower frequencies and at the front end of the IRA, an isotropic response. As the frequency increased, the antenna became more and more directive as the fields were forced in the direction of the focal point, by the parabolic reflector. The antenna was geometrically large therefore the simulation would have been computationally expensive and it was submitted to the CHPC for simulation. The simulation was meshed to run up to 6 GHz, but with some technicalities, only the first 2.2 GHz could be simulated.

After the IRA was built, it was measured and optimised using the time low-pass response of the HP8510 VNA. By analysing the reflection in the antenna system, a large inductive response was observed at the feeding point of the IRA. The positively polarised cable, feeding the antenna through a copper pipe, had a long centre conductor before it was connected to the conical-plate lines terminated onto dish. This was shortened, which removed the inductive response and significantly improved the reflection coefficient of the antenna. The return-loss, which was marginally above -10 dB at some frequency points, was completely below -10 dB after this improvement. Pictures of the improvements are shown in figures 4.40 and 4.41.

Chapter 5

Time-domain metrology

One of the most important phases probably in system design, is the measurement phase. During measurements your design can be demonstrated and tested which lead to pivotal conclusions for future improvements of the project. In chapter three a transmitting source, the impulse generator, was built, analysed and measured. The PGs are actively used in Stellenbosch laboratories for EMC, shielding and enclosure (RC) and TD antenna measurements. Chapter 3 also incorporated a kilovolt PG source built by Kentech industries. The CPS1 is bought to assist with TD measurements in the Karoo and future metrology and EMC work. This PG with the IRA, designed in chapter 4, will be used as a metrology system to characterise Meerkat systems in the Karoo. The CPS1 produces a 2.5 kV pulse with a rise-time of 150 ps. The bandwidth of a signal is directly coupled with the rise-time of the signal. The bandwidth achieved by these pulse characteristics are around 6 GHz with the bulk of the energy from DC - 1 GHz. The results for the CPS1 has been shown in chapter 3 section 3.3.

The benefit of a TD system is the large instantaneous bandwidth with the injection of one single TD pulse. Fast-rising impulse generators can be used for measuring the transient and FD response of microwave systems, such as the SE of components. Where SE is the power transmitted compared to the power received, after losses have been removed. Characterising microwave system are usually done in the FD. With a TD system using an impulse generator, multiple frequencies can be measured with one single injection of a pulse. This allows faster measurements without the loss of accuracy.

Before the system is deployed in the Karoo, careful calibration and characterisation is done to fully understand the output response of the antenna and PG source. Because of the high amplitude produced by the CPS1 pulser, any radiated E-fields towards electronic components can be damaging. If the generated power is known, the radiated power can be calculated. The average power of the pulse produced by the CPS1 PG can be derived using the voltage root-mean-square equation below and calculating the power separately from the known system resistance.

$$V_{RMS} = \sqrt{\frac{1}{T}\int_0^t v_{peak}^2 dt} \tag{5.0.1}$$

T is the period of the pulse, t is the width of the pulse and v_{peak} is the peak voltage of the pulse. Because the CPS1 is triggered every 1 ms and the width of the pulse is roughly 5 ns, an average voltage of 5.6 V_{RMS} is produced by the CPS1. This gives an average power of 625 mW into a 50 Ω system. The fast-rising short-duration impulse over this long period reduces the average power produced by the CPS1. Because of the long period and the short impulse, components are protected when the pulse is injected into and radiated form the IRA. With a faster repetition rate the average power would increase and could damage components used in the IRA or in the surrounding environment of the IRA.

The energy of the pulse would also decrease by a significant amount as soon as the pulse is radiated into free space. With Friis free-space path loss (FSPL) formula [19], the attenuation of an EM

wave in free-space (air) without reflections or refractions can be calculated.

$$FSPL = 20\log_{10}\left(\frac{4\pi R}{\lambda}\right) \tag{5.0.2}$$

Using this equation, with the simulated gain of the IRA and the power of the pulse produced by the CPS1, after cable losses in the system are removed, an estimated radiated power of the pulse can be calculated a few meters away from the antenna. If the radiated power is calculated the measurement can be modified and set to ensure expensive electronic equipment around the transmitting source are protected.

In this chapter the TD system is calibrated and tested with available measuring equipment before practical measurements in the Karoo. The PGs are measured on sampling oscilloscopes and a direct sampling system as mentioned in chapter 2 section 2.3.1. The first set of measurements consisted of a direct measurement between the PG sources and the sampling devices. Both the 30 V and CPS1 PGs are used. To achieve accurate measurements the limitations of each device are explained and investigated. For the second set of measurement the PGs will be connected with the IRA and measured a few meters away with a log-periodic dipole array (LPDA) and TEM-horn antenna. The IRA gain is roughly configured during these measurements, but more importantly to test the response of the antenna and PG as a whole. The last section will cover the final calibration measurements for practical metrology in the Karoo.

5.1 Direct measurements with transmitting sources and sampling devices

Before the antenna system is characterised and calibrated the transmitting sources are measured with the different measuring equipment. There are four devices at our disposal, as mentioned in chapter 2. A 50 GHz sampling oscilloscope, which requires an input signal to trigger, a 500 MHz sampling oscilloscope that can be run in an interleaved mode to achieve a larger bandwidth, the RATTY with two operating bands and RTA (based on RATTY) with four operating bands. The two transmitting sources are the 30 V and the CPS1 PG.

5.1.1 Direct measurement for 30V PG

The 30 V PG is measured on three of the four devices, the HP 54750A sampling oscilloscope, the DLM Yokogawa and RATTY. The PG is triggered by a 5 V 20 ns width pulse. At he output of the PG an external variable attenuator is placed which reduces the amplitude of the pulse to protect the measuring equipment. The FD response of the variable attenuator was measured and is depicted in appendix E. A picture of the measuring setup is illustrated in figure 5.1 below.

The time and frequency responses of the 30V pulse generator measured on three of the four systems are depicted in figures 5.2 and 5.3. The most accurate measuring tool of the three is the HP54750 50 GHz sampling oscilloscope. It has an extremely large bandwidth to allow accurate TD measurements. The Yokogawa results are the least accurate, but it is easier to use and is an effective device to test if a pulse is being transmitted. Because the Yokogawa is band-limited it filters out the high frequency components of the measured pulse. This reduces the amplitude and significantly degrades the spectrum when compared to the pulse measured on the 50 GHz sampling oscilloscope. The level of the pulse measured on the Yokogawa is almost three times lower, if compared to the one measured on the 50 GHz sampling scope. Because the pulse is band-limited and filtered in the Yokogawa scope all, the high-frequency content of the pulse are removed from 1.25 GHz onwards. From chapter three it was also shown that the high frequency content of the pulse improves the peak amplitude and rise-time of the pulse. Operating the Yokogawa in the interleaved mode allows a larger bandwidth, but the accuracy of the pulse after 500 MHz is reduced because of the filter response inside the Yokogawa.

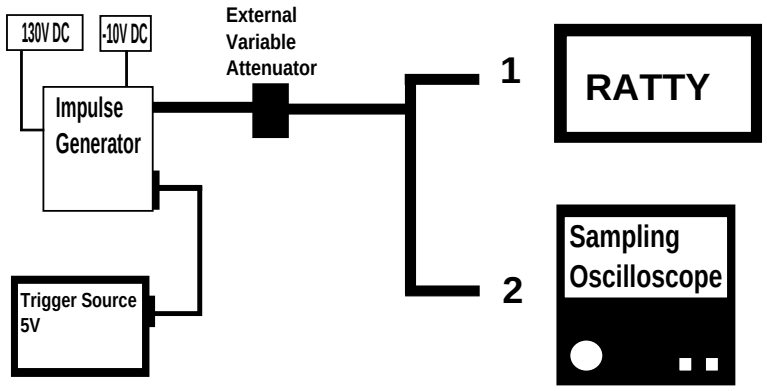

Figure 5.1: Measurement configuration of the 30 V PG for direct pulse measurements.

When the spectrum of the pulses measured on the two sampling oscilloscopes are compared, a similar response with less than 1 dB difference at the lower frequency is obtained. After 500 MHz the spectral content of the pulse measured on the Yokogawa drops significantly, which is caused by the low-pass filter inside the Yokogawa.

The third device used is RATTY. RATTY has two operating bands which filters, amplifies and mixes a signal into a single operating band. Band one operates roughly up to 800 MHz and band two from 800 MHz - 1.4 GHz. The TD pulses measured on RATTY are also displayed in figure 5.2. The shape of the pulses in their respective bands differ when compared. A TD signal can be shaped by applying certain filters to it. As mentioned in chapter 3, applying different capacitors in series at the output line of the pulse generator, a filtered characteristic response can be obtained. The 30 V PG has a low-pass filtered response so that it does not saturate RATTY and covers the operating band for the Stellenbosch RC. When the pulse is mixed and filtered into the selected operating bands of RATTY, the shape of the pulse is changed. The TD response still includes RATTY gain and attenuation. In the spectrum, RATTY gains and external attenuation are removed and an accurate amplitude of the signal is shown. The spectrum is 5 dB lower in band one when compared with the HP54750 and differs by less than 3 dB in band two.

The reason for a 5 dB difference between RATTY band one and the HP54750 can be explained by the following. The record length of one transient sampled on RATTY is 140 us. A pulse which is 2 ns with a peak of a few pico-seconds is not always sampled at the absolute maximum point of the pulse. This is also confirmed when measurements on the HP54750A and Yokogawa is done with a long time period. Because the pulse is significantly smaller than the sample length, the pulse is not accurately sampled. When multiple pulses are captured the amplitudes from each pulse will differ, causing it to look like an unstable PG that varies in amplitude, but it is the peak that is not always accurately sampled. A figure of multiple pulses captured by RATTY are depicted in figure 5.4. This phenomenon was tested with the HP54750. A PG source was measured over a long record length to ensure multiple pulses are captured. The pulses captured over the long record length varied in amplitude. The record length was reduced and each of the pulse were separately measured. After measuring each pulse separately and adding them onto the same figure their amplitudes were the same. This was done to show that the pulses do not change in amplitude and that this amplitude difference occurs when a small pulse or multiple pulses are sampled over a long record length. This results from this test with the HP54750A sampling oscilloscope can be found in appendix E.

All these pulses have different amplitudes and choosing the correct pulse for accurate measurements is pivotal. Two solutions are covered in this thesis. Taking the average of all the pulses or the maximum pulse. Averaging all the pulses in the TD requires each pulse to be perfectly aligned in time, added and then divided by the number of pulses. This is a complex method as all the pulses are

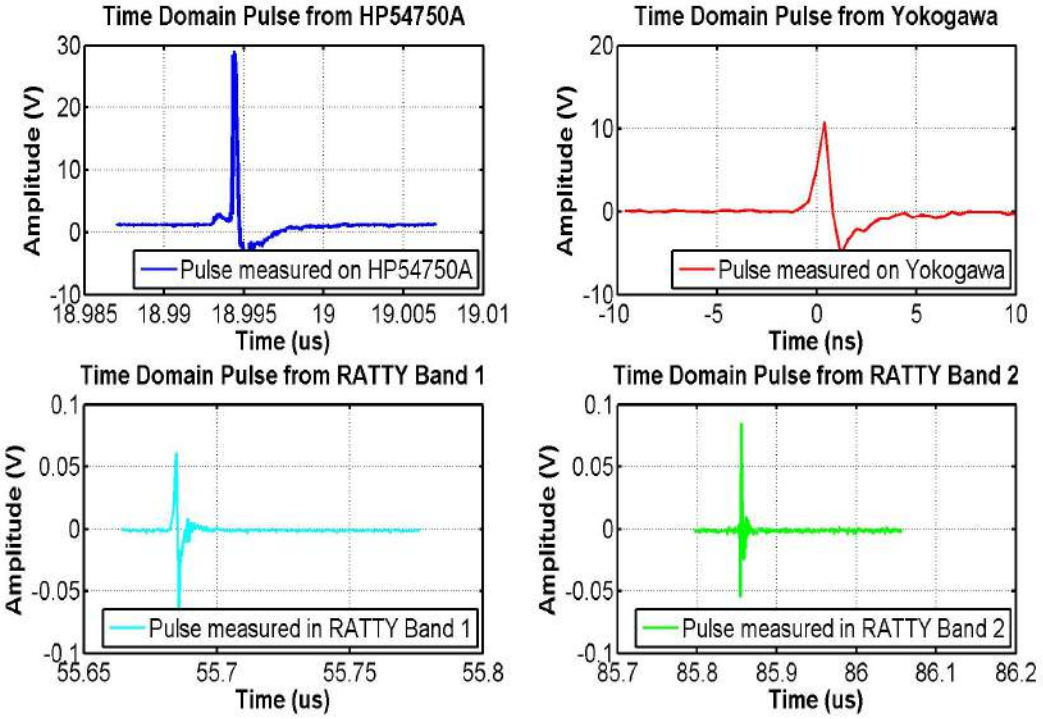

Figure 5.2: Transient response of pulses from the 30 V PG measured on measuring equipment.

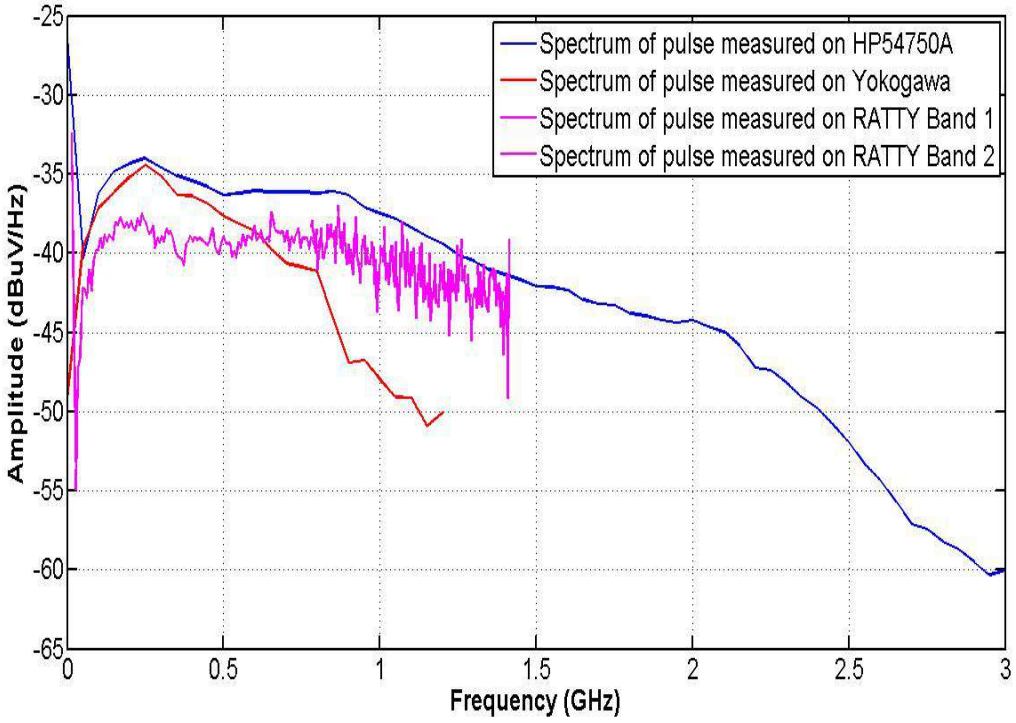

Figure 5.3: Frequency response of pulses from the 30 V PG measured on measuring equipment.

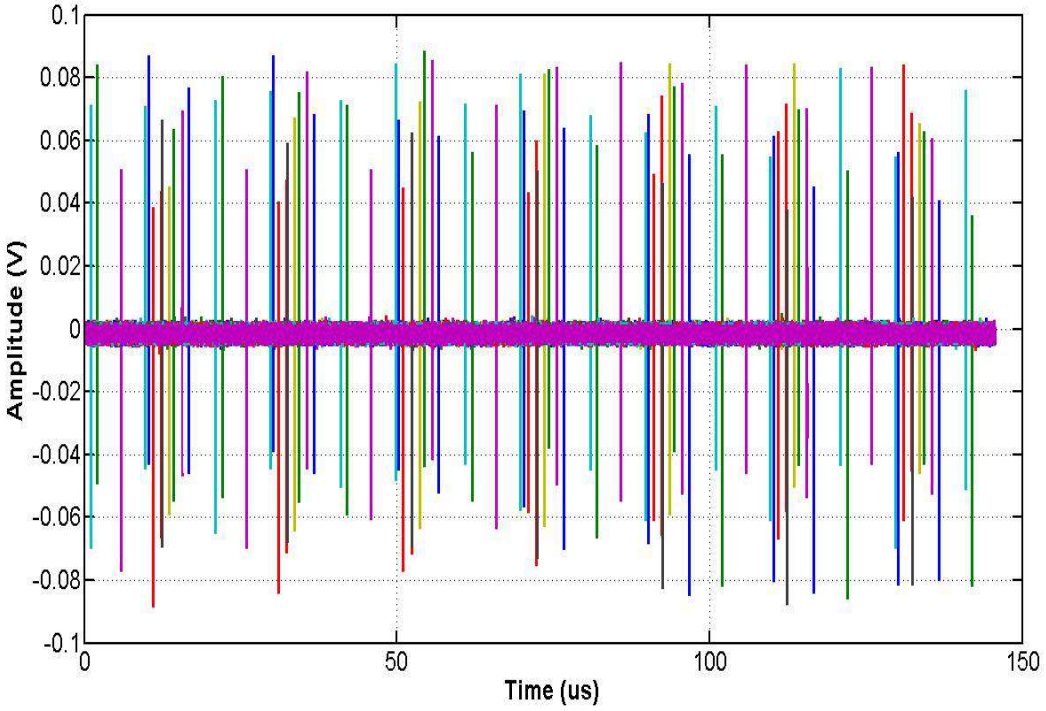

Figure 5.4: Multiple pulses captured by RATTY to indicate the varying amplitudes.

captured at different times. Another averaging method is FD averaging. FD averaging takes the FFT of each pulse added together and dividing it by the number of Fourier transformed pulses. This is an easier method and faster to calculate. The effect of averaging and selection between the maximum or averaged pulsess will be implemented with the CPS1 measurements.

5.1.2 Direct measurements for CPS1 PG

For the Karoo environment a high amplitude pulse is required. From previous measurements, the 30 V PG had an insufficient dynamic range and disappeared in the environmental RFI noise. The improved amplitude of the CPS1 increases the dynamic range of the pulse by 50 dB, which would have a significant improvement in results.

Calibrating and measuring the CPS1 pulser in the Stellenbosch laboratory proved difficult for multiple reasons. Because of its large amplitude, specific attenuators are required to decrease the power for measurements on our systems. The only available attenuator is a 30 dB 100 W 1 GHz attenuator. The attenuator is band-limited to 1 GHz with a PG that provides spectral content up to 6 GHz. The transmission coefficient of the 30 dB attenuator is measured and shown in appendix F. The 30 dB attenuator has a loss of around -33.5 dB for 1 GHz and degrades to -36 dB at 3.5 GHz. The optimal operating frequency range is up to 1 GHz, but it can be used up to 3.5 GHz. At this point the reflection coefficient moves above -10 dB and most of the energy injected into the attenuator will be reflected back into the system. Measurements with the CPS1 pulser in the laboratories is always used with the 30 dB attenuator to drop the 2.5 kV down to 80 V.

The second problem for measuring the CPS1 pulser is the slow triggering rate. In order to accurately measure it with the HP54750A sampling oscilloscope the pulser had to be triggered faster in order to improve the resolution bandwidth of the pulse. The CPS1 can not be triggered faster than 1 ms, because the stability of the pulse would be affected. As recorded in chapter 3 with stacked

transistors, a faster trigger increases the total average power in the system. This can overload the transistor and cause them to fail, or decreases the stability of the pulse. Slow trigger rates (1 ms) force the oscilloscope to a larger record length of 500 us. This is due to the time interval resolution limit explained of the HP 54750A shown in section 2.3.1. With a maximum of 4096 sampling points spaced over 500 us, the same problem with accuracy, as in RATTY, arise. The pulse rise-time and peak are not efficiently sampled by the scope or it is not sampled at all. A longer record length increases the time between samples and inaccurately samples a faster signal. Because of theses difficulties the CPS1 was measured and compared with RTA, RATTY and the Yokogawa. A diagram of the measuring configuration is depicted in figure 5.5.

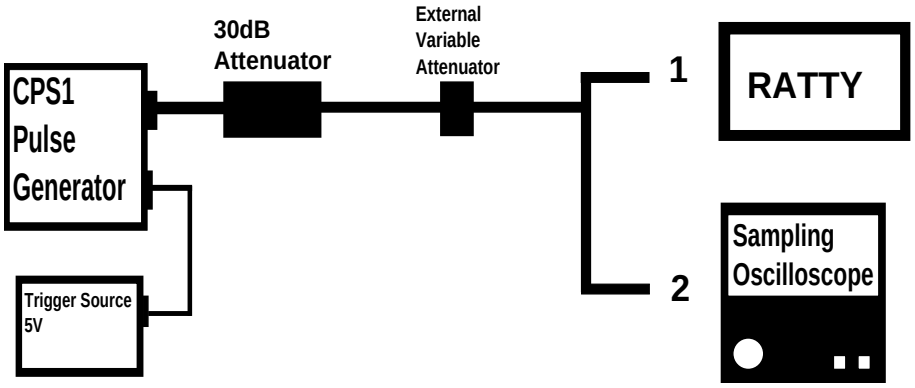

Figure 5.5: Measurement configuration of the CPS1 PG for direct pulse measurement.

When RATTY or RTA is used, multiple pulses are sampled in one .hdf5 file. This is the internal file type used in RATTY or RTA where measured results and calibration settings are stored. Taking the correct pulse is difficult and suggestions have been mentioned. With RATTY files the pulses are TD averaged and with RTA the spectrum is averaged. The CPS1 TD Pulses and the spectrum, from the various measuring equipment, are compared and depicted below. Measured pulses with RTA and the CPS1 pulser will be covered in the Karoo calibration section (5.3).

Figure 5.6 incorporates the TD pulses of the CPS1 impulse generator measured on the Yokogawa sampling oscilloscope and RATTY. The band limitation of the Yokogawa reduces the amplitude of the pulse. When compared with the calibrated pulse measured by Kentech industries the loss in amplitude can be seen. The RATTY measurements indicate two pulses. The red and green pulses show the maximum amplitude pulses selected from the multiple pulses stored in the .hdf5 file with the purple and blue pulses the time-domain averaging technique applied to all the pulses sampled by RATTY. The average results are expected to be lower than the maximum for both bands. From figure 5.4 it is clear that the pulses vary in amplitude and when the average pulse from these pulses are taken it will be lower than the maximum pulse. The difference between the maximum and average pulse in band one are small, compared to the difference between the pulses from band two. Band two of RATTY incorporate the higher frequency content of the pulse where the least amount of the energy of the pulse is located. This gives rise to the low pulse displayed in the figure when compared to band one of RATTY. At these frequencies the time difference at the peak of these pulses are extremely small and if it is sampled in the large record length of RATTY, the high frequency content of the average pulses can be inaccurately sampled. The same phenomenon that occur in the sampling oscilloscope can occur in RATTY.

From the spectrum, the blue curve is the calibrated spectrum of the CPS1 pulse from Kentech industries. The black line in figure 5.7 is the Yokogawa measurement and the dashed red and green lines are the maximum and averaged pulses measured by RATTY. The Yokogawa measurement loses a

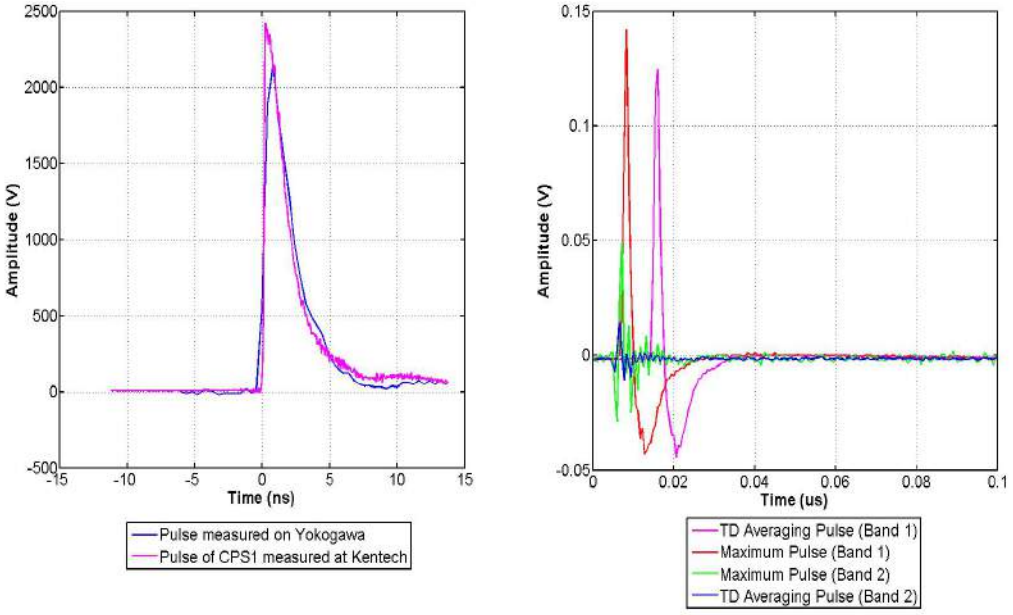

Figure 5.6: TD pulses of the CPS1 measured with different measuring equipment.

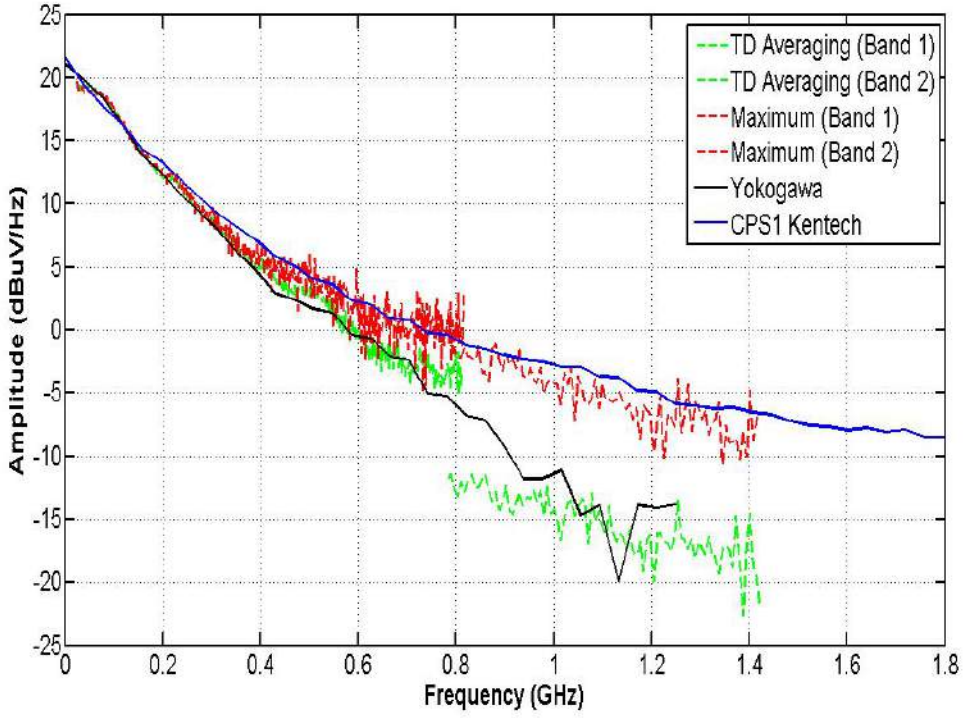

Figure 5.7: Spectrum of measured pulses with different measuring equipment.

significant amount of spectral content as it approaches the higher frequencies when compared with the calibrated pulse. As showed with the 30 V pulse the Yokogawa rolls off at the higher frequencies, because it is band-limited. Although the Yokogawa is a powerful and convenient measuring tool, it is not suited for accurate TD pulse measurements with rise-times faster than 700 ps. When the spectrum of the maximum and averaged pulses are compared, there is a miss-alignment between the average pulse levels between band one and two from RATTY. This can occur when the pulse in band two is inaccurately sampled because it forms part of the high frequency content of the pulse, which is small compared to the record length of RATTY. The bulk of the energy of the pulse is also in the lower frequencies. This makes it easier to sample the pulse at the lower frequencies than at the higher frequencies. The solution for RATTY and RTA measurements would be to take the maximum pulse in each file to ensure accurate results. When the maximum pulse from each band is compared, it aligns perfectly with the calibrated results with less than 1 dB difference. With these results confidence can be taken when RATTY is used for TD measurements with the IRA and CPS1. This measurement can also be used to calibrate measuring devices. Because the measurement provided by Kentech are assumed to be accurate, with the RATTY measurement varying with 1 dB across the band, the difference between the results can be used as an error function. The function can then be implemented to correct measurements done with RATTY.

5.1.3 Conclusion

Different techniques have been exploited in order to capture TD impulses. Four sampling devices have been used to measure a transient impulse. From the above transient responses it is clear that with a band-limited system such as the Yokogawa, the full pulse is not accurately sampled and the high frequency content of the pulse is filtered out. This causes an amplitude difference and a significant drop in the spectrum from 500 MHz onwards. With RATTY the TD pulses are sampled in certain operating bands, which are then Fourier transformed to show the spectrum. This affects the shape of the pulse but not the spectral content. However the long record length in RATTY causes some of the pulses not to be sampled at the absolute peak of the pulse. This can cause a amplitude difference in the spectrum as shown in figure 5.3. With the CPS1 PG the real-time transient analyser showed great potential for TD measurements. There can be some discrepancies when the average of the pulses are taken, but when the maximum pulse is taken a more accurate response can be obtained. The ideal measuring device with the best accuracy for the 30 V PG is the HP54750. With its high bandwidth all the frequency content produced by the pulse is accurately sampled and can be used to calibrate or compare with other devices. Although the HP547450A is the most accurate measuring device For smaller amplitude impulse generators with faster trigger rates, this oscilloscope has to be externally triggered to ensure precise measurements. The 50 GHz scope can accurately capture pulses and be used to compare or calibrate other measuring systems. The mobility of the scope is also limited and continuously moving the device can damage it. The Yokogawa is extremely mobile and easy to use, but as shown, it is the least accurate measuring device for high frequency TD measurements. For our work the Yokogawa is used as a testing system for transients during measurements. The solution for TD field measurements is RATTY or the real-time-analyser (RTA). It is impossible to use the 50 GHz sampling oscilloscope for multiple reasons and the Yokogawa with a band limitation at the higher frequencies, is inaccurate for bandwidths the transmitting source can achieve. RTA is an accurate measuring device which is can easily deployed for measurements in the Karoo.

5.2 Experimental measurements with IRA and PG sources into free-space

A set of experimental measurements with the two impulse generators and IRA is required before it is used for measurements in the Karoo. The IRA with the two PG sources will be used to relatively

calibrate the gain of the IRA with a two antenna method. Both measurements are conducted at Stellenbosch University to test the IRA response in the time and frequency domain.

5.2.1 Roof Measurement with the 30V PG and HP 54750A.

The IRA with a TEM Horn is tested in an outside environment. This is a rough measurement in order to test a TD pulse with the IRA. The experiment with components are displayed in figure 5.8. The 30 V impulse generator is connected to the IRA with a 5 m cable. From the IRA, the receiving antenna is placed 10 m away directly on boresight. From the TEM Horn (R_x) a 20 m cable is placed to connect to the HP54750A sampling oscilloscope. The reason for choosing 10 m is to ensure that the receiving antenna is outside of the Fresnel zone of the transmitting antenna at 2 GHz, which is calculated by the following equation:

$$f_r = \frac{2D^2}{\lambda} \tag{5.2.1}$$

where D is the largest geometrical dimension of the antenna and λ the EM wavelength at 2 GHz. The transmitted pulse is measured and compared to the received and expected pulse.

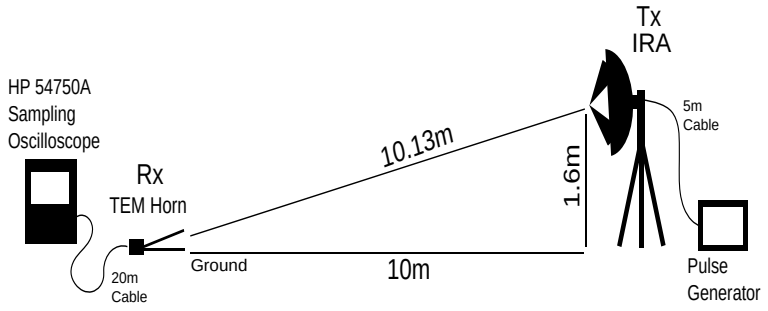

Figure 5.8: Dry-run configuration of IRA with TEM Horn and 30V pulse generator.

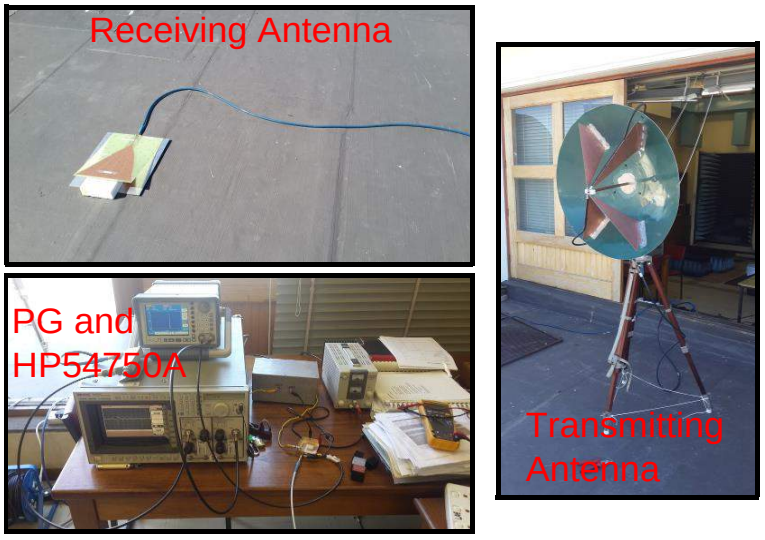

Figure 5.9: Picture of the dry-run configuration of IRA with TEM Horn and 30V pulse generator.

The results from this measurement is depicted in figures 5.10 and 5.11. The first remark that can be made is that the measured pulse is negative. With the IRA's two top conical plates positively polarised and bottom two negatively polarised, a negative pulse is formed in the far-field. Changing the

positive and negative connections will create a positive far-field pulse. The effect of ground reflection is also shown in the transient response. The blue pulse is the pulse measured with the TEM horn on the ground and the red pulse with the horn lifted from the ground. There is an increase in amplitude and change in pulse shape when the horn is lifted from the ground. This can be caused by a reflected pulse from the ground into the TEM horn. The main pulse (direct line of sight) is received at the horn and pico-seconds later the reflected pulse from ground arrives at the receiving antenna. If the main pulse and reflected pulse are in phase they will add and create a larger amplitude pulse similar to the result shown in 5.10. The two pulses measured with the sampling oscilloscope are identical in shape with only an amplitude difference. Both pulses have similar pre-pulses and small tail-ends when compared with the original transmitted impulse. The rise-times of the pulses are 200 ps for the pulse with TEM horn on the ground and 235 ps with the horn lifted from the ground. Because of small reflections the amplitude of the pulse is increased which increases the rise-time of the pulse by roughly 35 ps.

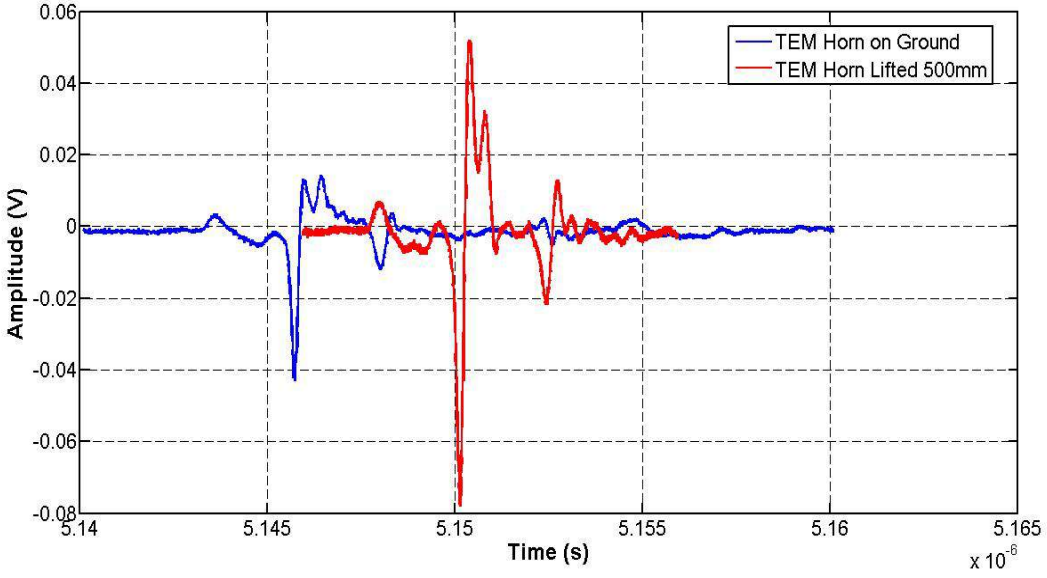

Figure 5.10: Time-domain pulses measured with TEM Horn on the ground and lifted 500 mm from the ground.

An expected spectrum with free-space losses and cable attenuation is compared with the Fourier transformed measured pulse which is displayed in figure 5.11. The expected spectrum is calculated by incorporating an interpolated gain from the FEKO simulation and taking the TEM Horn gain as 6 dB. Removing the FSPL and cable attenuation that are calculated from the cable data sheets and interpolated to the desired frequency points. The attenuation for the blue phase stable cables used are given in appendix F. The free-space FSPL can be calculated by using Friis transmission equation (equation 5.0.2).

With all the losses known, an estimated spectrum is calculated and compared to the measured pulse. The red line in the spectrum indicates the measured pulse and the green line the FSPL prediction after simulated gain and cable losses are removed. The blue line is the spectrum of the pulse being transmitted. The calculated pulse with the interpolated simulation gain, follow closely with the measured pulse of the IRA from 1 GHz onwards in the spectrum. The green and red lines differ by almost 10 dB at the lower frequencies, but after 1.5 GHz the difference between the expected and measured pulse vary with less than 3 dB. The discrepancies at the lower frequencies originate from the horn used as the receiving antenna for the pulse. The horn operates from 700 MHz and has an

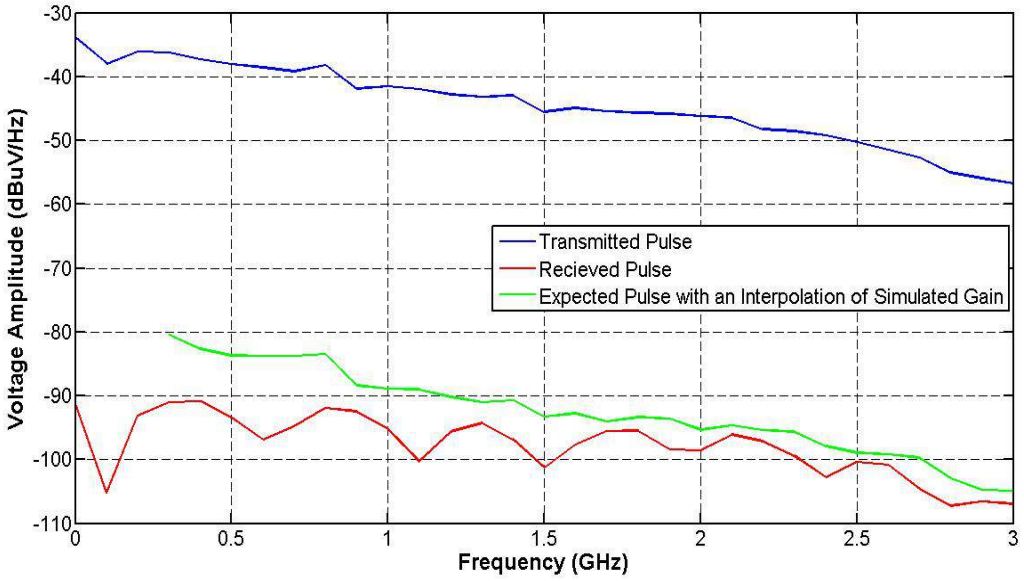

Figure 5.11: Spectrum of pulses measured with TEM Horn and HP54750A with a calculated expected spectrum.

increasing gain up to 1.5 GHz, before it has a constant gain (See appendix F for TEM-Horn response). Because a simulated gain is incorporated the small discrepancies after 1.5 GHz can be expected, but also indicate that the simulated gain of the IRA is a fairly accurate response of the true IRA gain. The correlation between the expected and measured FD responses give a good indication that the IRA is working and a predicted response can be calculated, as shown above. With a more accurate IRA and TEM Horn gain a precise estimation of the pulse spectrum, a certain distance away, can be formulated. This same measurements is conducted with the CPS1 PG, a LPDA antenna and RATTY in the next section.

5.2.2 Roof Measurements with CPS1 Pulse Generator and RATTY.

The antenna is also tested with the CPS1 as a transmitting source and RATTY as the receiver. The receiving antenna used for this measurements is a LPDA antenna that operates from 300 MHz up to 8 GHz with a gain between 5−6 dB. From the previous measurements the lower frequency band of the expected and measured pulse did not correlate. The TEM horn operates from roughly 700 MHz with an increasing gain. Using the LPDA for a receiving antenna allow a more accurate observation between the measured and calculated response at the lower frequencies. The measuring configuration is depicted in figure 5.12. The distance between the antenna is chosen to ensure that the receiving antenna is outside the Fresnel zone of the transmitting antenna at 1.4 GHz. The same cables used for the 30 V impulse generator test experiment were used during this setup. The transient and frequency results are depicted in figures 5.13 and 5.14.

The transient response measured with the LPDA and horn differ. With the TEM horn as shown in figure 5.10, the pulse is shaped and indicated without dispersion. When the LPDA is used as the receiving antenna, the pulse measured with RATTY is dispersed. The LPDA is designed to receive higher frequency signals first at the smallest dipole element at the tip of the antenna and as the pulse move along the antenna the lower frequencies couple onto the longer dipole elements which is then measured on RATTY. The pulse shape is affected by the dispersion, but none of the pulse content is lost.

The pulses shown in figure 5.13 are dispersed by the receiving LPDA. The amplitudes shown are

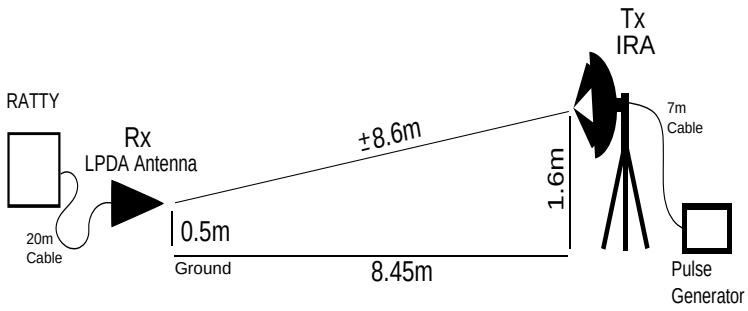

Figure 5.12: Dry-run configuration of IRA with LPDA and CPS1 impulse generator.

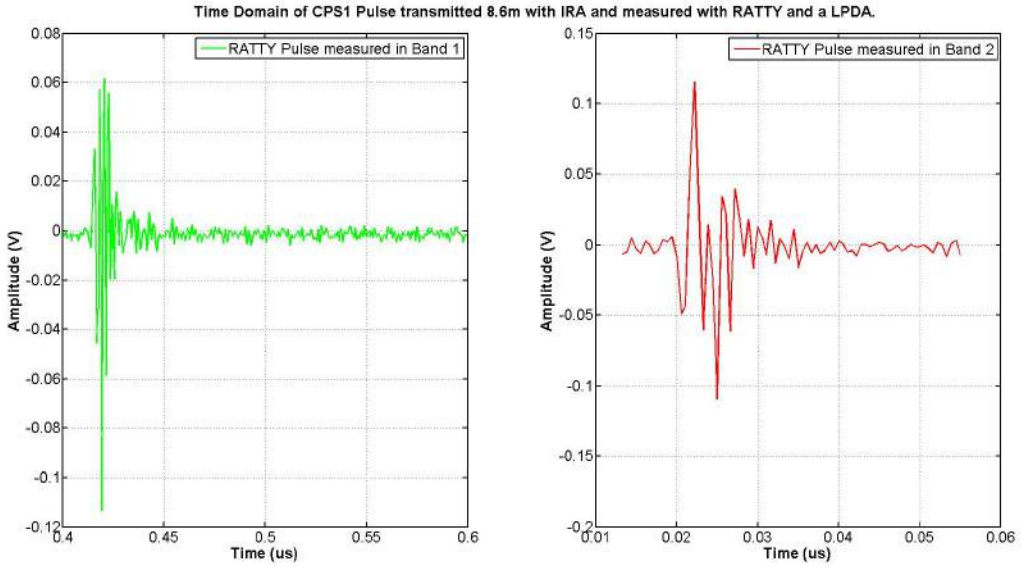

Figure 5.13: Transient measurement of IRA with LPDA and CPS1 impulse generator. Green pulse is from RATTY band 1 and red pulse is from RATTY band 2 to show the dispersion

with RATTY gain and external attenuation included. From the previous experimental measurement the maximum pulses are taken from each .hdf5 file and Fourier transformed to compare with a calculated expected spectrum. The two pulses indicated in the figure are measured in RATTY's two sampling bands.

The LPDA used for measurements has an operating band of roughly 300 MHz to 8 GHz. When the spectrum is observed, the energy of the pulse measured in the first 100 MHz is at $-45dB$. This can be neglected because it is outside of the LPDA bandwidth. From 350 MHz the spectrum rises to above $-35dB$ which is the energy of the pulse that is being measured. When the measured spectrum is compared with the expected spectrum, after FSPL and cable losses, there is $1-4\ dB$ differences at distinct frequency points and a $8\ dB$ difference at 630 MHz. These discrepancies occur from ground reflections because the LPDA was lifted a few millimetres from the ground. With the TEM-Horn a ground plane is automatically attached to the antenna (see figure 5.8). The LPDA does not have a ground plane and had to be lifted a few millimetres above the ground.

The overall correlation between the measured and calculated results are acceptable. Because both measurements with the different PG sources and receiving antennas were tested and obtaining similar results, future measurements over a distance can be mathematically calculated to indicate an expected response from the pulse being transmitted with the IRA. This is done by taking the power transmitted and de-embed the gains of the IRA and receiving antenna, as well as removing the cable

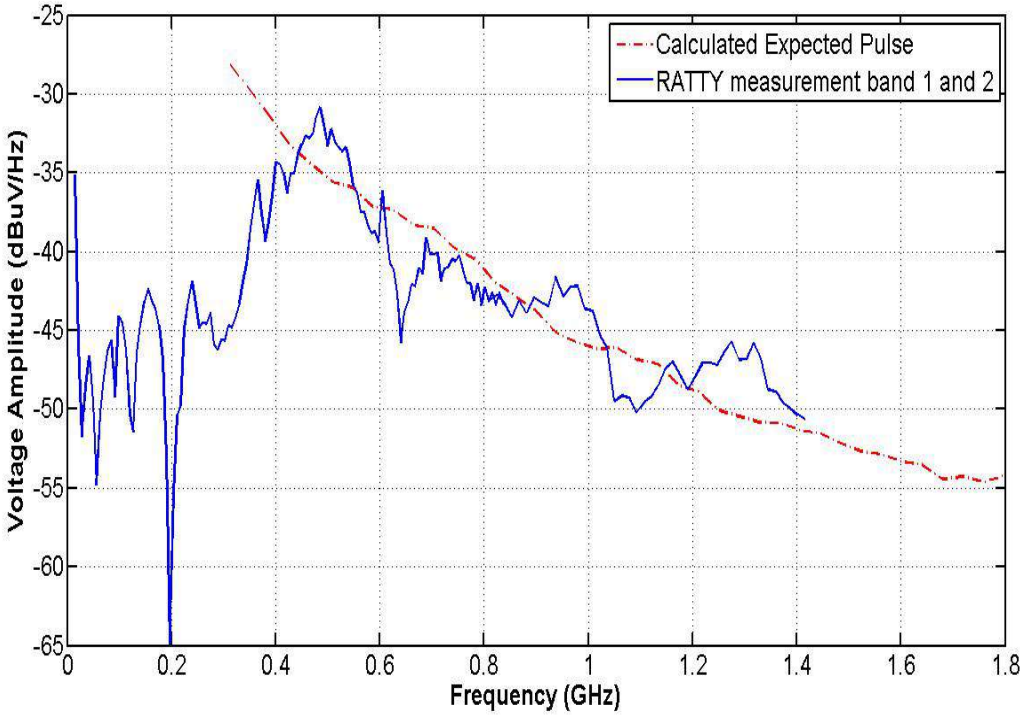

Figure 5.14: Spectrum of IRA with LPDA and CPS1 impulse generator.

losses, attenuators and FSPL in the measurement.

With these results more confidence can be placed on the IRA and deploying it in the EM sensitive Karoo environment. Because measuring results tie-up with expected results, an accurate prediction of the radiated energy with the CPS1, a certain distance away, can be made. There is still a strong desire to accurately measure the gain of the antenna. From both these measurements the simulated gain has been used to predict the spectrum of the pulse being measured. In the next section a technique will be discussed to measure the gain of the IRA inside an anechoic chamber or open-area test site (OATS).

5.2.3 Anechoic chamber measurements

The current IRA gain that has been used for measurements was obtained during the FEKO simulation. The simulation does not include the splitter and cables feeding the antenna and is not the most accurate representation of the IRA gain. From the TD measurements above an expected spectrum was compared with the measured pulse Fourier transformed. Calculating the expected spectrum included the simulated gain from FEKO. The two responses had good correlation which showed that the simulated IRA gain is a fairly accurate representation of the true IRA gain. There are a few methods that can be used to measure the gain of the antenna. The method most commonly used, is a three antenna method in an anechoic chamber or OATS.

Because of the geometrical size of the IRA, the Stellenbosch anechoic chamber is too small for accurate measurements with the IRA. Measurements with the IRA inside the chamber causes the receiving antenna to be in the Fresnel zone of the IRA, because it is too small for the electrical length of the antenna at the operating band of the chamber. The Stellenbosch anechoic chamber operates from 2 GHz up to 20 GHz and as shown above, the receiving antenna has to placed at least 10 m away to ensure the antenna is in the far-field of the antenna. The measurements are not ideal but it is done to implement and discuss the three antenna method [19] principle used to determine the gain of antennas. The HP8510 VNA is used for measurements and is calibrated from 45 MHz to 8 GHz. Only

at the lower frequencies will the receiving antenna be in the far-field, which is outside the chamber's effective operating band. The reflection coefficient of the IRA was already accurately measured in chapter 4 and only a gain measurement is desired.

With three unknown antennas, three measurements in different combinations can be made to determine the gain of each single antenna. Once the antennas are measured the gain of the antennas can be calculated from the following equations.

$$(G_a)_{dB} + (G_b)_{dB} = 20\log_{10}\left(\frac{4\pi R}{\lambda}\right) + 10\log_{10}\left(\frac{P_{rb}}{P_{ta}}\right) \tag{5.2.2}$$

$$(G_a)_{dB} + (G_c)_{dB} = 20\log_{10}\left(\frac{4\pi R}{\lambda}\right) + 10\log_{10}\left(\frac{P_{rc}}{P_{ta}}\right) \tag{5.2.3}$$

$$(G_b)_{dB} + (G_c)_{dB} = 20\log_{10}\left(\frac{4\pi R}{\lambda}\right) + 10\log_{10}\left(\frac{P_{rc}}{P_{tb}}\right) \tag{5.2.4}$$

Where the first term is Friis transmission equation and the second term S_{21} measured from the VNA. The gain of one single antenna can be simplified from these equations and calculated by:

$$(G_a)_{dB} = \frac{\left((S_{21})_{ab} + (S_{21})_{ac} - (S_{21})_{bc} - FSPL\right)}{2} \tag{5.2.5}$$

where S_{21} is the measured gain from each combination in decibels.

Four antennas were measured: the IRA, two LPDA antennas and a TEM Horn. The gain of the IRA with a simulated gain are compared and can be found in appendix F, figure F.4.

5.2.4 Conclusion

The following sections covered the basic metrology of the IRA system in free-space with three of the four measuring devices. The IRA transmitting the 30 V pulse was measured with a TEM horn and the HP54750A sampling oscilloscope. The change in pulse shape was shown when the receiving antenna was lifted from ground and compared to a ground level measurement. The change in shape originates from ground reflections which cause the pulse to be added or subtracted due to the phase of the signals. The spectrum of the pulse was also calculated and compared with the measured results. Good correlation was found between the measured and calculated results from 1.5 GHz to 3 GHz. The lower frequencies had some discrepancies, because the TEM-horn only operates from 700 MHz onwards. To obtain a better correlation between the measured and expected pulses at the lower frequencies the IRA and CPS1 PG was also measured with RATTY and a LPDA antenna. The LPDA operated from 300 MHz and has a gain between 5 dB and 6 dB. The results tied up with calculated measurements over the bandwidth of the LPDA. Because a good correlation was obtained from both the experimental free-space measurements, confidence can be taken in the simulated gain used for expected spectrum calculations. The simulated gain is a good representation of the true IRA gain. The last measurements in this section covered a three antenna gain measurement inside the Stellenbosch anechoic chamber. This method can be used to obtain an accurate measured gain of the IRA, but because the Stellenbosch anechoic chamber is too small for the geometrical size of the IRA, measurement results are not accurate. A larger anechoic chamber or OATS should be used for accurate gain measurements.

5.3 Final calibration of the IRA and CPS1 PG with RTA for practical Karoo metrology

In the previous sections direct and free-space measurements were conducted to test the IRA system and illustrate important metrology techniques before a system is fully deployed for field measure-

ments. Because a high-power PG is used, pre-cautious measurements had to be made to ensure the safety of expensive electronic equipment when the system will be used in the Karoo. The system is also tested beforehand on the available measuring device to prepare for field measurements. These dry-run experiments help the designer to understand the system and enable better preparation for final measurements. The final calibration and tests for the IRA and PG system is covered in this last section.

Before the TD system is deployed in the Karoo it was tested with RTA, a direct sampling system that originated from RATTY. The system used in the Karoo consisted of the following. The CPS1 impulse generator is used as the transmitter, because it provides high instantaneous power over a large bandwidth, and the IRA as the transmitting antenna. A LPDA antenna with a better low frequency response, compared to the one used for the experimental tests, will be used with RTA on the receiving end. RTA is a similar design to RATTY with four operating bands and is a further development of a direct sampling system in [4]. Band 1 operates from DC - 900 MHz, band 2 from 600 MHz - 1.2 GHz, band 3 from 850 MHz - 1.7 GHz and band 4 from 1.8 GHz - 2.7 GHz. Unlike RATTY, RTA uses a direct sampling method for each desired band which is amplified by the RTA gain function. The system-bandpass gain calibration and cut-off frequencies for each band is illustrated in figure 5.15. The bandpass gain level changes with each measurement and this is a representation of a single gain configuration used in RTA. The band cut-off frequencies remains the same for each gain calibration.

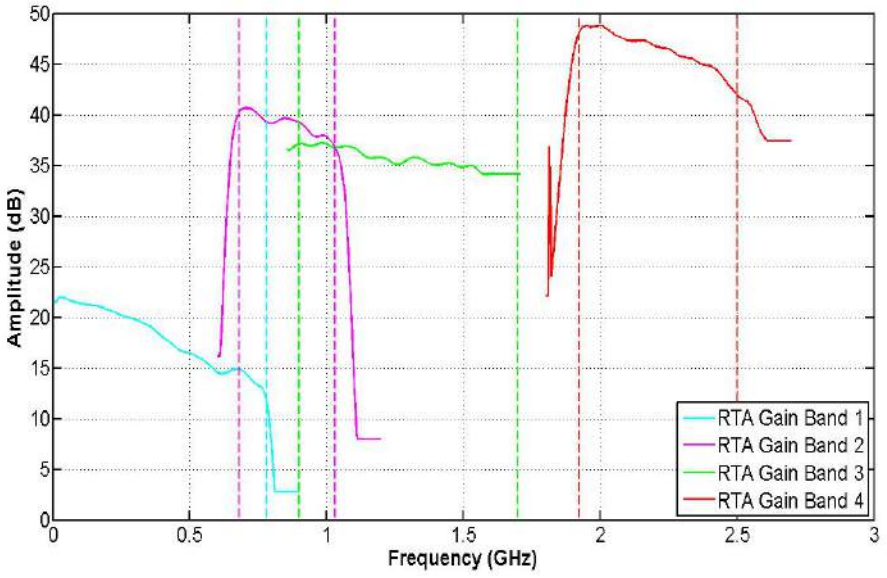

Figure 5.15: RTA gain calibration over the respective bands.

From the figure the different cut-off frequencies for each band is indicated by the dashed lines. The gain functions cut off at certain frequencies, which originate from the bandpass filters used within RTA. Band 1 is accurate up to 780 MHz from where the frequency instantly drops by more than 10 dB. Band 2 has a cut-in frequency at 680 MHz which drops by 2.5 dB over the operating band and has a cut-off at roughly 1 GHz. Band 2 acts as a cover-band between band 1 and 3. Band 3 is mostly accurate over the whole band, but results will be taken from 900 MHz - 1.7 GHz. The last band in RTA is separate from the other three bands and is accurate from around 1.925 GHz - 2.5 GHz. Plotting these results show each band's limitation, which is required for accurate measurements. Using the system-bandpass file located in the .hdf5 file of RTA when measured results are stored, the internal gain used during the measurements is de-embedded to represent an accurate response of

the pulse measured.

A direct measurement with the CPS1 and RTA is made to calibrate the response of the pulse on the RTA system. The CPS1 is connected to RTA via the 30 dB 100W attenuator, a 110 dB variable attenuator, a 3 dB pad and phase stable cables. The measurement configuration is shown in figure 5.16. The cable losses and attenuator responses were measured and can be found in appendix E.

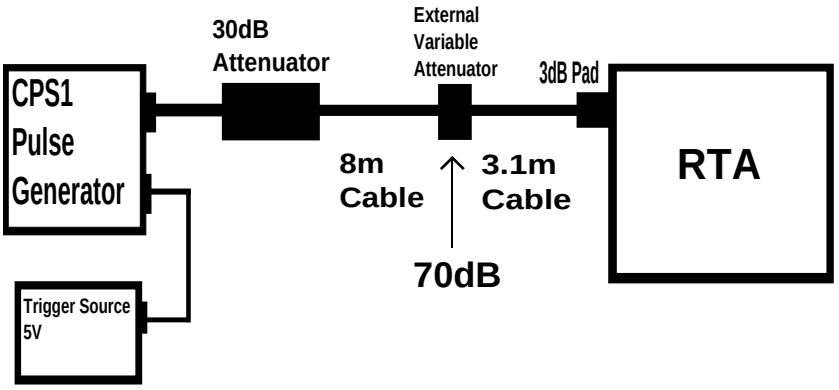

Figure 5.16: Configuration of a direct pulse measurement with RTA and the CPS1 pulser.

RTA stores results in a .hdf5 with multiple pulses in one file. The record length of a single sampled pulse is 140 us. For the direct CPS1 - RTA measurement, the output pulses, with their frequency responses in band 1, are displayed in figure 5.17. The TD pulses change in amplitude because not each pulse is sampled at its peak when received in RTA. This phenomenon occurs when a fast-rising transient pulse is sampled over a long record length. This decreases the a sampling resolution and has been confirmed in RATTY and sampling oscilloscope measurements. The red pulse in the spectrum is the maximum sampled pulse and the light blue pulse is a randomly selected pulse for frequency comparison between pulses. All the dark blue pulses are the transients sampled by RTA.

The spectrum is also depicted in figure 5.17. The light blue and red lines indicate the spectrum of the random selected pulse and the maximum pulse. The new green line indicate the average of all the pulses. The averaging technique applied in this case is a FD average. All the FFT's are added together and divided by the number of pulses. These three lines accurately follow each other over the bandwidth with small discrepancies. The averaged spectrum is $1-2$ dB lower than the maximum and random spectrum. This can be explained by the sampling of each pulse in RTA. Because not all of the pulses have the same peak amplitude, the average of all the pulses is expected to be a bit lower than the maximum and random spectrum.

It is important to note that only the pulse section from the whole record length of one sample should be selected and Fourier transformed. If the whole record length and TD data is sampled and Fourier transformed, the spectrum at the higher frequencies is full of noise. Because of the long record length extra noise is Fourier transformed with the pulse sampled. Thus the amount of energy in the pulse at the lower frequencies can be distinguished, but at the higher frequencies the energy of the pulse is small compared to the noise floor sampled before and after the pulse. This is indicated in the figure by the dark blue lines. The noise at the higher frequencies makes it impossible to distinguish the energy of the pulse in the spectrum. For an accurate spectrum of the pulse the pulse alone is gated out and Fourier transformed. The average, random and maximum pulses are all selected from each file excluding the unnecessary samples at either ends of the pulse to indicate the spectrum of the pulse without extra noise.

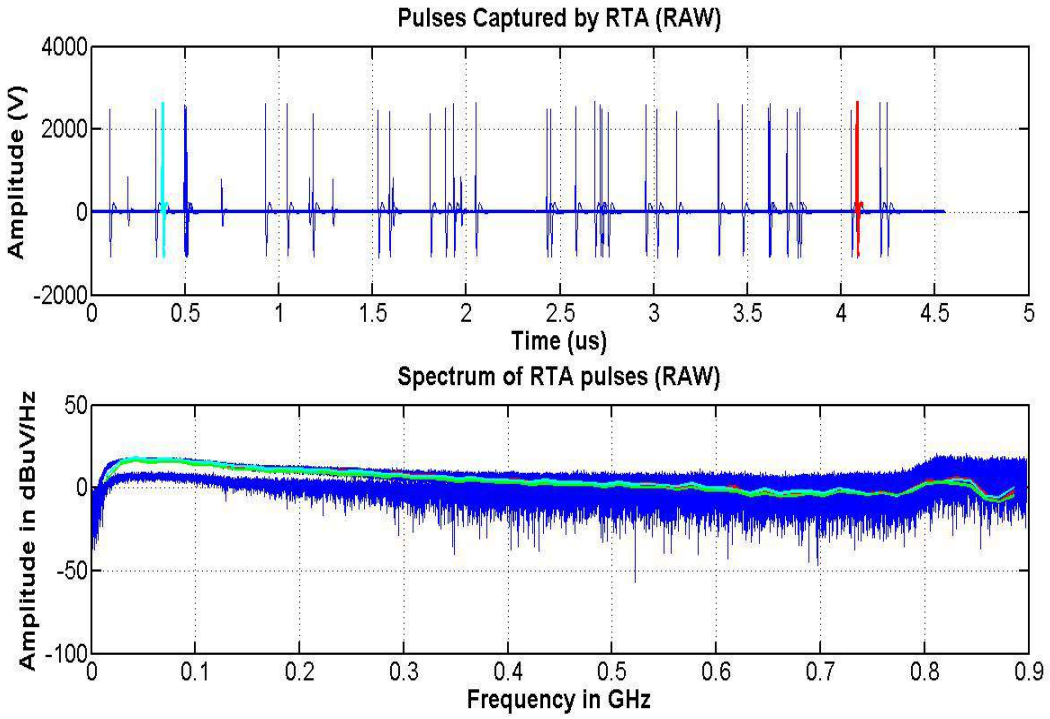

Figure 5.17: Direct measurement with RTA and the CPS1 pulser only for band 1.

When the pulse is gated, the whole pulse has to be gated without losing any valuable samples that form part of the original pulse. Reflections can be gated out, but the main pulse has to be accurately selected. To determine gating length or selection of the right pulse, the TD response is plotted in log-domain. This indicates where clear nulls are in the response and allows accurate gating of the full pulse. A figure of the pulses selected at two different lengths, 15.5 ns and 90 ns, are depicted in figure 5.18.

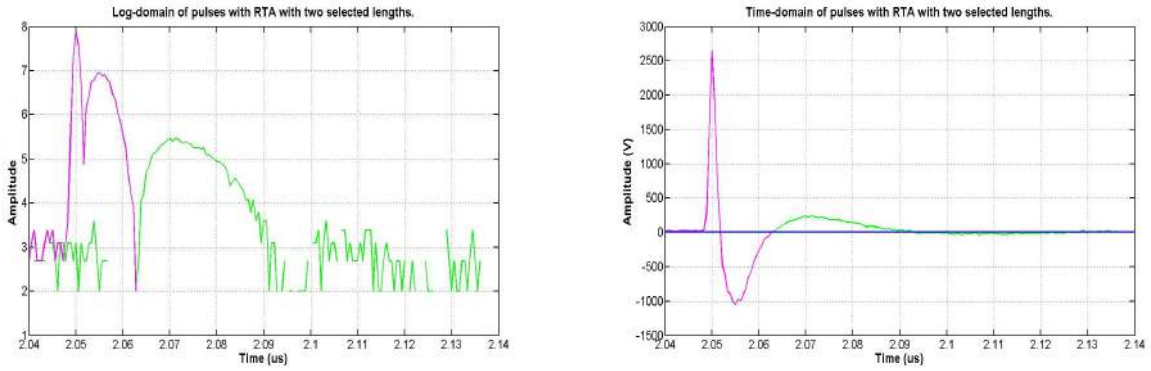

Figure 5.18: Log-domain and time-domain of selected pulses

The purple line in the figures indicate the pulse that is gated up to 15.5 ns and the green line indicate the 90 ns sampled pulse. Analysing the TD, show the shape of the pulse measured by RTA. Due to the filters in band 1 the filtered response, as recorded in chapter 3, can be seen at the tail end of the pulse. The calibrated CPS1 pulse has a width of 5 ns and when this is compared to the width of the pulse measured, dispersion occurs in RTA. The width of the main pulse is 4 ns, but with the tail-end included it is 34 ns. The log-domain is showed to indicate that the pulses, which are gated for accu-

racy, are gated at nulls. From both figures there is 25 ns of pulse content that is gated out between the 15.5 ns gated pulse and 90 ns gated pulse. This is part of the tail-end of the pulse and the difference between the pulse with the tail gated out and not gated out can only be explained by investigating the spectrum of both pulses. The spectrum of these two lengths from the average and maximum selected pulses are depicted in figure 5.19.

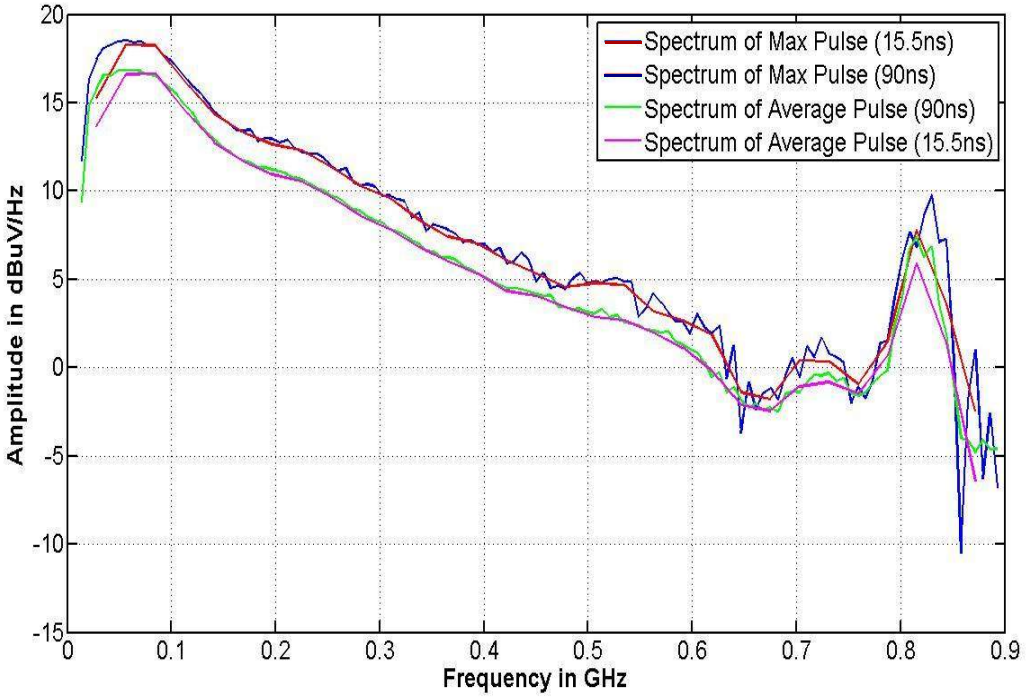

Figure 5.19: Spectrum from maximum and average pulses with two different time-gated lengths applied.

The difference between the maximum pulses and average pulses is around $1.5-1.7$ dB across the first band. If the gated pulses, with and without the tail-ends, are compared, there is little to no difference in the spectrum. There are small ripples (noise) on the 90 ns spectrum, which is the only difference when a gate is applied. For future measurements with RTA both time lengths will be shown, but only the maximum pulse will be taken from each .hdf5 file. To ensure nothing from the TD pulses are lost by gating, the longer gating function will mostly be shown and always compared with a shorter gating function. For complex measurements ground reflections has to be gated out, without gating important pulse content.

The difference between the average and maximum pulses, with the average spectrum increased by 1.7 dB to the same amplitude as the maximum spectrum, are shown in figure 5.20. From 200 MHz - 500 MHz there is less than 1 dB change between the maximum and average. After 650 MHz the difference increase because the spectral content of the maximum pulses decrease to the same spectrum amplitude of the averaged pulses. This is caused by the band limit and filter roll-off function as indicated in figure 5.15. Taking the average of the spectrum and comparing it with the maximum, indicates that spectral content is not lost that significantly influences the spectrum.

The direct CPS1 Pulse measured on all four bands of RTA are depicted in figure 5.21. All the cable losses and attenuator losses as measured in appendix E are applied to the measured results to calibrate the direct measurement with the CPS1 manufactured spectrum shown in chapter 3. A total

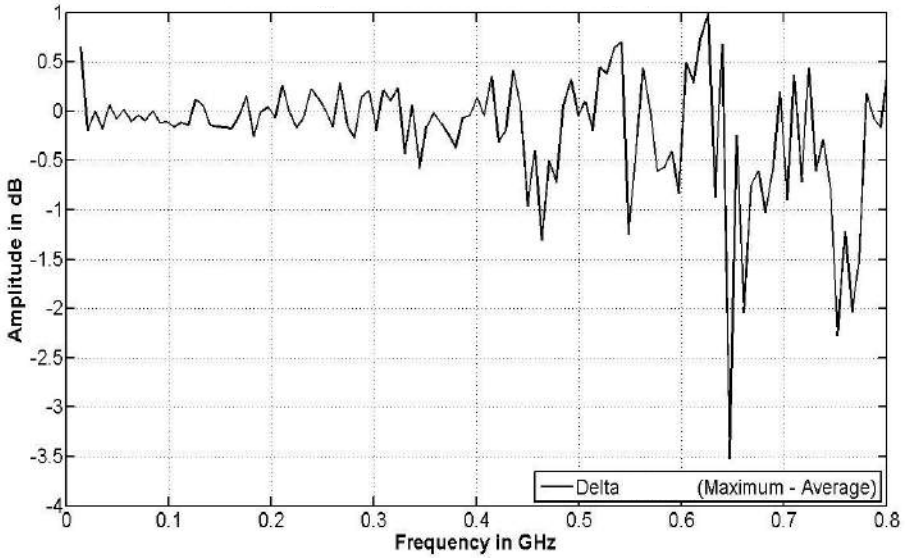

Figure 5.20: Delta between maximum and average spectrum.

length of 11.1 m of cables and 103 dB of attenuation are used as shown in the configuration (figure 5.16). The CPS1 calibration spectrum from Kentech industries is also included in the spectrum. The averaged spectrum is 1.7 dB lower than the maximum pulse in the first frequency band (DC - 780 MHz) with little to no difference between the maximum spectrum and calibrated CPS1 spectrum. In the second and third bands there are no difference between the maximum and average pulses and is 1 dB lower than the calibrated spectrum. Only in the fourth band is there more than a 2 dB change between the measured and calibrated pulses. This measurement is a good indication that the CPS1 pulse can accurately be measured with RTA over all four band, but more importantly that there is only $1-2$ dB differences between the results across the whole band. Because of the good correlation between the measured and calibrated pulse there is little to know external attenuation or losses in RTA over the first band. The small discrepancies between them as the frequency increases is low and acceptable. These measurements are done to calibrate the response and accuracy of RTA with the CPS1 pulse for the propagation and shielding effectiveness measurements in the Karoo.

As briefly mentioned in the beginning of this section, a larger bandwidth LPDA antenna will be used for the propagation and shielding measurements. The receiving antenna used for the Karoo measurements is a printed circuit board log periodic dipole antenna (PCB-LPDA) with a 50:1 bandwidth [47, 49]. The antenna characteristics are shown in appendix F. The operating band for the PCB-LPDA is from 180 MHz to 8 GHz with a constant gain of 5 dB across the band with no more than 1 dB variation to both ends of the spectrum. The reflection coefficient gives a good indication if the energy is radiated from the antenna or returned into the transmitter. The GLPDA's reflection coefficient is below -10 dB across the band, which indicates that most of the energy injected is radiated from the antenna and not returned back into the system.

5.4 Conclusion

In this section TD metrology with the PG and IRA system was briefly discussed. Four measuring devices were available for measurements and all of these devices were tested with two of the PG sources, covered in this study. The CPS1 and 30 V PG were used and measured with these four measuring devices. Through this, each of the devices' limitations could be investigated to ensure accurate measurements in the Karoo. After these measurements, the PG sources were connected to the IRA and a two antenna measuring technique was implemented to test the whole TD system. The last measurements

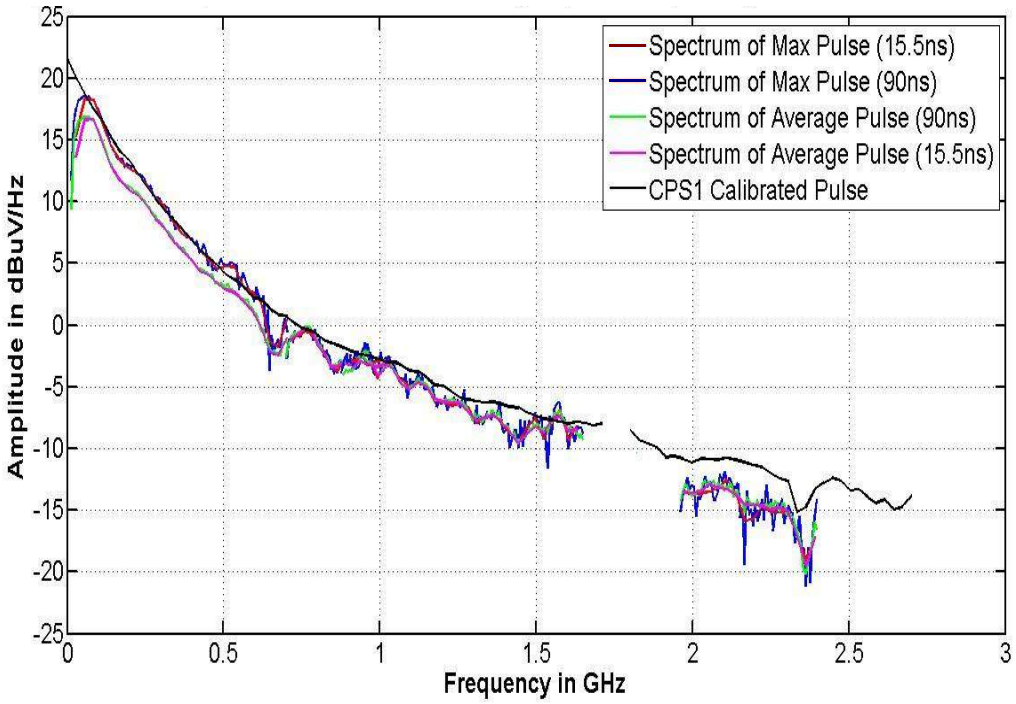

Figure 5.21: Spectrum of CPS1 Pulse on all four bands in RTA.

were final calibration measurements between the CPS1 PG and RTA, for practical measurements in the Karoo.

During the first set of measurements it was shown that the most accurate measuring device for the 30 V PG was the 50 GHz sampling oscilloscope. It has a large bandwidth and a time-interval accuracy of less than 8 ps. The sampling oscilloscope can also be used as a calibrating device for other measuring devices because of its precise measurements. The limit to this system is that it has to be externally triggered and requires a fast trigger to ensure accurate measurements. The time-interval resolution of the sampling scope is determined by the screen diameter and record length. A faster triggering pulse decreases the time record length, which increases the resolution bandwidth of the scope. Because the sample points and time record length of the scope determines the resolution displayed, pulses with slower repetition rates cannot be precisely characterised. The device is extremely sensitive and small vibrations can damage it. Continuously moving the device can put it at risk and it is thus best suited for measurements inside a laboratory. The Yokogawa sampling oscilloscope is an extremely powerful device, but is band-limited to 500 MHz. Most of the high frequency content is lost when this device is used. This caused lower amplitude pulses to be displayed and inaccurate spectral content, when compared to the 50 GHz scope and RATTY. This device is mostly used for testing, to ensure that pulses are transmitted. This is perfect for field measurements of transients with spectral content lower than 500 MHz. The devices that will be used for practical measurements in the Karoo are RATTY and RTA. Both of the devices are direct sampling systems, with different bandwidths. RATTY and RTA have shown promise for TD metrology and because of their mobility and large dynamic range, it is well suited for the intended propagation and SE measurements in the Karoo. Pulses were captured in .hdf5 files and processed to obtain the spectral content. In this chapter techniques were investigated to ensure that the data was accurately processed. From the measurements multiple pulses were captured when RATTY or RTA were used and selecting te right pulse for processing was important. The average of all the pulses was compared to the maximum pulse, sampled by these devices. The average of the pulses were expected to be lower because not all of the pulses sampled by RATTY and RTA, were at the peak of the pulse. The reason for this was already mentioned and

explained. Gating the correct pulse was also investigated. Decreasing the gated length improved the spectral resolution when compared to longer gates or pulses that are not gated at all.

A few free-space measurements were also conducted to test the response of the whole antenna system. During these measurements, expected pulses and spectral content were calculated using the gains, losses and FSPL in the measurement and this was compared to the measured results. Because an accurate gain of the IRA has not yet been measured, the simulated gain for the IRA was implemented for calculations. The results showed good correlation with small discrepancies that mostly originated from ground reflections.

The last measurement was implemented to calibrate RTA with the CPS1 PG. In the first band of RTA, the measured pulse and calibrated Kentech results corresponded with each other. In the second and third bands there were small differences of no more than 1 dB and only in the fourth band did results differ by 2 dB and more. Because there is good correlation between the measured and calibrated results, RTA can be used with confidence for measurements in the Karoo. In the next chapter the practical metrology of the TD system at the Karoo core-site will be discussed.

Chapter 6

Practical metrology of the TD system at the Karoo core-site

Previously RFI measurements in the Karoo were limited. A single frequency measurement had to be repeated multiple times to cover the spectrum. TD metrology allows speed-up without the loss of accuracy, therefore one pulse can cover a broad spectrum. The SKA core site near Carnarvorn is radio quiet, which makes it an ideal environment for RFI measurements. There is no interference from external transmitting sources and this allows for easier propagation and SE measurements. From previous measurements, in a more urban environment, the transmitted impulse proved difficult to measure because of more external sources that coupled into the system. The goal for this study is to deploy this TD system that was built, measured and calibrated as explained in the previous chapters, for metrology in the Karoo. This section will cover three practical measurements that were performed with this system and that can assist with the characterisation of the Karoo environment. The focus of this study was to design a TD system for measurements, therefore preliminary results, with brief interpretations, are also discussed.

The setup for the measurements consisted of the IRA with the CPS1 at the transmitting side and a PCB-LPDA antenna with RTA at the receiving end. This allowed accurate measurements for a large bandwidth. The CPS1 PG injects a 2.5 kV pulse into the IRA, which radiates the pulse into free space. The pulse is received by the PCB-LPDA antenna and directly sampled by RTA. The Karoo environment closely resembles an open-area test-site (OATS). This makes it ideal for an antenna pattern measurement, before the system will be used for propagation measurements and measuring the SE of a berm near the SKA processor building.

6.1 Antenna pattern measurement

In the previous chapters the IRA gain and reflection coefficient, have been measured and simulated. FEKO was also used to plot the far-field antenna pattern of the IRA. In this section, an antenna pattern measurement is done. An open area, to ensure no reflections, was used to for the measurement. The transmitting and receiving antennas were placed 10 m apart, with both of them at the same height of 1.6 m. A picture of the measurement as well as a diagram of the configuration figure, are illustrated in figures 6.1 to 6.3.

For the starting position, the IRA was placed at 20°from boresight. A pulse was transmitted and measured in the first three bands of RTA, before the antenna was moved 5°for the next measurement. This was done from 20°- 0°in order to get a rough polar pattern of the antenna at these angles. Due to the fact that the IRA is symmetrical, the same results were expected for the opposite side of the IRA

Figure 6.1: Picture of antenna pattern measurement.

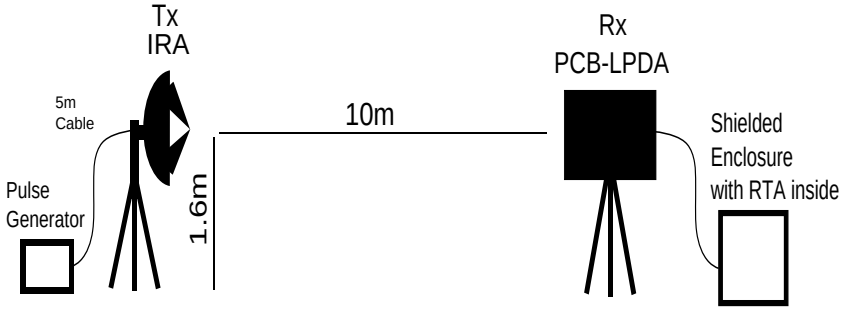

Figure 6.2: Antenna pattern measurement configuration - side view.

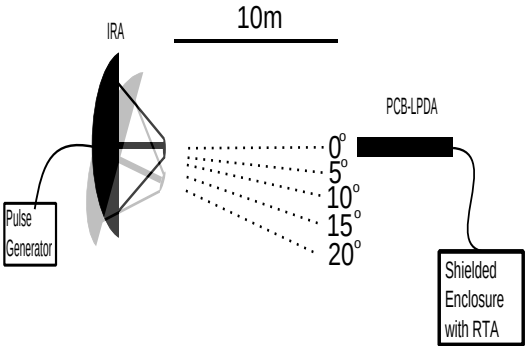

Figure 6.3: Antenna pattern measurement configuration - top view.

boresight. A Cartesian graph is depicted in figure 6.4 to show the directivity of the IRA.

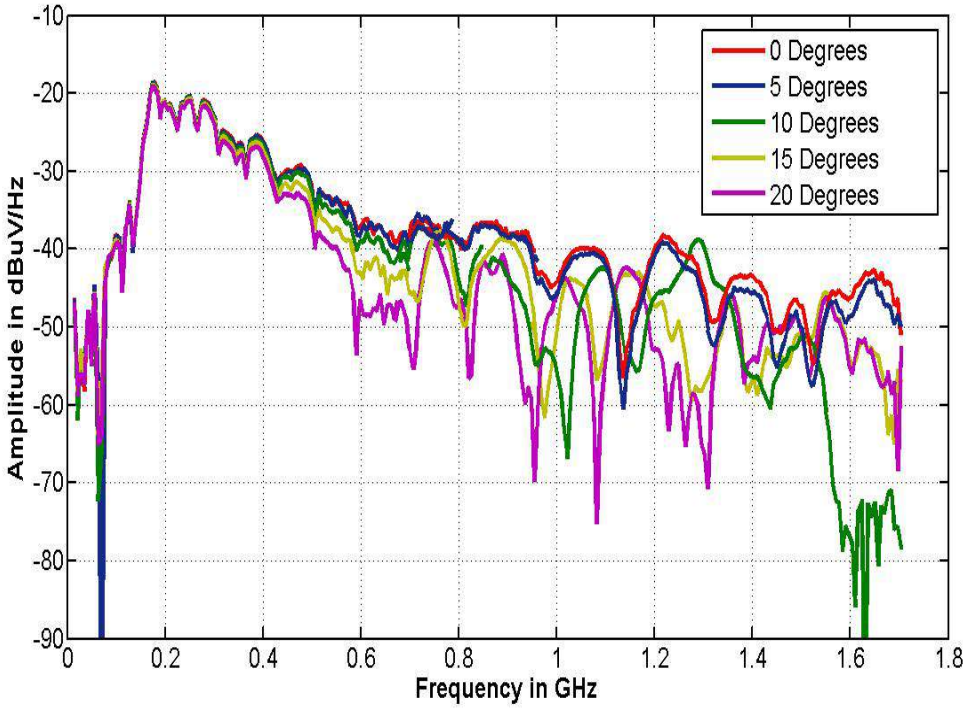

Figure 6.4: Spectrum of antenna pattern measurement.

From the figure, an estimate conclusion can be drawn for the antenna pattern of the IRA. From 180 MHz - 400 MHz there is less than 1 dB difference between the measurements, at all the different angles. This is an indication that the lower frequency antenna pattern agrees with FEKO simulation and polar patterns that are displayed displayed in figure 4.14 and 4.13. At the lower frequencies a cardioid pattern is formed and the antenna exhibits a broad beam at the lower frequencies. After 400 MHz the pattern starts to change into a more directive pattern. At a 20°angle the energy drops by 10 dB every 100 MHz, and when compared with boresight (0°), there is a 10 dB difference at 600 MHz. From 750 MHz the shape of the pattern changes rapidly. Different nulls at different angles and various frequencies are formed. The further away from boresight, the more nulls are formed. The fields around the IRA start to change with frequency, from an isotropic to a more directive pattern. This is also illustrated in the FEKO simulation, until a more directive pattern is formed at the highest frequency. The difference between boresight and 5°, is less than 2 dB at the higher frequencies and nearly the same up to 1 GHz. This gives a good indication of the width of the main beam. From symmetry the main beam from these results is between 5°and 10°, over this band (180 MHz - 1.7 GHz). Around 1.6 GHz, the 10°measurement drop below -70 $dBuV/Hz$, which could originate from data not accurately being sampled at those frequencies during the measurement.

From these results it can be concluded that the antenna is isotropic in the first 300 MHz of the band, thereafter it becomes more and more directive as the frequency increases. This was also confirmed in chapter 4 where the half power beamwidth was plotted. The beamwidth at the lower frequencies were almost 90°and dropped to 20°as the frequency increased. The main beam of these measurements are between 10°and 15°over 180 MHz to 1.7 GHz, with a $1-2$ dB difference between the 0°and 5°measurement, at the highest frequency of the spectrum.

6.2 Propagation measurements over distance

There is a strong desire to calibrate the propagation loss over the Karoo foliage. With the CPS1 and IRA, new propagation measurements can be planned to characterise propagation models designed for the Karoo environment. The first set of measurements that will be discussed, is a propagation measurement over a gravel road, over three distances. In this thesis, the limits of the TD system are also tested, through a long distance propagation measurement, as well as a comparison between measurements on a gravel road and over the Karoo foliage. An in-depth propagation methodology is not covered in this study and only preliminary measurements are made.

6.2.1 Gravel road and foliage propagation measurements

The first measurements of propagation are done over three set distances: 10 m, 100 m and 400 m. The pulse is propagated over a gravel road and over the Karoo foliage, for comparison. The 10 m measuring set-up was exactly the same as the antenna pattern measurement, with the 30 dB attenuator at the transmitter and the 110 dB variable attenuator at the receiving end. The two antennas were facing each other and then measurements were conducted from three different distances. For the 100 m and 400 m measurements, the 30 dB attenuator was removed from the transmitting end. A total of 15 m of cable was used for all of the measurements and cable-losses are removed from the measuring results. Pictures during these measurements are depicted in figure 6.5.

(a) Side view of the 10 m measurement.

(b) Transmiting side of the 10 m measurement.

(c) Receving side of the 100 m measurement.

(d) Direct line of sight from receving antenna to transmiting antenna for 400 m measurement.

Figure 6.5: Photographs of the propagation measurements at 10 m, 100 m and 400 m - taken by P.G. Wiid

The results from the first propagation measurements are portrayed in figure 6.6. The pulse is measured with RTA in three of the four bands. Both the transmitting and receiving antenna were placed at the same height of 1.6 m. The figure also displays a calculated spectrum for each distance, which include the FSPL, cable-losses and gains of the antennas. The solid lines in the figure indicate the measured results for each band and distance and the dotted lines indicate the FSPL spectrum for each distance. The measured results are compared to free-space loss and not to a propagation model of the Karoo environment.

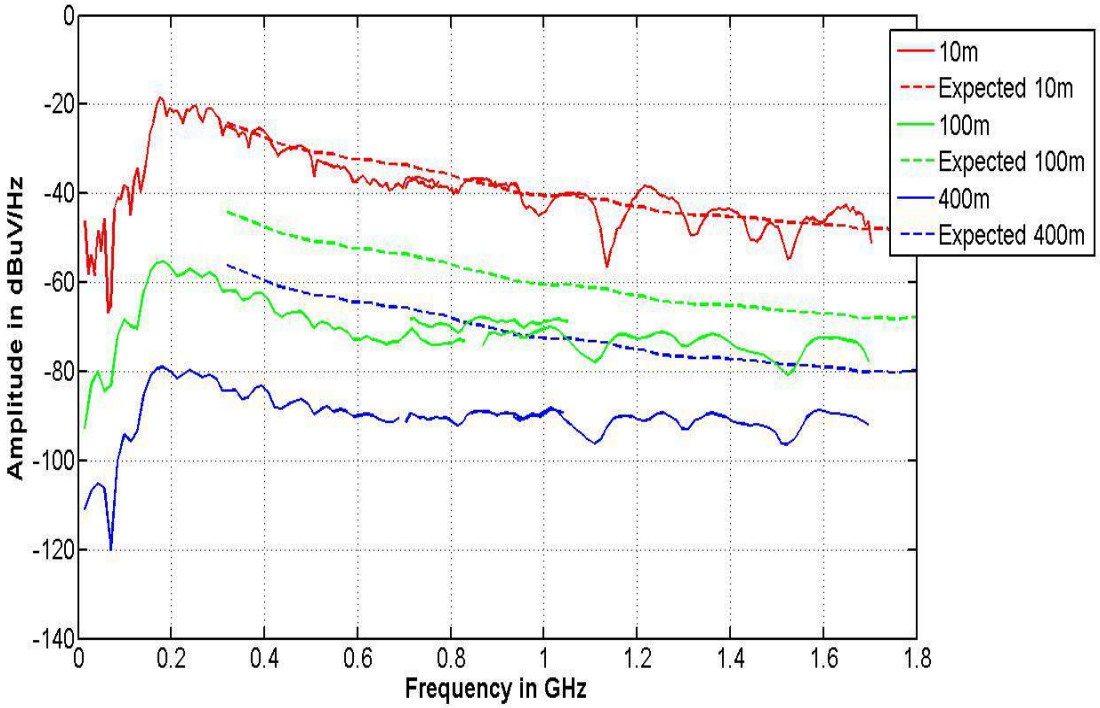

Figure 6.6: Propagation measurement over 10 m, 100 m and 400 m with a FSPL calculated spectrum.

For the measurement at 10 m, the expected pulse corresponds with the measured results, with only small discrepancies. When the expected pulses from the 100 m and 400 m are examined there is a 15 dB difference between the 100 m expected and measured result at 400 MHz and a 23 dB difference between the 400 m expected and measured result. As the frequency increase the difference becomes smaller, with a 5 dB difference for the 100 m at 1.6 GHz and 10 dB for the 400 m. From Frii's FSPL equation, the energy lost over the whole spectrum should be equal to 20 dB per-decade from 1 m. The expected difference between the 10 m and 100 m result should be 20 dB, but there is almost a 40 dB difference (20 dB more than calculated) at the lower frequencies. This indicates that there is significant attenuation in the Karoo environment when a EM wave is propagated over distances longer than 10 m. In this situation the attenuation at lower frequencies are more than the attenuation at the higher frequencies from both the 100 m and 400 m measurement. The difference between the propagation attenuation over the gravel road and free-space for both of the 100 m and 400 m results, are indicated in figure 6.7. The blue solid line is the difference between the measured and calculated spectrum at 400 m and the green solid line is the difference between the measured and calculated results at 100 m. At the lower frequencies the attenuation difference between free-space and the Karoo environment is almost 15 dB more than at the higher frequencies. This is affected by the Karoo soil properties and ground reflections which leads to a focussed study of propagation over different environments and this is not covered in this thesis.

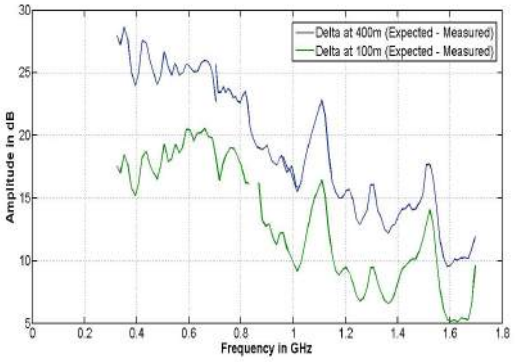

Figure 6.7: Difference between expected FSPL spectrum and measured propagation spectrum at 100 m and 400 m.

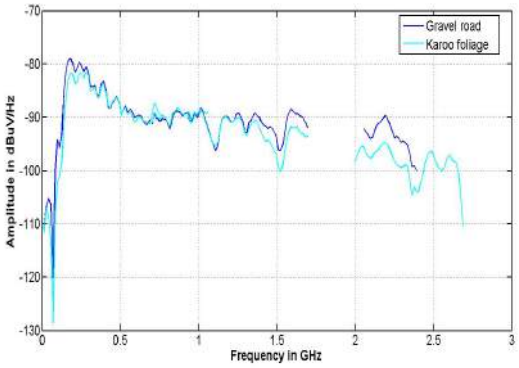

Figure 6.8: Propagation measurement at 400 m across the gravel road and over the Karoo foliage.

The effect of propagation over the Karoo foliage was also tested. Most of the emitted EM waves in the Karoo environment will propagate over the foliage instead of the gravel road. A comparison between these results show the attenuation between the foliage and the gravel road. The receiving antenna was placed in the Karoo vegetation and the transmitting antenna was placed on the gravel road. This is portrayed in a picture that is shown in figure 6.9. The results are compared with the gravel road propagation measurement at 400 m and are depicted in figure 6.8. In the figure the dark blue line is the propagation measurement over the gravel road and the light blue line is the measurement over the foliage. Between 180 MHz and 350 MHz and from 1.3 GHz, the results differ by 3 - 5 dB and between 400 MHz and 1.25 GHz, both of the results are the same. This is an indication that there are some effect of attenuation that is caused by the Karoo foliage, but because this is only preliminary measurements, facts cannot be presumed from this. Due to the fact that the measurements were conducted from a single height, the results are limited and will change due to different ground reflections at various heights.

This TD system is an effective and fast method for future propagation measurements in the Karoo and it allows another means of characterising the Karoo environment. The TD pulse covers a broad spectrum with a single pulse and by further investigation, detailed propagation models can be compared and characterised with results obtained by implementing this system. In the following section the propagation limit of this system is tested through three long-distance propagation measurements.

Figure 6.9: Pictures of propagation measurements over the Karoo foliage - taken by P.G. Wiid

6.2.2 Long distance propagation measurements

The last propagation measurements that were performed were a few long distance propagation tests. The receiving antenna was placed at distinct points, which were kilometers away from the transmitting antenna. The purpose of these measurements were mainly to test the limitation of the IRA and to see how far the pulses can be measured with this system. A Google Earth image of the measuring points is depicted in figure 6.10.

The transmitter is placed in front of the berm and faced towards Meysdam, M60 and M59. Meysdam is a farm a few kilometres from the Karoo array processor building (KAPB), houses all of the electronics for data processing and also diesel power generators for the telescopes. M59 and M60 are the positions where the $59th$ and $60th$ MeerKAT telescopes will be placed. M59 is the furthest telescope in a direct line of sight from the KAPB. Emissions that will be radiated from the KAPB area were attenuated and the level of attenuation, at the distinct points, were measured. The results are shown in this section. The distance between these points are indicated and displayed in table 6.1.

Receiving Point	Distance (km)
Meysdam	3.6 km
M60	4.92 km
M59	7.3 km

Table 6.1: Locations and distances of the long propagation measurement.

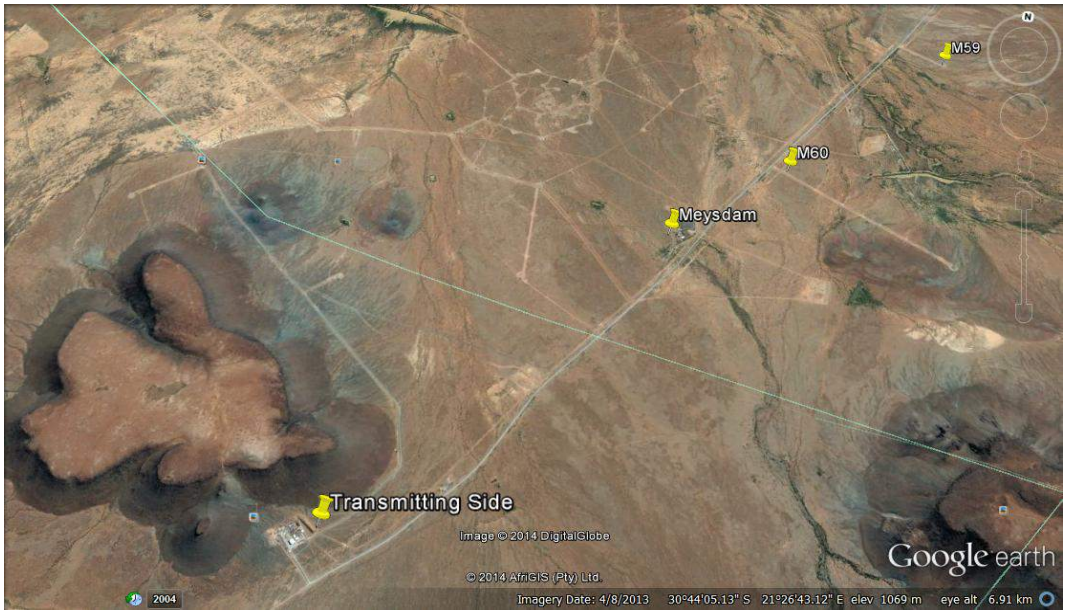

Figure 6.10: Google Earth map of long distance propagation.

The results for these measurements are displayed in figure 6.11. At the M60 and M59 receiving points, no data for band 1 is shown because the pulse could not be sampled in this band. The noise at the lower frequencies of the Karoo environment were more, which prohibited an accurate pulse to be clearly sampled by RTA and only noise was measured. From the previous results the attenuation at the lower frequencies were also higher than at the higher frequencies. The pulse that was transmitted had lost most of its low frequency content because of the higher propagation attenuation in the Karoo environment for the lower frequencies. The pulse was clearly sampled in the other bands

of RTA at all location. These measurements indicate that the IRA system can be used for propagation measurements over long distances. At 7.2 km and 4.92 km the pulses are clearly sampled in three of the four bands. Only at 3.6 km could the pulse be sampled in the first band. The bulk energy of the pulse transmitted, is at the lower frequencies. The attenuation at these frequencies are more than the attenuation at the higher frequencies, which resulted in the flat response that is seen in the spectrum. There is only a 10 dB drop over the measured band (180 MHz - 1.7 GHz), where previous results at shorter distances had a 20 dB - 30 dB drop (see figure 6.7). This again confirms that which was measured in figure 6.7. The attenuation at the lower frequencies, when compared to FSPL, are more than the attenuation at the higher frequencies. This system shows great promise for long distance propagation measurements. At the lower frequencies the known limitation for sampling a pulse with RTA in all the bands are at 3.6 km. For propagation measurements above 700 MHz in the Karoo, a pulse can clearly be sampled using the IRA with the CPS1 and RTA, up to 7.3 km.

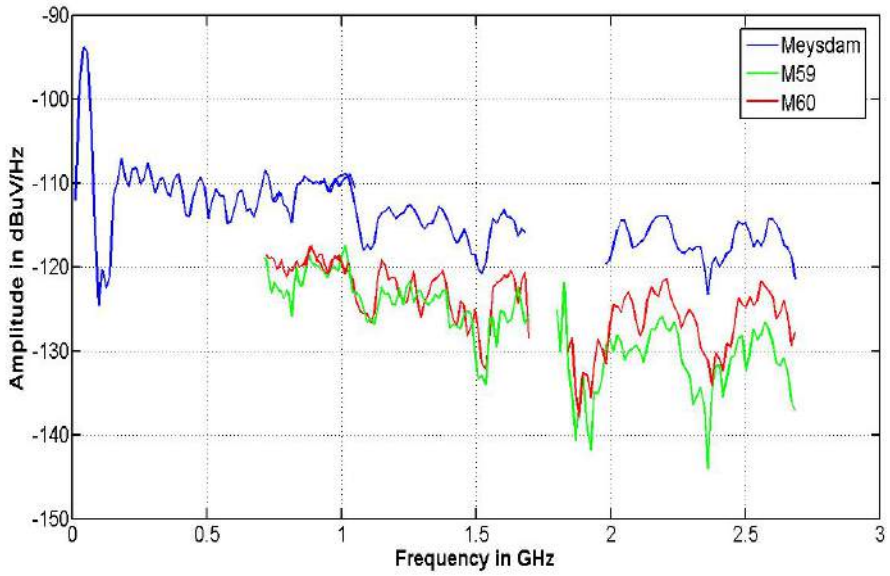

Figure 6.11: Propagation results at Meysdam, M60 and M59.

The propagation in the Karoo can be studied by deploying a system such as the IRA and CPS1 for measurements. In this thesis brief measurements were done to indicate the attenuation on a pulse which is propagated in the Karoo environment and over the foliage. The measurements were done from a single height and will change if different heights are applied. Adjusting the height will remove or vary the ground reflections of the pulse. There are higher levels of attenuation when signal is propagated over the Karoo environment than when it is propagated through free-space. The free-space prediction does not include ground reflections or Karoo soil and foliage on a propagating signal. The results have shown that most of the attenuation occurs over the lower frequency band and it seems that the higher frequencies penetrate easier through the vegetation. This can be important when propagation models are designed for the Karoo environment. In free-space a constant drop of the whole band is seen, but in the Karoo the lower frequencies are affected more than the frequencies. It was also shown that when the antennas are placed in the foliage of the Karoo, $3-5$ dB of attenuation were obtained at distinct frequency points. The foliage attenuate the signal by an extra few dBs, which should be considered when models are designed or future measurements are prepared. Long distance propagation measurements were done to test the limits of the system. A pulse could clearly be measured 7.3 km away from the point where the pulse was transmitted. The limit for this distance is that the lower part of the spectrum can not be measured because of the higher noise floor and the increased attenuation on the signal at the lower frequencies. The other bands can clearly be

sampled and specific propagation measurements can be planned for future investigation. A picture of the PCB-LPDA antenna during the long propagation measurements are illustrated in figure 6.12.

Figure 6.12: Picture of PCB-LPDA during a for propagation measurements during sunset - taken by P.G. Wiid.

6.3 Shielding effectiveness measurements of the berm

At the Karoo core site, where the radio telescopes are being assembled, the KAPB is built a few meters into the ground. The building is built with an EMC perspective to shield RF from coupling into and out of the building. RFI is a big concern for the SKA. Characterising the environment and putting safety mechanisms in place to detect RFI, are currently being investigated. The KAPB is located at Losberg and as mentioned, it houses all of the diesel power generators and processing systems. The KAPB is designed to enclose all of the RF noise produced by these systems and to shield it from the telescopes. The receivers used in these telescopes are extremely sensitive to RFI and any generated RF signals can cause receivers to saturate. The building is also built behind Losberg, which is used as an external shield for transmitting signals. All of the soil that was dug out for the KAPB was placed next to the building on the KAPB's north-easterly side to form Nuweberg (berm). This was another method to improve shielding and reduce RF levels emitted from the KAPB. A Google Earth image is depicted in figure 6.13.

In this section preliminary measurements are done to test the SE of the berm using propagation and scattering effects, at predetermined heights and distances across the berm. The transmitting antenna (CPS1 and IRA) is placed at three different heights in front of the berm (KAPB side) and measured with the PCB-LPDA and RTA at three points behind the berm. The distances of the receiving points behind the berm are 50 m, 200 m and 2500 m and these are taken from the centre of the berm. The width of the berm is roughly 45 m. The receiving antenna is placed in a direct line of sight with the IRA and the measuring setups are shown in figure 6.14. The respective heights are 8.5m, 4.2 m and 1.6m, and these are used for test-points (TP's) one, two and three which are labelled TP1, TP2, and TP3. TP1 and TP3 is $15-20$ m away from each other and TP1 and TP2 is 5 m away from each other. TP3 is around $20-25$ m away from the berm. RTA gain is removed from the measuring results and the first set of figures include the measurements at each transmitting point with the three distances behind the berm.

The propagation of the pulse over the berm greatly changes with the respective heights of the transmitter and how the pulses diffract across the berm. There are clear nulls from 600 MHz to

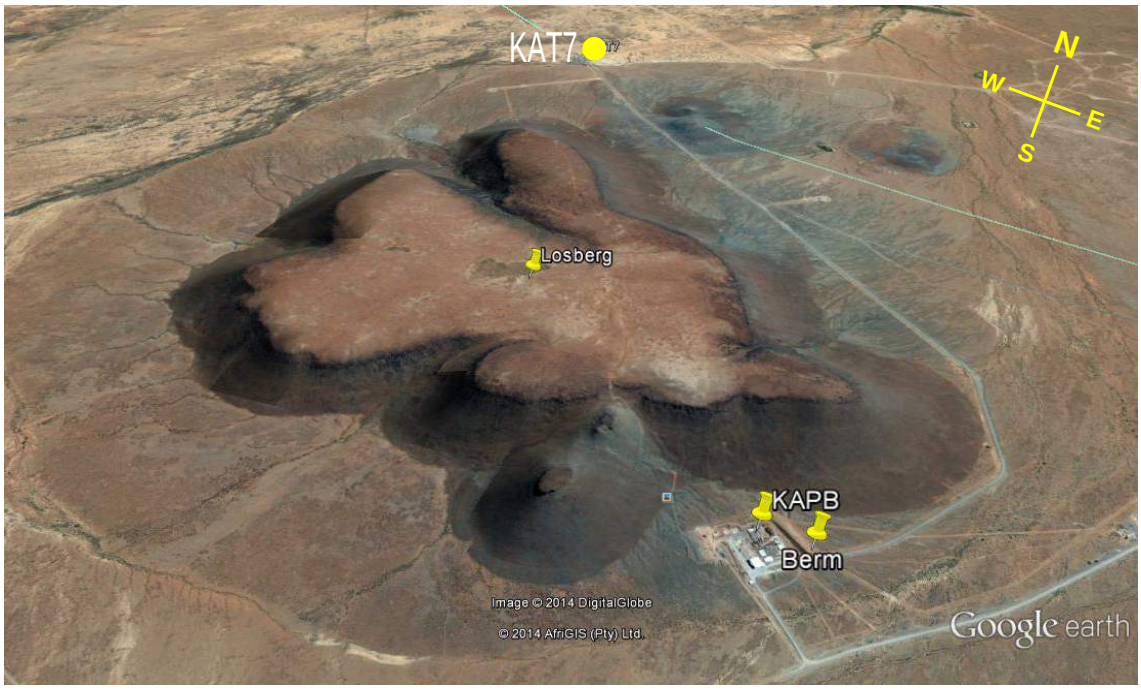

Figure 6.13: Karoo array processor building, berm and Losberg in perspective with KAT7.

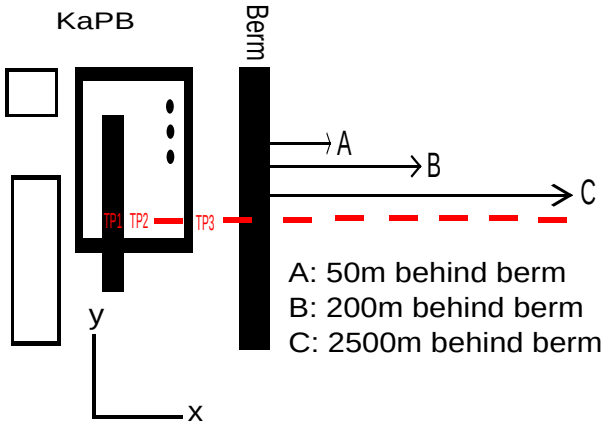

(a) Top view.

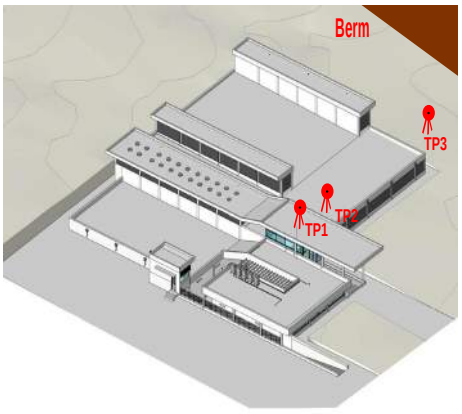

(b) 3D view of the KAPB.

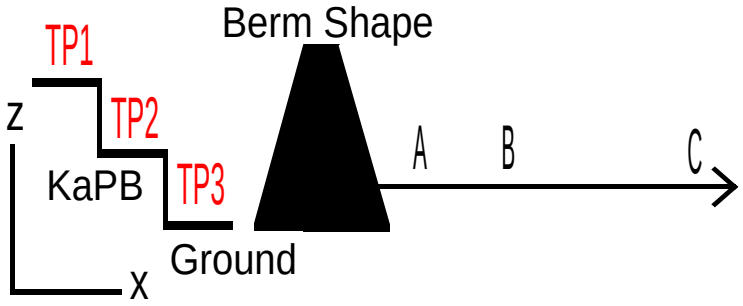

(c) Side view.

Figure 6.14: Berm measurement configuration.

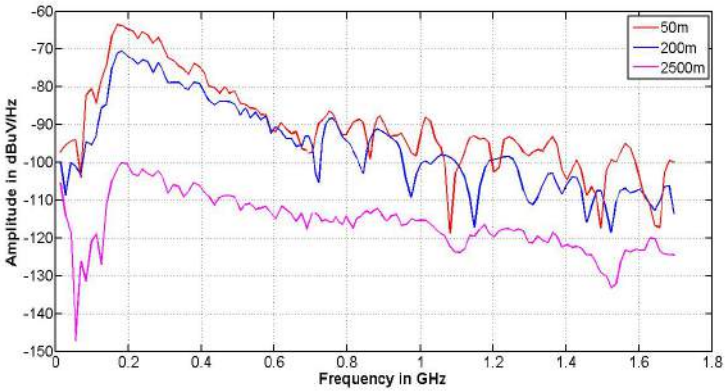

(a) Measurement of berm attenuation at TP1.

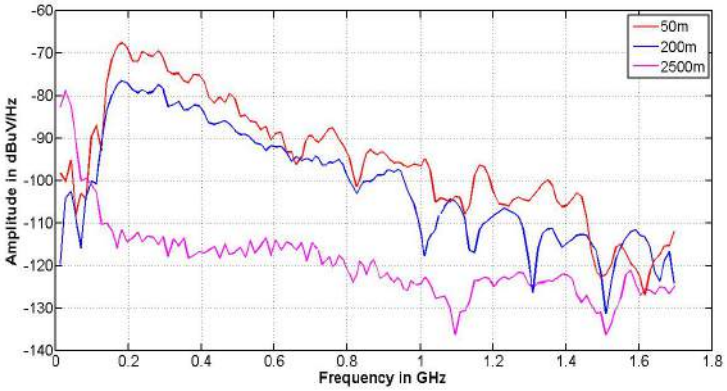

(b) Measurement of berm attenuation at TP2.

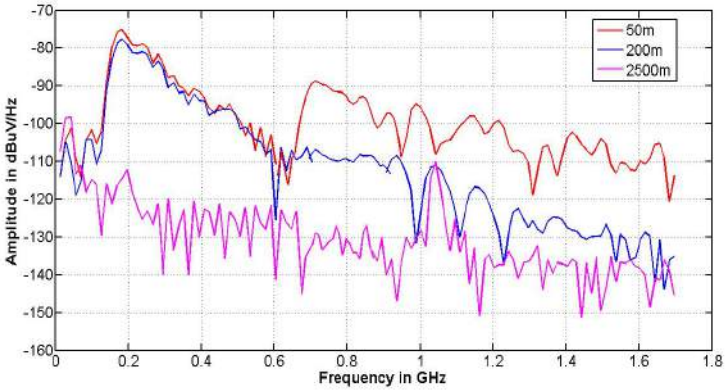

(c) Measurement of berm attenuation at TP3.

Figure 6.15: Measurement of berm attenuation with the IRA at all TP's and RTA at the different distances behind the berm.

1.7 GHz at 50 m and 250 m away from the berm, for each TP. These nulls originate from the diffracted pulse over the edge of the berm, which called knife-edge diffraction. Knife-edge diffraction changes with frequency, or more specifically wavelength and is explained by *Huygens-Fresnel* principle. The nulls that are formed in the spectrum is where the energy of the pulse is extremely low at that specific location after the point of diffraction. The nulls will shift in frequency as the receiver is changed to a different measuring points, which can be seen from all the TPs at 50 m and 250 m away from the berm. These nulls are mostly seen at small distances away from the berm. At 2500 m the nulls are further apart and only one or two nulls is indicated at these measuring distances. An interesting result is seen in figure 6.15c with the IRA on the ground. If the 50 m and 200 m results are compared, they align almost perfectly over the first band of the spectrum, but they have a 15 dB - 20 dB difference from band two and three of RTA. A reason for this can be explained by the following. Due to longer wavelengths at lower frequencies and because the IRA is placed on the ground and close to the berm, these longer wavelengths diffract differently across the berm. With the receiving antenna at 50 m, thus close to the berm, the longer wavelengths can be in such away that the receiving antenna is at a null behind the berm, causing the spectral amplitude to be the same as when the antenna is placed at 200 m. After 600 MHz, the wavelengths become short enough to diffract them in such a way, that they propagate into the antenna and are outside the null formed at the lower frequencies.

The shielding of the berm is also tested by comparing all three test points' results at 50 m, 200 m and 2500 m. These results are displayed in figure 6.17. The 50 m measurement is compared to the 100 m gravel road measurement. The total distance between the receiving and transmitting antenna for this configuration was roughly around 100 m. In this figure the berm definitely has some effect of shielding. TP1 is the highest transmitting point and it should be the least attenuated by the berm. At 200 MHz there is a 8 dB difference between the ground measurement and the measurement from TP1. As frequency increases, this difference increases to more than 20 dBs after 1 GHz. From this it can be noted that the berm shielding at the higher frequencies are more than the lower frequencies with the PCB-LPDA 50 m behind the berm. This comparison between the 100 m propagation measurement on ground and the 50 m berm measurement, could only be done for the 50 m berm measurement because the total distance of these measurement were similar. At the 200 m and 2500 m berm measurements, there were no other propagation measurements with similar distances available for comparison. The height of the different TPs still affect measurements and are briefly discussed. As mentioned earlier, the highest transmitting point will be the least attenuated by the berm. As the source is brought closer to ground level, the shielding of the berm increases and this is seen at all the receiving points. The difference between TP1 and TP2 at the 50 m measurement is less than 3 dB from 180 MHz to 300 MHz and thereafter they are roughly the same. The difference between TP1 and TP3 at this measuring point is roughly 15 dB. At the 200 m point, the difference between the three test points at 200 MHz are 6 db for TP1 and TP2 and 8 dB for TP1 and TP3. The difference between TP1 and TP2 becomes smaller as frequency increases and this is caused by the diffraction of the pulse across the berm. The difference between TP1 and TP3 increases by $1-2dBs$, but are mostly the same across the band. A similar response is seen in figure 6.16c.

The overall effect of the transmitting antenna placed at the various heights, shows that the berm has more attenuation on a signal that is propagated closer to ground. As the transmitting source is lifted, the SE of the berm becomes worse. These are preliminary measurements to test the SE of the berm. The SE of the berm has been measured in the FD at distinct frequency points and it is recorded and discussed by my colleague H. Pienaar in [50]. For future experiments specific receiving points closer to the berm, can be measured and compared to measurements at the same distances, without the berm. It can also be compared with the results obtained by H. Pienaar to get a more accurate characterisation of the berm.

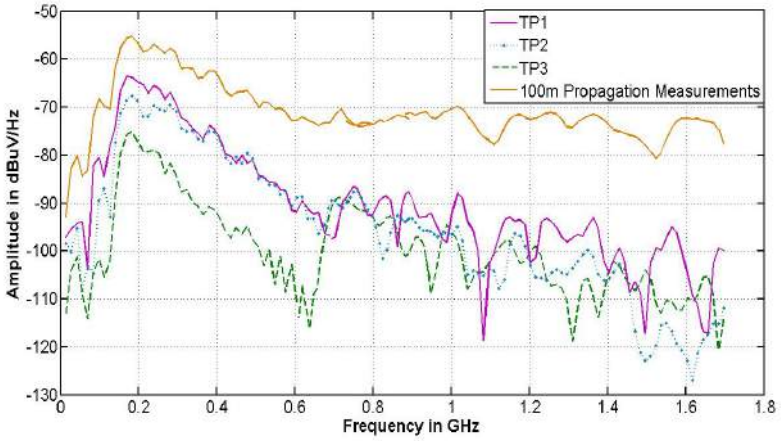

(a) All TPs compared at 50 m.

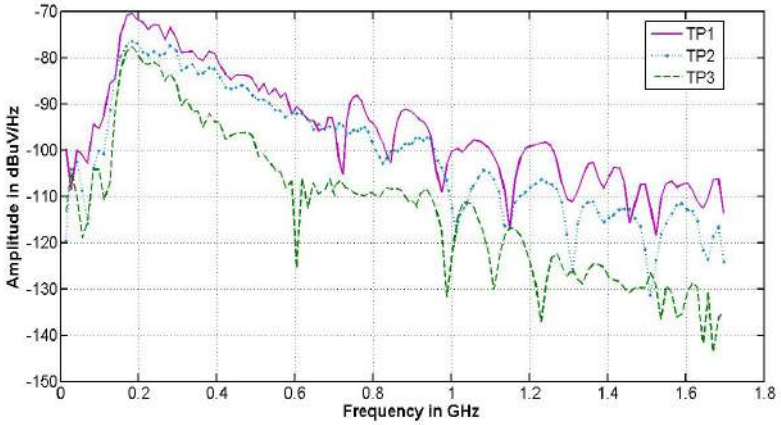

(b) All TPs compared at 200 m.

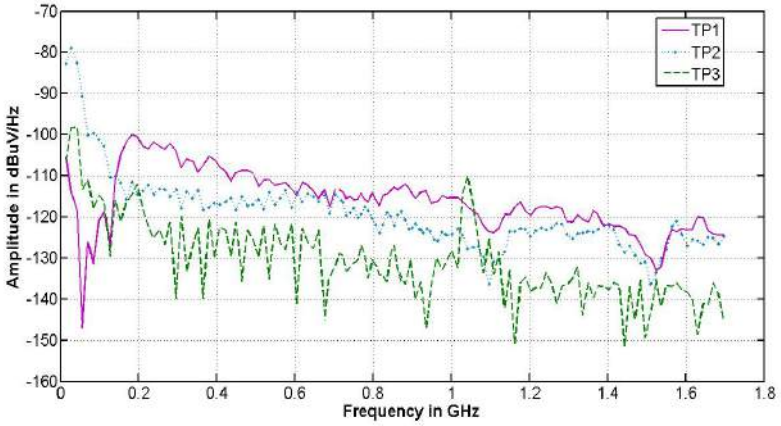

(c) All TPs compared at 2500 m.

Figure 6.16: Berm attenuation compared to three different transmitting heights at certain meters away from the berm.

6.4 Conclusion and recommendations

The IRA and CPS1 PG have been designed for TD metrology in the Karoo environment. In this chapter three experiments were done to test the system and preliminary characterise the environment for the MeerKAT systems. In these measurements the main pulse received on RTA was gated and Fourier transformed to analyse the spectral content of the pulse. The first experiment was part of an antenna calibration measurement to show the directivity of the IRA through an antenna pattern measurement. Because the Karoo environment closely resembles an OATS without nearby scatterers, it was ideal for such a measurement. With the directivity of the antenna known, experiments that were discussed in this chapter can accurately be examined. The CPS1 PG produced a 2.5 kV pulse which was radiated from the IRA and received by a PCB-LPDA antenna and a direct sampling system. The antennas were placed 10 m away from each other at one of the locations reserved for a MeerKAT telescope. The IRA was focused 20°off boresight for the first measurement and was decremented by 5°steps until the two antennas directly faced each other. The results from this measurement agreed with simulated polar pattern results, showed in chapter 4. At the lower frequencies up to 400 MHz, the antenna is isotropic. After 400 MHz the spectral content at the different angles started to differ as the IRA main beam was formed. The measured main beam of the IRA at 1.5 GHz was roughly 20°which also agreed with the half-power beamwidth simulated and shown in figure 4.15. The IRA gain and antenna pattern have not been accurately measured. With this direct sampling system, antenna pattern measurements that are done in FD, can now also be compared with TD results measured with RTA.

The second experiment incorporated the propagation of a TD pulse over three set distances across a gravel road. The receiving antenna was placed 10 m, 100 m and 400 m apart and the measured results were compared to a free-space prediction, calculated using Frii's FSPL equation. This measurement briefly indicated the propagation attenuation of a signal over the Karoo soil. The soil had little to no effect when the antennas were placed 10 m away from each other. At this short distance the pulse is not affected by the attenuation of the environment. The measured and calculated spectrum corresponded with only small discrepancies that originated from ground reflections that is not incorporated in the FSPL calculation. At 100 m and 400 m there were a significant difference between the measured and calculated results. For the 100 m measurement, the Karoo soil attenuated the lower frequencies by 20 dB and this decreased to below 5 dB after 1.2 GHz. A similar response was found with the 400 m measurement. The lower frequencies were attenuated by 25 dB which decreased to 5 dB at the higher frequencies. The Karoo soil definitely affects the attenuation of a signal and from these measurements it was shown that more attenuation occurs at the lower than at the higher frequencies. Another test, that incorporated the Karoo foliage, was also implemented. At 400 m the receiving antenna was placed inside the Karoo vegetation to see the effect of the foliage on the pulse. There were small discrepancies at some frequency points over the band, which indicated that foliage does have a small effect on an EM wave.The foliage causes extra reflections and scattering affects. These small discrepancies originate from these reflections and for this measurement were only seem at distinct frequency points. These were only preliminary measurements which can be investigated further with the use of this system. Changing the heights of both the receiving and transmitting antenna, will affect ground reflections and the overall spectrum. The last propagation measurements was done to test the limits of the transmitting and receiving system. Three long distance propagation measurements, 3.6 km, 4.9 km and 7.3 km, were done. With the dynamic range of RTA, the pulse could be measured at all of theses points, with some limiting factors after 3.6 km in the first band of RTA. The pulse in band one was too low compared to the noise floor, measured at 4.9 km and 7.3 km. The previous measurements showed that the lower frequency band had more propagation attenuation, which also reduced the spectral density of the pulse at these frequencies, making it more difficult to measure.

The last experiment done in this chapter, investigated the SE of a berm built with Karoo soil. The berm is built to reduce RF emission that might radiate from the KAPB. The CPS1 and IRA were

placed at three locations on the KAPB, each with different heights. The receiving antenna with RTA were placed at three distances behind the berm. The first distance was 50 m behind the berm. This measurement was compared with the 100 m propagation measurement mentioned above. The total distance between the transmitting and receiving antenna for this measurement, was around 100 m. As seen in the results, the berm provided 8 dB of shielding at the lower frequencies and this increased to above 15 dB at the higher frequencies. This is also compared with the transmitting antenna at the highest TP, which makes it easier for a pulse to propagate across the berm. As the transmitting antenna was moved to the other TPs, closer to ground and on ground, the shielding of the berm increased. When comparing both of the lower TPs with TP1 (the highest TP), it indicated that the lower frequencies of the berm provided more shielding than the higher frequencies. One of the reason for this ,as can be seen in the results, is related to Huygens-Fresnel principle of knife-edge diffraction. The longer wave lengths of the lower frequency content, diffract differently across the edge of the berm and because of its longer wavelengths, it was less affected. At the higher frequencies, with smaller wavelengths, the pulse is more attenuated and the berm significantly affects the pulse. At 50 m and 200 m for all of the TPS, the effect of knife-edge diffraction, with different nulls in the spectrum, are shown. The focus for this study was designing a TD signal for measurements in the Karoo. The effects of propagation and knife-edge diffraction are only shown, but not investigated. Due to the fact that this was only preliminary measurements to test the system, ground reflections and reflections from surrounding scatters are also not analysed. The environment around the KAPB is complex and, because the IRA has an isotropic pattern at the lower frequencies, reflections from nearby assembly and pedestal shed might affect these measurements. The berm definitely provides some sort of shielding which is increased when the transmitting source is at ground level. Raising the height of the transmitting source marginally reduces the SE effectiveness. For future experiments the antenna can be placed at the same heights and measured at more distances behind the berm. The same measurements should also be done without the berm, in order to accurately determine the SE effectiveness of the berm over a large spectrum. Knife-edge diffraction can also be studied by implementing this system and because this system covers a large band, diffraction at different frequencies can be analysed much quicker. Previous measurements were done in the FD. Incorporating the TD can cover limitations experienced in the FD, such as faster measurements to cover a large band. Pictures of the berm measurements are shown in the figures below.

(a) Transmitting side of the Berm.

(b) Receiving side of the Berm.

Figure 6.17: Panoramic pictures of the berm measurements and KAPB environment.

Chapter 7

Conclusion and recommendations

With the SKA entering into a significant phase of the project, multiple tests are done to ensure the best-possible operation of the telescopes. The ongoing development of TD and FD systems for metrology has strengthened this field. This opens a number of opportunities for future work related to improving the EM quietness. This can be done by characterising the environment for the SKA. A low electromagnetic background noise is essential for the SKA and therefore identifying RFI and characterising the environment are pivotal to ensure the safety of the telescopes. The telescopes are extremely sensitive and any RFI in the surrounding environment may cause the receivers to fail. In this study a TD system was developed to assist with the characterisation of the Karoo environment. Propagation measurements over distance were briefly investigated to characterise the propagation attenuation in the Karro. The SE of a berm built by soil was measured and the results were briefly discussed. The system that was developed consists of a fast-rising impulse generator source that is coupled to an impulse radiating antenna. The PG was designed by implementing avalanche breakdown of transistors and a SRD to sharpen the leading edge of the pulse. This chapter will conclude by briefly discussing the design and optimisation of the PGs, the design simulation and improvements made to the IRA, TD metrology inside the Stellenbosch laboratories and practical metrology in the Karoo. Recommendations for future work related to the SKA will be made.

7.1 Conclusion

Implementing the avalanche phenomenon in transistors allows the creation of fast-rising transients. This increases the current gain of the transistor above unity, which essentially creates the pulse. The pulse was sharpened with a fast-switching PIN diode and controlled through external circuitry around the transistor. Two PGs were built and are currently being used for future RC and TD metrology experiments at Stellenbosch University.

The IRA is modelled as an aperture antenna and solved by implementing the field equivalent principle and combining it with the uniqueness theorem. This allows you to obtain the radiated fields outside a closed area by selecting the sources within. The basic theory behind the IRA is a dirac-delta function that is observed in the far-field of the antenna. This originates from the differentiated step-like transient supplied to the antenna. A Stellenbosch IRA was designed, simulated, built and implemented for TD metrology experiments in the Karoo. The high-gain large-bandwidth of the antenna makes it an ideal antenna for radiating fast-rising impulse-like signals. The IRA had an isotropic response at the lower frequencies, which caused it to radiate in all directions with the same gain. As the frequencies increased, the antenna became more directive and a pulse could be focussed to structures or into specific directions for measurements.This characteristic was tested by implementing an antenna pattern measurement in the Karoo and was later used for boresight propagation measurements and the SE of a berm built by Karoo soil.

This study concluded with TD metrology measurements and the practical implementation of this TD system. These were only preliminary results to test and illustrate the potential of the system for future experiments. A commercial PG was bought from Kentech industries and coupled to the IRA. This PG produced kilovolt pulses with pico-second rise-times that enabled broad spectrum metrology. This is a powerful approach when used in conjunction with the IRA to derive propagation and scattering information from the Karoo environment. The direct sampling system used to receive the pulse had enough dynamic range and this ensured accurate measurements.

It is important to state that ground reflections, reflections and diffraction across the side of the berm and from external objects in the vicinity, can be included in these results which are not de-embedded. The environment around the KAPB is extremely complex and that had some affect in the results displayed throughout this thesis.

7.2 Recommendations

The 30 V PG has been optimised and is well suited for measurements inside the RC. The limitations of the 50 V PG were discussed, but the issue of a distorted pulse which occurred a couple of minutes into the measurement, is still unresolved. The stacking technique significantly increased the amplitude of the pulse and it can be implemented where more dynamic range at the lower frequencies is required. Suggestions to improve and stabilise this PG are to remove the SRD and to optimise the PG circuit, ensuring a stable pulse is produced without the SRD. Once confidence is established in the system without the SRD, the SRD can be included and tested. The current SRD breakdown voltage is 50 V. Designing a new circuit and changing the SRD to a more robust SRD, could potentially solve the problem that is currently in the design because the peak pulse amplitude produced by this PG is the limit of the current SRD. With these PGs, external filters can be designed for pulse shaping. If future projects require a specific shape or spectral content, these filters can be designed to shape and change the pulse.

The IRA is a fairly new antenna. It was designed for high-powered electromagnetics, where large gigavolt pulses were fired at structures for EMC testing and shielding. For the purpose of these measurements, the back-lobe of the IRA was of no importance, as long as an effective pulse was fired into the direction the antenna was facing. For measurements in the Karoo, where RFI can damage radio telescope receivers, a full understanding of the IRA far-field patterns are required. A recommendation for the IRA, is to fully characterise the antenna inside an anechoic chamber large enough for the IRA. Obtaining a better response of the IRA gain and a 360°polar pattern, can lead to changes to improve these responses. A component that can be investigated is the balun of the antenna. The cables used to feed the antenna may have an effect on the back radiation of the antenna, which can be improved by implementing a different balun. An example of this is used in [17]. The PG source is placed at the focal point of the antenna, removing the cables and balun required to feed the antenna. The cables used with the classical balun (implemented in this study) are not protected and therefore some of the energy couples onto the feeding cables which could radiate backwards.

The IRA with the CPS1 allow a different and new method to characterise the Karoo environment. Propagation and shielding measurements were briefly investigated with this system. This can be improved by planning specific measurements with different alterations. For propagation measurements, the antennas can be placed at different heights to determine the effect of ground reflections and it can be compared or used to help obtain propagation models for the Karoo soil. The shielding measurements can also be improved by selecting a wider range of distances behind the berm and comparing it to propagation measurements of the same distances and heights without the berm.

Additional measurements that can be done with the IRA in the Karoo, is to illuminate the KAPB building or one of the MeerKAT pedestals. With a current probe and spectrum analyser, the currents

on the illuminated object can be investigated. This can help with the characterisation of the object and electromagnetically harden it for thunderstorms. This system has a wealth of potential and implementing it in the Karoo environment for these measurements will contribute to current operations within the SKA. TD metrology is currently being investigated and improved. Combining it with the FD can improve the field of metrology and enhance our understanding of complex microwave systems.

Bibliography

[1] C. Bennett and G. Ross, "Time-domain electromagnetics and its applications," *Proceedings of the IEEE*, vol. 66, March 1978.

[2] J. Andriambeloson, P. Wiid, H. Reader, and A. Botha, "Reverberation chamber and current injection cable system study in frequency and time-domains," *Electrical and Electronic Engineering faculty Stellenbosch*, 2012.

[3] H. Reader, *Time-Domain Techniques for Antenna Analysis.* PhD Dissertation, University of Cambridge, September 1985.

[4] A. Botha, "Development of a real-time transient analyser for the SKA," Master's Thesis, Electronic Engineering, University of Stellenbosch.

[5] J. Bousek, "Electronics devices." `http://www.umel.feec.vutbr.cz/alspedit/description/`, November 2006. Visited: Aug 2012.

[6] D. A. Neamen, *Electronic Circuit Analysis and Design.* John Wiley and Sons,Inc, third ed., 2005.

[7] H.S.Schenkel and H. Statz, "Junction transistors with alpha greater than unity," *Proceedings of the IRE*, pp. 360–371, 1955.

[8] S. Miller and J. Ebers, "Alloyed junction avalanche transistors," *The Bell System - Technical Journal*, vol. 34, no. 5, 1955.

[9] M. L. N. Forrest, "Avalanche carrier multiplication in junction transistors and its implications in circuit design," *Journal Brit. I.R.E.*, pp. 429–439, June 1960.

[10] H. Rein and M.Zahn, "Subnanosecond-pulsegenerator with variable pulse width using avalanche transistors," *Electronic Letters*, vol. 11, pp. 21–23, January 1975.

[11] H. Packard, "Pulse and waveform generation with step recovery diodes," *Application Notes.* `http://www.hpmemory.org/an/pdf/an_918.pdf`, Note 918, Visited: September 2013.

[12] J. Andrews, "Picoseconds pulse generation techniques and pulse capabilities," *Picosecond Pulse Labs Application Notes*, November 2008. `www.overunity.com/12736/kapanadze-cousin-dally-free.../115338/`, Note 19, Visited: Aug 2012.

[13] S. Evans and H. Reader, "An impulse generator for antenna measurements in the time-domain," *J. Phys. E: Sci. Instrum.*, vol. 21, pp. 657–660, 1988.

[14] J. Andrews, B. Bell, and E. Baldwin, "Reference flat pulse generator," *National Bureau of Standards Note 1067*, pp. 4–5, October 1983. `www.glkinst.com/test-equipment/manuals/NBS-TN-1067.pdf`, Visited: September 2013.

[15] C. Baum, "Some limiting low-frequency characteristics of a pulse-radiating antenna," *Sensor and Simulations Notes*, October 1968. `http://www.ece.unm.edu/summa/notes/Sensor.html`, Note 65, Visited: September2013.

[16] C. Buchenauer, J. Tyo, and J. Schoenberg, "Aperture efficiencies of impulse radiating antennas," *Ultra-Wideband, Short-Pulse Electromagnetics*, no. 4, pp. 91–108, 1999.

[17] D. Giri, *High Power Electromagnetic Radiators: Nonlethal Weapons and other Application*. Harvard University Press, edition ed., 2004.

[18] L. Bowmen, E. Farr, G. Salo, J. Gwynne, C. Baum, W. Prather, and T. Tran, "Studies of an impulse radiating antenna and a pulse radiating antenna element for SAR and target identification applications," *Sensor and Simulation Notes*, March 2000. `http://www.farr-research.com/biblio.html`, Note 442, Visited: September 2013.

[19] C. A. Balanis, *Antenna Theory, Analysis and Design*. John Wiley and Sons,Inc, Third ed., 2005.

[20] C. Baum, "Radiation of impulse-like transient fields," *Sensor and Simulations Notes*, November 1989. `http://www.ece.unm.edu/summa/notes/Sensor.html`, Note 321, Visited: September2013.

[21] C. Baum and E. Farr, "Impulse radiating antenna, part 1," `http://www.ece.unm.edu/summa/notes/Sensor.html`, Visited:September 2013.

[22] C. Baum, E. Farr, and C. Buchenauer, "Impulse radiating antenna, part 2," `http://www.ece.unm.edu/summa/notes/Sensor.html`, Visited:September 2013.

[23] C. Baum and E. Farr, "Impulse radiating antenna, part 3," `http://www.ece.unm.edu/summa/notes/Sensor.html`, Visited:September 2013.

[24] A. Nicolson, C. Bennett, D. Lamensdorf, and L. Susman, "Applications of time-domain metrology to the automations of broad-band microwave-measurements," *IEEE Transactions on microwave theory and techniques*, vol. MTT-20, pp. 3–9, January 1972.

[25] J. Badenhorst, "Metrology and modeling of high frequency probes," Master's Thesis, Electronic Engineering, University of Stellenbosch, March 2008.

[26] N. Matthysen, "Impulse generator and time-domain metrology," November 2012.

[27] Q. Wu and W.Tian, "Design of electronic circuits of nanosecond impulser based on avalanche transistor," *11th International Conference on Electronic Packaging Technology and High Density Packaging*, 2010.

[28] J. Nilsson and S. Riedel, *Electronic Circuits*. Pearson Education Inc., eight ed., 2008.

[29] C. A. Balanis, *Advanced Engineering Electromagnetics Second Edition*. John Wiley and Sons,Inc, Second ed., 2012.

[30] N. Chadderton, "The ZTX415 avalanche mode transistor, an introduction to characteristics, performance and applications," *Application Note*, January 1996. `www.diodes.com/download/4539`, Note 8, Visited: June 2013.

[31] J. Pellegrin, "Increasing the stability of series avalanche transistor circuits," *Electronic Letters*, September 1969. `www.slac.stanford.edu/cgi-wrap/getdoc/slac-pub-0669.pdf`, Visited: September 2013.

[32] A. Zou, H. Wang, Y. Wang, and D. Cheng, "Nanosecond pulse based on serial connection of avalanche transistors," *10th International Conference on Measuring Technology and Mechatronics Automation*, pp. 753–755, 2010.

[33] L. Bowmen, E. Farr, and D. Lawry, "A dual-polarity impulse radiating antenna," *Sensor and Simulation Notes*, October 2003. http://www.farr-research.com/biblio.html, Note 479, Visited: September 2013.

[34] L. Bowmen, E. Farr, D. Lawry, and J. Tyo, "An ultra-compact impulse radiating antenna," *Sensor and Simulation Notes*, October 2004. http://www.farr-research.com/biblio.html, Note 494, Visited: September 2013.

[35] L. Bowmen, E. Farr, and W. Prather, "A high-voltage cable-fed impulse radiating antenna," *Sensor and Simulation Notes*, December 2005. http://www.farr-research.com/biblio.html, Note 507, Visited: September 2013.

[36] E. Farr and C. Baum, "Pre-pulse associated with the TEM feed of an impulse radiating antenna," *Sensor and Simulation Notes*, March 1992. http://www.farr-research.com/biblio.html, Note 337, Visited: September 2013.

[37] F. Yang and K. Lee, "Impedance of a two-conical plate transmission line," *Sensor and Simulation Notes*, November 1976. Note 221.

[38] J. Qiu, B. Sun, C. Zhang, and N. Wang, "Improved design of the reflector impulse radiating antenna (IRA)," *Ultra-wideband and Ultra-short Impulse Signals*, pp. 15–19, September 2008.

[39] M. Baretela and J. Tyo, "Selective trimming of impulse radiating antenna apertures to increase prompt radiated field," *Sensor and Simulation Notes*, November 2001. Note 461.

[40] M. Abramovitz and I. A. Stegun, *Handbook of Mathematical functions with formulas, Graphs and Mathematical Tables*, vol. 9. National Bureau of Standards, November 1970.

[41] E. Farr and L. Bowen, "The relationship between feed-arm position and input impedance in reflector impulse radiating antennas," *Sensor and Simulation Notes*, April 2005. http://www.farr-research.com/biblio.html, Note 499, Visited: September 2013.

[42] M. Manteghi and Y. Rahmat-Samii, "Improved feeding structures to enhance the performance of the reflector impulse radiating antenna (IRA)," *IEEE Transactions on antennas and propagation*, vol. 54, pp. 823 – 834, March 2006.

[43] L. Bowen and E. Farr, "Results of optimization experiments on a solid reflector IRA," *Sensor and Simulation Notes*, January 2002. http://www.farr-research.com/biblio.html, Note 463, Visited: September 2013.

[44] C. E. Baum, "Configurations of TEM feed for an IRA," *Sensor and Simulation Notes*, April 1991. http://www.ece.unm.edu/summa/notes/Sensor.html, Note 327, Visited: September2013.

[45] D. M. Pozar, *Microwave Engineering*. John Wiley and Sons,Inc, Third ed., 2005.

[46] A. Technologies, "Agilent time-domain analysis using a network analyser," *Application Note 1287-12*. cp.literature.agilent.com/litweb/pdf/5989-5723EN.pdf, Application Note 1287-12, Visited: January 2014.

[47] P. Wiid, K. Palmer, P. van der Merwe, and H. Reader, "A practical 50:1 bandwidth PCB-LPDA antenna for MeerKAT RFI studies," *International Conference on Electromagnetics in Advanced Applications*, 2012.

[48] D. Singh, D. Pande, and A. Bhattacharya, "A new feed for reflector based 100 Ω Impulse Radiating Antenna," *Progress in Electromagnetics research symposium proceedings.*, pp. 1635–1639, March 2012.

[49] P. Wiid, "Lower uncertainty PCB-LPDA antenna measurement on open area test site," *International Conference on Electrmagnetics in Advanced Applications*, 2013.

[50] H. Pienaar, "Karoo array telescope site shielding: Laboratory, computational and multi-copter studies," Master's Thesis, Electronic Engineering, University of Stellenbosch.

Appendix A

Final components and values for the PG and IRA

In this appendix the components for the final designs of both PGs and IRA antenna can be found.

A.1 30 V PG Design components and PCB

The following components and lengths of the 30 V PG is given in the table below. The PCB of the PG is sown in figure A.1.

Component	**Value**	**Component**	**Value**
NPN transistor	2N2369A	Z_{SL}	100 Ω
Step recovery diode	MMD820-T86	Z_O	50 Ω
R_C	120 $k\Omega$	Z_C	21.5 Ω
R_B	75 Ω	V_{CC}	130 V
R_E	1.1 $k\Omega$	V_{BB}	-7.5 V
C_{IN}	33 nF	V_{CC} Feed-through Cap	10 nF - 250 V
C_{OUT}	33 pF	V_{BB} Feed-through Cap	10 nF - 70 V
C_{SL}	1 x 47 nF	L_B	1 μH
	1 x 100 uF		
	1 x 4.7 nF		
Microstrip line lengths			
Shorted line length	16.34 mm	Collector line length	90 mm

Table A.1: Table including all the component values for the 30 V PG.

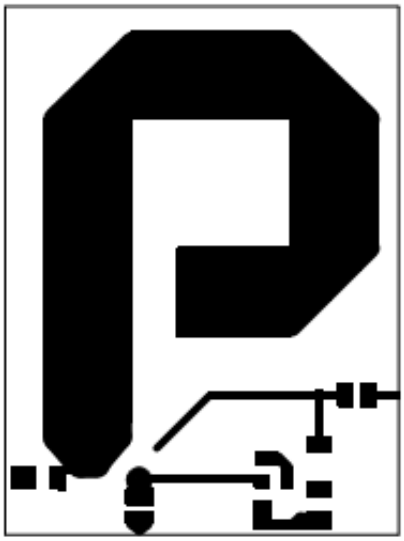

Figure A.1: 30 V PCB scaled 1:1.

A.2 50 V PG Design components and PCB

The following components and lengths of the 50 V stacked PG is given in the table below. The PCB of the PG is sown in figure A.2

Component	**Value**	**Component**	**Value**
NPN transistor	2x 2N2369A	Z_{SL}	100 Ω
Step recovery diode	MMD810-T86	Z_O	50 Ω
R_C	10 $k\Omega$	Z_C	21.5 Ω
R_B	75 Ω	V_{CC}	130 V
R_E	1.1 $k\Omega$	V_{BB}	-7.5 V
C_{IN}	33 nF	V_{CC} Feed-through Cap	10 nF - 250 V
C_{OUT}	33 pF	V_{BB} Feed-through Cap	10 nF - 70 V
C_{SL}	1 x 47 nF	L_B	1 μH
	1 x 100 uF		
	1 x 4.7 nF		
Microstrip line lengths			
Shorted line length	24.5 mm	Collector line length	90 mm

Table A.2: Table including all the component values for the 50 V PG.

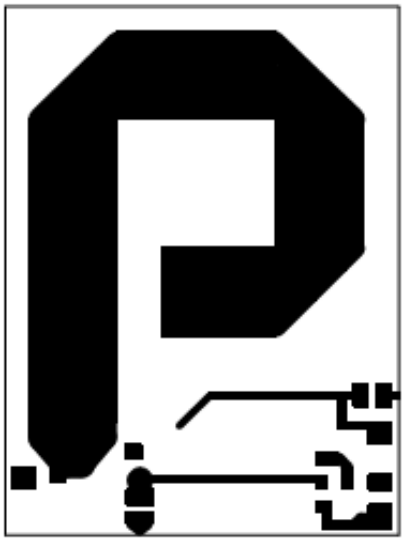

Figure A.2: 50 V PCB scaled 1:1.

A.3 Splitter first and second design

In this section the components, substrate and PCB of both the splitters are given. Table A.3 contain all the components, substrate characteristics and the scaled PCBs are shown in figure A.3.

Component	**Value**
Substrate: ϵ_r	3.55
Electrical length (tand)	0.0027
height (h)	3.048 mm
Width (50Ω) line	6.9246 mm
Width (75Ω) line	3.3449 mm
N-type panel mount connectors	2x 75 Ω
	1x 50 Ω

Table A.3: Components and characteristics of splitter.

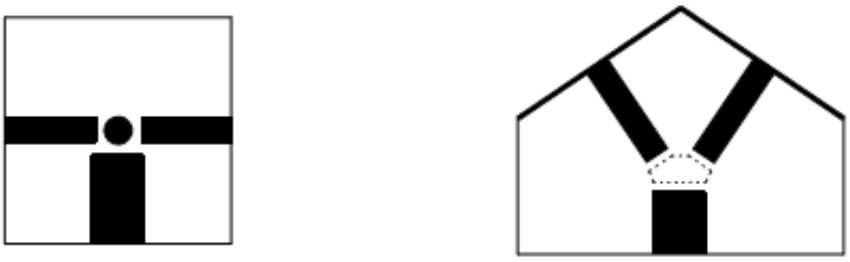

Figure A.3: PCB of both the splitters scaled 1:1.

Appendix B

Matlab code for calculations, figures and measuring equipment

B.1 Pulse generators

B.1.1 Desired pulse with increase in spectrum

```
%Multiplication of Real Part ALone

%Skripsie
%Lift spectrum by 10dbv
for n = 1:2049
    X_Amp_skripsie_10dbinc(1,n)= X_Amp_skripsie(1,n)*sqrt(10);%power
end
for n = 1:4096
     X_skripsie_10dbinc(1,n)= real(X_skripsie(1,n))*sqrt(10)+(j*imag(X_skripsie(1,n)
         ));%volts
end

%JAA PG
%Linear increase real and imag
f = [[1:1:100],zeros(1,3896),[100:-1:1]];
for n = 1:1:2049
    X_Amp_JAA_linearinc_a(1,n)= X_Amp_JAA(1,n)*(10^(10e-3*f(1,n)));%power
    X_Amp_JAA_linearinc_b(1,n)= X_Amp_JAA(1,n)*(10^(15e-3*f(1,n)));%power
end
for n = 1:1:4096
    X_JAA_linearinc_a(1,n)= real(X_JAA(1,n))*(10^(10e-3*f(1,n)))+(j*imag(X_JAA(1,n))
        );%power
    X_JAA_linearinc_b(1,n)= real(X_JAA(1,n))*(10^(15e-3*f(1,n)))+(j*imag(X_JAA(1,n))
        );%power
end
```

B.1.2 Calculating collector line and shorted line lengths and widths

```
%Plot Capacitance of microstrip line to width

Er = 3.38;
d = 1.524e-3;
t = 17e-6;
c = 299792458;
W100 = 0.888799;
W = [0.0017:2.1754e-004:0.0141];
Eeff100 = (Er+1)/2 + (Er-1)/(2*sqrt(1 + (12*d/W100)));
R = [75:-1:18];

 for n = 1:58
       Eeff(1,n) = (Er+1)/2 + (Er-1)/(2*sqrt(1 + (12*d/W(1,n))));
       Cl(1,n) = (2.64e-11*(1.41+Er))/log(5.98*d/((0.8*W(1,n))+t));
       Zc(1,n) = 120*pi/sqrt(Eeff(1,n))/(W(1,n)/d + 1.393 + (0.667*log(W(1,n)/d + 1
           .444)))
 end

% Plot data
a = 1;
figure(a)

%Figure Maximise
set(a, 'PaperPositionMode', 'auto')
set(a,'units','normalized','outerposition',[0 0 1 1]);

plot(Zc, Cl*10^12/1000,'-b','LineWidth',2);
xlabel ('Microstrip line impedance','Fontweight','b');
ylabel ('Capacitance per unit length (pF/mm)','Fontweight','b');
title ('Capacitance of microstrip line over impedance','Fontweight','b')
grid on;

%Set all lines widths
set(gca,'LineWidth',2)
%Set all text size on figure
set(findall(a, '-property', 'FontSize'), 'FontSize', 18)

% Plot data
a = 2;
figure(a)

%Figure Maximise
set(a, 'PaperPositionMode', 'auto')
set(a,'units','normalized','outerposition',[0 0 1 1]);

plot(W*10^3, Cl*10^12/1000,'-r','LineWidth',2);
xlabel ('Microstrip line width (mm)','Fontweight','b');
ylabel ('Capacitance per unit length (pF/mm)','Fontweight','b');
title ('Capacitance of microstrip line over width of line','Fontweight','b')
grid on;

%Set all lines widths
set(gca,'LineWidth',2)
%Set all text size on figure
set(findall(a, '-property', 'FontSize'), 'FontSize', 18)

%speed of em wave on microstrip line and length of a line
timerise = 400e-12/2;          %400ps/2 because wave travels there and back!
v100 = c/sqrt(Eeff100);
SL = timerise*v100*100      %length of shorted line in cm
```

B.2 IRA

B.2.1 Calculating size of conical plate parameters

```
%Calculating conical parameters from diameter and depth of dish

% F_D = 0.4;
% D = 0.46;
% F = D*F_D;

D = 0.68; %Diameter
H = 0.290 %Depth

F = 0.34265350877193%(D^2)/(16*H)
H_CTM = (D^2)/(16*F)

no = 377;
Zc = 360;

fg = Zc/no;
i_fg = 1/fg

%for Zc = 400 m = 0.56737
%for Zc = 200 m = 0.04532
%for Zc = 300 m = 0.272
%fpr Zc = 366 m = 0.44 (give or take)
m = 0.272;
k = m^(0.5);

B0 = atand (1/((2*F/D)-(1/(8*F/D))))
B1 = 2*atand (sqrt(k)*tand(B0/2))
B2 = 2*atand (tand(B1/2)/k)
b0 = D/2

b1 = tand(B1/2)/tand(B0/2)*b0
b2 = tand(B2/2)/tand(B0/2)*b0

b0check = sqrt(b1*b2)
```

B.3 Metrology

B.3.1 Pulses on measuring systems - reading files from figures

```
clear all;
close all ;
%HP54750A PULSE
%%%%%%%%%%%%%%%%%%%%%%%%%%%%%%%%%%%%%%%%%%%%%%%%%%%%%%%%%%%%%%%%%%%%%%%%%%%%%%%

% Load figure file
h=hgload('Pulse_Noschottky_33pf.fig');

% find figure file data handle
get(h);
ch=get(h,'Children');
l=get(ch,'Children');

% Read Data
t = get(l,'Xdata');
```

```
Pulse_Amp =get(l,'Ydata').*10^(45/20);


%Yokogawa PULSE
%%%%%%%%%%%%%%%%%%%%%%%%%%%%%%%%%%%%%%%%%%%%%%%%%%%%%%%%%%%%%%%%%%%%%%

% Load figure file
h=hgload('Yokogawa\Better_Focused_PG_Pulse.fig');

% find figure file data handle
get(h);
ch=get(h,'Children');
l=get(ch,'Children');

% Read Data
t_yok = get(l,'Xdata')*10^-9;
Pulse_Amp_yok =get(l,'Ydata');


%RATTY PULSES
%%%%%%%%%%%%%%%%%%%%%%%%%%%%%%%%%%%%%%%%%%%%%%%%%%%%%%%%%%%%%%%%%%%%%%
% Load figure file
h=hgload('NM_Pulse_RATTY1.fig');

% find figure file data handle
get(h);
ch=get(h,'Children');
l=get(ch,'Children');

% Read Data
t_ratty1 = get(l,'Xdata');
Pulse_Amp_ratty1 = get(l,'Ydata');


% Load figure file
h=hgload('NM_Pulse_RATTY2.fig');

% find figure file data handle
get(h);
ch=get(h,'Children');
l=get(ch,'Children');

% Read Data
t_ratty2 = get(l,'Xdata');
Pulse_Amp_ratty2 = get(l,'Ydata');

% Plot data
%%%%%%%%%%%%%%%%%%%%%%%%%%%%%%%%%%%%%%%%%%%%%%%%%%%%%%%%%%%%%%%%%%%%%%

a = 1;
figure(a)

%Figure Maximise
set(a, 'PaperPositionMode', 'auto')
set(a,'units','normalized','outerposition',[0 0 1 1]);

subplot(2,2,1)
plot(t*10^6,Pulse_Amp,'LineWidth',2);
title('Time Domain Pulse from HP54750A','fontweight','b');
xlabel('Time (us)','fontweight','b');
ylabel('Amplitude (V)','fontweight','b');
grid on;
%Set all lines widths
set(gca,'LineWidth',2)
```

```
80
81  %Set all text size on figure
82  set(findall(a, '-property', 'FontSize'), 'FontSize', 18)
83
84  subplot(2,2,2)
85  plot(t_yok*10^9,Pulse_Amp_yok,'-r','LineWidth',2);
86  title('Time Domain Pulse from Yokogawa','fontweight','b');
87  xlabel('Time (ns)','fontweight','b');
88  ylabel('Amplitude (V)','fontweight','b');
89  grid on;
90
91  %Set all lines widths
92  set(gca,'LineWidth',2)
93
94  %Set all text size on figure
95  set(findall(a, '-property', 'FontSize'), 'FontSize', 18)
96
97  subplot(2,2,3)
98  plot(t_ratty1*10^6,Pulse_Amp_ratty1,'-c','LineWidth',2);
99  title('Time Domain Pulse from RATTY Band 1','fontweight','b');
100 xlabel('Time (us)','fontweight','b');
101 ylabel('Amplitude (V)','fontweight','b');
102 grid on;
103
104 %Set all lines widths
105 set(gca,'LineWidth',2)
106
107 %Set all text size on figure
108 set(findall(a, '-property', 'FontSize'), 'FontSize', 18)
109
110 subplot(2,2,4)
111 plot(t_ratty2*10^6,Pulse_Amp_ratty2,'-g','LineWidth',2);
112 title('Time Domain Pulse from RATTY Band 2','fontweight','b');
113 xlabel('Time (us)','fontweight','b');
114 ylabel('Amplitude (V)','fontweight','b');
115 grid on;
116
117 %Set all lines widths
118 set(gca,'LineWidth',2)
119
120 %Set all text size on figure
121 set(findall(a, '-property', 'FontSize'), 'FontSize', 18)
122
123 %Saving figure
124 thesis_doc = 'C:\Users\Nardus\Documents\Thesis\Report\contents\Pictures\Chapter4';
125 saveas(a,strcat('TD_Pulse_30V'),'fig');
126 saveas(a,strcat('TD_Pulse_30V'),'jpg');
127 %saveas(a,strcat(thesis_doc,'T_junction_simulation_awr_cst'),'jpg');
128
129 %--------------------------------------------------------------------------
130 % SPECTRUM CALCULATION
131 %--------------------------------------------------------------------------
132 % Find the Next power of 2 from the length of the Pulse data
133 NFFT = 2^nextpow2(length(Pulse_Amp));
134 % Calculate FFT
135 X = fft(Pulse_Amp, NFFT)/length(Pulse_Amp);
136 % Amplitude of the spectrum
137 X_Amp = 2*abs(X(1:length(X)/2+1));
138 % Calculate the Frequency bandwidth
139 dt = (t(length(t)) - t(1))/(length(t)-1); % Sampling time
140 Fs = 1/dt; % Sampling frequency
141 F = Fs/2*linspace(0,1,length(X)/2+1); % Spectrum bandwidth
142 % Plot spectrum
143
```

```
%--------------------------------------------------------------------------
% SPECTRUM CALCULATION dBuV/Hz
%--------------------------------------------------------------------------
T_size = t(length(t)) - t(1);
Amp_dBuVperHz = X_Amp*T_size*1e6;
%

%YOKOGAWA

% Find the Next power of 2 from the length of the Pulse data
NFFT_yok = 2^nextpow2(length(Pulse_Amp_yok));
% Calculate FFT
X_yok = fft(Pulse_Amp_yok, NFFT_yok)/length(Pulse_Amp_yok);
% Amplitude of the spectrum
X_Amp_yok = 2*abs(X_yok(1:length(X_yok)/2+1));
% Calculate the Frequency bandwidth
dt_yok = (t_yok(length(t_yok)) - t_yok(1))/(length(t_yok)-1); % Sampling time
Fs_yok = 1/dt_yok; % Sampling frequency
F_yok = Fs_yok/2*linspace(0,1,length(X_yok)/2+1); % Spectrum bandwidth
% Plot spectrum

%--------------------------------------------------------------------------
% SPECTRUM CALCULATION dBuV/Hz
%--------------------------------------------------------------------------
T_size_yok = t_yok(length(t_yok)) - t_yok(1);
Amp_dBuVperHz_yok = X_Amp_yok*T_size*1e6;

Amp_dBuVperHz_yok_int = interp1 (F_yok,Amp_dBuVperHz_yok,F);


%RATTY
% Load figure file
h=hgload('FD_NM_Pulse_RATTY.fig');

% find figure file data handle
get(h);
ch=get(h,'Children');
l=get(ch,'Children');

% Read Data
f1 = get(l,'Xdata');
Amp1 = get(l,'Ydata');

% Plot data
a = 2;
figure(a)

%Figure Maximise
set(a, 'PaperPositionMode', 'auto')
set(a,'units','normalized','outerposition',[0 0 1 1]);

plot(F*1e-9,20*log10(Amp_dBuVperHz),'-b','LineWidth',2);
hold all;
plot(F*1e-9,20*log10(Amp_dBuVperHz_yok_int),'-r','LineWidth',2);
xlim ([0 3]);
grid on;
title('Frequency Domain of 30V Pulse from HP54750A Sampling Oscilloscope ','
    fontweight','b');
xlabel('Frequency (GHz)','fontweight','b');
ylabel('Amplitude (dBuV/Hz)','fontweight','b');
%legend ()

%Set all lines widths
set(gca,'LineWidth',2)
```

```
207
208 %Set all text size on figure
209 set(findall(a, '-property', 'FontSize'), 'FontSize', 18)
210
211 %Saving figure
212 thesis_doc = 'C:\Users\Nardus\Documents\Thesis\Report\contents\Pictures\Chapter4';
213 saveas(a,strcat('FD_Pulse_30V'),'fig');
214 saveas(a,strcat('FD_Pulse_30V'),'jpg');
```

B.3.2 Reading HDF5 Files

```
1  %Processing Old HDF5 files
2  clc;
3  clear all;
4  close all;
5
6
7  %%%% HDF5 FILENAME
8  Filename = {'Extras\Direct_pulse\band1direct.time.h5'; %1
9              'Extras\Direct_pulse\band2direct.time.h5'; %2
10             'Extras\Direct_pulse\band3direct.time.h5'; %3
11             'Extras\Direct_pulse\band4direct.time.h5'}; %4
12 %            EXternal Atten 103
13
14
15 % Load figure file ATTENUATOR
16 h=hgload('atten_30dB.fig');
17
18 % find figure file data handle
19 get(h);
20 ch=get(h,'Children');
21 l=get(ch,'Children');
22
23 % Read Data
24 F_atten =get(l,'Xdata');
25 Atten =get(l,'Ydata');
26
27 % Load figure file ATTENUATOR
28 h=hgload('FFT of CPS1 Pulse dBuV_Hz.fig');
29
30 % find figure file data handle
31 get(h);
32 ch=get(h,'Children');
33 l=get(ch,'Children');
34
35 % Read Data
36 F_CPS1 =get(l,'Xdata');
37 CPS1 =get(l,'Ydata');
38
39 %%%%  LOOPING THROUGH THE FOUR BANDS OF RATTY (3 IF ONLY THREE WERE USED)
40 for x = 1:1:4
41
42 % Measurement attenuation
43 %Tx_atten = input('External attenuation Tx');
44 S = ['Band ',num2str(x), ' Ext: '];
45 band_ext = input(S);
46
47
48 %Ratty Characteristics
49 F = 1800e6;
50 Filenamex = char(Filename(x,1));
```

```
51
52 adc_v_scale_factor = double(hdf5read(Filenamex, '/adc_v_scale_factor'));
53 %system_bandpass = double(hdf5read(Filenamex, '/rf_atten_bandpasses')); %% RATYY
       CALIBRATION FILE (OLD CALIBRATION SETUP)
54 system_bandpass = double(hdf5read(Filenamex, '/system_bandpass')); %% RATYY
       CALIBRATION FILE (NEW CALIBRATION SETUP)
55 system_bandpass_mean  = mean(system_bandpass);
56 rf_atten = double(hdf5read(Filenamex, '/rf_atten')); %% INTERNAL ATTENUATION USED
57 freq = double(hdf5read(Filenamex, '/freqs'));
58 Fs = double(hdf5read(Filenamex, '/sample_clk'));
59
60  if x == 1
61      tmp = double(hdf5read(Filenamex,'/adc_raw'))*(10^(band_ext/20))*
            adc_v_scale_factor;
62  elseif x == 2
63      tmp = double(hdf5read(Filenamex,'/adc_raw'))*(10^(band_ext/20))*
            adc_v_scale_factor;
64  elseif x == 3
65      tmp = double(hdf5read(Filenamex,'/adc_raw'))*(10^(band_ext/20))*
            adc_v_scale_factor;
66  elseif x == 4
67      tmp = double(hdf5read(Filenamex,'/adc_raw'))*(10^(band_ext/20))*
            adc_v_scale_factor;
68  end
69
70
71
72 %%%%%%%%%%%%%%%%%%%%%%%%%%%%%%%
73 %ALL THE PULSES
74 %%%%%%%%%%%%%%%%%%%%%%%%%%%%%%%
75
76
77 T = [0:1:length(tmp)-1]/(Fs);
78 T_size = T(length(T)) - T(1);
79
80 for m = 1:length(tmp(1,:)) - 1
81     data(:,m) = tmp(:,m);
82     [X(:,m),Amp_X(:,m),F] = FFT_Pulse(T,data(:,m));
83 end
84
85  Amp_X_dBuVperHz = Amp_X*T_size*1e6;
86
87 if x == 1
88     F = F;
89     system_bandpass_interp1 = SystemBandPass_Interp(freq,system_bandpass,F,Amp_X);
90  elseif (x == 2) | (x == 3)
91     F = Fs - F;
92 %     if (x == 3)
93 %         F = F(length(F):-1:1);
94 %     end
95     system_bandpass_interp1 = SystemBandPass_Interp(freq,system_bandpass,F,Amp_X);
96  elseif (x == 4)
97     F = Fs + F;
98     system_bandpass_interp1 = SystemBandPass_Interp(freq,system_bandpass,F,Amp_X);
99  end
100
101
102 %%%%%%%%%%%%%%%%%%%%%%%%%%%%%%%%%%%%%%%%%%%%%%%
103 %Getting The Maximum Pulse with two record lengths
104 %%%%%%%%%%%%%%%%%%%%%%%%%%%%%%%%%%%%%%%%%%%%%%%
105
106 [A, index] = max (tmp);
107 [B, col] = max (A);
108 row = index(1, col);
```

```
n=0;

%%%%%%%%%%%%%%%%%% 38.5ns
for M = -25:1:23
   n = n + 1;
   data_max (1,n) = tmp((row+M),col);
   time_max (1,n) = T(1,(row+M));
end

t = [0:1:length(data_max)-1]/(Fs);
[X_max,Amp_X_max,F_max] = FFT_Pulse(t,data_max);
t_size = t(length(t)) - t(1);

Amp_X_dBuVperHz_max = Amp_X_max*t_size*1e6;

if x == 1
    F_max = F_max;
    system_bandpass_interp1_max = SystemBandPass_Interp(freq,system_bandpass,F_max,
        Amp_X_max);
 elseif (x == 2) | (x == 3)
    F_max = Fs - F_max;
%     if (x == 3)
%         F_max = F_max(length(F_max):-1:1);
%     end
    system_bandpass_interp1_max = SystemBandPass_Interp(freq,system_bandpass,F_max,
        Amp_X_max);
 elseif (x == 4)
    F_max = Fs + F_max;
    system_bandpass_interp1_max = SystemBandPass_Interp(freq,system_bandpass,F_max,
        Amp_X_max);
end

%%%%%%%%%%%%%%%%%% 90ns
for M = -25:1:155
   n = n + 1;
   data_maxb (1,n) = tmp((row+M),col);
   time_maxb (1,n) = T(1,(row+M));
end

tb = [0:1:length(data_maxb)-1]/(Fs);
[X_maxb,Amp_X_maxb,F_maxb] = FFT_Pulse(tb,data_maxb);
t_sizeb = tb(length(tb)) - tb(1);

Amp_X_dBuVperHz_maxb = Amp_X_maxb*t_sizeb*1e6;

if x == 1
    F_maxb = F_maxb;
    system_bandpass_interp1_maxb = SystemBandPass_Interp(freq,system_bandpass,F_maxb
        ,Amp_X_maxb);
 elseif (x == 2) | (x == 3)
    F_maxb = Fs - F_maxb;
%     if (x == 3)
%         F_maxb = F_maxb(length(F_maxb):-1:1);
%     end
    system_bandpass_interp1_maxb = SystemBandPass_Interp(freq,system_bandpass,F_maxb
        ,Amp_X_maxb);
 elseif (x == 4)
    F_maxb = Fs + F_maxb;
    system_bandpass_interp1_maxb = SystemBandPass_Interp(freq,system_bandpass,F_maxb
        ,Amp_X_maxb);
end


%%%%%%%%%%%%%%%%%%%%%%%%%%%%%%%%%%%%%%%%%%%%
```

```
%Taking the 3rd Pulse
%%%%%%%%%%%%%%%%%%%%%%%%%%%%%%%%%%%%%%%%%%%%%%%
[A, col] = max (tmp(:,3));
n=0;
%time = T(2)-T(1);

for M = -25:1:50
   n = n + 1;
   data_3 (1,n) = tmp((col+M),3);
   time_3 (1,n) = T(1,(col+M));

end

t_3 = [0:1:length(data_3)-1]/(Fs);
[X_3,Amp_X_3,F_3] = FFT_Pulse(t,data_3);
t_size_3 = t_3(length(t_3)) - t_3(1);

Amp_X_dBuVperHz_3 = Amp_X_3*t_size_3*1e6;

 if x == 1
    F_3 = F_3;
    system_bandpass_interp1_3 = SystemBandPass_Interp(freq,system_bandpass,F_3,
        Amp_X_3);
 elseif (x == 2) | (x == 3)
    F_3 = Fs - F_3;
%     if (x == 3)
%         F_3 = F_3(length(F_3):-1:1);
%     end
    system_bandpass_interp1_3 = SystemBandPass_Interp(freq,system_bandpass,F_3,
        Amp_X_3);
 elseif (x == 4)
    F_3 = Fs + F_3;
    system_bandpass_interp1_3 = SystemBandPass_Interp(freq,system_bandpass,F_3,
        Amp_X_3);
 end


%%%%%%%%%%%%%%%%%%%%%%%%%%%%%%%%%%%%%%%%%%%%%%%
%Average of all pulses with 2 record lenghts
%%%%%%%%%%%%%%%%%%%%%%%%%%%%%%%%%%%%%%%%%%%%%%%
v = 0;
for b = 1:length(tmp(1,:)) - 1

    [C, col] = max (tmp(:,b));
    n=0;

    %time = T(2)-T(1);
    if (col > 25)&(col < 8142)
        v = v + 1;
    for V = -25:1:23
        n = n + 1;
        data_avg (n,v) = tmp((col+V),b);
        time_avg (n,v) = T(1,(col+V));
    end
    end
end

t1 = [0:1:length(data_avg)-1]/(Fs);

for a = 1:1:v
    [X_avg(:,a),Amp_X_avg(:,a),F_avg] = FFT_Pulse(t1,data_avg(:,a));
end
    t_size = t1(length(t1)) - t1(1);
    Amp_X_dBuVperHz_avg = Amp_X_avg*t_size*1e6;
```

```
228
229   if x == 1
230     F_avg = F_avg;
231     system_bandpass_interp1_avg = SystemBandPass_Interp(freq,system_bandpass,F_avg,
          Amp_X_avg);
232  elseif (x == 2) | (x == 3)
233     F_avg = Fs - F_avg;
234 %     if (x == 3)
235 %         F_avg = F_avg(length(F_avg):-1:1);
236 %     end
237     system_bandpass_interp1_avg = SystemBandPass_Interp(freq,system_bandpass,F_avg,
          Amp_X_avg);
238  elseif (x == 4)
239     F_avg = Fs + F_avg;
240     system_bandpass_interp1_avg = SystemBandPass_Interp(freq,system_bandpass,F_avg,
          Amp_X_avg);
241  end
242
243 for e = 1:length(Amp_X_avg(:,1))
244    avg_AMP_X (1,e) = mean(20*log10(Amp_X_dBuVperHz_avg(e,:)));
245    system_bandpass_interp1_avg_mean (1,e) = mean (system_bandpass_interp1_avg(e,:));
246 end
247
248 %%%%%%%%%%%%%%%%%%%%%%%%% 90ns
249 v = 0;
250 for b = 1:length(tmp(1,:)) - 1
251
252     [C, col] = max (tmp(:,b));
253     n=0;
254
255     %time = T(2)-T(1);
256     if (col > 25)&(col < 8037)
257         v = v + 1;
258     for V = -25:1:155
259         n = n + 1;
260         data_avgb (n,v) = tmp((col+V),b);
261         time_avgb (n,v) = T(1,(col+V));
262     end
263     end
264 end
265
266 t1b = [0:1:length(data_avgb)-1]/(Fs);
267
268 for a = 1:1:v
269     [X_avgb(:,a),Amp_X_avgb(:,a),F_avgb] = FFT_Pulse(t1b,data_avgb(:,a));
270 end
271     t_sizeb = t1b(length(t1b)) - t1b(1);
272     Amp_X_dBuVperHz_avgb = Amp_X_avgb*t_sizeb*1e6;
273
274   if x == 1
275     F_avgb = F_avgb;
276     system_bandpass_interp1_avgb = SystemBandPass_Interp(freq,system_bandpass,F_avgb
          ,Amp_X_avgb);
277  elseif (x == 2) | (x == 3)
278     F_avgb = Fs - F_avgb;
279 %     if (x == 3)
280 %         F_avgb = F_avgb(length(F_avgb):-1:1);
281 %     end
282     system_bandpass_interp1_avgb = SystemBandPass_Interp(freq,system_bandpass,F_avgb
          ,Amp_X_avgb);
283  elseif (x == 4)
284     F_avgb = Fs + F_avgb;
285     system_bandpass_interp1_avgb = SystemBandPass_Interp(freq,system_bandpass,F_avgb
          ,Amp_X_avgb);
```

```
 end

for e = 1:length(Amp_X_avgb(:,1))
   avg_AMP_Xb (1,e) = mean(20*log10(Amp_X_dBuVperHz_avgb(e,:)));
   system_bandpass_interp1_avg_meanb (1,e) = mean (system_bandpass_interp1_avgb(e,:)
       );
end

%-------------------------------------------------------------------------
%
%                            Cable Loss Calclation
%
%-------------------------------------------------------------------------

l = input('Enter length of cable used during measurements: ');

cable_loss_interp_max = interp1 ((freqcables*1e9), CableLoss, F_max);
cable_loss_interp_maxb = interp1 ((freqcables*1e9), CableLoss, F_maxb);
cable_loss_interp_avg = interp1 ((freqcables*1e9), CableLoss, F_avg);
cable_loss_interp_avgb = interp1 ((freqcables*1e9), CableLoss, F_avgb);

Atten_interp_max = interp1(F_atten, Atten,F_max);
Atten_interp_maxb = interp1(F_atten, Atten,F_maxb);
Atten_interp_avg = interp1(F_atten, Atten,F_avg);
Atten_interp_avgb = interp1(F_atten, Atten,F_avgb);

CPS1_interp = interp1 ((F_CPS1*1e9), CPS1,F_max);

%%%%%%%%%%%%%%%%%%%%%%%%%%%%%%%%%%%%%%%%%%%%%%%%%%%%%%%%%%%%
% PLOTs
%%%%%%%%%%%%%%%%%%%%%%%%%%%%%%%%%%%%%%%%%%%%%%%%%%%%%%%%%%%%
%%%%%%%%%%%%%%%%%%%%%%%%%%%%%%%%%%%%%%%%%%%%%%%%%%%%%%%%%%%%
%FIFURE 1
%%%%%%%%%%%%%%%%%%%%%%%%%%%%%%%%%%%%%%%%%%%%%%%%%%%%%%%%%%%%
% Plot data
a = 1;
figure(a)

%Figure Maximise
set(a, 'PaperPositionMode', 'auto')
set(a,'units','normalized','outerposition',[0 0 1 1]);

subplot(2,1,1);
plot (T*1e6,data/(10^(system_bandpass_mean/20)), '-b','LineWidth',0.5);
hold all
plot (time_max*1e6,data_max/(10^(system_bandpass_mean/20)), '-r','LineWidth',2);
plot (time_3*1e6,data_3/(10^(system_bandpass_mean/20)), '-c','LineWidth',2);
xlabel ('Time (us)','fontweight','b');
ylabel ('Amplitude (V)','fontweight','b');
title('Pulses Captured by RTA (RAW)','fontweight','b');
%legend ('All the Pulses','Maximum Pulse','Random 3rd pulse in .hdf5 file','Averaged
    Pulse');
grid on;


%Set all lines widths
set(gca,'LineWidth',2)

%Set all text size on figure
set(findall(a, '-property', 'FontSize'), 'FontSize', 18)

%%%%%%%%%%%%%%%%%%%%%%%%%%%%%%%%%%%%%%%%%%%%%%%%%%%%%%%%%%%%%%%%%%%%%%%%%%%
%FIFURE 2
%%%%%%%%%%%%%%%%%%%%%%%%%%%%%%%%%%%%%%%%%%%%%%%%%%%%%%%%%%%%%%%%%%%%%%%%%%%
```

```
% Plot data
% a = 2;
% figure(a)
%
% %Figure Maximise
% set(a, 'PaperPositionMode', 'auto')
% set(a,'units','normalized','outerposition',[0 0 1 1]);
subplot(2,1,2);
plot(F*1e-9,(20*log10(Amp_X_dBuVperHz)-system_bandpass_interp1), '-b','LineWidth',0.5);
hold all;
plot (F_max*1e-9,(20*log10(Amp_X_dBuVperHz_max) - system_bandpass_interp1_max'), '-r','LineWidth',2);
plot (F_3*1e-9,(20*log10(Amp_X_dBuVperHz_3) - system_bandpass_interp1_3'), '-c','LineWidth',2);
plot(F_avg*1e-9,(avg_AMP_X-system_bandpass_interp1_avg_mean), '-g','LineWidth',2);
grid on;
xlabel('Frequency in GHz','fontweight','b');
ylabel('Amplitude in dBuV/Hz','fontweight','b');
title ('Spectrum of RTA pulses (RAW)','fontweight','b');
%legend ('All the Pulses','Maximum Pulse','Random 3rd pulse in .hdf5 file','Averaged Pulse');


%Set all lines widths
set(gca,'LineWidth',2)

%Set all text size on figure
set(findall(a, '-property', 'FontSize'), 'FontSize', 18)

%%%%%%%%%%%%%%%%%%%%%%%%%%%%%%%%%%%%%%%%%%%%%%%%%%%%%%%%%%%%%%%%%%%%%%%%%%%%%%%
%FIFURE 3
%%%%%%%%%%%%%%%%%%%%%%%%%%%%%%%%%%%%%%%%%%%%%%%%%%%%%%%%%%%%%%%%%%%%%%%%%%%%%%%
% Plot data
a = 3;
figure(a)

%Figure Maximise
set(a, 'PaperPositionMode', 'auto')
set(a,'units','normalized','outerposition',[0 0 1 1]);

plot (time_avgb*1e6,data_avgb/(10^(system_bandpass_mean/20)), '-g','LineWidth',2);
hold all
plot (time_avg*1e6,data_avg/(10^(system_bandpass_mean/20)), '-m','LineWidth',2);
plot (time_maxb*1e6,data_maxb/(10^(system_bandpass_mean/20)), '-b','LineWidth',2);
plot (time_max*1e6,data_max/(10^(system_bandpass_mean/20)), '-r','LineWidth',2);
xlabel ('Time (us)','fontweight','b');
ylabel ('Amplitude (V)','fontweight','b');
xlim ([2.04 2.14])
title ('Time-domain of pulses with RTA with two selected lengths.','fontweight','b');
%legend ('Average Pulse 1st null','Average Pulse 2nd null','Max Pulse 1st null','Max Pulse 2nd null');
grid on;

%%%%%%%%%%%%%%%%%%%%%%%%%%%%%%%%%%%%%%%%%%%%%%%%%%%%%%%%%%%%%%%%%%%%%%%%%%%%%%%
%FIFURE 4
%%%%%%%%%%%%%%%%%%%%%%%%%%%%%%%%%%%%%%%%%%%%%%%%%%%%%%%%%%%%%%%%%%%%%%%%%%%%%%%
% Plot data
%Set all lines widths
set(gca,'LineWidth',2)

%Set all text size on figure
set(findall(a, '-property', 'FontSize'), 'FontSize', 18)
```

```
406
407 % Plot data
408 a = 4;
409 figure(a)
410
411 %Figure Maximise
412 set(a, 'PaperPositionMode', 'auto')
413 set(a,'units','normalized','outerposition',[0 0 1 1]);
414
415 plot(F_maxb*1e-9,(20*log10(Amp_X_dBuVperHz_maxb)- (system_bandpass_interp1_maxb' -
        cable_loss_interp_maxb -30 - Atten_interp_maxb)), '-b','LineWidth',2);
416 hold all;
417 plot (F_max*1e-9,(20*log10(Amp_X_dBuVperHz_max) - (system_bandpass_interp1_max' -
        cable_loss_interp_max -30 - Atten_interp_max)), '-r','LineWidth',2);
418 plot(F_avgb*1e-9,(avg_AMP_Xb - (system_bandpass_interp1_avg_meanb -
        cable_loss_interp_avgb -30 - Atten_interp_avgb)), '-g','LineWidth',2);
419 plot(F_avg*1e-9,(avg_AMP_X - (system_bandpass_interp1_avg_mean -
        cable_loss_interp_avg -30 - Atten_interp_avg) ), '-m','LineWidth',2);
420 plot(F_max*1e-9, CPS1_interp, '-k', 'LineWidth',2);
421 grid on;
422 xlabel('Frequency in GHz','fontweight','b');
423 ylabel('Amplitude in dBuV/Hz','fontweight','b');
424 %title ('Spectrum of maximum and average RTA pulses with two selected record lengths
        ','fontweight','b');
425 title ('Spectrum of RTA pulses with selected record lengths, maximum, average and
        CPS1 Calibrated Pulse.','fontweight','b');
426 legend ('Spectrum of Max Pulse (15.5ns)','Spectrum of Max Pulse (90ns)','Spectrum of
         Average Pulse (90ns)','Spectrum of Average Pulse (15.5ns)','CPS1 Calibrated
        Pulse');
427 %legend ('Spectrum of Max Pulse (15.5ns)','Spectrum of Max Pulse (90ns)','Spectrum
        of Average Pulse (90ns)','Spectrum of Average Pulse (15.5ns)');
428
429 %Set all lines widths
430 set(gca,'LineWidth',2)
431
432 %Set all text size on figure
433 set(findall(a, '-property', 'FontSize'), 'FontSize', 18)
434
435 % % Plot data
436 % a = 5;
437 % figure(a)
438 %
439 % %Figure Maximise
440 % set(a, 'PaperPositionMode', 'auto')
441 % set(a,'units','normalized','outerposition',[0 0 1 1]);
442 %
443 % for p = 1:1:length(Amp_X_dBuVperHz_maxb)
444 %
445 % delta_change(1,p) = (20*log10(Amp_X_dBuVperHz_maxb(1,p)) - (
        system_bandpass_interp1_maxb(p,1) - cable_loss_interp_maxb(1,p) -30 -
        Atten_interp_maxb(1,p)))-(avg_AMP_Xb(1,p) - (system_bandpass_interp1_avg_meanb
        (1,p) - cable_loss_interp_avgb(1,p) -30 - Atten_interp_avgb(1,p))+ 1.7);
446 % end
447 % plot (F_maxb*1e-9,delta_change, '-k','LineWidth',2);
448 % grid on;
449 % xlabel('Frequency in GHz','fontweight','b');
450 % ylabel('Amplitude in dB','fontweight','b');
451 % xlim([0 0.8])
452 % title ('Delta change between maximum and average spectrum','fontweight','b');
453 % legend ('Delta Change (Maximum - Average)','Location','SouthEast');
454 %
455 % %Set all lines widths
456 % set(gca,'LineWidth',2)
457 %
```

```
% %Set all text size on figure
% set(findall(a, '-property', 'FontSize'), 'FontSize', 18)

end
```

B.3.2.1 Calculating expected pulse

```
%Karoo Expected Pulse Callibration From CPS1

%--------------------------------------------------------------------------
%
%                                LOAD FILES
%
%--------------------------------------------------------------------------

% Load figure file CPS1 FFT
h=hgload('CPS1Kentech Results\FFT of CPS1 Pulse dBuV_Hz.fig');

% find figure file data handle
get(h);
ch=get(h,'Children');
l=get(ch,'Children');

% Read Data
F =get(l,'Xdata')*1e9;
CPS1_Amp =get(l,'Ydata');

% Load figure file IRA Gain FFT
h=hgload('MeasuredGainsUSAnechoic\MeasuredGainIra.fig');

% find figure file data handle
get(h);
ch=get(h,'Children');
l=get(ch,'Children');

% Read Data
FIra =get(l,'Xdata')*1e9;
IRA_Amp =get(l,'Ydata');

% Load IRA Gain FFT Simulation
IRA_sim_Gain = interp1 (data(:,1), data(:,2),F);

% Load figure file LPDA2 Gain FFT
h=hgload('MeasuredGainsUSAnechoic\MeasuredLPDA2Gain.fig');

% find figure file data handle
get(h);
ch=get(h,'Children');
l=get(ch,'Children');

% Read Data
FLPDA =get(l,'Xdata')*1e9;
LPDA2_Amp =get(l,'Ydata');

close all;

IRA_Gain = interp1(FIra,IRA_Amp,F);
LPDA2_Gain = interp1(FLPDA,LPDA2_Amp,F);

%--------------------------------------------------------------------------
%
```

```
%                              FSPL Calculation
%
%--------------------------------------------------------------------------

R1 = input('Enter the free space distance 1 : ');
R2 = input('Enter the free space distance 2 : ');
R3 = input('Enter the free space distance 3 : ');
N = length(F);

for x = 1:1:N
    FSPL1(1,x) = 20*log10(F(1,x)*10^-6)+20*log10(R1)-27.55;
    FSPL2(1,x) = 20*log10(F(1,x)*10^-6)+20*log10(R2)-27.55;
    FSPL3(1,x) = 20*log10(F(1,x)*10^-6)+20*log10(R3)-27.55;
end

%--------------------------------------------------------------------------
%
%                           Cable Loss Calclation
%
%--------------------------------------------------------------------------

l = input('Enter length of cable used during measurements: ');

CableLoss = [0.02
0.05
0.07
0.09
0.1
0.13
0.15
0.16
0.17
0.18
0.21
0.22
0.22
0.23
0.24
0.32
]*l;

freqcables = [0.01
0.05
0.1
0.15
0.2
0.3
0.4
0.45
0.5
0.6
0.8
0.85
0.9
0.95
1
1.8
];


cable_loss_interp = interp1 ((freqcables*1e9), CableLoss, F);

%--------------------------------------------------------------------------
%
```

```
%                                Attenuation at Tx
%
%--------------------------------------------------------------------------

attenuation = input('Attenuation added at transmitting side: ');


%--------------------------------------------------------------------------
%
%                            Processing Expected FFT
%
%--------------------------------------------------------------------------

for y = 1:1:N
   Expected_FFT1(1,y) = CPS1_Amp(1,y) + IRA_sim_Gain(1,y) + 6 - FSPL1(1,y) -
       cable_loss_interp(1,y) - attenuation;
   Expected_FFT2(1,y) = CPS1_Amp(1,y) + IRA_sim_Gain(1,y) + 6 - FSPL2(1,y) -
       cable_loss_interp(1,y) - attenuation;
   Expected_FFT3(1,y) = CPS1_Amp(1,y) + IRA_sim_Gain(1,y) + 6 - FSPL3(1,y) -
       cable_loss_interp(1,y) - attenuation;
end


figure;
plot (F*1e-9, Expected_FFT1,'-b',F*1e-9,Expected_FFT2,'-r',F*1e-9,(Expected_FFT3),'-
    g',F*1e-9,(CPS1_Amp-cable_loss_interp),'-m',F*1e-9, FSPL1,':b',F*1e-9,FSPL2,':r'
    ,F*1e-9,(FSPL3),':g','LineWidth',2);
title ('Expected FFT');
xlabel('Frequency GHz');
ylabel('Amplitude dBuV/Hz');
%legend('ExpectedPulse','FreeSpaceLoss','TransmittedPulse(2.5kV)')
xlim ([0  2]);
grid on;
```

Appendix C

Data sheet of SRD

Silicon Step Recovery Diodes

AEROFLEX METELICS

Ceramic Packaged

Model	V_{BR} MIN V	C_J MIN pF	C_J MAX pF	τ MIN ns	τ TYP ns	t_t TYP ps	t_t MAX ps	C_P TYP pF	L_P TYP pF	Package
MMD805-E28 / 28X	60	3.1	3.6	80	100	250	300	0.08	0.4	E28 / 28X
MMD805-H20	60	3.2	3.7	80	100	250	300	0.18	0.5	H20
MMD805-T86	60	3.2	3.7	80	100	250	300	0.18	1.0	T86
MMD805-T89	60	3.3	3.8	80	100	250	300	0.25	0.4	T89
MMD805-0805-2	60	3.1	3.6	80	100	250	300	0.06	0.4	0805-2
MMD810-E28 / 28X	50	2.1	2.6	40	70	200	250	0.08	0.4	E28 / 28X
MMD810-H20	50	2.2	2.7	40	70	200	250	0.18	0.5	H20
MMD810-T86	50	2.2	2.7	40	70	200	250	0.18	1.0	T86
MMD810-T89	50	2.3	2.8	40	70	200	250	0.25	0.4	T89
MMD820-E28 / 28X	40	1.4	1.8	30	60	80	100	0.08	0.4	E28 / 28X
MMD820-H20	40	1.5	1.9	30	60	80	100	0.18	0.5	H20
MMD820-T86	40	1.5	1.9	30	60	80	100	0.18	1.0	T86
MMD820-0805-2	40	1.4	1.8	30	60	80	100	0.06	0.4	805-2
MMD830-E28 / 28X	25	0.83	1.1	15	30	60	80	0.08	0.4	E28 / 28X
MMD830-H20	25	0.93	1.2	15	30	60	80	0.18	0.5	H20
MMD830-T86	25	0.93	1.2	15	30	60	80	0.18	1.0	T86
MMD830-0805-2	25	0.81	1.1	15	30	60	80	0.06	0.4	805-2
MMD832-E28 / 28X	20	0.68	0.9	10	15	60	80	0.08	0.4	E28 / 28X
MMD832-H20	20	0.78	1.0	10	15	60	80	0.18	0.5	H20
MMD832-T86	20	0.78	1.0	10	15	60	80	0.18	1.0	T86
MMD832-0805-2	20	0.66	0.88	10	15	60	80	0.06	0.4	805-2
MMD835-E28 / 28X	15	0.58	0.81	10	20	50	70	0.08	0.4	E28 / 28X
MMD835-H20	15	0.62	0.85	10	20	50	70	0.12	0.4	H27
MMD835-T86	15	0.68	0.91	10	20	50	70	0.18	1.0	T86
MMD835-0805-2	15	0.56	0.78	10	20	50	70	0.06	0.4	805-2
MMD837-E28 / 28X	20	0.38	0.51	5	10	50	70	0.08	0.4	E28 / 28X
MMD837-H27	20	0.42	0.55	5	10	50	70	0.12	0.4	H27
MMD837-T86	20	0.48	0.61	5	10	50	70	0.18	1.0	T86
MMD837-0805-2	20	0.36	0.48	5	10	50	70	0.06	0.4	805-2
MMD840-E28 / 28X	15	0.38	0.51	7	15	50	70	0.08	0.4	E28 / 28X
MMD840-H27	15	0.42	0.55	7	15	50	70	0.12	0.4	H27
MMD840-T86	15	0.48	0.61	7	15	50	70	0.18	1.0	T86
MMD840-0805-2	15	0.36	0.48	7	15	50	70	0.06	0.4	0805-2
MMD830-E28 / 28X	14	0.28	0.36	1.0	4.0	30	38	0.08	0.4	E28 / 28X
MMD830-0402	14	0.25	0.32	1.0	4.0	30	38	0.05	0.2	0402
MMD830-0805-2	14	0.26	0.33	1.0	4.0	30	38	0.06	0.4	0805-2
MMD835-E28 / 28X	16	0.25	0.31	1.0	4.0	35	45	0.08	0.4	E28 / 28X
MMD835-T86	16	0.22	0.28	1.0	4.0	35	45	0.05	0.2	0402
MMD835-0805-2	16	0.23	0.29	1.0	4.0	35	45	0.06	0.4	0805-2
MMD845-E28 / 28X	25	0.24	0.31	3.0	8.0	45	58	0.08	0.4	E28 / 28X
MMD845-T86	25	0.21	0.28	3.0	8.0	45	58	0.05	0.2	0402
MMD845-0805-2	25	0.22	0.29	3.0	8.0	45	58	0.06	0.4	0805-2
Test Conditions	I_R = 10 µA	V_R = 6 V F = 1 MHz		I_F = 10 mA I_R = 6 mA Measured at 50% Recovery		I_F = 10 mA V_R = 10 V I_F = 3 mA V_R = 7 V		F = 1 MHz		

Figure C.1: Data sheet of the SRD with biasing currents.

Appendix D

Air breakdown calculations

Electrical breakdown in a dielectric or air is caused when the potential applied across it exceeds the breakdown voltage of that specific material. In this study a 2.5 kV Pulse is propagated through a foam polyethylene (PE) coaxial cable and over a microstrip line. To ensure that electrical breakdown is prohibited, the breakdown limits of the coaxial cable are calculated. In this appendix the equations necessary to calculate the peak power handling of a coax cable will be shown.

D.1 Peak power handling of a coaxial cable

The E-field in a coaxial cable can be calculated by the following equation:

$$E(\rho) = \frac{V_0}{\rho ln(\frac{a}{b})} \tag{D.1.1}$$

where ρ is donated to the radial coordinate system, a and b is the radii of the inner and outer conductor and V_0 is the peak voltage applied to the coaxial cable at the centre conductor. Rearranging this equation for maximum peak voltage.

$$V_{peak} = E_d a ln(\frac{b}{a}) \tag{D.1.2}$$

where E_d is the breakdown strength in $\frac{V}{m}$ for the dielectric inside the coaxial cable. To know the peak power that can be applied to the coaxial cable the following equation can be used.

$$P_{peak} = \frac{V_{peak}^2}{2Z_0} \tag{D.1.3}$$

with the characteristic impedance of a coaxial cable as:

$$Z_0 = \frac{ln(\frac{b}{a})}{2\pi} \frac{\delta_0}{\sqrt{\epsilon_r}} \tag{D.1.4}$$

the peak power of handling of a coaxial cable can be calculated with:

$$P_{peak} = \frac{\pi E_d^2 a^2 ln(\frac{b}{a}) \sqrt{\epsilon_r}}{\delta_0} \tag{D.1.5}$$

where δ_0 is the impedance of free-space (377). All these equations are obtained in [45]. A LMR-400 75 Ω cable is used for the antenna and CPS1 PG. Using equation D.1.5 the peak voltage and power applied to this coaxial cable can be calculated. These values assume the breakdown strength of solid PE ($E_d = 21.7\ MV/m - 50\ MV/m$).

The peak power looks like an extremely large value, but with the foam PE used in the LMR-400-75 the peak power reduces to 10 kW (from the data sheet), because of air filled in the PE. The dielectric

Cable	**Inner Conductor**	**Outer Conductor**	**Peak Voltage**	**Peak Power**
LMR-400-75	1.65 mm	7.39 mm	2 kV – 4.6 kV	460 kW - 2.4 MW

strength of air is much less than PE and when combined the breakdown strength reduces. With these equations the peak voltage and power can be calculated using the dimensions of a coaxial cable.

Appendix E

Pulse generator external measurements

In this appendix all the external test done during the design of the impulse generators will be shown. The SRD was biased at different voltage levels and its effects on the pulse are shown in section E.1. The effect of sampling many pulses over a long record length changes the amplitudes of the pulses sampled. Because there is a limit to the number of samples, the time between samples are increased as the record length is increased. This causes some of the peaks of the pulse to be miss-sampled and reduce the amplitude of the pulse. Although the pulses look like they vary in amplitude over the long record length, once they are sampled over a smaller range, the amplitude of each pulse will be the same. This is shown in section E.2.

E.1 Biasing SRD at different voltage levels

The effect of biasing the SRD with different biasing amplitudes are depicted in the figure below.

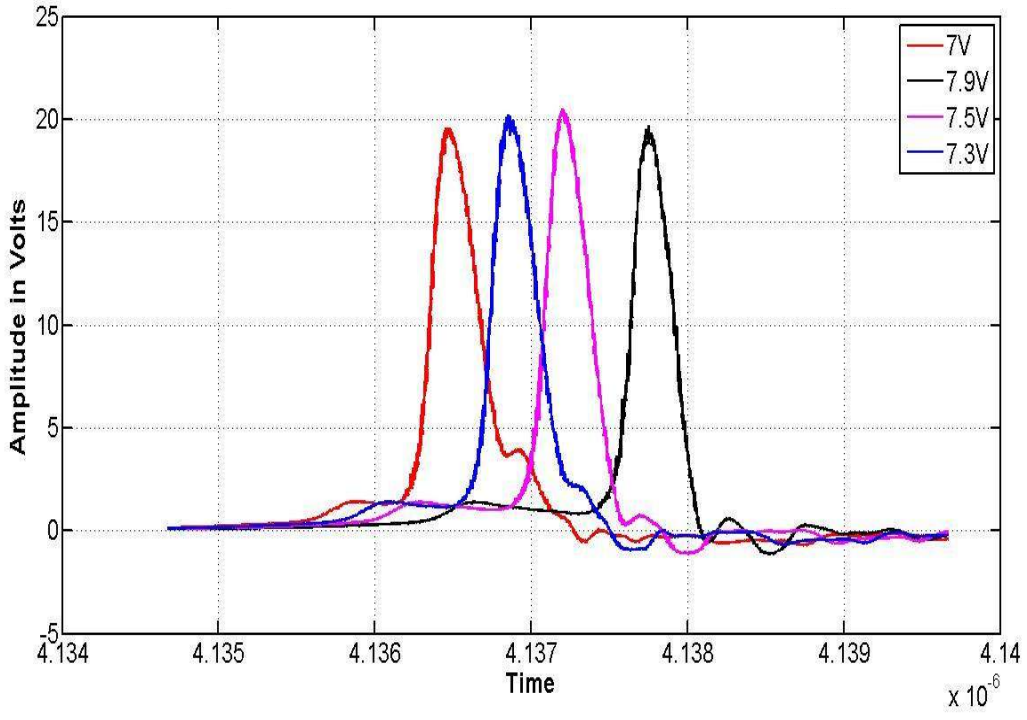

Figure E.1: SRD biased with four different biasing voltages.

Small changes (0.2 V - 0.4 V) in biasing voltage can increase the peak amplitude of the pulse. The biasing current affect the amount of charge in the SRD, which directly influences the amplitude and rise-time of the pulse.

E.2 Amplitude changes over a long record length

From figure E.2 the amplitude difference between the four pulses can be distinguished. Taking those same pulses and sampling each of them separately indicate that their amplitudes are the same. This is illustrated in E.3.

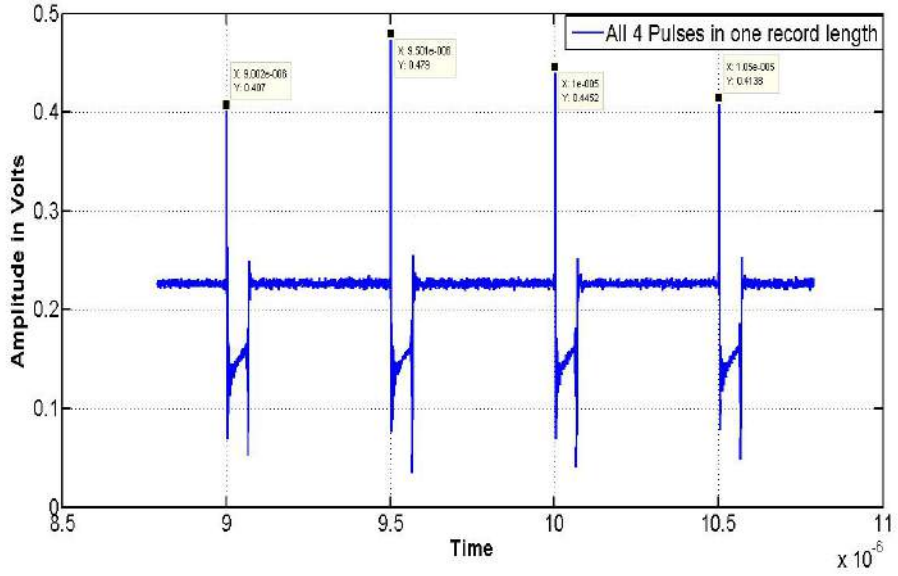

Figure E.2: All four pulses sampled in one record length with different amplitudes.

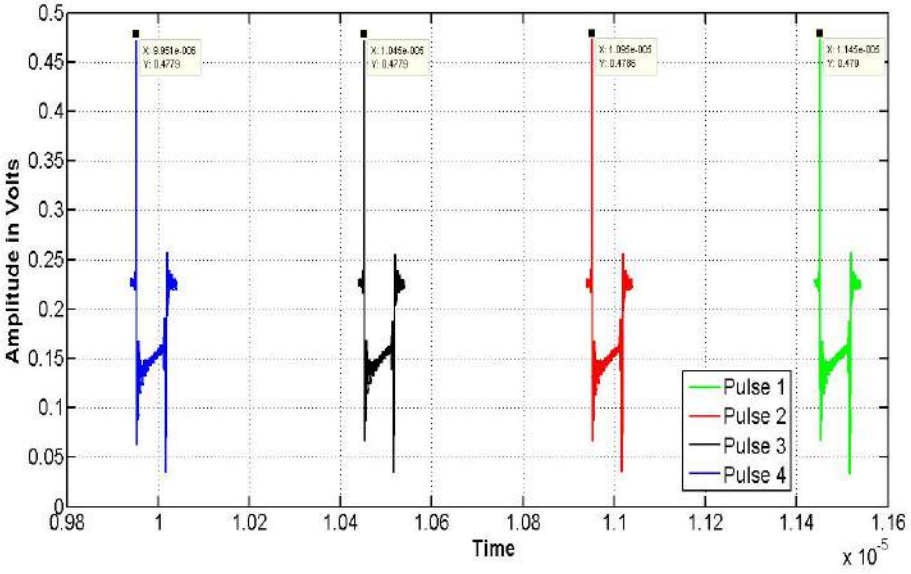

Figure E.3: All four pulses separately sampled and displayed on one graph.

Appendix F

Components and cable responses

F.1 Cable losses

The cables used during the measurements were Sucoflex phase stable cables. Some of the cable losses were measured and the others mathematically calculated from Huber and Suhner's Sucoflex datasheets. THe cable losses of a Sucoflex 104 3.1 *m* and 8 *m* cable are illustrated in figure F.1. Mathematical calculations are shown after the figure. The attenuation in the cable can be calculated by using the values in table F.1.

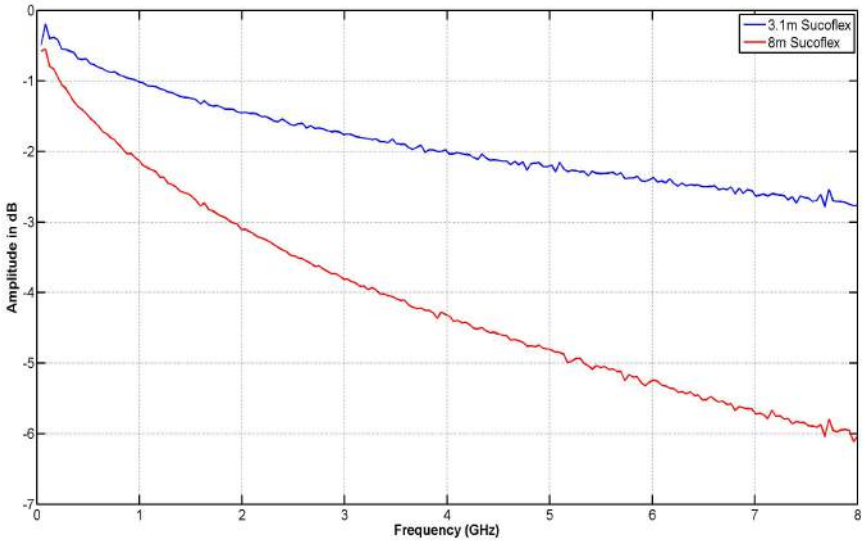

Figure F.1: Cable Losses of a Sucoflex 104 3.1 *m* and 8 *m* cable.

Frequency (GHz)	**Attenuation** (dB/m)	**Frequency (GHz)**	**Attenuation** (dB/m)
0.01	0.02	0.90	0.22
0.05	0.05	0.95	0.23
0.10	0.07	1.00	0.24
0.15	0.09	1.80	0.32
0.20	0.10	1.90	0.33
0.30	0.13	2.00	0.34
0.40	0.15	2.40	0.37
0.45	0.16	3.00	0.42
0.50	0.17	4.00	0.49
0.60	0.18	5.00	0.55
0.80	0.21	6.00	0.60
0.85	0.22	8.00	0.70

Table F.1: Cable attenuation table from Huber and Suhner

F.2 30 dB 100W and 110 dB 4 GHz attenuators spectrum

The two attenuators used during all the measurements are measured and displayed in this appendix. The 30 dB 100 W attenuator response is displayed in figure F.2 and the 110 dB variable attenuator is shown in figure F.3.

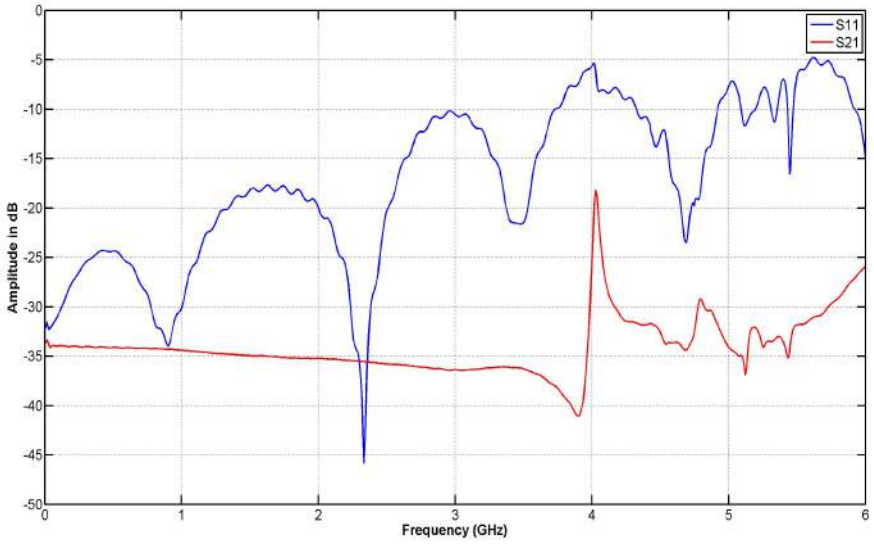

Figure F.2: Reflection and transmission coefficient of the 30 dB 100 W 1 GHz attenuator.

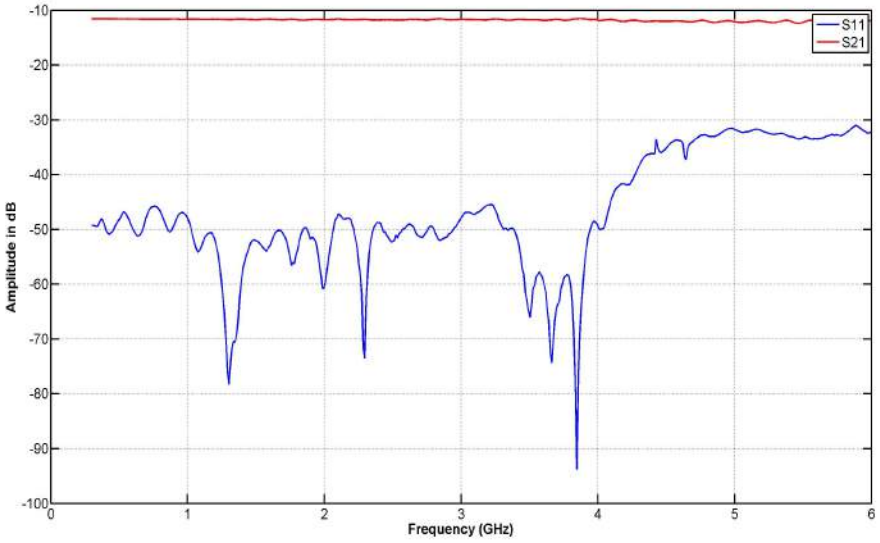

Figure F.3: Reflection and transmission coefficient of the 110 dB 4 GHz variable attenuator on a 10 dB setting.

F.3 Anechoic chamber measurements

For the three antenna measurement in chapter 5, to characterise the gain of the IRA, the Stellenbosch anechoic chamber was used. The results from these measurements are depicted in figure F.4. The gain of the IRA is also compared to the simulated gain in FEKO.

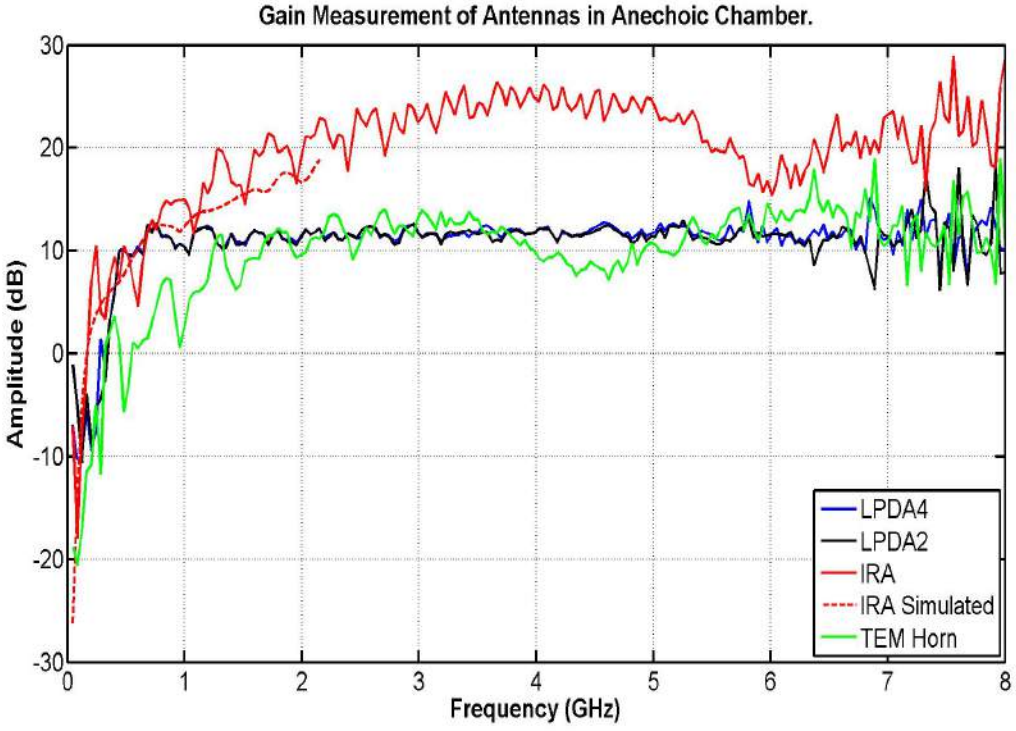

Figure F.4: Gain measurements in anechoic chamber.

F.4 GLPDA gain, reflection coefficient and antenna factor

The receiving antenna used for the measurements that were conducted in the Karoo was a PCB-LPDA antenna from [47, 49]. The characteristics of this antenna are depicted in figures F.5 - F.10. The gain, reflection coefficient and antenna factor are shown.

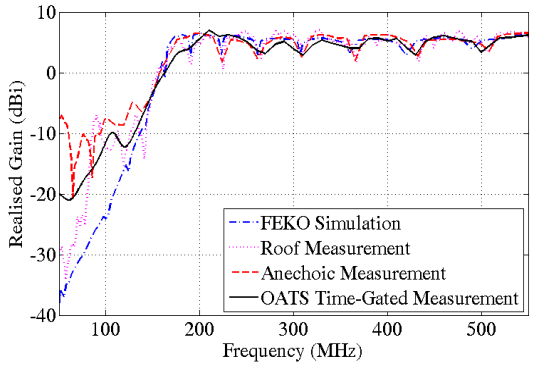

Figure F.5: GLPDA Gain at the lower frequencies.

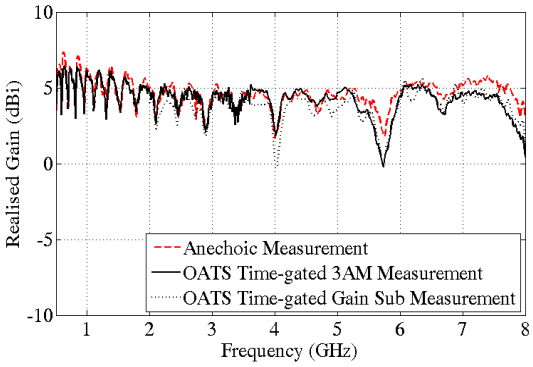

Figure F.6: GLPDA Gain.

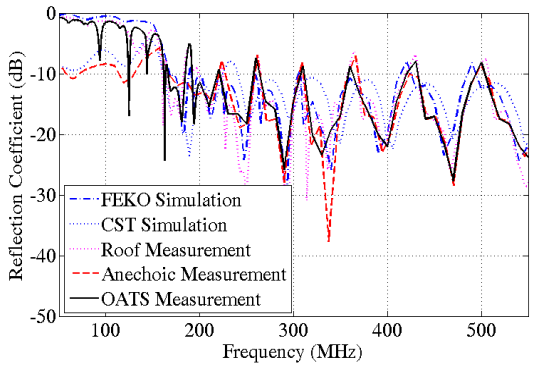

Figure F.7: GLPDA reflection coefficient at the lower frequencies.

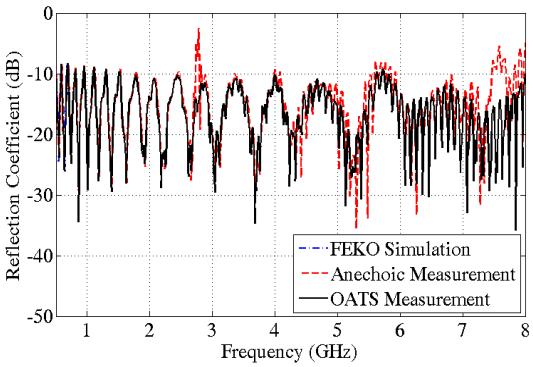

Figure F.8: GLPDA reflection coefficient.

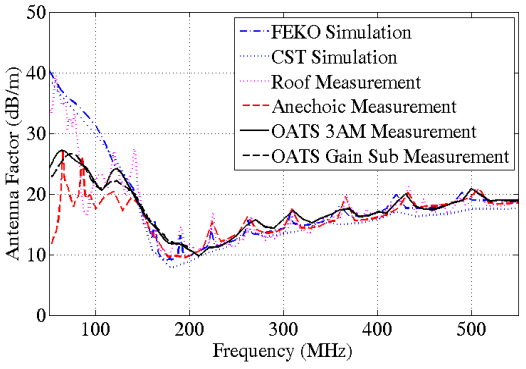

Figure F.9: GLPDA Antenna Factor at the lower frequencies.

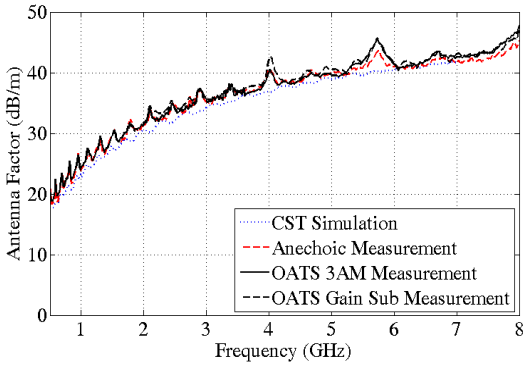

Figure F.10: GLPDA Antenna Factor.